FATIGUE DAMAGE EVOLUTION PROCESSES OF ASPHALT PAVEMENT UNDER DIFFERENT LOADING MODES: FROM LABORATORY ASSESSMENT TO FULL-SCALE APT INVESTIGATION

LI YI

PhD

The Hong Kong Polytechnic University

This program is jointly offered by The Hong Kong Polytechnic University and Tongji University

2025

The Hong Kong Polytechnic University

Department of Civil and Environmental Engineering

Tongji University

College of Transportation Engineering

Fatigue Damage Evolution Processes of Asphalt Pavement under Different Loading Modes: from Laboratory Assessment to Full-Scale APT Investigation

Li Yi

A thesis submitted in partial fulfillment of the requirements for the degree of Doctor of Philosophy

Jan 2024

CERTIFICATE OF ORIGINALITY

I hereby declare that this thesis is my own work and that, to the best of my knowledge and belief, it reproduces no material previously published or written, nor material that has been accepted for the award of any other degree or diploma, except where due acknowledgment has been made in the text.

_____ (Signed)

LI YI (李伊) (Name of student)

I dedicate this dissertation to my parents and my husband.

ABSTRACT

Fatigue damage critically threatens the integrity of asphalt pavements and remains a central challenge for reliable performance prediction. This study aims to propel this field forward by developing a predictive model that not only intricately characterizes the fatigue damage process but also reveals the role of fatigue loading modes in shaping the damage progression. This novel approach not only sheds light on the mechanisms driving fatigue progression but also bridges the gap between laboratory fatigue assessments and the fatigue behaviors observed in asphalt layers of in-service pavements. Central to the findings is the realization that fatigue damage is not solely governed by tensile fatigue loading but rather by complex tensile-shear fatigue loading modes. This key insight is pivotal for pinpointing critical damage locations within pavement structures, offering a strategic advantage for enhancing pavement design and maintenance practices.

To achieve the objective, the first task conducts an in-depth laboratory program using indirect tensile fatigue (ITFT) and four-point bending (4PB) tests. It initially examined the impact of various loading parameters, including tensile fatigue loading modes, on the initial stiffness and fatigue life of asphalt mixtures. Consequently, a versatile fatigue life equation was formulated across tensile fatigue loading modes and damage states. Subsequently, to gain a comprehensive understanding of fatigue damage progression in the laboratory setting, seven nonlinear models were explored, particularly highlighting the structural behavior function (SBF) and the Weibull survival function (WSF). This methodological approach led to a foundation for accurately modeling fatigue damage development, with the SBF distinguished from others for its reliability and applicability. Additionally, the analysis of various loading parameters, most notably the fatigue loading mode, was intricately woven into the predictive models, significantly enhancing the interpretability of the model parameters and providing a deeper insight into asphalt mixture fatigue behaviors.

The second task of this study expanded to full-scale accelerated pavement testing (F-sAPT) on in-situ asphalt layers with various types of bases, including semi-rigid and granular bases. A key fatigue damage indicator was assessed using the falling weight deflectometer (FWD), portable seismic pavement analyzer (PSPA), and uniaxial compression tests. These measurements were

further refined by applying temperature correction and frequency adjustment methodologies. The investigation then delved into analyzing the damage progressions across different depths and orientations of asphalt layers. Both the SBF and WSF proved effective in modeling the measured deterioration processes, with the SBF being recognized as accurately depicting damage evolution within pavement structures. The study's integration of field measurements with advanced analytical techniques enhanced the understanding of pavement deterioration dynamics, validating methods used and offering practical insights for future pavement damage assessment.

In the third phase of the study, a meticulous analysis of the mechanical mechanisms influencing fatigue damage in asphalt layers was conducted, leveraging the findings from F-sAPT. This investigation led to a pivotal discovery: In-situ fatigue damage in asphalt layers is not exclusively governed by tensile fatigue loading but is profoundly impacted by complex tensile-shear fatigue loading modes. The identification of these modes is critical for accurately pinpointing key damage points within asphalt layers. Additionally, a novel tensile-shear loading mode factor was proposed. This enhancement provides a more comprehensive understanding of asphalt layer fatigue and its practical implications.

The fourth task was dedicated to bridging the gap between laboratory findings and in-situ observations regarding asphalt fatigue damage. A key strategy involved the alignment of damage progression curves from controlled laboratory experiments with those observed under real-world conditions. This entailed a systematic comparison and correlation of model parameters derived from both laboratory tests and F-sAPT data. By substituting in-situ loading parameters into the laboratory-based model parameter interpretation equations, the study effectively achieved a calibrated lab-to-field translation. This approach not only validated the laboratory findings but also provided a robust framework for predicting in-situ pavement performance.

PUBLICATIONS ARISING FROM THE THESIS

[1] Chen, Z., Liang, Y., Guo, Z., **Li, Y.**, Xu, T., Liu, L., and Sun, L. A novel technique for asphalt pavement interlayer contact condition diagnosis. *Chinese Science Bulletin*, 2020, 65(30): 3318-3327.

[2] Cheng, H., Liu, L., Sun, L., **Li, Y.**, and Hu, Y. Comparative analysis of strain-pulse-based loading frequencies for three types of asphalt pavements via field tests with moving truck axle loading. *Construction and Building Materials*, 2020(247): 118519.

[3] Cheng, H., Wang, Y., Liu, L., Sun, L., Hu, Y., and **Li, Y**. Back-calculation of the moduli of asphalt pavement layer using accelerated pavement testing data. In *Accelerated Pavement Testing to Transport Infrastructure Innovation: Proceedings of 6th APT Conference*, Springer International Publishing, 2020: 379-388.

[4] Hu, Y., Sun, L., Cheng, H., and **Li, Y.** Modulus attenuation of semi-rigid asphalt pavement layer in accelerated pavement testing with MLS66. *International Journal of Transportation Science and Technology*, 2023, 1(12): 62-70.

[5] Li, C., **Li, Y.**, Hu, Y., Jin, T., and Sun, L. A new approach to measure asphalt mixture fatigue performance using the circular-plate specimens. In *Transportation Research Board 103th Annual Meeting*, Washington, D.C., 7-11 Jan. 2024.

[6] **Li, Y.**, Li, J., Cheng, H., Liu, L., and Sun, L. Asphalt Concrete (AC) modulus reduction process at various AC depths in accelerated pavement testing. In *Transportation Research Board 99th Annual Meeting*, Washington, D.C., 12-16 Jan. 2020.

[7] **Li, Y.**, Li, J., Hu, Y., and Sun, L. Frequency adjustment method for field seismic modulus of asphalt concrete. *International Journal of Pavement Engineering*, 2022, 23(7): 2342-2350.

[8] **Li, Y.**, Li, J., Liu, L., and Sun, L. Accelerated fatigue damage profile of asphalt concrete placed on semi-rigid layer. In *Accelerated Pavement Testing to Transport Infrastructure Innovation: Proceedings of 6th APT Conference*, Springer International Publishing, 2020: 90-99.

[9] **Li, Y.**, Liu, L., and Sun, L. Temperature field prediction model for thick asphalt layer. *Journal of Tongji University (Natural Science)*, 2020, 48(3): 377-382.

[10] **Li, Y.**, Ma, Z., Wang, G., Liu, L., and Sun, L. Evaluation of the cumulative fatigue damage in different asphalt layers with portable seismic pavement analyzer. In *Transportation Research Board 98th Annual Meeting*, Washington, D.C., 13-17 Jan. 2019.

[11] **Li, Y.**, Sun, L., Hu, Y., and Li, J. Modulus detection and damage analysis of asphalt layer. *China Journal of Highway and Transport*, 2020, 33(10): 304-315.

[12] **Li, Y.**, Sun, L., Lin, P., Liu, X., and Leng, Z. Diagnostic method for interlayer bonding condition of asphalt pavement. In *Advances in Materials and Pavement Performance Prediction*, Hong Kong, 22-24 May. 2023.

ACKNOWLEDGMENTS

As I am near the end of my academic journey at both The Hong Kong Polytechnic University and Tongji University, I am filled with a mix of emotions reflecting on the journey that brought me here. It is with heartfelt gratitude that I recognize the key individuals who have significantly contributed to my personal and academic development throughout this journey.

Foremost, I extend my sincerest thanks to my supervisors, Prof. SUN Lijun and Prof. LENG Zhen. Their deep insights and expertise in road engineering have been invaluable, lighting my path with their profound knowledge and guidance. They have adeptly unraveled the intricacies of this challenging field, thereby deepening my understanding and fostering a genuine appreciation for it. Their unwavering commitment and meticulous approach to research have indelibly shaped my academic endeavors. I am profoundly thankful for their mentorship and for guiding me through the complexities of road engineering.

I am equally grateful to Prof. LIU Liping, who has been a steadfast support since my undergraduate days. Her attention to detail and responsible approach towards research have ingrained in me the importance of scientific precision and integrity. Her kindness and compassion have also provided immense comfort and solace in my personal journey.

Additionally, my heartfelt thanks go to the faculty and staff at both universities. I am particularly indebted to Prof. CHEN Zhang for his assistance with FWD coordination and to Prof. TU Huizhao and XIAO Feipeng for their invaluable guidance on my first English journal paper. Their collective wisdom and support have been crucial in my academic progression. I would also like to express my appreciation to the technician team, especially CAI Chuanbin, for his invaluable guidance and assistance in experimental work, and to ZHU Tangliang, LIU Yi, and QIAO Yaoming for their help in facilitating experimental equipment and arrangements. Their support made even the most challenging days manageable.

I extend my gratitude to my senior Ph.D. colleagues, MA Zexin and ZANG Guoshuai, for their insightful advice and unwavering support. Special thanks are also to my junior Ph.D. colleagues, LI Jiahao, HU Yue, YANG Ruikang, and JIN Tian, for their instrumental help in the experimental

work. The solidarity and support within our research group have greatly enriched my academic experience, transforming the solitary pursuit of research into a collaborative and enjoyable journey.

Lastly, but most importantly, I owe the deepest gratitude to my parents and my husband for their endless care, encouragement, and understanding. Their love has been the guiding light through the challenges and triumphs, providing strength and resilience in the face of adversities. Their unconditional support, beautifully encapsulated in their assurance that ‘Your success is not what matters most to us,’ will forever be a source of inspiration and courage.

With deepest appreciation,

LI Yi

TABLE OF CONTENTS

1 INTRODUCTION

Asphalt pavements are integral to contemporary road infrastructure, underpinning the vast networks that bolster modern transportation systems. The pivotal role of these pavements extends beyond mere facilitation of travel; they are instrumental in the seamless movement of goods, people, and services, which in turn fuels social and economic development. The effectiveness and reliability of transportation networks are intrinsically linked to the condition and durability of asphalt pavements. Ensuring pavements remain in optimal condition is crucial for maintaining high service levels, encompassing user safety, comfort, and efficiency.

Nevertheless, the performance and longevity of asphalt pavements are constantly challenged by various types of distress, including cracking, permanent deformation, and raveling. Of particular concern is fatigue cracking, predominantly induced by repetitive vehicle loads. This type of distress results from the cumulative effect of vehicular stress or strain, gradually diminishing the stiffness of the asphalt layers and, consequently, undermining the structural integrity and functional capabilities of pavements. Issues such as traffic safety, ride comfort, and noise reduction are all adversely impacted by the onset of fatigue cracking.

Confronting these challenges, pavement engineers and managers are tasked with maintaining road networks to an acceptable standard, ensuring they meet both functional and structural requirements. However, in heavily trafficked pavements, frequent maintenance can lead to undesirable disruptions in traffic flow, reduced network availability, and increased congestion. This dilemma necessitates a balance between maintaining road quality and minimizing network disruptions. The solution lies in developing cost-effective, long-lasting, and low-maintenance pavement solutions. Such an approach demands precise prediction models for pavement fatigue performance, which should be integral to pavement design methodologies. These models are also essential for predicting the timing, type, and extent of maintenance required to maintain pavements in prime condition.

Given this context, the fatigue performance of asphalt pavements has emerged as a focal point of research in pavement engineering. The investigation into this issue dates back to the early studies by Porter in 1942 [38] and has since evolved into a sophisticated field of study.

1.1 Fatigue Life

Research spanning over seven decades in fatigue performance of asphalt layers and mixtures has led to significant advancements and the evolution of diverse analytical methods. Key among these are phenomenological approaches, dissipated energy theory, continuum damage mechanics, and fracture mechanics. These methodologies have been developed to analyze fatigue life, which means the number of load cycles an asphalt mixture can withstand before failure occurs, offering insights from macroscopic, mesoscopic, and microscopic perspectives. This multifaceted approach has enabled a continuous refinement of theories, enriching the understanding of fatigue performance and contributing to the field's ongoing advancement.

The phenomenological approach represents the foundational and most prevalent methodology employed in analyzing fatigue life within asphalt pavement engineering. Central to this approach is establishing a quantifiable relationship between the fatigue life of asphalt mixtures and their respective stress or strain responses. This method has found extensive application across diverse pavement design frameworks, notably including the Shell, Asphalt Institute (AI), and Mechanistic-Empirical (M-E) pavement design methods [18]. Despite its widespread usage, the phenomenological approach exhibits certain limitations, particularly in treating fatigue damage. Notably, it does not comprehensively encapsulate the cumulative nature of fatigue damage arising from repetitive loading. The approach's analytical outcomes are inherently influenced by several key factors: the specific definition adopted for fatigue life, the methodologies employed in testing, and the characteristics of the fatigue loading modes [7,29]. These dependencies may lead to variability in the interpretation and application of the results, highlighting a need for careful consideration in its use.

The dissipated energy theory, initially proposed by Van Dijk [34], provides an insightful analysis of the energy dissipation characteristics in linear viscoelastic materials subjected to loading. Central to this theory are several key indices: the initial dissipated energy [25,33], which indicates

the energy loss during the early loading cycles; the cumulative dissipated energy [33,35], representing the total energy dissipated over the material's lifespan; the Dissipated Energy Ratio (DER) [1], a metric for assessing the proportion of energy lost per loading cycle; and the Ratio of Dissipated Energy Change (RDEC) [2,6], which measures the rate of change in energy dissipation as fatigue progresses. These indices provide a detailed framework for evaluating the fatigue life of asphalt mixtures. By focusing on the energy aspects of material response under load, the dissipated energy theory offers a more sophisticated and refined understanding of fatigue damage mechanisms in asphalt mixtures, surpassing the insights offered by traditional phenomenological approaches.

The continuum damage mechanics approach, anchored with constitutive equations [32], elucidates the mechanical laws that trace the evolution of damage as it correlates with deformation and delineates the pathway leading to eventual failure. This approach bifurcates into two primary methodologies [18]: the effective stress-based approach and the Viscoelastic Continuum Damage (VECD) model. The former, deeply rooted in the concepts of effective stress and strain equivalence principle [8,14], quantifies damage through the modulus reduction ratio to provide a tangible measure of the material's deterioration. The approach further extends to formulate damage evolution equations that intricately link the material's stress response to its evolving damage state [3,4,13]. In contrast, VECD, leveraging Schapery's viscoelastic constitutive equations [26,28], focuses on predicting the fatigue life of asphalt mixtures by analyzing fatigue behavior under continuous damage conditions. This method distinguishes itself by employing a pseudo-stiffness metric, a novel approach that effectively captures the ongoing damage parameters within the asphalt mixtures [10,12]. Despite providing a detailed understanding of initial microcracking stages, continuum damage mechanics faces challenges in accurately depicting macroscopic crack propagation and in the complexity of applying these models to in situ pavement structures, thus limiting its direct applicability in real-world scenarios.

The fracture mechanics approach delineates fatigue cracking in asphalt pavements into three stages: initiation, stable crack propagation, and unstable fracture, as noted in various studies [19]. This method predominantly utilizes Paris' Law to articulate the dynamics of steady crack growth [23]. In-depth investigations have involved monitoring variations in crack length and opening displacement within the plastic zone. Through these observations, researchers have established a correlation between stress intensity factors at crack tips and crack propagation rates, facilitating

more accurate fatigue life predictions. This approach comprehensively incorporates the viscoelastic properties of asphalt [27] alongside considerations of its self-healing capabilities [16,17,37] and varying degrees of aging [15] of asphalt. Despite its effectiveness in describing macroscopic crack propagation, fracture mechanics primarily addresses the stable phase of crack growth and relies heavily on extensive empirical data for accurate crack growth rate assessments. Additionally, its reliance on temperature-sensitive stress intensity factors [30] adds a layer of complexity, especially under varying environmental conditions.

In summary, the theoretical landscape for analyzing the fatigue performance of asphalt mixtures has undergone significant development and refinement over the past seventy-plus years. Researchers have applied diverse analytical approaches to assess the fatigue life of asphalt mixtures, achieving substantial and practical outcomes. Despite these advancements, translating these theoretical insights into practical, in situ assessments of fatigue performance in actual pavement structures continues to be a complex and largely uncharted domain. This gap underscores the need to further explore and adapt these models to real-world conditions. Additionally, while the bulk of existing research has concentrated on evaluating fatigue life, there is a notable lack of studies that systematically track the progression of fatigue damage. This area, vital for a comprehensive understanding of pavement longevity and performance, presents a fertile ground for future research endeavors.

1.2 Fatigue Damage

In the evolving field of asphalt fatigue research, the scope of inquiry has broadened significantly. The primary focus has transitioned from merely assessing the fatigue life of asphalt layers and mixtures to a more nuanced understanding of the fatigue damage process. This process is recognized as helping design more durable asphalt pavement and predict the timing, type, and extent of maintenance required to maintain pavements in prime condition. To effectively analyze and track this evolution, there is a pressing need to identify a damage variable that possesses a well-defined physical significance and is practically measurable.

In addressing this need, the field of damage mechanics has become integral to the analysis process. This theoretical framework employs a damage variable as a vital tool for examining the

mechanisms of material deterioration under repetitive loads. Fatigue damage, within the realm of damage mechanics, is characterized across multiple scales: micro, meso, and macro scales. At the micro level, fatigue damage is manifested through micro-stress accumulation. These stresses are typically localized around structural irregularities within the material, such as crystal grain dislocations, slips, micro-voids, or micro-cracks [5]. At this granular level, the initial signs of fatigue begin to emerge. Moving to the mesoscopic level, fatigue damage encompasses the growth and merging of micro-defects, culminating in the initiation of cracks. This process is aptly described by the VECD theory, which employs the concept of pseudo-stiffness as a continuous damage variable to characterize the evolution of fatigue damage [9,11]. At the broadest scale, fatigue damage is observable through the deterioration of the material's physical and mechanical properties [38], such as modulus reduction. This decline is a macroscopic manifestation of the cumulative effects of damage at the micro and meso levels. Utilizing these visible physical-mechanical indicators as variables provides a practical means to quantify the extent of fatigue damage in asphalt layers and mixtures.

Based on the various fatigue damage variables proposed, researchers have been able to quantify the extent of fatigue damage. This has facilitated the development of diverse evolutionary models for fatigue damage, each offering unique insights into the progression of damage under different conditions. These models can be broadly categorized into three distinct types, each underpinned by a different foundational principle, and will be reviewed in detail in Chapter 2.

The first is the model based on Miner's rule. These models employ Miner's linear cumulative damage rule, a widely recognized approach in fatigue analysis. This rule is based on the principle that fatigue damage accumulates linearly with repeated loading. Models rooted in this rule are known for their simplicity and ease of application. However, they tend to oversimplify the fatigue process by not accounting for the nonlinearity of fatigue damage progression, which can lead to conservative estimations.

The second type of model derives from the principles of continuum damage mechanics and offers a nonlinear approach to modeling fatigue damage development. They are characterized by their ability to link damage evolution directly to the loading process, considering variables such as stress amplitude, mean stress, temperature, and loading frequency. This category represents a more sophisticated modeling approach, capturing the complexities of fatigue damage more accurately

than linear models. However, the complexity of these models and the challenge of determining accurate material parameters can limit their practical application in field conditions.

The third category of models incorporates the stiffness reduction ratio (SRR) as a pivotal variable in monitoring fatigue damage. These models are notably effective in depicting the nonlinear characteristics of fatigue damage and are appreciated for their simplicity and practical application value in engineering contexts. However, they do not fully address the interaction of numerous influencing factors, lacking a direct representation of their comprehensive impact on the damage process. Moreover, these models often do not reflect the relationship between laboratory and in-situ fatigue characteristics. A significant proportion of these models remain at the experimental laboratory stage without verification in real-world asphalt pavement scenarios. This gap raises questions about their applicability and reliability in actual pavement conditions.

In summary, despite developing various models to measure and predict fatigue damage in asphalt mixtures, current research remains somewhat nascent, especially concerning the evolution of fatigue damage in real-world asphalt layers. A significant gap persists between the theoretical models derived from laboratory settings and their practical applicability in in-situ pavement analysis. This disconnect is primarily due to the complex interplay of factors influencing fatigue damage and the intricacies of the damage evolution process, which are not fully captured in laboratory-based models. The need for future research is thus evident, focusing on bridging this gap by enhancing the understanding and modeling of fatigue damage in a manner that is both theoretically robust and practically viable for real-world pavement engineering. This involves developing predictive models that not only accurately characterize the fatigue damage process but also adapt seamlessly to the dynamic conditions of in-situ pavements. Such advancements are crucial for a more comprehensive and effective approach to assessing fatigue in asphalt pavements, ensuring the models' relevance and utility in actual pavement maintenance and management.

1.3 Influencing Factors of Fatigue

A wide array of factors influences the evolution of fatigue damage in asphalt pavements, each adding to the complexity of this process. Gaining a precise understanding of the impact of each factor on fatigue damage is essential for a thorough analysis of fatigue damage progression. Such

an understanding is key to correlating the fatigue behavior observed in laboratory-prepared asphalt mixtures with that in in-situ asphalt layers. This in-depth analysis is vital for developing accurate predictive models and formulating effective pavement design and maintenance strategies.

Research has effectively classified the factors influencing asphalt fatigue life into two primary categories: internal and external. When examining internal factors, a substantial body of research highlights a distinct correlation between the stiffness modulus of asphalt mixtures and their susceptibility to fatigue damage. These observations underline those factors affecting the stiffness modulus - such as the type and content of asphalt, air void content, aggregate type, and gradation – which are integral in determining the fatigue life of asphalt mixtures.

External factors influencing fatigue life in asphalt pavements primarily include load-related factors and environmental considerations. Among environmental factors, temperature has been the principal focus of current research. Regarding loading factors, critical aspects encompass the loading duration, frequency, waveform, and the rest period between loads.

Another particularly crucial external factor is the fatigue loading mode, defined as the method by which stress and strain vary during repeated loading [30]. Research indicates a strong correlation between the fatigue life of asphalt layers and their fatigue loading mode [20,24,25,31], influencing asphalt material design choices.

Pioneering research by Monismith and Deacon [21,22] introduced the concept of mode factor (MF) to quantify the fatigue loading mode in asphalt layers. Utilizing multi-layer elastic theory, their studies analyzed various asphalt pavement structures under repetitive loading. They investigated how tensile stress and strain at the bottom of the asphalt layer change following a reduction in average stiffness modulus and how MF varies with the layer's thickness. Findings from their research suggest that asphalt layers thicker than 15.24 cm (6 inches) are best suited to a controlled stress mode, while layers thinner than 5.08 cm (2 inches) align more with a controlled strain mode. In 2004, Witczak and El-Basyouny [36] applied similar principles in developing and calibrating a fatigue cracking model for the M-E design guidelines. However, their study differed because it deemed asphalt layers over 20.32 cm (8 inches) appropriate for a controlled stress mode. They posited a combined controlled stress and strain mode for intermediate thicknesses (between 5.08 cm and 20.32 cm). However, their research did not conclusively determine the precise loading mode for these intermediate thicknesses.

According to these two studies, currently, two main fatigue loading modes are adopted in laboratory tests of asphalt mixtures: the stress-controlled mode, where the load force or stress magnitude remains constant, and the strain-controlled mode, where the specimen's deformation or strain magnitude is kept constant. However, the effectiveness of these laboratory-established loading modes in realistically simulating the loading conditions of in-situ asphalt pavements remains a subject of ongoing debate and research.

1.4 Challenges and Objectives

Despite notable advancements over the past seventy-plus years, the study of fatigue damage of asphalt pavements continues to present significant challenges. While extensive research has been dedicated to understanding the fatigue life of asphalt mixtures and employing various analytical methods, a considerable gap remains in the comprehensive tracking and analysis of fatigue damage progression in real-world asphalt layers. This shortfall is particularly critical given the complexity of factors that influence fatigue damage and the intricate nature of its evolution process. The absence of thorough studies in this area limits the understanding of pavement longevity and performance, underscoring the pressing need for future research efforts. These efforts should aim to provide deeper insights into the fatigue damage processes occurring within in-situ asphalt layers.

Second, a significant challenge in fatigue damage research is the absence of extensive studies on the most suitable fatigue loading modes for asphalt pavements. Research to date indicates that thicker asphalt layers exceeding 20.32 cm (8 inches) are generally best suited for controlled stress loading modes, whereas layers thinner than 5.08 cm (2 inches) tend to correspond more effectively with controlled strain modes [36]. This dichotomy, however, poses a challenge because most asphalt layers are of intermediate thickness, making the selection of an appropriate loading mode complex. Additionally, the real-world efficacy of the fatigue loading modes commonly used in laboratory tests, which are intended to emulate in-situ pavement conditions, remains a subject of ongoing debate and investigation.

Last, despite the advancement of various theoretical models for predicting fatigue damage in asphalt mixtures, the field is still relatively nascent, especially in terms of translating these models into practical assessments for in-situ asphalt layers. A significant gap persists between theoretical

models developed under controlled laboratory conditions and their application in real-world pavement scenarios. This disparity arises from the complex interplay of factors influencing fatigue damage and the intricate nature of its progression, which are not always fully captured or replicated in laboratory settings. Thus, there is a clear and pressing need for future research to bridge this gap. Future studies should establish a more direct and applicable relationship between laboratory-tested asphalt mixtures and the fatigue damage observed in actual pavement structures, thereby enhancing the practical utility of these models in pavement engineering and maintenance.

Addressing these identified challenges, this research seeks to advance the understanding of fatigue damage evolution in asphalt pavements by meticulously analyzing both in-situ asphalt layers and laboratory-prepared asphalt mixtures. Central to this endeavor is the development of a nuanced analytical method that comprehensively examines fatigue loading modes, coupled with establishing a robust relationship between indoor and field fatigue damage. Therefore, this research is geared towards an objective: to provide a detailed characterization of the fatigue damage process that elucidates the role of fatigue loading modes in its progression and bridge the gap between laboratory fatigue assessments and the fatigue behaviors observed in asphalt layers. This innovative approach is expected to significantly refine the accuracy of fatigue damage identification and prediction in real-world pavement scenarios. By bridging the theoretical insights gained from laboratory assessments with the practical observations of fatigue behaviors in service, the research will offer critical insights into the mechanics driving fatigue progression. This will not only enhance the precision of asphalt pavement design but also provide strategic insights for optimizing pavement maintenance practices. The culmination of these efforts is anticipated to pinpoint critical damage areas within pavement structures, thereby transforming current practices and theories in pavement engineering.

1.5 Organization of the Dissertation

This dissertation consists of the following eight chapters:

Chapter 1: Introduction. This chapter sets the stage by introducing the critical aspects of fatigue life and damage in asphalt pavements. It outlines the three primary challenges in current fatigue damage research and defines the research objectives.

Chapter 2: Literature Review. Divided into five parts, this chapter presents a comprehensive literature review covering fatigue test methods, analytical approaches for fatigue life, the evolution process of fatigue damage, and the various influencing factors, including fatigue loading modes. It also explores methodologies for correlating laboratory findings with in-situ fatigue behaviors.

Chapter 3: Methodology. This chapter details the research approach and methodologies employed in the study, laying out the framework for the experimental and analytical processes.

Chapter 4: Analysis of Fatigue Damage in Laboratory Asphalt Mixtures. Focusing on laboratory analysis, this chapter discusses the fatigue behaviors of asphalt mixtures using ITFT and 4PB tests. It explores the development of a versatile fatigue life equation and the application of seven nonlinear predictive models to characterize fatigue damage progressions. It also integrates various loading parameters, most notably the tensile fatigue loading mode, into the predictive models to enhance the interpretability of the model parameters and provide a deeper insight into asphalt mixture fatigue behaviors.

Chapter 5: Analysis of Fatigue Damage in In-Situ Asphalt Mixtures. This chapter extends the research to full-scale accelerated pavement testing on in-situ asphalt layers, employing various testing techniques to assess key fatigue damage indicators. It analyzes and predicts damage progressions in pavement layers and recommends practical predictive models.

Chapter 6: Fatigue Loading Modes and Critical Damage Locations in Asphalt Layers. This chapter presents an analysis of the mechanics of fatigue damage in asphalt layers, highlighting a pivotal discovery from the study's third phase. The chapter also discusses how these mechanics affect the identification of critical damage points within asphalt layers and the fatigue loading modes.

Chapter 7: Relationship between Laboratory and In-situ Asphalt Fatigue Damage. Dedicated to establishing a correlation between laboratory and in-situ fatigue damage models, this chapter presents a systematic comparison and correlation of model parameters derived from both laboratory tests and F-sAPT data. By substituting in-situ loading parameters into the laboratory-derived model parameters, the chapter shows a calibrated lab-to-field translation.

Chapter 8: Conclusions and Contributions. The final chapter synthesizes the findings, conclusions, and recommendations from the research, highlighting the contributions to the field of pavement engineering.

References

[1] Carpenter, S. H., & Jansen, M. Fatigue behavior under new aircraft loading conditions. In *Proceedings of Aircraft Pavement Technology in the Midst of Change*. Seattle: American Society of Civil Engineering, 1997:259-271.

[2] Carpenter, S. H., Khalid, A., Ghuzlan, K., & Shen, S. A fatigue endurance limit for highway and airport pavement. *Journal of Transportation Research Record*, 2003, 1832:131-138.

[3] Chaboche, J. L. Continuous damage mechanics - a tool to describe phenomena before crack initiation. *Nuclear Engineering & Design*, 1981, 64(2):233-247.

[4] Chaboche, J. L., & Lesne, P. M. A non-linear continuous fatigue damage model. *Fatigue & Fracture of Engineering Materials & Structures*, 1988, 11(1):1-17.

[5] Ghuzlan, K A. *Fatigue damage analysis in asphalt concrete mixtures based upon dissipated energy concepts*. Urbana: University of Illinois at Urbana-Champaign, 2001.

[6] Ghuzlan, K. A., & Carpenter, S. H. An energy-derived/damage-based failure criteria for fatigue testing. *Journal of Transportation Research Record*, 2000, 1723:131-141.

[7] Ghuzlan, K. A., & Carpenter, S. H. Fatigue damage analysis in asphalt concrete mixtures using the dissipated energy approach. *Canadian Journal of Civil Engineering*, 2006, 33(7):890-901.

[8] Kachanov, L. M. Rupture time under creep conditions. *International Journal of Fracture*, 1999, 97, 1:11-18.

[9] Kim, R. Y., & Little, D. N. One-dimensional constitutive modeling of asphalt concrete. *Journal of Mechanics*, 1990, 116(4):751-772.

[10] Kim, R. Y., Lee, H. J., & Little, D. N. Fatigue characterization of asphalt concrete using viscoelasticity and continuum damage theory. *Journal of the Association of Asphalt Paving Technologists*, 1997, 66:520-569.

[11] Kim, Y. R., Baek, C., Underwood, B. S., et al. Application of viscoelastic continuum damage model based finite element analysis to predict the fatigue performance of asphalt pavements. *KSCE Journal of Civil Engineering*, 2008, 12(2):109-120.

[12] Lee, J. H., & Kim, R. Y. Viscoelastic constitutive model for asphalt concrete under cyclic loading. *Journal of Engineering Mechanics*, 1998, 124(1):32-40.

[13] Lemaitre, J. Coupled elasto-plasticity and damage constitutive equations. *Computer Methods*

in Applied Mechanics and Engineering, 1985, 51(1-3):31-49.

[14] Lemaitre, J., & Chaboche, J. L. Aspect phénoménologique de la rupture par endommagement. *Journal De Mecanique Appliquee*, 1978, 2(3):317-365.

[15] Luo, X., Luo, R., & Lytton, R. L. Modified Paris's Law to predict entire crack growth in asphalt mixtures. *Journal of Transportation Research Record*, 2013, 2373:54-62.

[16] Lytton, R. L., Gu, F., Zhang, Y., et al. Characteristics of undamaged asphalt mixtures in tension and compression. *International Journal of Pavement Engineering*, 2018, 19(3):192-204.

[17] Lytton, R. L., Uzan, J., Fernando, E. G., et al. *Development and validation of performance prediction models and specifications for asphalt binders and paving mixes*. Washington, D.C.: Strategic Highway Research Program, 1993.

[18] Ma, Z. *Research on the fatigue performance and the method for estimation of remaining fatigue life of in-service asphalt mixture*. Shanghai: Tongji University, 2018.

[19] Majidzadeh, K., Kauffmann, E. M., & Ramsamooj, D. V. Application of fracture mechanics in the analysis of pavement fatigue. *Journal of the Association of Asphalt Paving Technologists*, 1971, 40:227-246.

[20] Monismith, C. L. *Fatigue response of asphalt-aggregate mixes*. Washington, D.C.: Strategic Highway Research Program, 1994.

[21] Monismith, C. L., & Deacon, J. A. Fatigue of asphalt paving mixtures. *Transportation Engineering Journal of ASCE*, 1969, 95(2):317-346.

[22] Monismith, C. L., Inkabi, K., McLean, D. B., et al. *Design consideration for asphalt pavements*. Berkeley: University of California, Berkeley, 1977.

[23] Paris, P. C., & Erdogan, F. A critical analysis of crack propagation laws. *Journal of Basic Engineering*, 1963, 85(4):528-533.

[24] Pell, P. S. Characterization of fatigue behavior. In *Proceedings of 52nd Annual Meeting of the Highway Research Board*. Columbia: Highway Research Board, 1973:49-64.

[25] Rowe, G. M. Performance of asphalt mixtures in the trapezoidal fatigue test. *Journal of Asphalt Paving Technologists*, 1993, 62:344-384.

[26] Schapery, R. A. A theory of crack initiation and growth in viscoelastic media. *International Journal of Fracture*, 1975, 11(1):141-159.

[27] Schapery, R. A. A method for predicting crack growth in nonhomogeneous viscoelastic media.

International Journal of Fracture, 1978, 14(3): 293-309.

[28] Schapery, R. A. Correspondence principles and a generalized j integral for large deformation and fracture analysis of viscoelastic media. *International Journal of Fracture*, 1984, 25(3):195-223.

[29] Shen, S., & Carpenter, S. H. *Dissipated energy concepts for HMA performance: fatigue and healing*. Urbana: University of Illinois at Urbana-Champaign, 2006.

[30] Tangella, S. C., Craus, J., Deacon, J. A., et al. *Summary report on fatigue response of asphalt mixtures*. Washington, D.C.: Strategic Highway Research Program, 1990.

[31] Tsai, B. W. *High-temperature fatigue and fatigue damage process of aggregate-asphalt mixes*. Berkeley: University of California, Berkeley, 2003.

[32] Underwood, B. S., Kim, Y. R., & Guddati, M. N. Improved calculation method of damage parameter in viscoelastic continuum damage model. *International Journal of Pavement Engineering*, 2010, 11(6):459-476.

[33] Van Dijk, W. Practical fatigue characterization of bituminous mixes. *Journal of Asphalt Paving Technologists*, 1975, 44:38.

[34] Van Dijk, W., Moreaud, H., Quedeville, A., & Uge, P. The fatigue of bitumen and bituminous mixes. In *Proceedings of Third International Conference of the Structural Design of Asphalt Pavements*. London: International Society for Asphalt Pavement, 1972:354-366.

[35] Van Dijk, W., & Visser, W. The energy approach to fatigue for pavement design. *Journal of Asphalt Paving Technologists*, 1977, 46:1-40.

[36] Witczak, M. W., & El-Basyouny, M. M. *Guide for mechanistic-empirical design of new and rehabilitated pavement structures (Appendix ii-1: calibration of fatigue cracking models for flexible pavements)*. Champaign: ARA, Inc., ERES Division, 2004.

[37] Zhang, Y., Gu, F., Birgisson, B., et al. Viscoelasticplastic–fracture modeling of asphalt mixtures under monotonic and repeated loads. *Journal of Transportation Research Record*, 2017, 2631:20-29.

[38] Zhu, J. *Evaluation and critical damage position for fatigue behavior of asphalt pavement considering the full temperature profile*. Shanghai: Tongji University, 2016.

2 LITERATURE REVIEW

This chapter unfolds with an in-depth literature survey intricately aligned to the specific areas of interest pertinent to this research. Focused on the critical aspect of fatigue in asphalt mixtures and layers—a key determinant of pavement longevity and durability—the initial section delves into various test methods and the evolution of analytical approaches for assessing fatigue life in these materials. Attention then shifts to the central theme of this study: the mechanisms of fatigue damage and their progression in asphalt. This is followed by an analysis of the key factors influencing this progression, with a particular emphasis on the different modes of fatigue loading. Concluding the chapter, the methodologies used to correlate laboratory research outcomes with actual in-situ performance are explored, an essential step for applying theoretical insights to real-world pavement scenarios.

2.1 Test and Analytical Methods for Fatigue Life

2.1.1 Overview of Test Methods

This section provides a comprehensive overview of the prevalent testing methodologies utilized in the fatigue analysis of asphalt mixtures. It focuses on categorizing various test types, which encompass laboratory tests, accelerated pavement testing (APT), and field road tests. Additionally, the section discusses the relevance and application of these tests in diverse scenarios, ensuring a clear understanding of their practical utility in fatigue studies.

2.1.1.1 Laboratory Fatigue Tests

Significant advancements have been made in asphalt mixture fatigue research over the past several decades, particularly in developing various laboratory fatigue testing methods. These methods are essential for accurately simulating the fatigue behavior of asphalt mixtures. Among the most utilized testing methods are the four-point bending test (4PB), two-point bending test (2PB), uniaxial tensile fatigue test (UTFT), and the indirect tensile fatigue test (ITFT). For a visual reference, photographs of these four test methods are presented in Figure 2-1.

(a) 4PB

(b) 2PB

(c) UTFT

(d) ITFT

Figure 2-1 Laboratory fatigue testing methods: (a) 4PB, (b) 2PB, (c) UTFT, and (d) ITFT

The 4PB test method, standardized in 1994 by the Strategic Highway Research Program (SHRP) [80], is a widely recognized method for laboratory fatigue testing. This method is often chosen for its capacity to operate both stress-controlled and strain-controlled loading modes. Several significant advantages distinguish this method: it ensures a uniform stress distribution across the specimen's mid-section, provides an effective means for evaluating the impact of void ratios on fatigue life, and delivers results with high reliability and consistency. Its widespread use in determining the fatigue properties of asphalt mixtures and in studying the healing properties of fatigue damage and fatigue limits has cemented its status as a fundamental tool in the field.

The 2PB test method originated in France and has become a crucial component in asphalt mixture fatigue testing and significantly influences pavement structure design, particularly in Europe. This method is highly regarded for its efficiency. It utilizes the same equipment and specimens for measuring fatigue characteristics and determining the dynamic modulus of the material. In comparative studies, such as the SHRP-A-404 project [21], the 2PB test has been assessed alongside the 4PB method. These studies reveal that the results obtained from both methods are largely comparable, with no significant differences. However, the 4PB test offers a slight advantage in terms of testing convenience, as it does not require the attachment of specimens.

The UTFT is a method primarily employed in the United States, prized for its capacity to produce uniform stress and strain in test specimens consistently. Despite its advantages, the UTFT method has its challenges. A significant limitation is the necessity for specimen adhesion, which can complicate the testing procedure. Additionally, the unpredictable nature of crack formation within the specimen during tests poses a risk to the dependability of the findings. Kim et al. [17,89] have innovatively applied the viscoelastic continuum damage model to evaluate the fatigue performance using data derived from UTFT. This approach has substantially contributed to fatigue research, enhancing our understanding of the fatigue behavior of asphalt mixtures.

The IDFT is recognized for its efficient and straightforward testing mechanism, particularly notable for its stress-controlled mode that significantly reduces test durations. Xu et al. [99] have conducted an extensive comparative study between bending fatigue tests and IDFT, uncovering a discernible correlation between their results. Highlighting the IDFT's advantages, such as its simplicity, reduced testing time, and high repeatability, they advocate for its adoption as the optimal method for conducting laboratory fatigue testing of asphalt mixtures. Furthermore, research by Kim et al. [39,40] has demonstrated that the outcomes obtained through IDFT align effectively with the principles of viscoelastic continuum damage mechanics, underscoring the test's applicability and reliability in this context.

Beyond the laboratory fatigue testing methods previously mentioned, researchers have utilized diverse test methodologies to examine the fatigue characteristics of asphalt mixtures. These methods encompass the uniaxial tension-compression test [50], overlay tester [27,104], UGR-FACT [67], semi-circular bend fatigue test [35], indirect tensile asphalt cracking test (IDEAL-CT), and Overlay Test (OT). Notably, IDEAL-CT screens mixture cracking susceptibility under monotonic tensile-dominated states and provides an orthogonal brittleness indicator quantitatively related to early-stage fatigue damage slope. The OT evaluates reflective-cracking under cyclic joint opening and corresponds to a strain-controlled regime. Here, OT findings conceptually bracket high-strain conditions and help interpret the mode factor spectrum when relating lab parameters to field responses. The findings derived from these tests demonstrate a significant correlation with both the commonly used fatigue testing procedures and the real-world fatigue behavior observed in asphalt mixtures. Despite their relevance, these methods are less widely used in practice, and thus, a detailed discussion of them is not included in this context.

The diverse range of laboratory fatigue tests available equips researchers with a comprehensive toolkit for assessing the fatigue properties of asphalt mixtures. Due to the variability of results contingent on the testing methods and conditions used, it is imperative for researchers to meticulously select methods and conditions that are congruent with their specific research goals. This selection process plays a pivotal role in precisely evaluating the fatigue performance and enabling the derivation of conclusions that are pertinent and applicable to real-world scenarios.

2.1.1.2 Accelerated Pavement Testing (APT)

APT is a specialized technique used in pavement engineering to assess the long-term performance of pavement structures. This approach involves the controlled application of wheel loads, typically at or above standard legal limits, to a pavement system. The objective is to replicate the cumulative effects of real-world traffic and environmental conditions over an extended period but within a significantly condensed timeframe. This test method allows engineers to monitor and analyze the pavement's responses and behaviors. This accelerated simulation of traffic loads offers valuable data for understanding and predicting how pavements will behave under actual service conditions. The process yieldsreliable insights for advancing pavement technology and enhancing road durability.

APT is primarily divided into two distinct categories: full-scale tests and scaled-down tests. The scaled-down tests are typically conducted in controlled laboratory environments. The primary focus of these tests is to examine the rutting and fatigue properties of road materials. By simulating traffic loads in a condensed time frame, these scaled-down tests provide valuable insights into the durability and performance of various pavement materials under repeated stress. In contrast, full-scale tests are more comprehensive and expansive in scope. These tests are designed to emulate the mechanical responses of actual pavement structures under real-life conditions. The testing process involves subjecting full-scale pavement structures to accelerated loading conditions that closely resemble those encountered in real-world scenarios. This approach allows for a more accurate assessment of the pavement’s behavior under typical traffic loads, including its susceptibility to rutting and fatigue. This section delves into a comprehensive review of research findings pertinent to full-scale accelerated pavement tests (F-sAPT). It aims to provide a detailed analysis of their applications, outcomes, and implications.

Applications of F-sAPT

The modern era of F-sAPT began in the 1950s with the initiation of the AASHO Road Test by the Association of State Highway Officials in the United States. This foundational study established the groundwork for the rapid development and widespread application of F-sAPT methods, marking a turning point in pavement research and testing.

F-sAPT equipment, essential for these studies, is generally categorized into two main types: circular and linear loading. The linear loading types, notable for their practical applications, include the Accelerated Load Facility (ALF), Heavy Vehicle Simulator (HVS), and Mobile Load Simulator (MLS). These systems have been implemented globally, with usage in over twenty countries, demonstrating their universal applicability in the field.

In the United States, the deployment and utilization of these F-sAPT systems are widespread among various research institutions. The Federal Highway Administration (FHWA) and the Louisiana Department of Transportation and Development, for instance, use the ALF system. Similarly, the California and Florida Departments of Transportation employ the HVS, and the Texas Department of Transportation utilizes the MLS. This widespread adoption underscores the importance and reliability of F-sAPT in the field of pavement research. Additionally, a landmark in F-sAPT history was achieved in 2001 when the FHWA, collaborating with 15 state highway agencies, invested in the ALF system. This partnership led to the construction of 12 full-scale test lanes using different modified asphalt mixtures in 2002, as shown in Figure 2-2. The outcomes of these F-sAPTs have provided valuable data supporting numerous studies on the fatigue performance and lifespan prediction of modified asphalt mixtures, significantly contributing to the field.

Parallel to developments in the United States, China has also been active in F-sAPT research. The introduction of the ALF system in 1986 from Australia marked the beginning of F-sAPT in China. Since then, extensive APT experiments have been conducted in various regions, including Beijing, Hebei, Shanxi, and Zhejiang provinces. Moreover, several Chinese universities and research institutions, like Southeast University and Tongji University, have different F-sAPT equipment, including both circular and linear loading types. This diversification in equipment and regional studies highlights China’s commitment to advancing pavement testing and research.

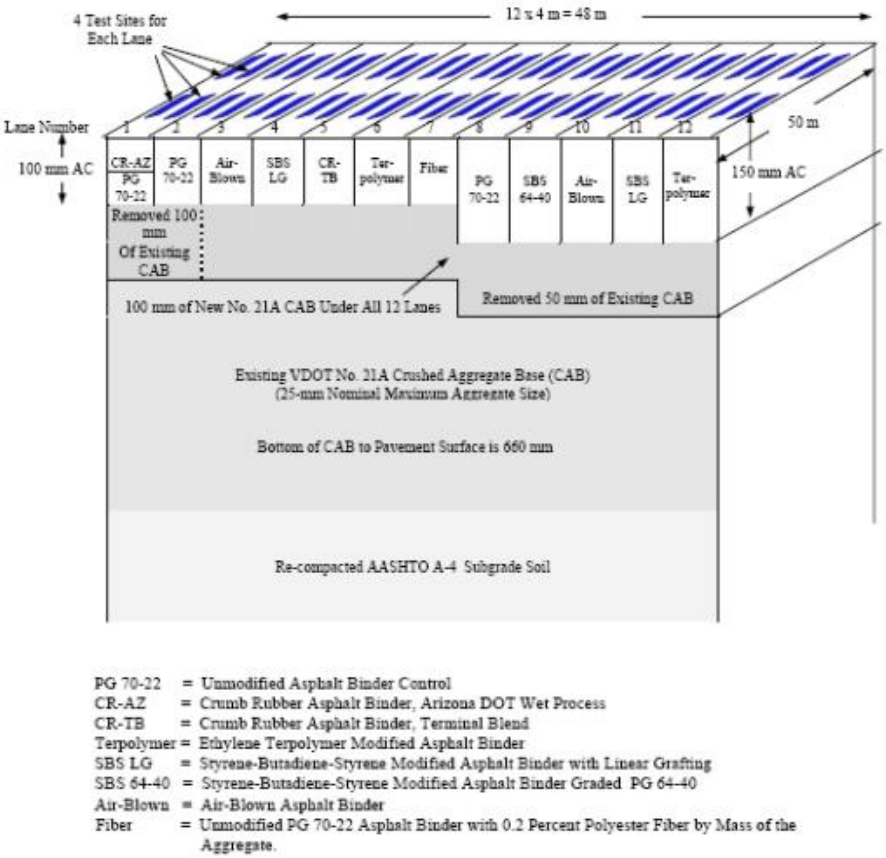

Figure 2-2 Pavement structures for the 12 full-scale test lanes [57]

Outcomes and Implications of F-sAPT

The study of fatigue damage in asphalt pavements using F-sAPT has yielded significant outcomes and implications, which can be summarized into three key aspects.

The first critical aspect is its significant contribution to the simulation and understanding of fatigue cracking in asphalt pavements. This innovative approach has been pivotal in elucidating the intricacies of both bottom-up and top-down fatigue cracking mechanisms. Notable research, spearheaded by experts such as Suh et al. [81] and Zou et al. [106], has harnessed the capabilities of F-sAPT to delve into these complex fatigue behaviors. Their groundbreaking work encompasses the creation of advanced models and algorithms that are specifically tailored to assess various material parameters and to investigate the influence of aging on the longevity and resilience of pavement structures. These advancements provide a deeper understanding of the fatigue characteristics of asphalt materials and the evolution of cracks under various conditions.

The second key outcome of the F-sAPT studies is the advancement in mechanical analysis and numerical simulations of asphalt pavements. The strain and modulus data derived from F-sAPT are instrumental in evaluating the mechanical performance of various asphalt pavement structures and

materials. This data is not only essential for understanding the physical behavior of pavements under different loads but also serves as a critical input for numerical simulations. A notable example of this application is the work by Coleri et al. [15], who utilized strain and displacement distribution data obtained from F-sAPT loading zones to establish finite element pavement models. This approach, detailed in their study, demonstrates the effective use of F-sAPT data in creating robust and reliable numerical simulations.

The last aspect is bridging laboratory and field fatigue assessment. This process is vital for aligning laboratory fatigue testing results with actual pavement performance in real-world scenarios, a critical factor for making precise predictions and assessments regarding the lifespan and performance of pavements. Tsai et al.'s research [87] is a notable example of this application. They have intricately studied the initiation and progression of cracking in asphalt pavements, integrating these insights with data on the decay of pavement stiffness modulus. Their work has led to the development of conversion factors that effectively bridge the gap between laboratory fatigue life estimations and in-situ pavement conditions. Similarly, the research conducted by Bai [2] further illustrates the potential of F-sAPT in correlating laboratory and field data. Bai's study focuses on establishing a direct relationship between laboratory-based fatigue life prediction equations for asphalt mixtures and the fatigue performance observed in field ALF test roads. This correlation is essential for validating laboratory tests and ensuring they are representative of real-world conditions.

2.1.1.3 Field Road Tests

Field road testing is a vital in-situ technique for assessing the fatigue performance of asphalt mixtures. This method has been a cornerstone in pavement research since the 1950s. It involves real-world testing scenarios to understand how asphalt pavements behave under various conditions, including traffic load, environmental factors, and material properties.

The history of field road testing is marked by groundbreaking projects like the Western Association of State Highway Officials (WASHO) and AASHO road tests in the United States. These early tests were pivotal in advancing the understanding of asphalt pavement behavior. For instance, the WASHO tests led to the innovation of the Beckman Beam, a device used for measuring deflection under slow-moving loads. These tests also underscored the critical role of pavement

thickness in enhancing fatigue resistance and established a correlation between pavement deflection, traffic volume, and the likelihood of fatigue failure [63].

Following these initial studies, the AASHO Road Test further deepened the understanding, notably influencing the methods used in pavement design. This rich legacy of field road testing continued with subsequent projects such as WesTrack [86], the Minnesota Road [59], Virginia Smart Road [1], and the National Center for Asphalt Technology (NCAT) Test Track [94]. Each of these projects contributed unique insights, enhancing the overall knowledge in the field.

In Europe, significant contributions to asphalt fatigue research have come from field road tests like the LCPC [31] in France and CEDEX [60] in Spain. These studies have paralleled the advancements in the United States, enriching the global understanding of asphalt pavement performance. Meanwhile, in China, the RIOHTRACK [92], along with various university and institute-led field road experiments, have played a crucial role. These studies have been particularly focused on the fatigue performance of semi-rigid base asphalt pavements, a critical area in China's road infrastructure. By applying field road tests, these experiments have provided valuable data and insights, helping to shape pavement design and maintenance strategies in diverse climatic and traffic conditions.

2.1.1.3 Limitations of APT

While APT enables controlled and repeated trafficking, several limitations matter for fatigue studies: (i) aging during long campaigns can shift modulus and apparent damage rates; (ii) boundary/ confinement effects from finite length/width bias strain fields; (iii) temperature management can blur frequency-temperature equivalence; (iv) scale and traffic wander differ from highways; and (v) instrumentation survivability may limit depth coverage. This study mitigates these via temperature/ frequency corrections and explicit depth-wise modeling.

2.1.2 Development of Analytical Approaches for Fatigue Life

Following the test methods, this section transitions into a discussion on the evolution of analytical approaches to understanding and predicting the fatigue life of asphalt mixture. This involves a critical review of theories and models developed over the years, from empirical to mechanistic-empirical and more recent physics-based models. The merits and limitations of these approaches are

examined, providing a comprehensive understanding of how fatigue life has been quantitatively assessed in the field.

2.1.2.1 Phenomenological Approach

The phenomenological approach, focusing on the relationship between fatigue life and stress or strain responses, has been a cornerstone in analyzing fatigue life in asphalt mixtures. Established as the simplest and most widely applied method for describing fatigue performance, it has been fundamental in various pavement design frameworks.

The seminal work in this area began in the early 1970s with Monismith and Pell's pioneering research. Monismith in 1971 and Pell [73] in 1973 independently developed fatigue life equations for asphalt mixtures under strain-controlled and stress-controlled fatigue testing modes, as shown in Equation 2-1 and Equation 2-2 separately.

$$N_f = A \cdot \varepsilon_t^{-B} \quad 2\text{-}1$$

$$N_f = C \cdot \sigma_t^{-D} \quad 2\text{-}2$$

where N_f is the number of load cycles to fatigue failure, ε_t and σ_t are the applied tensile strain and stress, and A, B, C, D are material parameters. These models effectively related asphalt mixture fatigue life with stress and strain, proving particularly applicable for describing the fatigue life of a single asphalt mixture type.

In 1985, Monismith [63] proposed an advanced version of his early model, incorporating the initial stiffness of the asphalt mixture as a factor influencing fatigue life. This version of the equation took the form:

$$N_f = A \cdot \varepsilon_t^{-a} \cdot S_{initial}^{-b} \quad 2\text{-}3$$

where $S_{initial}$ is the initial stiffness modulus of the mixture, and A, a, and b are experimentally determined material parameters. This modification acknowledged the initial stiffness as a composite index reflecting various factors like mixture gradation, air void content, and asphalt content. It offered a nuanced perspective on the fatigue life of different asphalt mixture types.

Later, more factors and variables were introduced into the fatigue life equation to encompass a comprehensive range of elements influencing fatigue life. These new components include the Ring and Ball (R&B) softening point temperature, denoted as $T_{R\&B}$, and the Penetration Index (PI) of the bitumen. Moreover, parameters derived from the master curve of stiffness, alongside various

environmental and mixture properties, have been integrated into the model. These enhancements aim to provide a more robust and accurate representation of the fatigue life of materials under diverse conditions, as indicated by references [4].

The phenomenological approach, valued for its simplicity and practicality, has been incorporated into various asphalt pavement design methods, including those developed by Shell, the Asphalt Institute, and the mechanistic-empirical (M-E) pavement design approach [57]. However, the phenomenological approach is not without its limitations. One significant drawback is its less comprehensive treatment of the cumulative nature of fatigue damage caused by repetitive loading on pavements. The effectiveness and accuracy of this approach largely hinge on several key factors: the specific definition of fatigue life, the methodologies used for testing, and the characteristics of the fatigue loading modes [25,80].

2.1.2.2 Dissipated Energy Theory

Dissipated energy theory, originally proposed by Van Dijk [91] in 1972, pivots on energy dissipation during fatigue testing of asphalt mixtures, marking a significant shift in approach and perspective in asphalt mixture fatigue life research.

The initial studies in this area [91] introduced the concept of energy loss in linear viscoelastic materials for a single loading cycle, which is expressed as:

$$W_i = \pi \sigma_i \varepsilon_i \sin \phi_i \quad 2\text{-}4$$

where W_i is the dissipated energy, σ_i and ε_i are the stress and strain amplitudes, and ϕ_i is the phase angle in the i^{th} loading cycle.

Then, Van Dijk and Visser [90] observed a strong correlation between cumulative dissipated energy and fatigue life, shown as. It is independent of loading mode, frequency, temperature, and rest periods but has a notable material dependency.

$$W_{FAT} = A(N_{FAT})^z \quad 2\text{-}5$$

where N_{FAT} is the fatigue life, W_{FAT} represents the cumulative dissipated energy, and A and z are material-specific parameters.

However, as the application of dissipated energy theory expanded, researchers noted that not all dissipated energy contributes to fatigue damage. Carpenter et al. [6] proposed the concept of

Dissipated Energy Ratio (DER) to address the changes in dissipated energy across loading cycles, linking DER to fatigue life.

$$DER = (W_{i+1} - W_i)/W_i \quad 2\text{-}6$$

where W_i and W_{i+1} are the dissipated energy in the i^{th} and $(i+1)^{th}$ loading cycles, respectively. This shift in focus led to the introduction of the Ratio of Dissipated Energy Change (RDEC) and its plateau value (PV) as indicators of an asphalt mixture's resistance to fatigue [8,80].

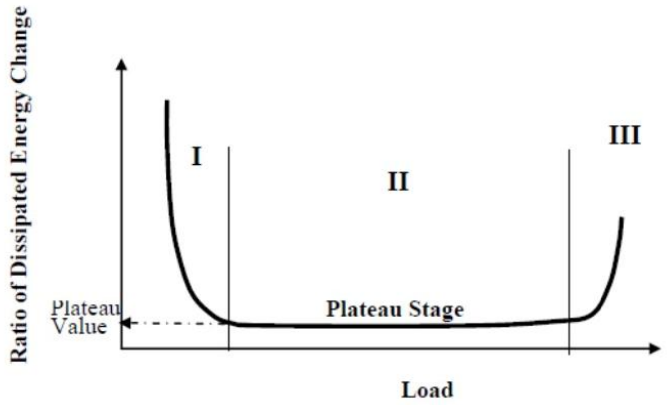

Figure 2-3 Typical RDEC Plot [8]

$$RDEC = \frac{1}{N}\sum_{i=1}^{N} DER = \frac{1}{N}\sum_{i=1}^{N} \frac{W_{i+1} - W_i}{W_i} \quad 2\text{-}7$$

$$PV = cN_f^d \quad 2\text{-}8$$

where N is the total number of loading cycles over which the REDC is calculated, c and d are regression coefficients. Subsequent studies applied RDEC to various fatigue testing methods, validating its suitability for analyzing fatigue test results. Researchers like Shen [80], Daniel et al. [18], and Moreno et al. [68] have extended the application of RDEC to different test methods like the 4PB, uniaxial tensile fatigue, and UGR-FACT fatigue tests.

In summary, the dissipated energy theory represents a significant advancement in understanding asphalt mixture fatigue, moving beyond conventional models to capture the complex interplay of energy dissipation and fatigue damage. However, Carpenter and Shen [7] noted limitations in small strain fatigue tests, pointing out that this approach does not account for healing in mixtures.

2.1.2.3 Continuum Damage Mechanics Approach

Continuum Damage Mechanics (CDM), introduced by Kachanov in 1958 [38], is primarily concerned with the study of damage evolution in structural materials. In CDM, the traditional

constitutive equations, which define the mechanical properties of materials, are expanded to incorporate damage variables. These variables enable a more nuanced and continuous representation of damage evolution within the material. Generally, there are two primary methodologies within CDM.

Effective Stress-Based Approach

This method revolves around modifying the conventional stress measures in a material by factoring in the damage. It is called effective stress in the form of [38]:

$$\tilde{\sigma} = \frac{\sigma}{1 - D} \quad 2\text{-}9$$

Where $\tilde{\sigma}$ and σ are the effective stress and measure stress, respectively, and D represents the damage status. Then, Lemaitre [47] proposed the strain equivalence hypothesis, positing that strain in a damaged material is solely related to this effective stress.

Based on these preliminary studies, Chaboche [11,12] and Lemaitre [47] conducted extensive research on metal fatigue, proposing a general model that consider the effects of stress amplitude and temperature on the fatigue damage evolution.

$$\frac{dD}{dN} = f(\sigma, D, T) \quad 2\text{-}10$$

Building upon this model, researchers have applied CDM principles to asphalt mixtures. Zhou [104], Sun [82], and Ge et al. [23] developed fatigue damage models for various asphalt mixtures.

Viscoelastic Continuum Damage (VECD) Theory

VECD is an advanced extension of CDM, integrating damage mechanics with viscoelasticity. This approach is grounded in three core principles. Firstly, it utilizes pseudo-variables, deriving from elastic principles to address viscoelastic problems, thus facilitating accurate fatigue damage modeling. Secondly, VECD employs continuum damage theory, providing a mechanistic framework for modeling microcrack growth. Lastly, the time-temperature superposition principle used in VECD streamlines fatigue testing by efficiently addressing the evolution of damage.

Specifically, the VECD approach extends Schapery's correspondence principle and work potential theory to quantify pseudo-variables. These pseudo-variables, applying elastic principles, enable the solution of viscoelastic problems and the calculation of microcracking damage [26,28]. The approach translates the stress-strain relationship for linear viscoelastic materials (Equation 2-

11) into an elastic framework by replacing strain with pseudostrain (Equation 2-12) [44,46]. This methodology allows for a more accurate analysis of viscoelastic materials by leveraging elastic models.

$$\sigma = \int_0^t E(t-\tau)\frac{d\varepsilon}{d\tau}d\tau \quad 2\text{-}11$$

$$\varepsilon^R = \frac{\sigma_{(t)}}{E_R} = \frac{1}{E_R}\int_0^t E(t-\tau)\frac{d\varepsilon}{d\tau}d\tau \quad 2\text{-}12$$

where σ and ε are stress and strain respectively, E_R is the reference modulus taken as unity, $E(t)$ is the relaxation modulus, and ε^R is the pseudostrain.

Building on this foundation, Schapery's continuum damage theory introduces three essential equations for a comprehensive understanding [53,71,89]. First, Equation 2-13, which defines the pseudostrain energy density function, is crucial for measuring energy changes in stressed materials; second, Equation 2-14, which articulates the stress-pseudostrain relationship, is essential for understanding material deformation; and third, Equation 2-15, the damage evaluation law, is imperative for assessing material damage progression. These equations collectively provide a comprehensive framework for analyzing viscoelastic material behavior.

$$W^R = f(\varepsilon^R, S) \quad 2\text{-}13$$

$$\sigma = \frac{\partial W^R}{\partial \varepsilon^R} \quad 2\text{-}14$$

$$\dot{S} = \frac{dS}{dt} = \left(-\frac{\partial W^R}{\partial S}\right)^{\alpha} \quad 2\text{-}15$$

where W^R is the pseudostrain energy density function, $\dot{S}$ is the internal state variable damage rate, α is a material-dependent constant determined by the material fracture characteristics, fatigue test modes, and relaxation modulus [46,53].

The VECD approach was first introduced into the fatigue analysis of mixture by Kim and Little in 1990. This innovative method was primarily employed to quantify the fatigue damage in prismatic beams subjected to cyclic loadings. Subsequent research efforts focused on validating and refining this approach through uniaxial tests, as referenced in several studies [41,42,51]. Central to this approach is the derivation of loading-independent constitutive equations for viscoelastic materials, as follows. These equations, crucial for understanding and predicting material behavior under various stress conditions, form the foundation of the VECD approach [44].

$$\sigma = IC(S)\varepsilon^R \quad 2\text{-}16$$

$$W^R = \frac{1}{2}C(S)(\varepsilon^R)^2 \quad 2\text{-}17$$

where I is the initial pseudo stiffness, and $C(S)$ means the pseudo stiffness express by the damage parameter S.

Then, using the chain rule, the general damage evolution law can be expressed by Equation 2-18, and the damage parameter for each cycle can be calculated by Equation 2-19.

$$\frac{dS}{dN}f = \left[-\frac{I}{2}(\varepsilon^R)^2\frac{dC}{dN}f\right]^{\frac{\alpha}{1+\alpha}} \quad 2\text{-}18$$

$$S_{N+\Delta N} \cong S_N + \left(\frac{\Delta N}{f}\right)^{\frac{\alpha}{1+\alpha}}\left[-\frac{I}{2}(\varepsilon^R)^2(C_{N+\Delta N} - C_N)\right]^{\frac{\alpha}{1+\alpha}} \quad 2\text{-}19$$

These equations establishes a relationship between the pseudo stiffness coefficient C and the damage parameter S. Extensive research in the field, as cited in sources [37,45,69], demonstrates that this relationship typically adheres to a power regression model, as illustrated in Equation 2-20. This power regression model serves as a foundational framework for developing a predictive model to estimate the fatigue life of materials, a concept further elaborated in Equation 2-21.

$$C(S) = C_1 - C_2(S)^{C_3} \quad 2\text{-}20$$

$$N_f = \frac{f\left(S_f\right)^k}{k\left(\frac{I}{2}C_2C_3\right)^{\alpha}}|G^*|^{-2\alpha}(\varepsilon_0)^{-2\alpha} \quad 2\text{-}21$$

Where C_1, C_2, and C_3 are regression coefficients. $k = 1 + (1 - C_3)\alpha$, f means the loading frequency, S_f represents the damage parameter at the fatigue failure, and $|G^*|$ means the complex modulus.

Following up, efforts have been made to simplify the application of this theory. A simplified VECD (S-VECD) was developed by Underwood et al. [89] in 2010, requiring two key types of input data: linear viscoelastic properties and damage characteristic relationships. The linear viscoelastic properties are determined through temperature and frequency sweep tests, measuring the axial dynamic modulus and phase angle. These properties are further characterized using Prony series representations for the relaxation modulus. Additionally, the damage characteristic relationship is assessed using controlled crosshead tests in CX/CS/COS modes, recording stress and strain peaks, valleys, and cycle numbers or cumulative test time.

In summary, the VECD framework brings several benefits. Primarily, it produces a damage characteristic curve that is unaffected by changes in loading conditions and temperature. This is

particularly noteworthy in the context of asphalt materials, where the damage characteristic curve presents a fundamental link between material damage and integrity. This curve is deemed more applicable in practical scenarios compared to the traditional, empirically based fatigue laws.

However, despite its detailed insights into the initial stages of microcracking, continuum damage mechanics encounter difficulties in accurately representing the progression of macroscopic cracks. Additionally, the complexity inherent in adapting these models for use in real-world pavement structures limits their direct practical application. This limitation underscores the ongoing challenge of translating theoretical models into effective tools for real-world engineering problems.

2.1.2.4 Fracture Mechanics Approach

The VECD and S-VECD methods, focused on microcracking in asphalt materials, assume continuous crack growth but fall short in explaining crack behavior post-macrocracking. To address this, some researchers have integrated mechanical fracture approaches into asphalt fatigue analysis. This approach, grounded in Griffith's fracture mechanics, views fatigue in asphalt mixtures as a three-phase process: crack initiation, stable crack growth, and unstable crack propagation Figure 3-7.

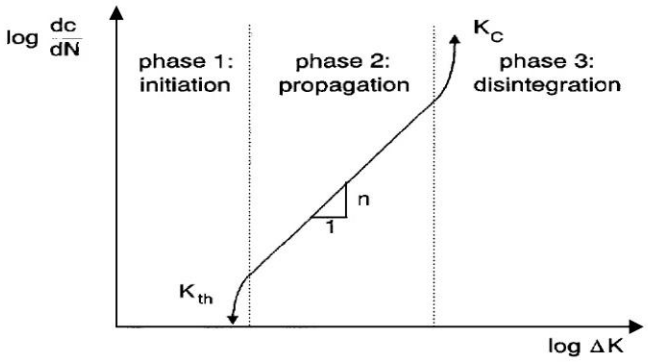

Figure 2-4 Three phases of cracking [77]

In the initiation phase of fatigue, known as Phase 1, the concept of a threshold stress intensity factor, denoted as K_{th} is pivotal. This threshold represents the minimum level of stress intensity required to initiate crack growth in asphalt materials. When the stress intensity exceeds K_{th}, there is a rapid escalation in the rate of crack growth, leading to a consistent propagation speed in the subsequent phase, Phase 2, as depicted in Figure 2-4.

The majority of the fatigue life of asphalt materials is consumed during this propagation phase. It is in this context that the application of fracture mechanics to develop quantitative models

becomes particularly relevant. One of the seminal models in this area was proposed by Paris and Erdogan, known as Paris' Law [70]. This model was developed based on empirical data and regression analysis. According to Paris' Law, the rate at which a crack propagates in a material is determined by the stress intensity factor and can be mathematically described by a specific formula as follows:

$$\frac{dc}{dN} = AK^n \qquad 2\text{-}22$$

where $dc\ /\ dN$ means the crack growth per cycle, K is the stress intensity factor describing the stress conditions near the crack tip, A, and n are the constants determined by the material properties and test conditions. Then, in Phase 3, the crack growth rate escalates to an infinite value, signifying a rapid progression toward material disintegration. A key parameter in this context is the critical stress intensity factor, denoted as K_c, commonly referred to as fracture toughness. Fracture toughness is an inherent material property that remains consistent regardless of the type of loading applied or the dimensions of the specimen under consideration. This characteristic distinguishes it from the stress intensity factor K, which is influenced by the overall stress conditions and the specific geometry of the crack [36].

To use the fracture mechanics approach in practice, particularly for viscoelastic materials like asphalt mixtures, it is necessary to determine the A and n of Paris' Law. Schapery's contribution is pivotal in this context. He developed a comprehensive crack growth theory known as the generalized J-integral theory. This theory, shown in Equation 2-23, is specifically tailored for viscoelastic media and is primarily concerned with Mode I cracking, which is characterized by tensile or pure bending stresses [79].

$$\frac{dc}{dN} = AJ^n \qquad 2\text{-}23$$

According to Schapery's theory, the constants A and n from Paris' law can be accurately ascertained through straightforward testing methods or by utilizing nomographs, as referenced in source [30]. This approach offers significant advantages, notably in its capacity to predict fatigue data across a spectrum of temperatures and for materials with different geometric characteristics. Moreover, Schapery's theory allows for a comprehensive evaluation of the impact of diverse material properties on fatigue behavior. This is achieved without necessitating an exhaustive array of fatigue tests, thereby streamlining the analysis process.

The refinement of Schapery's theory in the study of asphalt mixture behavior has seen significant advancements through various researchers' contributions. Lytton et al. [56] have been instrumental in developing micro-mechanics fracture healing models, enhancing Paris' Law to assess asphalt mixture cracking more accurately. This enhancement provides a more nuanced understanding of the cracking process, integrating critical factors such as fracture and healing dynamics. Furthermore, Luo et al. [54] have made notable strides by incorporating damage density parameters into an improved version of Paris' equation. This modification allows for a more comprehensive representation of the cracking process. Subsequently, Lytton et al., in their recent studies [55,103], proposed viewing pavement cracking through the lens of both fracture and healing processes, offering a more holistic approach to understanding pavement deterioration.

In summary, while the fracture mechanics approach offers valuable insights into the behavior of asphalt mixtures, it is not without its challenges. This approach primarily focuses on the stable phase of crack growth and requires extensive empirical data to accurately assess crack growth rates. This reliance on empirical data can be a limitation, especially in complex, real-world scenarios. Moreover, the method's dependency on temperature-sensitive stress intensity factors introduces an additional layer of complexity. This sensitivity to temperature variations poses challenges, particularly under fluctuating environmental conditions, complicating its direct application in the field.

2.2 Fatigue Damage and Its Evolution Processes

As the research continues, recent advancements have shifted the emphasis towards a more holistic understanding of the fatigue damage process, especially under the influence of multiple concurrent factors. The essence of this shift lies in the realization that merely quantifying the lifespan of materials under fatigue is not sufficient to fully grasp the complexity of their degradation process. Instead, there is a growing consensus on the necessity to develop and utilize a damage variable – a parameter that not only has a clear physical significance but is also feasible to measure and apply in practical scenarios. Such a damage variable would enable a more nuanced analysis of the fatigue damage evolution, providing insights into the intricate interplay of factors that contribute to material degradation.

This approach goes beyond traditional methods, offering a dynamic perspective on how materials deteriorate under various conditions. It encompasses not just the endpoint of material failure but the entire journey from initial use to final breakdown. By focusing on the evolution of fatigue damage, researchers can gain a deeper understanding of the mechanisms at play, leading to more robust and durable material designs and effective maintenance strategies for infrastructure that employs asphalt layers and mixtures.

The following sections will delve into the specifics of this evolved understanding of fatigue damage, exploring the development of suitable damage variables and examining how these variables can be effectively applied to monitor and predict the degradation process in asphalt materials.

2.2.1 Fatigue Damage Variables

The evolution of fatigue studies in asphalt mixtures and layers has led to the integration of damage mechanics into fatigue analysis. This approach, rooted in mechanical theory, investigates material deterioration under repeated loadings. It articulates damage across three scales: microscopic, mesoscopic, and macroscopic.

At the microscopic level, fatigue damage is the result of material grain dislocations, slips, or the accumulation of micro-stresses near micro-voids and micro-cracks [24,13,34]. The concept of a fatigue damage variable D can be expressed mathematically, signifying the reduction in the effective bearing cross-sectional area from A_0 to $\tilde{A}$ due to micro-defects. The equation is defined as [13,34,52]:

$$D = \frac{A_0 - \tilde{A}}{A_0} \qquad 2\text{-}24$$

This definition, while physically meaningful, poses challenges in direct experimental quantification.

Fatigue damage at the mesoscopic level refers to the initiation and expansion of cracks due to micro-defects [13,24]. The VECD studies this process, using pseudo stiffness as the continuous damage variable to characterize the fatigue damage evolution [43].

At the macroscopic level, fatigue damage is typically associated with a decline in the physical-mechanical properties of the material. Consequently, these macroscopic properties can serve as variables to measure the damage in asphalt concrete. Among various indicators, the stiffness reduction ratio (SSR) is frequently utilized, defined as [3,9,10,16,88]:

$$D = \mathrm{SRR} = 1 - \frac{E_N}{E_0} \quad 2\text{-}25$$

Where E_0 is the stiffness of undamaged asphalt concrete, and E_N is the stiffness after N loading repetitions. The SSR has been employed to define fatigue damage in both laboratory asphalt mixtures and in-situ asphalt layers [26,61,101], as it provides a clear physical-mechanical interpretation and is relatively easy to measure.

An alternative macroscopic fatigue damage variable, ω, has been derived using the dynamic modulus master curve of damaged asphalt concrete in the CalME design method [61,88]. This variable is represented as:

$$\log(E_N) = \delta + \frac{\alpha(1-\omega)}{1+\exp[\beta+\gamma\log(f_r)]} \quad 2\text{-}26$$

$$\omega = \frac{\log\left({}^{E_0}/_{E_N}\right)}{\log\left({}^{E_0}/_{E_{\min}}\right)} \quad 2\text{-}27$$

where ω represents the fatigue damage level, with $\omega = 0$ indicating $E_N = E_0$ and $\omega = 1$ signifying $E_N = E_{min} = 10^{\delta}$.

Upon comparing different fatigue damage variables, it becomes evident that the SRR not only possesses a distinct physical-mechanical meaning but also facilitates ease in measurement and application in pavement response calculations. Most importantly, SRR effectively evaluates the damage level of both laboratory and in-situ asphalt materials, thus enabling the establishment of a correlation between the two. Consequently, this study adopts the SRR as the fatigue damage variable for analyzing the fatigue damage process in both laboratory asphalt mixtures and in-situ asphalt layers.

2.2.2 Fatigue Damage Evolution Models

The development of models to predict the evolution of fatigue damage in asphalt layers has been a focal point in material research for over seven decades. These models generally fall into three categories: those based on Miner's rule, models grounded in continuum damage theory, and nonlinear models employing the SSR as the damage variable.

2.2.2.1 Models Based on Miner's Rule

Miner's rule, a fundamental concept in evaluating cumulative fatigue damage, postulates that failure occurs when the sum of the ratios of the number of applied cycles to the number of cycles to failure at each stress level equals one [62]. This can be mathematically expressed as:

$$D = \sum_{i=1}^{n} \frac{N_i}{N_{fi}} \leq 1 \qquad 2\text{-}28$$

Where, N_i represents the number of cycles at stress level σ_i, and N_{fi} is the number of cycles to failure at the same stress amplitude. Miner's rule essentially assumes a linear accumulation of fatigue damage, meaning that the amount of damage inflicted by the same load remains constant regardless of the material's damage state, and that damage from different load levels is additive.

Pioneering applications of Miner's linear fatigue damage accumulation principle in asphalt mixture studies were conducted by Monismith et al. [65] and Deacon [19], who validated that the rule holds true across different strain levels. Miner's rule has since been widely applied in fatigue damage analysis of asphalt mixtures and layers [101,105], with various researchers proposing fatigue life prediction equations based on this rule. An equation for predicting fatigue life under variable amplitude conditions, using Miner's rule, can be formulated as [20,72]:

$$N_f = \frac{1}{\frac{p_1}{N_{f1}} + \frac{p_2}{N_{f2}} + \cdots + \frac{p_n}{N_{fn}}} = 1 \Big/ \sum_{i=1}^{n} \frac{p_i}{N_{fi}} \qquad 2\text{-}29$$

where p_i represents the relative proportions of stress levels with corresponding fatigue lives N_{fi}.

However, Miner's rule overlooks the nonlinear nature of fatigue damage progression and does not account for the varying rates of damage accumulation at different stages. This led to the development of nonlinear fatigue damage evolution models, with the earliest proposed by Marco and Starke [58]. Their model is expressed as:

$$D = \sum_{i=1}^{n} \left(\frac{N_i}{N_{fi}}\right)^{x_i}, x_i > 1 \qquad 2\text{-}30$$

where x_i is a constant determined experimentally and is related to stress level and loading sequence, though it can be challenging to ascertain. Following this, Hopman et al. [32] improved upon the Marco-Starke model by incorporating the study of dissipated energy in fatigue damage. They proposed a model where:

$$D = \left(\frac{N_i}{N_f}\right)^{x} \qquad 2\text{-}31$$

This model divides the fatigue damage progression into three phases: crack initiation, crack propagation, and fatigue failure, with distinct values of x for each phase.

In summary, while Miner's rule and its derived models have been widely used, they have limitations. First, they do not consider the impact of load rest periods on fatigue damage evolution, leading to conservative estimates of fatigue life. Second, these models rely on the fatigue life N_{fi} under different load levels, which can vary significantly based on the criteria used to define fatigue failure. This variability can lead to differing results in model analysis.

2.2.2.2 Models Grounded in Continuum Damage Theory

Models based on continuum damage mechanics represent a nonlinear approach, characterizing the evolution of damage in relation to the loading process. In these models, fatigue damage is a function of various parameters, including stress amplitude, average stress, temperature, and loading frequency [97,100]. Notably, in these models, the damage effect of the same load varies at different stages of damage, and the sequence of loading influences the extent of damage.

Two prominent models in this category were proposed by Chaboche in 1981 and Lemaitre in 1985. Chaboche's model [11], based on the hypothesis that fatigue damage correlates with plastic micro-strain, is expressed in the following incremental form:

$$\frac{dD}{dN} = \left[1-(1-D)^{\beta+1}\right]^{\alpha}\left[\frac{\Delta\sigma}{M(\bar{\sigma})(1-D)}\right]^{\beta} \quad 2\text{-}32$$

where $\Delta\sigma$ is the stress amplitude, $\bar{\sigma}$ is the average stress, and α, β, and $M(\bar{\sigma})$ are temperature-dependent material parameters. Integration of this equation yields a one-dimensional fatigue damage evolution model:

$$D = 1-\left[1-\left(\frac{N}{N_f}\right)^{\frac{1}{1-\alpha}}\right]^{\frac{1}{1+\beta}} \quad 2\text{-}33$$

where N is the number of loading repetitions, and N_f is the number of repetitions to failure.

Lemaitre's model [47], similarly based on the assumption that plastic micro-strain causes fatigue damage, proposes a generalized fatigue damage evolution model:

$$\frac{dD}{dN} = 2\int_{\sigma_m}^{\sigma_M} G_F(\sigma, D, T)\, d_\sigma \quad 2\text{-}34$$

where σ_m and σ_M are the minimum and maximum stress amplitudes, respectively.

Another model considering the impact of stress amplitude on fatigue damage increment is given by [100]:

$$D = 1 - \left(1 - \frac{N}{N_f}\right)^{\frac{1}{1+\alpha+\beta}} \quad 2\text{-}35$$

$$N_f = \frac{1}{1+\alpha+\beta}\left(\frac{\sigma}{2M(\bar{\sigma})}\right)^{-\alpha} = \frac{S^{-\alpha}}{(1+\alpha+\beta)[2M(\bar{\sigma})]^{-\alpha}}\left(\frac{1}{\varepsilon}\right)^{\alpha} \quad 2\text{-}36$$

where S is the stiffness of the asphalt mixture, and ε is the strain amplitude ($\sigma = S \cdot \varepsilon$). The fatigue life prediction can be further simplified as:

$$N_f = k\left(\frac{1}{\varepsilon}\right)^{\alpha} \quad 2\text{-}37$$

with

$$k = \frac{S^{-\alpha}}{(1+\alpha+\beta)[2M(\bar{\sigma})]^{-\alpha}} \quad 2\text{-}38$$

This model essentially parallels the phenomenological fatigue life prediction model, offering a physical interpretation of conventional phenomenological analysis methods.

In summary, models based on continuum damage theory correlate the damage evolution process to loading conditions, factoring in stress amplitude, average stress, temperature, and loading frequency. They represent a nonlinear approach that accounts for loading sequence effects. However, these models are complex and involve parameters that are challenging to determine accurately.

2.2.2.3 Models Employing the SSR as the Damage Variable

In the field of asphalt concrete fatigue analysis, the SSR, as shown in Equation 2-25, has been employed by several researchers to develop nonlinear fatigue damage evolution models. These models utilize the SAR to characterize the progression of fatigue damage in a more nuanced manner.

The Weibull survival function, initially proposed by Weibull in 1939 [93], is a significant model in this context. Weibull's statistical distributions of material strength have been extensively applied across various fields, but its application in describing asphalt concrete fatigue damage was not prominent until Tsai's study in 2003 [85]. Tsai suggested that the stiffness reduction process in asphalt concrete caused by load repetitions could be described by the Weibull survival function:

$$D = \mathrm{SSR} = 1 - \frac{E_N}{E_0} = 1 - \exp(-\lambda N^{\gamma}) \quad 2\text{-}39$$

where γ and λ are model parameters. This model was later validated by Ma using measured seismic modulus data from in-situ asphalt layers [57].

Subsequent studies by Wu & Zhang [98] and Yang [100] proposed different relationships between the SSR and loading repetitions. Wu & Zhang found that the SR exhibited an exponential increase with loading repetitions, modeled as:

$$D = \text{SSR} = 1 - \frac{E_N}{E_0} = 1 - me^{\frac{-N/N_f}{s}} - t \quad \text{2-40}$$

where m, s, and t are regression coefficients. Yang, on the other hand, suggested a logarithmic relationship:

$$D = \text{SSR} = 1 - \frac{E_N}{E_0} = a_1 \ln\left[b_1\left(\frac{N}{N_f}\right) + 1\right] \quad \text{2-41}$$

where a_1, and b_1 are regression coefficients being functions of loading frequency and stress level.

Luan [52] took the same test methods adopted in Yang's research but posited a different prediction approach, arguing that fatigue damage changes as a power function with increasing loading repetitions. The ExpAssoc model was used to describe this relationship:

$$D = \text{SSR} = 1 - \frac{E_N}{E_0} = A_1\left(1 - e^{-\frac{N/N_f}{t_1}}\right) + A_2\left(1 - e^{-\frac{N/N_f}{t_2}}\right) \quad \text{2-42}$$

The parameters A_1, A_2, t_1, and t_2 in this model are functions of temperature, loading intervals, and stress level.

Wu in 2014 improved upon this approach, considering boundary conditions and monotonicity required for the damage variable, and proposed a new fatigue damage evolution model [97], where:

$$D = \text{SSR} = 1 - \frac{E_N}{E_0} = \left(1 - \frac{E_f}{E_0}\right)\left(\frac{N_i}{N_f}\right)^m \quad \text{2-43}$$

where E_f is the stiffness modulus of asphalt mixture at fatigue failure, and m is a model parameter related to the strain level. This model, similar to the ExpAssoc model, reflects the power function variation of fatigue damage and is influenced by loading sequence and history.

In summary, while the SSR is a commonly used variable for fatigue damage in asphalt concrete, its application in SSR-based evolution models offers an improved characterization of the nonlinear fatigue damage process. These models are simpler and highly valuable for engineering applications. However, most of these models still involve the fatigue life of the asphalt concrete, which is influenced by the criteria for fatigue failure and the loading mode. Therefore, the determination of fatigue life within these models can be challenging, subsequently affecting the accuracy of predictions made by SSR-based models.

2.3 Factors Influencing Fatigue Characteristics

Numerous factors influence the characteristics of fatigue, playing a significant role in the intricate process of fatigue damage evolution. A precise comprehension of the effects exerted by each factor on fatigue characteristics is essential. This understanding facilitates a detailed analysis of the fatigue damage evolution process. It is also crucial for correlating the fatigue characteristics of laboratory-prepared asphalt mixtures with those of the asphalt layers used in real-world pavement structures.

2.3.1 Impact of Tensile Fatigue Loading Modes

The tensile fatigue loading mode is one of the most important factors. It refers to the stress and strain variation methodology during repeated loadings. Two primary modes used in laboratory tests are the stress-controlled mode, which maintains constant stress amplitude, and the strain-controlled mode, which keeps strain amplitude constant. These modes differ in various aspects, such as fatigue failure definition, fatigue life, test data dispersion, number of specimens required, aging effects, sensitivity to mixture properties, energy dissipation rate, crack propagation speed, and the impact of load rest periods [100].

Numerous studies have demonstrated that the fatigue characteristics of asphalt mixtures are related to the tensile fatigue loading mode [100], and different fatigue characteristics lead to various asphalt mixture designs. Therefore, researchers need to identify which fatigue loading mode can more accurately simulate the changes of stress and strain in the asphalt layers of on-site pavement structures.

For this purpose, the Mode Factor (MF) was proposed by Monismith and Deacon [64,66], as shown in the equation:

$$\text{Mode Factor} = \frac{|A| - |B|}{|A| + |B|} \qquad 2\text{-}44$$

Here, A and B represents the percentage change in tensile stress and strain within the asphalt layer, respectively, when its percentage reduction in the average stiffness modulus is C. Under controlled stress mode, the MF value is -1, and under controlled strain mode, it is +1. For other fatigue loading modes where both stress and strain change during repeated loading, the MF value lies between -1 and +1.

Then, Monismith and Deacon [64] analyzed the MF of different asphalt pavement structures. They applied elastic multi-layered theory to study the effect of changes in the average stiffness modulus of asphalt layers on the bottom layer's tensile stress and strain, determining the variation of the MF with asphalt layer thickness. Their research suggested that layers thicker than 15.24 cm (6 inches) should take the controlled stress mode, while those thinner than 5.08 cm (2 inches) fit the controlled strain mode.

Witczak and El-Basyouny [95], while establishing and calibrating the M-E fatigue cracking model in 2004, employed similar conclusions but considered layers thicker than 20.32 cm taking the controlled stress mode. In pavements with such thick asphalt layers, the asphalt serves as the primary load-bearing layer. Its stiffness modulus decreases with an increasing number of load applications, leading to gradually increasing tensile strains at the bottom of the layer. However, the variation in tensile stress is not significant, aligning the tensile fatigue loading mode more closely with a controlled stress mode. Conversely, in pavement structures with thin asphalt layers (less than 5.08 cm thick), the asphalt layer is not the primary load-bearing element. Here, the magnitude of tensile strain at the bottom of the asphalt layer is mainly influenced by the stiffness of the underlying layers rather than the stiffness modulus of the asphalt layer itself, making the tensile fatigue loading mode more akin to a controlled strain mode. For asphalt layers with thicknesses between 5.08 cm and 20.32 cm, the study suggests a combined mode of controlled stress and strain. However, it does not provide a definitive answer, leaving the exact nature of the tensile fatigue loading mode in these cases uncertain.

Although these two studies adopted different thicknesses of asphalt layers taking the controlled stress mode, both simply assumed that the same tensile fatigue loading mode applies to the same pavement structure. However, research by Zhu [105] indicates that even within the same pavement structure, the tensile fatigue loading mode at different depths may vary, an aspect that has not been fully explored.

Additionally, the fatigue life of asphalt mixtures under different loading modes varies. Researchers have attempted to establish conversion functions for fatigue life under various loading modes and a unified equation to estimate the fatigue life of asphalt layers in pavement structures based on limited laboratory asphalt mixture fatigue tests. Monismith was a pioneer in this research area, noting in his 1994 SHRP-A-404 report that the fatigue life of asphalt mixture under controlled

strain mode is approximately 2.4 times that under controlled stress mode [63]. Witczak and Mirza later developed numerical conversion functions for fatigue life under different loading modes and established a generalized fatigue life prediction equation applicable to different modes and pavement structures [96]. Their equations for fatigue life prediction under controlled strain and stress modes are as follows:

$$N_{f\varepsilon} = [4.102PI - 0.205PI(V_b) + 1.094V_b - 2.707]^5 \varepsilon_t^{-5} E^{-1.8} \quad 2\text{-}45$$

$$N_{f\sigma} = [0.300PI - 0.015PI(V_b) + 0.080V_b - 0.198]^5 \varepsilon_t^{-5} E^{-1.4} \quad 2\text{-}46$$

where $N_{f\varepsilon}$ and $N_{f\sigma}$ are the fatigue lives under controlled strain and stress modes, respectively. PI means the penetration index of the asphalt, V_b is the asphalt content, ε_t is the initial tensile strain during the fatigue test, and E denotes the initial flexural stiffness modulus of the asphalt mixture.

Comparing these equations, Witczak and Mirza identified a quantitative relationship between the fatigue lives under strain-controlled and stress-controlled modes, which can be expressed by the function F:

$$F = \frac{N_{f\varepsilon}}{N_{f\sigma}} = 6.74^5 E^{-0.4} = 13909E^{-0.4} \quad 2\text{-}47$$

For intermediate thicknesses of asphalt layers, they suggested a fatigue life conversion function based on the Sigmoidal model, leading to a generalized fatigue life prediction equation:

$$F'' = 1 + \frac{F}{1 + \exp^{(1.354h_{ac} - 5.408)}} = 1 + \frac{13909E^{-0.4}}{1 + \exp^{(1.354h_{ac} - 5.408)}} \quad 2\text{-}48$$

$$N_f = F'' N_{f\sigma} \quad 2\text{-}49$$

where h_{ac} is the thickness of the asphalt layer.

Yu [102], following the methodology proposed by Witczak and Mirza, advanced the formula for the ratio of fatigue lives under two conventional loading modes:

$$R = \frac{N_{f\sigma}}{N_{f\varepsilon}} = 0.362E^{0.436}(VFA)^{-0.846} \quad 2\text{-}50$$

Here, VFA represents the effective asphalt saturation of the asphalt mixture. Differing from Witczak and Mirza, this study introduced a thickness adjustment coefficient k_1 and an amplification factor k_2, leading to a new fatigue life conversion function and a generalized fatigue life prediction equation:

$$TF = \left(F + \frac{1 - F}{1 + \exp^{(k_1 h_{ac} - 5.408)}}\right)^{k_2} \quad 2\text{-}51$$

$$N_f = (TF)[1.509 \times 10^{16} \varepsilon_t^{-3.973} E^{-1.589} (VFA)^{2.720}] \quad 2\text{-}52$$

Through regression analysis, the values of k_1 and k_2 were determined to be 0.237 and 3.333, respectively.

In summary, research generally suggests that thin asphalt layers (less than 5.08 cm) should take the strain-controlled modes, while thick layers (more than 20.32 cm) fit stress-controlled modes. However, determining the appropriate tensile fatigue loading mode is challenging for most asphalt layers with thicknesses between these ranges. Additionally, even within the same road structure, different depths of asphalt mixture may require different tensile fatigue loading modes, an area that needs further exploration. Also, most studies have analyzed the mode factor for flexible base asphalt pavements, considering the bottom of the asphalt layer as the critical position for fatigue damage. These analyses use the tensile stress and strain at the bottom of the asphalt layer to calculate the mode factor. However, many domestic asphalt pavements use semi-rigid bases, necessitating a reevaluation of the critical damage position and mode factor. Last, the impact of fatigue loading mode on the fatigue damage evolution process has been less studied and requires further research.

2.3.2 Additional Influential Factors

Besides loading mode, various studies have identified both internal and external factors influencing the fatigue characteristics of asphalt mixtures and layers [102]. The internal factors primarily concern the material properties that affect the stiffness of the mixture. These include asphalt type, asphalt dosage, air void content, mineral type, and aggregate gradation. The external factors encompass loading factors such as loading time, frequency, load waveform, rest-time period, and environmental factors, notably temperature.

Loading factors are critical in determining the fatigue behavior of asphalt concrete. They mainly comprise load waveform, loading time, frequency, and rest-time period. Laboratory fatigue tests often employ sine, half-sine, rectangular, and triangular waves. Raithby and Sterling [76] observed that rectangular waves could shorten the fatigue life of asphalt mixtures, whereas triangular waves had the opposite effect. However, Leykauf and Kawohol [48] found no significant relationship between fatigue life and load waveform. Moreover, considering that under the actual load of vehicle tires, the longitudinal stress and strain (along the direction of travel) in the asphalt layer exhibit a ‘compression-tension-compression’ change process that approximates a sine curve,

and the transverse stress and strain (perpendicular to the direction of travel) change approximately follows a half-sine curve [83], fatigue tests of asphalt mixtures typically utilize either sine or half-sine waves.

In terms of loading time and frequency, there is a divergence of views among researchers. Some studies, like those of Tian et al. [84] and Ge et al. [23], suggest that loading frequency has negligible effects under the controlled-stress loading mode, provided the variation in this factor is limited. Contrarily, Gao [22] argued that lower loading frequencies in controlled-stress tests make the fatigue life more sensitive to frequency changes. Huang et al. [34] concluded that in controlled-stress tests, the fatigue life increases with frequency. Under controlled-strain tests, the fatigue life of asphalt mixtures decreases with increasing frequency, as noted by Gao [22] and Li [49].

Additionally, most researchers agree that asphalt concrete can gradually heal during rest periods, with the rest time prolonging fatigue life. However, Van Dijk et al. [91] suggested that the effect of rest time becomes insignificant beyond a certain loading interval. Raithby & Sterling [76] proposed that this threshold is temperature-dependent. Additionally, studies by Bonnaure et al. [4], Hsu & Tseng [33], and Guo [28] suggested that the fatigue life is influenced not only by the rest-time period but also by the ratio of rest-time to loading duration.

Beyond loading factors, temperature is another significant environmental factor impacting the fatigue characteristics of asphalt mixtures and layers. Numerous studies have shown that under controlled stress mode, the fatigue life of asphalt mixtures increases with decreasing temperature. Conversely, under controlled-strain mode, fatigue life increases with rising temperature [22,23,76], although this conclusion is valid only when strain exceeds 200-250 microstrain.

In the aspect of internal factors, many researchers believe that the fatigue characteristics of asphalt mixtures are significantly related to their stiffness modulus. Generally, under controlled stress mode, an increase in stiffness modulus leads to a decrease in strain for the same stress conditions, thereby prolonging fatigue life. Conversely, under the controlled-strain mode, the required stress for the same strain conditions increases, reducing fatigue life. Factors affecting the stiffness modulus of asphalt mixtures, such as asphalt type, dosage, air void content, mineral type, and aggregate gradation, also influence their fatigue characteristics. Among these, asphalt dosage and air void content are particularly critical [24], with Harvey noting that air void content has a more pronounced effect on fatigue characteristics [29].

In summary, while most studies have analyzed the impact of various factors on fatigue life, few have delved into their effects on the evolution of fatigue damage. It is challenging for researchers to effectively describe the fatigue damage evolution process under the combined influence of multiple factors. Additionally, the way these factors influence the fatigue characteristics of asphalt mixtures is closely related to the fatigue loading mode. Therefore, further research analyzing the fatigue loading mode in conjunction with these factors is essential.

2.4 Correlating Laboratory and In-situ Fatigue Performance

The final section addresses the methodologies employed to establish correlations between laboratory fatigue test results and in-situ performance. Throughout the history of fatigue characteristic research, despite the development of various fatigue damage variables and the establishment of both linear and nonlinear fatigue damage evolution models, most models are based on laboratory fatigue analysis of asphalt mixtures. Few models effectively apply to the fatigue damage analysis and performance prediction of in-situ asphalt layers. Therefore, researchers have attempted to forecast the fatigue damage evolution process of asphalt layers by analyzing the relationship between laboratory and in-situ fatigue damage.

A widely adopted approach is the analysis method based on Miner's rule, which can be summarized in the following steps [57,95,105]:

(1) Establish a fatigue life prediction equation for asphalt mixtures based on laboratory fatigue test results.

(2) Calculate the tensile strain or stress at the bottom of the asphalt layer under loading level i and environmental condition j, and input these into the fatigue life prediction equation to obtain the fatigue life N_{fij}.

(3) Assuming p_{ij} is the proportion of the number of applications under loading level i and environmental condition j to the total number of load applications, the theoretical fatigue life N_f of the asphalt layer can be calculated using Miner's rule:

$$N_f = \frac{1}{\frac{p_{11}}{N_{f11}} + \cdots + \frac{p_{1m}}{N_{f1m}} + \frac{p_{21}}{N_{f21}} \cdots + \frac{p_{nm}}{N_{fnm}}} = 1 \Big/ \sum_{i=1}^{n} \sum_{j=1}^{m} \frac{p_{ij}}{N_{fij}} \quad \text{2-53}$$

(4) Define the fatigue life of the asphalt layer (N_c) as the standard axle load application number at

which the crack ratio of the wheel path reaches a predetermined value.

(5) Determine the Shift Factor (SF) to converse the laboratory fatigue life into the in-situ fatigue life:

$$N_c = \mathrm{SF} \cdot N_f \quad 2\text{-}54$$

However, this shift factor can vary widely. Various research shows that the SF is related to the material properties of the asphalt mixture [75], the thickness of the asphalt layer [74], the tensile fatigue loading mode [5,14], and environmental factors [14], typically ranging between 5-400, and sometimes even 0.1-1200.

In addition to calibrating the numerical value of the shift factor, researchers have also attempted to analyze its relationship with various influencing factors. In 1998, Harvey et al. [29] used the above analysis method based on Miner's rule to propose a power function relationship between the shift factor and the tensile strain at the bottom of the asphalt layer:

$$\mathrm{SF} = 3.1833 \times 10^{-5} \varepsilon^{-1.3759} \quad \varepsilon \geq 0.000040 \quad 2\text{-}55$$

Later, Witczak and El-Basyouny [95] utilized data from the Long-Term Pavement Performance (LTPP) program to establish the relationship between the shift factor and asphalt layer thickness using a Sigmoidal function:

$$\mathrm{SF} = \frac{1}{0.000398 + \frac{0.003602}{1 + e^{11.02 - 3.46 h_{ac}}}} \quad 2\text{-}56$$

In 2007, Chen [13] used the data from the ALF accelerated loading test section to calibrate the fatigue life prediction model under controlled strain mode, finding a good linear relationship between the shift factor and asphalt thickness:

$$\mathrm{SF} = \begin{cases} 15.12 - 0.97 h_{ac} & 0 < h_{ac} \leq 15\ \mathrm{cm} \\ 0.266 & h_{ac} > 15\ \mathrm{cm} \end{cases} \quad 2\text{-}57$$

In summary, the shift factors calibrated in various studies vary greatly, leading to either insufficient or conservative asphalt layer thickness design. Previous research that utilized Miner's rule for analysis often failed to capture the complexities of fatigue damage in pavements. This approach predominantly focused on the tensile strain or stress at the bottom of the asphalt layer, neglecting the possibility of fatigue-related failures at other depths within the pavement. Furthermore, the traditional definition of asphalt layer fatigue life is somewhat imprecise and does not adequately address the impact of "top-down" cracking, particularly in the wheel paths. Another

significant issue is the reliance on laboratory-based fatigue life prediction equations. These equations are typically derived under controlled strain or stress conditions, which do not accurately reflect the real-world loading scenarios experienced by most pavement structures. This discrepancy suggests a need for more representative models that align better with the actual conditions pavements endure, ensuring more accurate and reliable asphalt layer thickness designs.

2.5 Summary

The study of fatigue damage in asphalt mixtures and asphalt layers has been a focal point in the field of asphalt pavements for over 70 years, with numerous researchers dedicating extensive work to this topic. This research encompasses several key areas. Firstly, based on laboratory fatigue tests, various fatigue analysis theories have been developed. These include phenomenological methods, dissipated energy theories, continuum damage mechanics, and fracture mechanics. These theories have been instrumental in establishing equations for predicting the fatigue life of asphalt mixtures. Secondly, the definition of fatigue damage has been expanded from a damage mechanics perspective to encompass micro, meso, and macro scales. This broader view has led to the development of several evolution models: models based on Miner's rule, models grounded in continuum damage mechanics, and nonlinear fatigue damage evolution models based on modulus reduction rate. Thirdly, qualitative and quantitative analyses have been conducted on the material, load, and environmental factors that influence the evolution of fatigue damage. Understanding these factors is crucial for predicting and mitigating fatigue damage in asphalt pavements. Lastly, the relationship between laboratory asphalt mixture fatigue damage and on-site asphalt layer fatigue damage has been analyzed. This analysis has been pivotal in exploring the conversion factors between these two contexts, offering insights into how laboratory findings can be translated to real-world applications. This comprehensive approach to studying fatigue damage in asphalt pavements reflects the depth and breadth of research in this field, highlighting its importance in maintaining and improving pavement infrastructure.

Although extensive work has been done, there are notable research gaps that merit further investigation:

(1) The majority of studies concentrate on laboratory asphalt mixtures' fatigue life and damage,

with fewer addressing the fatigue damage evolution process within pavement structures. Precise quantification of fatigue life and damage level in asphalt layers within structures is challenging due to the multitude of influencing factors and the complex nature of the evolution process, making analysis and modeling arduous.

(2) Existing fatigue damage evolution models have limitations: models based on Miner's rule overlook the nonlinearity of fatigue damage evolution; those based on continuum damage mechanics are complex, with material parameters that are difficult to ascertain; apart from the Weibull survival function, models based on stiffness reduction ratio involve definitions of fatigue life that are often inconsistent and influenced by modulus, affecting the values and thereby the damage evolution models.

(3) Research on tensile fatigue loading mode is insufficient. Current studies suggest layers thicker than 20.32 cm suit the controlled stress mode, and those thinner than 5.08 cm suit the controlled strain mode. However, there is a lack of systematic research on layers with intermediate thicknesses. While existing research correlates fatigue loading mode with asphalt layer thickness, recent studies indicate that even within the same pavement structure, the fatigue loading mode may differ at various depths, an area that has not been thoroughly explored.

(4) Most studies have focused on flexible subgrade asphalt pavements, considering the bottom of the asphalt layer as the critical failure position and only accounting for tensile strains or stresses at that level. Yet, in China, most asphalt pavements use semi-rigid subbases, and the critical failure positions, fatigue loading modes, and damage evolution processes in these cases require further study.

(5) Researchers have used shift factors and their empirical values to analyze the relationship between laboratory asphalt mixture fatigue life and that within pavement structures. However, they have not established a correlation for fatigue damage between the two.

This study aims to address these issues, deepen the understanding of fatigue damage evolution, propose fatigue loading modes, and analysis methods for asphalt pavements. Establishing a relationship between laboratory asphalt mixtures' fatigue damage and that within pavement structures lays the necessary foundation for precision-engineered asphalt pavements, ensuring their performance and longevity.

References

[1] Al-qadi, I. L., & Elseifi, M. A. Viscoelastic modeling and field validation of flexible pavements. *Journal of Engineering Mechanics*, 2006, 132(2):172-178.

[2] Bai, J. *Study fatigue performance of asphalt pavement based on accelerated loading test*. Shandong: Shandong Jianzhu University, 2011.

[3] Benedetto, H. D., Roche, C. D. L., Baaj, H., et al. Fatigue of bituminous mixtures. *Materials & Structures*, 2004, 37(267):202-216.

[4] Bonnaure, F. P., Huibers, A., & Boonders, A. A laboratory investigation of the influence of rest periods on the fatigue characteristics of bituminous mixes. *Journal of the Association of Asphalt Paving Technologists*, 1982, 51:104-128.

[5] Brown, S. F., Brunton, J. M., & Stock, A. F. The analytical design of bituminous pavements. *Proceedings of the Institution of Civil Engineers*, 1985, 79(1):1-31.

[6] Carpenter, S. H., & Jansen, M. Fatigue behavior under new aircraft loading conditions. *In Proceedings of Aircraft Pavement Technology in the Midst of Change*. Seattle: American Society of Civil Engineering, 1997:259-271.

[7] Carpenter, S., & Shen, S. Dissipated energy approach to study hot-mix asphalt healing in fatigue. *Journal of Transportation Research Record*, 2006,1970(1):178-185.

[8] Carpenter, S., Ghuzlan, K., & Shen, S. Fatigue endurance limit for highway and airport pavements. *Journal of Transportation Research Record*, 2003, 1832:131-138.

[9] Castro, M., & Sánchez, J. A. Damage based model for prediction of asphalt concrete fatigue curves. *Journal of materials in civil engineering*, 2007, 19(8):700-702.

[10] Castro, M., & Sánchez, J. A. Estimation of asphalt concrete fatigue curves–a damage theory approach. *Construction and Building Materials*, 2008, 22(6):1232-1238.

[11] Chaboche, J. L. Continuous damage mechanics - a tool to describe phenomena before crack initiation. *Nuclear Engineering & Design*, 1981, 64(2):233-247.

[12] Chaboche, J. L., & Lesne, P. M. A non-linear continuous fatigue damage model. *Fatigue & Fracture of Engineering Materials & Structures*, 1988, 11(1):1-17

[13] Chen, S. Study on fatigue performance of asphalt pavement by accelerated pavement test. Guangdong: South China University of Technology, 2007.

[14] Chen, J., & Huang, X. Fatigue performance of old pavement asphalt mixtures after overlay. *Journal of Southeast University (Natural Science Edition)*, 2008, 38(05):516-519.

[15] Coleri, E., & Harvey, J. T. A fully heterogeneous viscoelastic finite element model for full-scale accelerated pavement testing. *Construction & Building Materials*, 2013, 43(6):14-30

[16] Collop, A. C. *Effects of traffic and temperature on flexible pavement wear*. Cambridge: Cambridge University, 1994.

[17] Daniel, J. S., & Kim, Y. R. Laboratory evaluation of fatigue damage and healing of asphalt mixtures. *Journal of Materials in Civil Engineering*, 2001,13(6):434-440.

[18] Daniel, J. S., Bisirri, W., & Kim, Y. R. Fatigue evaluation of asphalt mixtures using dissipated energy and viscoelastic continuum damage approaches. J*ournal of the Association of Asphalt Paving Technologists*, 2004,73:557-583.

[19] Deacon, J. A. *Fatigue of Asphalt Concrete*. Berkeley: University of California, Berkeley, 1965.

[20] Deacon, J. A., & Monismith, C. L. Laboratory flexural fatigue testing of asphalt concrete with emphasis on compound loading tests. *Highway Research Record*, 1967, 158:1-31.

[21] Deacon, J. A., Tayebali, A., Coplantz, J., et al. *Fatigue response of asphalt aggregate mixes*. Washington, D.C.: National Research Council, 1994.

[22] Gao, S. *Research on fatigue damage mechanism of asphalt mixture*. Chongqing: Chongqing Jiaotong University, 2008.

[23] Ge, Z., Huang, Z., & Huang, S. Study on effect factors of asphalt mixes fatigue properties. *Journal of Highway and Transportation Research and Development*, 2002, 06:1-4.

[24] Ghuzlan, K. A. *Fatigue damage analysis in asphalt concrete mixtures based upon dissipated energy concepts*. Urbana: University of Illinois at Urbana-Champaign, 2001.

[25] Ghuzlan, K. A., & Carpenter, S. H. Fatigue damage analysis in asphalt concrete mixtures using the dissipated energy approach. *Canadian Journal of Civil Engineering*, 2006, 33(7):890-901.

[26] Gibson, N., Qi, X., Shenoy, A., et al. *Performance testing for Superpave and structural validation*. McLean: Federal Highway Administration, 2012.

[27] Gu, F., Luo, X., Zhang, Y., et al. Using overlay test to evaluate fracture properties of field-aged asphalt concrete. *Construction & Building Materials*, 2015,101:1059-1068.

[28] Guo, R. *Predicting in-service fatigue life of flexible pavements based on accelerated pavement testing*. Austin: The University of Texas at Austin, 2007.

[29] Harvey, J. T., Hoover, T., Coetzee, N. F., et al. Caltrans accelerated pavement test (CAL/APT) program - test results: 1994–1997. *Journal of the Association of Asphalt Paving Technologists*, 1998, 67:644-689.

[30] Heukelom, W., Klomp, A. Road design and dynamic loading, *Journal of the Association of Asphalt Paving Technologists*, 1964, 33:92-125.

[31] Hines, M. L., De La Roche, C., & Chaverot, P. Evaluation of fatigue behavior of hot mix asphalt with the LCPC nantes test track and SHRP testing tools. *Journal of the Association of Asphalt Paving Technologists*, 1998, 67:717-737.

[32] Hopman, P. C., Kunst, P. A. J. C., & Pronk, A. C. A renewed interpretation method for fatigue measurement, verification of Miner's Rule. In *Proceedings of the 4th Eurobitume Symposium*. Madrid: European Bitumen Association, 1989:557-561.

[33] Hsu, T. W., & Tseng, K. H. Effect of rest periods on fatigue response of asphalt concrete mixtures. *Journal of Transportation Engineering*, 1996, 122(4):316-322.

[34] Huang, C., Gao, D., & Zhu, H. Influence of loading frequency on fatigue performance of fiber reinforced asphalt concrete. *Journal of North China Institute of Water Conservancy and Hydroelectric Power*, 2012, 33(06):106-111.

[35] Huang, B., Shu, X., & Zuo, G. Using notched semi-circular bending fatigue test to characterize fracture resistance of asphalt mixtures. *Engineering Fracture Mechanics*, 2013, 109(3):78-88.

[36] Jacobs, M. M. J., *Crack growth in asphaltic mixes*. Delft: Delft University of Technology, 1995.

[37] Johnson, C., Bahia, H., & Wen, H. Practical application of viscoelastic continuum damage theory to asphalt binder fatigue characterization. *Journal of the Association of Asphalt Paving Technologists*, 2009, 78:597-638.

[38] Kachanov, L. M. Rupture time under creep conditions. *International Journal of Fracture*, 1999, 97, 1:11-18.

[39] Kim, J., & Koh, C. Development of a predictive system for estimating fatigue life of asphalt mixtures using the indirect tensile test. *Journal of Transportation Engineering*, 2012, 138(12):1530-1540.

[40] Kim J, West RC. Application of the Viscoelastic Continuum Damage Model to the Indirect Tension Test at a Single Temperature[J]. *Journal of Engineering Mechanics*, 2010,136(4): 496-505.

[41] Kim, R. Y., Lee, H. J., & Little, D. N. Fatigue characterization of asphalt concrete using viscoelasticity and continuum damage theory. *Journal of the Association of Asphalt Paving Technologists*, 1997, 66:520-569.

[42] Kim, Y. R., Little, D. N., & Burghardt, R. SEM analysis on fracture and healing of sand-asphalt mixtures. *Journal of materials in civil engineering*, 1991, 3(2):140-153.

[43] Kim, Y. R., Baek, C., Underwood, B. S., et al. Application of viscoelastic continuum damage model-based finite element analysis to predict the fatigue performance of asphalt pavements. *KSCE Journal of Civil Engineering*, 2008, 12(2):109-120.

[44] Kim, Y. R., Little, D. N., Lytton, R., et al. Use of dynamic mechanical analysis (DMA) to evaluate the fatigue and healing potential of asphalt binders in sand asphalt mixtures. *Journal of the Association of Asphalt Paving Technologists*, 2002, 71:176-206.

[45] Kutay, M. E., Gibson, N. H., & Youtcheff, J. Conventional and viscoelastic continuum damage (VECD)-based fatigue analysis of polymer modified asphalt pavements (with discussion). *Journal of the Association of Asphalt Paving Technologists*, 2008, 77:395-434.

[46] Lee, H. J., Daniel, J. S., & Kim, Y. R. Continuum damage mechanics-based fatigue model of asphalt concrete. *Journal of Materials in Civil Engineering*, 2000:12(2):105-112.

[47] Lemaitre, J. Coupled elasto-plasticity and damage constitutive equations. *Computer Methods in Applied Mechanics and Engineering*, 1985, 51(1-3):31-49.

[48] Leykauf, G., & Kawohl, W. J. Structural design of full-depth-asphalt-pavements and field tests in comparison with German standardized asphalt pavements. In *Proceedings of the Third International Conference on the Structural Design of Asphalt Pavements*. London: International Society for Asphalt Pavements, 1972:1049-1060.

[49] Li, B. *Fatigue characteristic of various modified asphalt mixture*. Shanghai: Tongji University, 2016.

[50] Li, N., Pronk, A., Molenaar, A., et al. Comparison of uniaxial and four-point bending fatigue tests for asphalt mixtures. *Journal of Transportation Research Record*, 2013, 2373(2373):44-53.

[51] Little D. N., Lytton R. L., Williams D., et al. An analysis of the mechanism of microdamage healing based on the application of micromechanics first principles of fracture and healing. *Journal of the Association of Asphalt Paving Technologists*, 1999, 68:501-542.

[52] Luan, L., & Tian, X. Non-linear analysis of fatigue damage of asphalt mixture. *Journal of Building Materials*, 2012, 15(4):508-512.

[53] Lundström, R., & Isacsson, U. An investigation of the applicability of Schapery's work potential model for characterization of asphalt fatigue behavior. *Journal of the Association of Asphalt Paving Technologists*, 2004, 73:657-695.

[54] Luo, X., Luo, R., & Lytton, R. L. Modified Paris's Law to predict entire crack growth in asphalt mixtures. *Journal of Transportation Research Record*, 2013, 2373:54-62.

[55] Lytton, R. L., Gu, F., Zhang, Y., et al. Characteristics of undamaged asphalt mixtures in tension and compression. *International Journal of Pavement Engineering*, 2018, 19(3):192-204.

[56] Lytton, R. L., Uzan, J., Fernando, E. G., et al. *Development and validation of performance prediction models and specifications for asphalt binders and paving mixes*. Washington, D.C.: Strategic Highway Research Program, 1993.

[57] Ma, Z. *Research on the fatigue performance and the method for estimation of remaining fatigue life of in-service asphalt mixture*. Shanghai: Tongji University, 2018.

[58] Marco, S. M., & Starkey, W. L. A concept of fatigue damage. *Journal of Engineering Materials and Technology*, 1954, 76(4):627-632.

[59] Mateos, A., & Snyder, M. Validation of flexible pavement structural response models with data from the Minnesota road research project. *Plant Physiology & Biochemistry*, 2002, 1806(1):19-29.

[60] Mateos, A., Ayuso, J. P., & Jáuregui, B. C. Shift factors for asphalt fatigue from full-scale testing. *Journal of Transportation Research Record*, 2011, 2225: 128-136.

[61] Mateos, A., Ayuso, J. P., Cadavid, B., et al. Lessons learned from the application of CalME asphalt fatigue model to experimental data from CEDEX test track. *Advances in Pavement Design through Full Scale Accelerated Pavement Testing*, 2012: 483-492.

[62] Miner, M. A. Cumulative damage in fatigue. *Journal of Applied Mechanics*, 1945, 12(03):159-164.

[63] Monismith, C. L. *Fatigue response of asphalt-aggregate mixes*. Washington, D.C.: Strategic Highway Research Program, 1994.

[64] Monismith, C. L., & Deacon, J. A. Fatigue of asphalt paving mixtures. T*ransportation Engineering Journal of ASCE*, 1969, 95(2):317-346.

[65] Monismith, C. L., Secor, K. E., & Blackmer, E. W. Asphalt mixture behaviour in repeated flexure. *Journal of the Association of Asphalt Paving Technologists*. 1961, 30:188-222.

[66] Monismith, C. L., Inkabi, K., McLean, D. B., et al. *Design consideration for asphalt pavements*. Berkeley: University of California, Berkeley, 1977.

[67] Moreno-Navarro, F. & Rubio-Gámez, M. C. Effect of aggregate nature on the fatigue-cracking behavior of asphalt mixes. *Materials & Design*, 2013, 47(5):61-67.

[68] Moreno-Navarro, F. & Rubio-Gámez, M. C. Mean damage parameter for the characterization of fatigue cracking behavior in bituminous mixes. *Materials & Design*, 2014, 54(2):748-754.

[69] Mun, S., & Lee, S. Fatigue resistance potential for hot mix asphalt using viscoelastic continuum damage analysis. *Fatigue & Fracture of Engineering Materials & Structures*, 2012, 35(3):205-218.

[70] Paris, P. C., & Erdogan, F. A critical analysis of crack propagation laws. *Journal of Basic Engineering*, 1963, 85(4):528-533.

[71] Park, S. W., Kim, Y. R., & Schapery, R. A. A viscoelastic continuum damage model and its application to uniaxial behavior of asphalt concrete. *Mechanics of materials*, 1996, 24(4):241-255.

[72] Pell, P. S. Fatigue of asphalt pavement mixes. In *Proceedings of the Second International Conference on the Structural Design of Asphalt Pavements*. Ann Arbor: International Society for Asphalt Pavement, 1967:577-594.

[73] Pell, P. S. Characterization of fatigue behavior. In *Proceedings of 52nd Annual Meeting of the Highway Research Board*. Columbia: Highway Research Board, 1973:49-64.

[74] Pierce, L. M., Jackson N. C., & Mahoney, J. P. Development and implementation of a mechanistic, empirically based overlay design procedure for flexible pavements. *Journal of Transportation Research Record*, 1993, 1388:120-128.

[75] Prowell, B. D. Estimate of fatigue shift factors between laboratory tests and field performance. *Journal of Transportation Research Record*, 2010, 2181:117-124.

[76] Raithby, K.D., & Sterling, A. B. The effect of rest periods on the fatigue performance of hot-rolled asphalt under reversed axial loading. *Journal of the Association of Asphalt Paving Technologists*, 1970, 39:134-152.

[77] Sabouri, M., & Kim, Y. R. Development of a failure criterion for asphalt mixtures under

different modes of fatigue loading. *Journal of Transportation Research Record*, 2014, 2447:117-125.

[78] Schapery, R. A. Correspondence principles and a generalized J integral for large deformation and fracture analysis of viscoelastic media. *International Journal of Fracture*, 1984, 25(3):195-223.

[79] Schapery, R. A. A theory of mechanical behavior of elastic media with growing damage and other changes in structure. *Journal of the Mechanics and Physics of Solids*, 1990, 38(2):215-253.

[80] Shen, S. *Dissipated energy concepts for HMA performance: fatigue and healing*. Urbana, Illinois, University of Illinois at Urbana-Champaign, 2006.

[81] Suh, Y., Mun, S., & Yeo, I. Fatigue life prediction of asphalt concrete pavement using a harmony search algorithm. *KSCE Journal of Civil Engineering*, 2010, 14(5):725-730.

[82] Sun, Z. *Research on the fatigue damage of the asphalt pavement based on damage mechanics*. Nanjing: Southeast University, 2008.

[83] Tangella, S. C., Craus, J., Deacon, J. A., et al. *Summary report on fatigue response of asphalt mixtures*. Washington, D.C.: Strategic Highway Research Program, 1990.

[84] Tian, X., Zheng, J., Xu, Z., et al. Fatigue response of asphalt concrete at low loading frequency. C*hina Journal of Highway and Transport*, 2002, 15(1):19-19.

[85] Tsai, B. W. *High-temperature fatigue and fatigue damage process of aggregate-asphalt mixes*. Berkeley: University of California, Berkeley, 2003.

[86] Tsai, B. W., Harvey, J., and Monismith, C. WesTrack fatigue performance prediction using Miner's Law. *Journal of Transportation Research Record*, 2002, 1809(1):137-147.

[87] Tsai, B. W., Bejarano, M. O., Harvey, J.T., et al. Prediction and calibration of pavement fatigue performance using two-stage Weibull approach. *Journal of the Association of Asphalt Paving Technologists*, 2005, 74:697-732.

[88] Ullidtz, P., Harvey, J. T., Tsai, B. W., et al. *Calibration of incremental-recursive flexible damage models in CalME using HVS experiments*. Davis: University of California Pavement Research Center, 2005.

[89] Underwood, B. S., Kim, Y. R., & Guddati, M. N. Improved calculation method of damage parameter in viscoelastic continuum damage model. *International Journal of Pavement*

Engineering, 2010, 11(6):459-476.

[90] Van Dijk, W., & Visser, W. The energy approach to fatigue for pavement design. *Journal of Asphalt Paving Technologists*, 1977, 46:1-40.

[91] Van Dijk, W., Moreaud, H., Quedeville, A., & Uge, P. The fatigue of bitumen and bituminous mixes. *In Proceedings of Third International Conference of the Structural Design of Asphalt Pavements*. London: International Society for Asphalt Pavement, 1972:354-366.

[92] Wang, X. Design of pavement structure and material for full-scale test track. *Journal of Highway and Transportation Research and Development*, 2017, 34(6): 30-37.

[93] Weibull, W. A statistical theory of strength of materials. *Ingenjörs Vetenskaps Akademien Handlingar*, 1939, 151:1-45.

[94] West, R., Timm, D., Willis, J. R., et al. *Phase IV NCAT pavement test track findings: draft report*. National Center for Asphalt Technology, Auburn University, 2012.

[95] Witczak, M. W., & El-Basyouny, M. M. *Guide for Mechanistic-Empirical design of new and rehabilitated pavement structures (Appendix ii-1: calibration of fatigue cracking models for flexible pavements)*. Champaign: ARA, Inc., ERES Division, 2004.

[96] Witczak, M. W., & Mirza, M. W. *AC fatigue analysis for 2002 design guide*. Tempe: Arizona State University, 2000.

[97] Wu, Z. *Research on cumulative fatigue damage of asphalt mixture and asphalt layer based on multi-level amplitude loading*. Guangdong: South China University of Technology, 2014.

[98] Wu, K., & Zhang, X. Experimental research on uniform model for nonlinear evolution equation of fatigue damage of asphalt mixture. *Highway*, 2007, 05:125-129.

[99] Xu, Z., Li, S., Gao, Y., et al. Research on fatigue characteristic of asphalt mixture. *Journal of Traffic and Transportation Engineering*, 2001,1(1):20-24.

[100] Yang, Y. *Research on fatigue damage of asphalt mixture under different loading frequencies*. Changsha: Changsha University of Science and Technology, 2009.

[101] Yeo, I., Suh, Y., & Mun, S. Development of a remaining fatigue life model for asphalt black base through accelerated pavement resting. *Construction & Building Materials*, 2008, 22(8):1881-1886.

[102] Yu, J. *Study on fatigue characteristics of asphalt mixture*. Guangdong: South China University of Technology, 2005.

[103] Zhang, Y., Gu, F., Birgisson, B., et al. Viscoelasticplastic–fracture modeling of asphalt mixtures under monotonic and repeated loads. *Journal of Transportation Research Record*, 2017, 2631:20-29.

[104] Zhou, F., Hu, S., Chen, D. H., et al. Overlay Tester: simple performance test for fatigue cracking. *Journal of Transportation Research Record*, 2007, 2001(1):1-8.

[105] Zhu, J. *Evaluation and critical damage position for fatigue behavior of asphalt pavement considering the full temperature profile*. Shanghai: Tongji University, 2016.

[106] Zou, J., Roque, R., & Byron, T. Effect of HMA ageing and potential healing on top-down cracking using HVS[J]. *Road Materials & Pavement Design*, 2012,13(3): 518-533.

3 RESEARCH METHODOLOGIES

As outlined by Chapter 1 and Chapter 2, the field of asphalt pavement research confronts three significant challenges. Firstly, there is a crucial gap in effectively tracking and analyzing fatigue damage progression in real-world asphalt layers, a complex task given the multifaceted factors influencing damage evolution. Secondly, there is uncertainty regarding the most suitable fatigue loading modes for asphalt layers, with a notable lack of comprehensive studies to guide this selection, especially for layers placed on semi-rigid bases. Lastly, a notable disparity exists between theoretical models predicting fatigue damage in asphalt mixtures and their practical application in in-situ conditions, underscoring a need for models that effectively bridge laboratory findings with real-world pavement behaviors.

Addressing these challenges, the objective of this research is centered on developing a predictive model that intricately characterizes the fatigue damage process in asphalt mixtures and layers, with a particular emphasis on the role of fatigue loading modes. This model seeks to bridge the gap between laboratory and field observations, offering a more holistic understanding of fatigue behaviors in asphalt pavements. Additionally, it aims to address the limitations of existing fatigue damage evolution models and to enhance the understanding of tensile fatigue loading modes across different pavement structures.

Methodologically, the approach of this study is threefold. Firstly, it involves an in-depth laboratory investigation using techniques such as ITFT and 4PB tests to understand the fatigue life and damage progression in asphalt mixtures under various loading conditions. This phase includes exploring a range of nonlinear models to accurately depict the fatigue damage development process. Secondly, the study extends its analysis to in-situ conditions through F-sAPT, enabling the assessment and modeling of fatigue damage in real-world pavement layers. Thirdly, the study focuses on establishing a correlation between laboratory and in-situ fatigue damage evolution, as well as identifying and understanding the critical damage points in asphalt layers.

In this chapter, each methodology employed in the study will be detailed, justifying their selection and discussing how they collectively contribute to achieving the research objective. The

aim is to provide a clear, coherent, and comprehensive understanding of the methodologies that form the backbone of this research, ensuring that the study is grounded in robust and reliable scientific practices.

3.1 Setting the Demand and the Selected Approaches

3.1.1 Fatigue Test Methods

3.1.1.1 Laboratory Fatigue Test Methods

In the pursuit of an effective approach to evaluate fatigue damage in asphalt mixtures, it is essential to select laboratory fatigue test methods that meet specific demands to ensure accuracy, repeatability, and applicability. The chosen methods must satisfy the following criteria:

(1) Simple and available equipment settings: The test method should utilize equipment that is not only simple and readily available but also reliable in terms of functionality and maintenance.

(2) Widely applied and verified efficiency: The chosen method should be well-established, with proven efficiency and widely recognized for its accuracy and reliability.

(3) Adjustable for different loading conditions: The method must be adaptable to various loading conditions, encompassing aspects such as loading frequency or loading time, rest periods, and temperature settings. This flexibility is crucial for simulating a wide range of real-world pavement conditions.

(4) Applicability for different tensile fatigue loading modes: The method should be suitable for either stress-controlled or strain-controlled loading modes, providing a comprehensive understanding of the material's response under different stress states.

(5) Capability to record stiffness variations: The method can accurately record the initial stiffness of the material and monitor the stiffness variation throughout the loading process. This data is essential for understanding the material's fatigue behavior under repeated loading conditions.

As discussed in Chapter 2, there are numerous laboratory fatigue test methods for asphalt mixtures, including 2PB, 4PB, UTFT, ITFT, etc. Researchers and institutions worldwide have conducted comparative evaluations of these various fatigue test methods [2,5]. Based on this foundation, this

study has selected the stress-controlled ITFT and the strain-controlled 4PB as the fatigue test methods for laboratory asphalt mixtures.

The ITFT, shown in Figure 3-1(a), has been extensively used in early research on the fatigue characteristics of asphalt mixtures due to its simplicity and the general availability of the testing apparatus. This method is highly effective for evaluating the fatigue properties of core samples from asphalt layers. According to the SHRP-A-404 report [2,5], ITFT is slightly less sensitive to material and test condition variations compared to the 4PB, but it offers lower variability in fatigue life test results. Therefore, ITFT with a stress-controlled loading mode is chosen as one of the laboratory fatigue test methods in this study. The IPC UTM-25 will be used to conduct ITFT. This machine allows for custom programming to control the displacement and force of the load sensor, enabling both stress-controlled and strain-controlled fatigue loading modes. During the test, the machine automatically collects and records data from each loading cycle, including displacement and force from the load sensor and data from the LVDT sensor.

(a) ITFT

(b) 4PB

Figure 3-1 The selected laboratory fatigue test methods for asphalt mixtures: (a) ITFT and (b) 4PB

The 4PB, shown in Figure 3-2(b) is currently the most widely applied laboratory fatigue test method, known for its strong operability, good repeatability, and high sensitivity to material and test condition variations. Therefore, 4PB with a strain-controlled loading mode has been selected as another laboratory fatigue test method in this study.

3.1.1.2 Field Test Methods

One focus of this research is to characterize the fatigue damage process in in-situ asphalt layers. To address this, specific demands are set for field test methods that are capable of evaluating long-term fatigue damage progression:

(1) Condensed timeframe assessment: The test method must be capable of assessing long-term fatigue damage progression within a significantly condensed timeframe. This requirement is crucial for simulating years of pavement use and environmental impact in a shorter duration, like the duration of this PhD research.

(2) Controlled test conditions: It is imperative that the test method allows for the control of various test conditions, including wheel loads, temperature, and moisture conditions. This control is essential for the analyzability, reliability, and applicability of the test results.

(3) Integration with other field damage test methods: The method should be compatible with other field testing methods, such as the Falling Weight Deflectometer (FWD), for comprehensive modulus detection. This integration allows for a more holistic understanding of the pavement structure's condition, offering insights into in-situ fatigue damage progressions.

Considering all these demands, the selected approach for field testing in this research is full-scale accelerated pavement testing (F-sAPT). This choice is underpinned by several considerations, as highlighted in Chapter 2. First, F-sAPT is a specialized technique in pavement engineering, designed to simulate actual pavement structures, traffic, and environmental conditions while accelerating the damage process. This methodology involves applying wheel loads, typically exceeding standard legal limits, in a controlled manner to emulate the cumulative effects of real-world traffic over an extended period but within a significantly condensed timeframe. Second, compared to scaled-down accelerated testing, typically conducted in controlled laboratory environments, F-sAPT offers a more comprehensive and expansive scope. It is designed to mimic the mechanical responses of actual pavement structures under real-life conditions, thereby providing a more accurate assessment of the pavement's behavior, particularly its susceptibility to fatigue.

For this study, the chosen equipment for F-sAPT is Tongji University's MLS66, a linear loading device with an effective loading length of 6.6 meters. As illustrated in Figure 3-2, this equipment features six sets of loading wheels, with a maximum loading speed of 6000 cycles per hour, equivalent to approximately 6 m/s or 22 km/h. This equipment's capability is further enhanced by its compatibility with other testing methods like the FWD and Portable Seismic Pavement Analyzer (PSPA). The integration of these methods with MLS66 allows for a thorough assessment of the modulus of asphalt layers within pavement structures, providing critical data to support the analysis of the fatigue damage evolution process in these layers.

(a) The appearance of MLS66

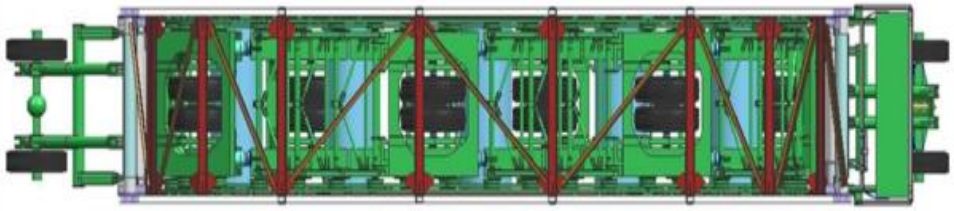

(b) The load settings of MLS66

Figure 3-2 The MLS66 at Tongji University: (a) The appearance and (b) The load settings

3.1.2 Fatigue Damage Evolution Models

One of the main objectives of this research centers on developing a predictive model that intricately characterizes the fatigue damage process in both asphalt mixtures and layers. This model is expected to surpass existing models in terms of capturing the complexity of fatigue damage evolution and enhancing the understanding of tensile fatigue loading modes in various pavement structures. Basically, such kind of model is required to meet the following specific demands:

(1) Reflecting the entire damage process: The model should accurately represent the full extent of fatigue damage progression in both asphalt mixtures and layers.

(2) Monotonic increase of damage variable: The fitted damage variable D must increase monotonically with the number of load applications.

(3) Boundary conditions: The model must satisfy essential boundary conditions. Damage D approaches 0 as the number of load applications approaches 0, and D approaches 1 as the number of load applications tends towards infinity.

(4) Simplicity and clarity: The model should be simple in form, with clearly defined parameters that have a straightforward physical interpretation and are easy to obtain.

(5) Incorporation of key influencing factors: model parameters should reflect the factors significantly influencing the fatigue damage evolution process, particularly the fatigue loading mode.

To choose a model that can characterize the fatigue damage process and satisfy these demands, this research selected and compared seven nonlinear models as demonstrated in Table 3-1.

Table 3-1 The selected nonlinear damage evolution models

No.	Author(s)	Model	Parameters	Loading Mode
①	Weibull [6]	$D = 1 - \exp(-\lambda N^{\gamma})$	λ, γ	Any
②	Sun [4]	$D = \exp\left[-\left(\frac{\alpha}{N}\right)^{\beta}\right]$	α, β	Any
③	Chaboche [1]	$D = 1 - \left(1 - \frac{N}{N_f}\right)^{m}$	m	Controlled stress
④	Yang [9]	$D = a_1 \ln\left[b_1\left(\frac{N}{N_f}\right) + 1\right]$	a_1, b_1	Controlled stress
⑤	Luan &Tian [3]	$D = 2A\left(1 - e^{-\frac{N/N_f}{t}}\right)$	A, t	Controlled stress
⑥	Wu & Zhang [8]	$D = 1 - ae^{\frac{-N/N_f}{b}} + c$	a, b, c	Controlled strain
⑦	Wu [7]	$D = \left(1 - \frac{E_f}{E_0}\right)\left(\frac{N}{N_f}\right)^{k}$	k	Controlled strain

Note: D is the damage variable. N and N_f are the loading repetitions and the material fatigue life, respectively. E_0 and E_f are the material initial stiffness and the stiffness at the fatigue failure, respectively.

3.1.3 Methods to Correlate the Laboratory and In-situ Fatigue Damage Evolution

The research objectives pivot on correlating laboratory findings with field observations. This correlation is expected to be not merely about assessing fatigue life but extend to a nuanced understanding of fatigue damage evolution and its diverse implications across different settings. For this purpose, the correlation methods are required to satisfy the following specific demands:

(1) Focus beyond fatigue life: The method should transcend traditional focus on fatigue life, delving into the intricate correlations of fatigue damage and its evolution. This shift is critical in comprehensively understanding the damage process.

(2) Entire fatigue damage progression: The approach must encompass the entire spectrum of fatigue damage progression, capturing the complexities and variations from initiation to critical stages.

(3) Acknowledging nonlinearity: The method must accommodate the nonlinearity inherent in fatigue damage progression. This entails considering the varying states of damage and how they influence the overall behavior and integrity of the asphalt.

(4) Accuracy and predictability: Ensuring the method can accurately predict and model fatigue damage under diverse real-world conditions.

In response to these demands, this research adopted a novel approach. It involved a comparative analysis, juxtaposing model parameters from laboratory and field-based predictive models. This comparative framework facilitated a coherent alignment of damage predictive models, effectively bridging lab and in-situ findings. It underscores the universality of the model parameters, ensuring their relevance across different testing conditions and environments.

3.2 Methodology

This part will provide an introduction of the entire research methodology, offering a clear and concise overview of the experimental and analytical approaches employed. Figure 3-3 gives the overview of the research methodology.

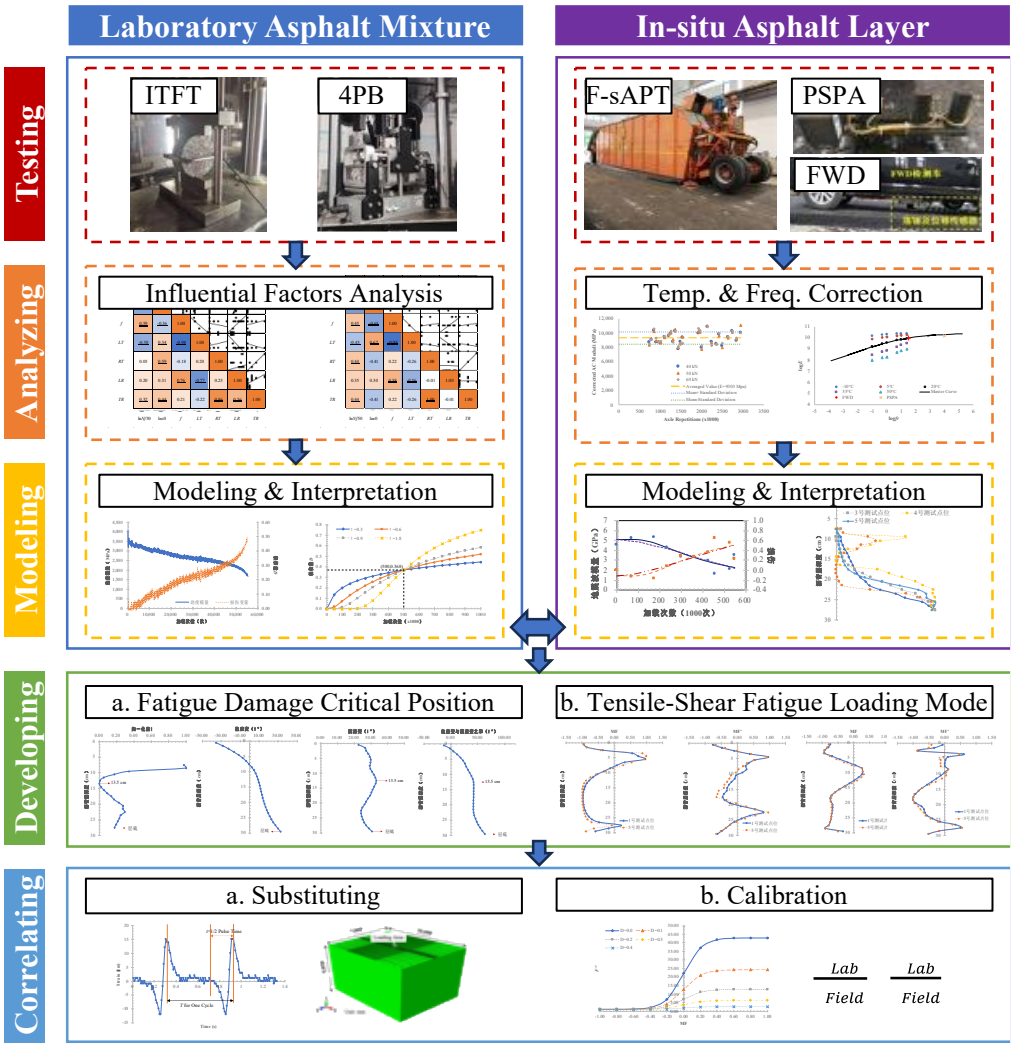

Figure 3-3 The overview of the research methodology

3.2.1 Analysis of Fatigue Damage in Laboratory Asphalt Mixtures

The primary objective of this task is to conduct a comprehensive analysis and modeling of the evolution of fatigue damage in asphalt mixtures, with a particular focus on understanding the impact of tensile fatigue loading modes on the damage progression process. The detailed tasks involve:

(1) Performing ITFT and 4PB fatigue tests: These tests are pivotal in assessing the fatigue behavior of asphalt mixtures under various loading conditions.

(2) Analyzing the impact of loading factors on initial stiffness and fatigue life: Evaluate the influence of initial strain amplitude, loading frequency or time, rest period, loading rate, and the ratio of rest period to loading time under both controlled-stress and controlled-strain modes.

(3) Applying and comparing nonlinear models: Utilize seven nonlinear models to fit the fatigue damage evolution process in laboratory asphalt mixtures and conduct a comparative analysis of these models in terms of their rationality and fitting effectiveness. This step is essential to recommend the most suitable model that accurately describes the fatigue damage development process under the influence of multiple factors.

(4) Enhancing model interpretability: Integrate the analysis of various loading parameters, especially the tensile fatigue loading mode, into the predictive models. This integration is aimed at significantly improving the interpretability of model parameters. It allows for a deeper insight into the fatigue damage progressions of asphalt mixtures, particularly in how they respond to different types of tensile fatigue loading.

3.2.2 Analysis of Fatigue Damage in In-situ Asphalt Layers

The second task focuses on a comprehensive analysis of the damage progression within in-situ asphalt layers and the establishment of a damage evolution model, with an investigation of the interpretation of the model parameters. The detailed tasks involve:

(1) Conducting F-sAPTs: Conduct F-sAPTs on the newly-built asphalt layers placed on the semi-rigid base and granular base, separately.

(2) Modulus detection using various techniques at the predetermined load repetitions during the F-sAPTs: Employ FWD, PSPA, and uniaxial compression dynamic modulus test to evaluate the modulus of asphalt layers and develop temperature and frequency correction coefficients for the in-situ detected modulus of asphalt layers.

(3) Analysis and modeling of in-situ damage progression: Examine the development of damage in different sections of the pavement at various depths, locations, and orientations. Then, employ the Weibull survival function (Model ① in Table 2-1) and the structural behavior function (Model ② in Table 2-1) to model this damage progression process. Conduct a comparative analysis of the different models for their rationality, fitting effectiveness, and interpretability, with the goal of recommending the most appropriate model to describe fatigue damage development in in-situ asphalt layers.

3.2.3 Fatigue Loading Mode and Critical Damage Location in Asphalt Layers

The primary goal of this task is to analyze the critical damage locations and fatigue loading modes within the structure of pavement asphalt layers. This analysis is pivotal in understanding the complex dynamics of fatigue damage, particularly how different loading modes affect the integrity and lifespan of in-service pavements. The detailed tasks involve:

(1) Analysis of mechanical mechanism underlying fatigue damage: The task begins with a meticulous analysis of the mechanical mechanisms influencing fatigue damage in asphalt layers, leveraging the findings from F-sAPTs.

(2) Analysis of critical damage locations in semi-rigid and flexible asphalt pavements: A significant part of the task involves analyzing where critical damage is most likely to occur within different types of pavement structures, specifically comparing semi-rigid and flexible asphalt pavements. This analysis is aimed at identifying potential weak points susceptible to fatigue damage.

(3) Introduction of a new tensile-shear loading mode factor: Recognizing the limitations of traditional tensile fatigue loading in fully capturing the complexity of in-situ conditions, a new tensile-shear loading mode factor is introduced. This factor is designed to more accurately represent the responses experienced by asphalt layers under actual service conditions.

3.2.4 Relationship between Laboratory and In-situ Asphalt Fatigue Damage

The main objective of the third task is to establish a relationship between fatigue damage in laboratory asphalt mixtures and that in structural asphalt layers within pavement structures. This endeavor aims to bridge the gap between controlled laboratory conditions and real-world pavement scenarios. By doing so, it enhances the practical applicability of laboratory findings to actual pavement design and maintenance practices. This task is divided into two primary components:

(1) Substitution: substitute in-situ loading parameters into the laboratory-based model parameter interpretation equations. This process is crucial for ensuring a straightforward comparison between the damage predictive models obtained from laboratory settings and those derived from

field observations.

(2) Calibration: Establish a conversion factor that effectively links the model parameters derived from both laboratory tests and F-sAPTs data. The conversion factors intricately consider the nonlinear fatigue damage progression as delineated by the predictive models. This aspect is crucial for translating laboratory fatigue test results into a format that is directly applicable to real-world pavement conditions.

3.3 Summary

This chapter meticulously outlines the research methodologies, bridging the identified gaps from the literature review with the experimental design. This chapter detailed the demands and selection of specific laboratory and field test methods, such as ITFT and 4PB for laboratory settings and F-sAPT for field tests, emphasizing their alignment with the study objectives. It also discusses the rationale behind choosing various fatigue damage evolution models, focusing on their ability to accurately represent the fatigue process and their applicability in both laboratory and in-situ settings. The methodologies discussed here are not only pivotal for ensuring the accuracy and reliability of the findings but also instrumental in advancing our understanding of fatigue damage in asphalt pavements, setting the stage for the empirical chapters that follow. This cohesive approach underscores the potential of this study to significantly contribute to the field of pavement engineering by linking theoretical models to practical, real-world applications.

References

[1] Chaboche, J. L. Continuous damage mechanics - a tool to describe phenomena before crack initiation. *Nuclear Engineering & Design*, 1981, 64(2):233-247.

[2] Deacon, J. A., Tayebali, A., Coplantz, J., et al. *Fatigue response of asphalt aggregate mixes*. Washington, D.C.: National Research Council, 1994.

[3] Luan, L., & Tian, X. Non-linear analysis of fatigue damage of asphalt mixture. *Journal of Building Materials*, 2012, 15(4):508-512.

[4] Ma, Z. *Research on the fatigue performance and the method for estimation of remaining*

fatigue life of in-service asphalt mixture. Shanghai: Tongji University, 2018.

[5] Tangella, S. C., Craus, J., Deacon, J. A., et al. *Summary report on fatigue response of asphalt mixtures*. Washington, D.C.: Strategic Highway Research Program, 1990.

[6] Weibull, W. A statistical theory of strength of materials. *Ingenjörs Vetenskaps Akademien Handlingar*, 1939, 151:1-45.

[7] Wu, Z. *Research on cumulative fatigue damage of asphalt mixture and asphalt layer based on multi-level amplitude loading*. Guangdong: South China University of Technology, 2014.

[8] Wu, K., & Zhang, X. Experimental research on uniform model for nonlinear evolution equation of fatigue damage of asphalt mixture. *Highway*, 2007, 05:125-129.

[9] Yang, Y. *Research on fatigue damage of asphalt mixture under different loading frequencies*. Changsha: Changsha University of Science and Technology, 2009.

4 ANALYSIS OF FATIGUE DAMAGE IN LABORATORY ASPHALT MIXTURES

According to Chapter 2, while substantial research has been conducted on the fatigue properties of asphalt mixtures, notably in fatigue life, a significant gap exists in understanding the detailed process of fatigue damage evolution. To bridge this gap, this chapter delves into performing ITFT and 4PB tests, which are critical in assessing the fatigue behavior of asphalt mixtures under varied loading conditions. It further involves a detailed analysis of the influence of key loading factors on the initial stiffness and fatigue life of these mixtures. This chapter also undertakes the task of applying and critically comparing a range of nonlinear models to accurately fit the fatigue damage evolution observed in laboratory settings. This comparative study aims to identify the most suitable model that encapsulates the fatigue damage development process, considering the multifaceted influence of various factors. Additionally, the chapter strives to enhance the interpretability of these models, especially in terms of their response to different types of tensile fatigue loading, thereby providing a more profound insight into the fatigue damage mechanisms in asphalt mixtures.

4.1 Laboratory Fatigue Tests

According to Chapter 3, ITFT with stress-controlled loading mode and 4PB with strain-controlled loading mode were selected as the laboratory fatigue tests, emphasizing their alignment with the study objectives.

4.1.1 Materials

In this research, a consistent type of AC-13 asphalt mixture was employed for both ITFT and 4PB tests. This mixture comprised 70# base asphalt along with aggregates of limestone (0-5 mm) and basalt (5-15 mm). The Marshall parameters and aggregate gradation of this mixture are detailed in Table 4-1 and Figure 4-1.

Table 4-1 The asphalt mixture used for laboratory fatigue tests

Mixture	Asphalt Content (%)	Density (g/cm³)	VV (%)	VMA (%)	VFA (%)	Stability (kN)
AC-13	5.1	2.432	3.3	14.7	77.6	10.60

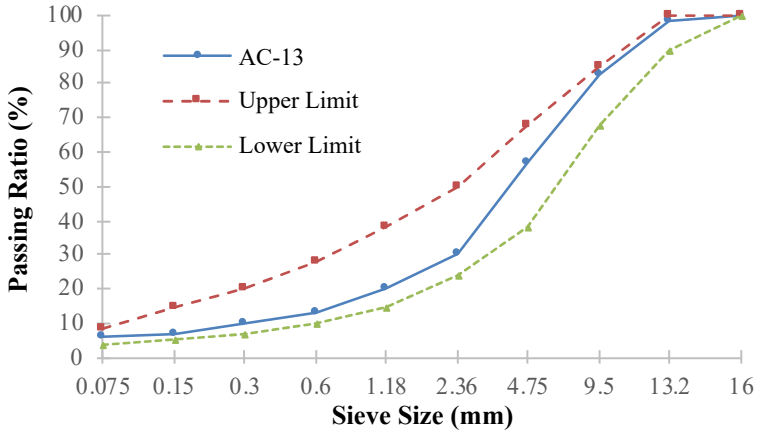

Figure 4-1 Aggregate gradation of the asphalt mixture

4.1.2 Experimental Scheme of ITFT

The specimens for the ITFT were prepared from core samples extracted from actual asphalt layers. These cores, with a diameter of 100±2.0 mm and a height of 300 mm, were sectioned at various depths to prepare test specimens. The specimen used in ITFT, with a height of 40±2.0 mm and smooth ends, was selected from the same depth range to ensure consistency in testing.

Table 4-2, as referenced, outlines the ITFT experimental scheme under controlled stress mode. This scheme encompasses a comprehensive analysis of six loading factors reviewed in Chapter 2: initial strain amplitude (ε_0), loading frequency (f) or loading time (LT), rest period (RT), loading rate (LR), and the ratio of the rest period to the loading time (TR). Notably, f is the reciprocal of LT, and LR is defined as the ratio of ε_0 to LT.

Table 4-2 ITFT experimental scheme under controlled stress mode

Group	No.	ε_0 (με)	f (Hz)	LT (s)	RT (s)	LR (με/s)	TR
①	1	33.32	10	0.1	0	333.18	0
	2	37.20	10	0.1	0	372.03	0
②	3	44.05	10	0.1	0	440.46	0
	4	46.86	10	0.1	0	468.61	0
	5	48.85	10	0.1	0	488.51	0

Group	No.	ε_0 (με)	f (Hz)	LT (s)	RT (s)	LR (με/s)	TR
③	6	66.02	10	0.1	0	660.25	0
	7	66.05	10	0.1	0	660.48	0
	8	69.86	10	0.1	0	698.63	0
④	9	74.90	10	0.1	0	748.96	0
	10	80.08	10	0.1	0	800.84	0
	11	81.96	10	0.1	0	819.61	0
⑤	12	63.64	2.5	0.4	0	159.11	0
	13	71.14	2.5	0.4	0	177.86	0
	14	94.75	2.5	0.4	0	236.88	0
⑥	15	56.74	5	0.2	0	283.72	0
	16	62.93	5	0.2	0	314.63	0
⑦	17	40.63	12.5	0.08	0	507.91	0
	18	42.71	12.5	0.08	0	533.84	0
⑧	19	70.88	10	0.1	0.1	708.75	1
	20	71.93	10	0.1	0.1	719.25	1
	21	72.45	10	0.1	0.1	724.50	1
	22	73.50	10	0.1	0.1	735.00	1
	23	75.60	10	0.1	0.1	756.00	1
	24	77.18	10	0.1	0.1	771.75	1
⑨	25	85.05	10	0.1	0.1	850.50	1
	26	88.20	10	0.1	0.1	882.00	1
	27	90.83	10	0.1	0.1	908.25	1
	28	99.23	10	0.1	0.1	992.25	1
	29	106.05	10	0.1	0.1	1060.50	1
⑩	30	83.48	10	0.1	0.2	834.75	2
	31	88.20	10	0.1	0.2	882.00	2
⑪	32	91.35	10	0.1	0.4	913.50	4
	33	99.75	10	0.1	0.4	997.50	4
⑫	34	63.53	2.5	0.4	0.2	158.81	0.5
	35	72.98	2.5	0.4	0.2	182.44	0.5
⑬	36	97.65	2.5	0.4	0.2	244.13	0.5
	37	110.25	2.5	0.4	0.2	275.63	0.5
	38	111.30	2.5	0.4	0.2	278.25	0.5
⑭	39	145.95	2.5	0.4	0.2	364.88	0.5

According to Table 4-2, the following analysis can be drawn:

(1) Impact of ε_0: Groups ① to ④, ⑧ and ⑨, and ⑫ to ⑭ are used to assess the influence of ε_0 on the ITFT results.

(2) Effect of f or LT: The impact of these factors is analyzed using data from Groups ① to ⑦.

(3) Role of RT and TR: Groups ⑧ to ⑭ provide insights into how RT and TR affect the ITFT

outcomes.

(4) Influence of LR: The effect of LR is evaluated using data from Groups ① and ⑥.

4.1.3 Experimental Scheme of 4PB

The 4PB tests were conducted under controlled strain conditions. The experimental scheme for the 4PB, as shown in Table 4-3, considers the same key loading factors as that considered in the ITFT.

Table 4-3 4PB experimental scheme under controlled strain mode

Group	No.	ε_0 (με)	f (Hz)	LT (s)	RT (s)	LR (με/s)	TR
①	1	385.53	10	0.1	0	3855.29	0
	2	448.95	10	0.1	0	4489.53	0
②	3	597.42	10	0.1	0	5974.24	0
	4	623.64	10	0.1	0	6236.37	0
	5	629.29	10	0.1	0	6292.93	0
③	6	753.67	10	0.1	0	7536.70	0
	7	797.98	10	0.1	0	7979.77	0
④	8	465.95	12.5	0.08	0	5824.39	0
	9	480.12	12.5	0.08	0	6001.45	0
	10	507.76	12.5	0.08	0	6346.99	0
⑤	11	761.12	8	0.125	0	6088.95	0
	12	835.53	8	0.125	0	6684.25	0
	13	836.94	8	0.125	0	6695.55	0
⑥	14	555.95	10	0.1	0.1	5559.50	1
	15	571.20	10	0.1	0.1	5712.02	1
	16	572.60	10	0.1	0.1	5726.04	1
	17	580.76	10	0.1	0.1	5807.60	1
	18	586.43	10	0.1	0.1	5864.26	1
	19	746.58	10	0.1	0.1	7465.82	1
⑦	20	552.76	10	0.1	0.2	5527.64	2
	21	559.85	10	0.1	0.2	5598.51	2
	22	572.61	10	0.1	0.2	5726.14	2

According to Table 4-3, the following analysis can be drawn:

(1) Impact of ε_0: Groups ① to ③ of the test are designed to investigate the impact of initial strain amplitude on the test results.

(2) Effect of f or LT: Groups ① to ⑤ focus on assessing the influence of loading frequency or loading time.

(3) Role of RT and TR: By comparing results from Groups ① to ③ and ⑥ to ⑦, the influence

of rest period or the ratio of rest period to loading time on the test outcomes can be analyzed.

(4) Influence of LR: Groups ②, ④, and ⑤ are set to determine whether the loading rate impacts the test results.

4.2 Influential Factors of Initial Stiffness and Fatigue Life

The subsequent analysis, which builds upon the ITFT and 4PB tests discussed in Section 4.1, delves into a comprehensive examination of the impact that the fatigue loading modes and the six loading factors, as delineated in Table 4-2 and Table 4-3, have on the initial stiffness and fatigue life of the asphalt mixtures. This analysis is pivotal in discerning the intricate relationships between these influential factors and the fatigue characteristics of the asphalt mixtures.

4.2.1 Calculation of Initial Stiffness and Fatigue Life

The first subsection aims to introduce the methodologies employed to calculate initial stiffness and fatigue life from the ITFT and 4PB test results.

4.2.1.1 Initial Stiffness

For the ITFT test, the processing of stiffness follows the Equations 4-1 to 4-3.

$$\sigma_n = \frac{2F_n}{\pi \cdot h \cdot \Omega} \quad 4\text{-}1$$

$$\varepsilon_{R,n} = \left(\frac{2\Delta H_{R,n}}{\Omega}\right)\left[\frac{1+3\nu}{4+\pi\nu-\pi}\right] \cdot 10^6 \quad 4\text{-}2$$

$$S_{\mathrm{mix},n} = \frac{\sigma_n}{\varepsilon_{R,n}} \cdot (1+3\nu) \cdot 10^6 \quad 4\text{-}3$$

In Equation 4-1, σ_n and F_n are the stress amplitude (MPa) and the maximum test load (N) at the n^{th} cycle, respectively. h is the specimen height (mm), and Ω is the specimen diameter (mm). In Equation 4-2, $\varepsilon_{R,n}$ and $\Delta H_{R,n}$ are the resilient strain amplitude (μm/m) and the radial resilient deformation (mm) at the n^{th} cycle, respectively. $S_{\mathrm{mix},n}$ is the stiffness (MPa) at the n^{th} cycle and ν represents the Poisson's Ratio (0.35).

For the 4PB tests, the analysis of the collected data follows a distinct methodology to calculate the stress and strain amplitudes, as well as the stiffness:

$$\sigma_t = \frac{L \cdot F_n}{b \cdot c} \quad 4\text{-}4$$

$$\varepsilon_t = \frac{12\delta \cdot c}{3L^2 - 4m^2} \quad 4\text{-}5$$

$$S_{\mathrm{mix},n} = \frac{\sigma_t}{\varepsilon_t} \quad 4\text{-}6$$

where σ_t, ε_t, and δ are the tensile stress amplitude (Pa), tensile strain amplitude (m/m), and the maximum strain at the beam center (m) at the n^{th} cycle, respectively. L represents the beam length (0.357 m), b is the beam width (m), c is the beam height (m), and m is the distance between the centers of adjacent supports (0.119 m).

Currently, the stiffness modulus at the 50th or 100th cycle is commonly used as the initial stiffness of asphalt mixtures [13,16,28]. Based on this, this study considers the average stiffness modulus between the 50th and 100th cycles as the initial stiffness modulus $S_{\mathrm{mix},0}$ of the specimen.

4.2.1.2 Fatigue Life

To accurately determine the fatigue life of asphalt mixture specimens, this research initially conducts a comparative analysis of different fatigue failure criteria.

In the controlled strain mode, the amplitude of strain remains constant throughout each loading cycle, while the amplitude of stress decreases as the number of loading cycles increases. Since fatigue failure in this mode does not manifest as evident breakage, the failure criteria are generally based on changes in the specimen's stiffness or dissipated energy patterns. A widely adopted method considers the degradation of the specimen's stiffness modulus to 50% of its initial value as the fatigue failure criterion, denoted as N_{f50} [5,6,17,20]. Another commonly used approach is to identify fatigue failure when the product of the stiffness modulus and loading cycles reaches a peak value, referred to as N_{fNM} [19]. As discussed in Chapter 2, this research adopts the Stiffness Reduction Ratio (SRR) as the fatigue damage variable to study the damage evolution process in asphalt mixtures, thereby adopting N_{f50} as the defining criterion for fatigue life under controlled strain mode.

In the controlled stress mode, where the amplitude of stress remains constant and the strain amplitude increases with each loading cycle until specimen failure, different criteria have been proposed. Some studies [1,8,16] suggest using complete specimen breakage as the fatigue failure criterion in this mode. However, this approach often entails a degree of subjectivity. An alternative

and more objective method is the energy ratio approach, first conceptualized by Van Dijk & Visser [23] and later formalized by Hopman et al. [10]. The energy ratio ER is defined as:

$$ER = \frac{n \cdot W_0}{W_n} \cdot 10^6 \cong n \cdot S_{\text{mix},n} \cong \frac{n}{\varepsilon_{R,n}} \cdot 10^6 \qquad 4\text{-}7$$

Here, W_0 is the initial dissipated energy, and W_n is the dissipated energy at the n^{th} cycle. Initially, the energy ratio versus loading cycle curve is linear, representing a damage-free line indicative of consistent dissipated energy across loading cycles. Hopman et al. [10] observed that when cracking occurs and cracks propagate, the curve starts deviating from this damage-free line. Thus, the point of deviation is used as the criterion for fatigue failure, denoted as N_{fER}.

For controlled stress mode, a comparative analysis between N_{fER} and N_{f50} (as shown in Figure 4-2) reveals close alignment in their results. To maintain consistency across different fatigue loading modes and ensure data comparability, while correlating with the selected fatigue damage variable, this study continues to define fatigue life under controlled stress mode using N_{f50}.

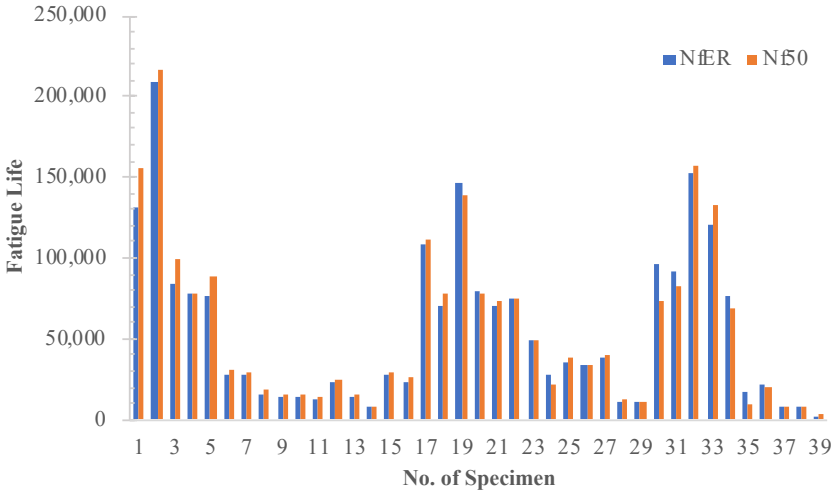

Figure 4-2 Comparisons between N_{fER} and N_{f50}

4.2.1.2 Calculation Results

Based on the data processing from ITFT and 4PB tests, the calculation results of the initial stiffness modulus for each specimen are shown in Table 4-4 and Table 4-5.

Table 4-4 Initial stiffness and fatigue life derived from the controlled stress mode

Group	No.	$S_{mix,0}$ (MPa)	N_{f50}
①	1	6842	156335
	2	6067	216458
②	3	6653	98661
	4	6356	77365
	5	6095	88419
③	6	5462	31351
	7	5485	29018
	8	7390	18276
④	9	5972	14901
	10	6442	15526
	11	5567	14701
⑤	12	4809	24876
	13	4291	15764
	14	3208	8476
⑥	15	5218	29690
	16	4674	26097
⑦	17	7214	111404
	18	6867	78501
⑧	19	7377	138143
	20	7193	78429
	21	7136	72904
	22	6159	75001
	23	4828	49281
	24	6762	21100
⑨	25	6050	38597
	26	7001	33796
	27	5753	40219
	28	6258	12894
	29	5829	11329
⑩	30	6213	73333
	31	5891	81798
⑪	32	5648	157238
	33	5192	132847
⑫	34	4998	68438
	35	5737	9608
⑬	36	4299	20068
	37	4657	7839
	38	4582	8428
⑭	39	4299	2691

Table 4-5 Initial stiffness and fatigue life derived from the controlled strain mode

Group	No.	$S_{mix,0}$ (MPa)	N_{f50}
①	1	4079	763005
	2	3764	649789
②	3	3426	139951
	4	3322	143376
	5	3484	130676
③	6	3352	59784
	7	2997	76426
④	8	4157	458647
	9	3750	396651
	10	3990	316315
⑤	11	3360	72476
	12	3386	69114
	13	3462	58665
⑥	14	3692	523015
	15	3627	238719
	16	4037	113901
	17	3618	106492
	18	3254	184478
	19	3795	22851
⑦	20	3914	75815
	21	3481	288453
	22	3473	10808

4.2.2 Impacts of Loading Factors on Initial Stiffness

In this subsection, the impacts of the six loading factors on the initial stiffness modulus ($S_{\mathrm{mix},0}$) were quantitatively analyzed. The analysis is grounded on the calculation results of $S_{\mathrm{mix},0}$, employing Pearson correlation coefficients to systematically evaluate the influence of each loading factor. The findings from stress-controlled tests (ITFT) and strain-controlled tests (4PB) are organized in Table 4-6 and Table 4-7. These tables illustrate the variation of $S_{\mathrm{mix},0}$ with initial strain amplitude (ε_0), loading frequency (f), loading time (LT), rest time (RT), the ratio of rest time to loading time (TR), and loading rate (LR). Additionally, the tables include Pearson correlation coefficients between $S_{\mathrm{mix},0}$ and each loading factor, where red and blue colors signify positive and negative correlations, respectively, with deeper shades indicating stronger correlations.

Table 4-6 Analysis results of the initial stiffness from stress-controlled tests

Factor	$\ln(\varepsilon_0)$	f (Hz)	LT(s)
$\ln(S_{mix,0})$	-0.48	0.86	-0.84
	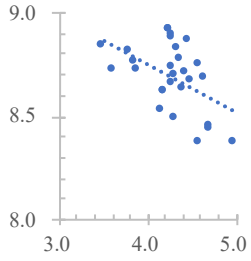	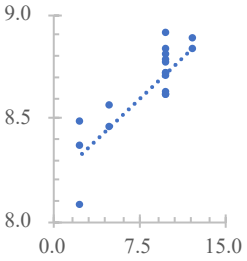	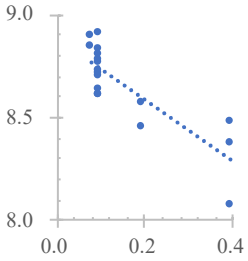
Factor	***RT*** **(s)**	***TR***	***LR*** **(με/s)**
$\ln(S_{mix,0})$	-0.44	0.10	0.54
	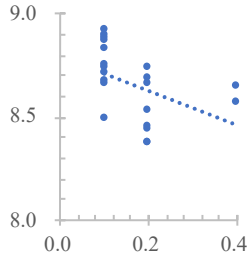	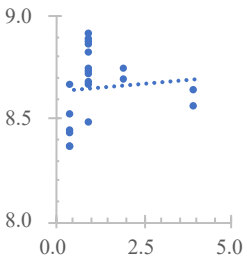	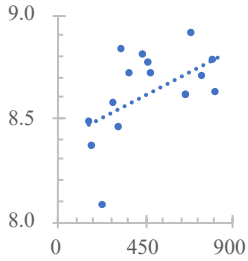

Table 4-7 Analysis results of the initial stiffness from strain-controlled tests

Factor	$\ln(\varepsilon_0)$	f (Hz)	LT(s)
$\ln(S_{mix,0})$	-0.95	0.59	-0.54
	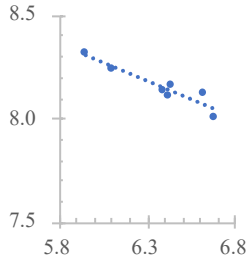	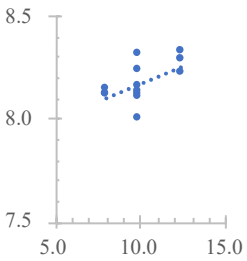	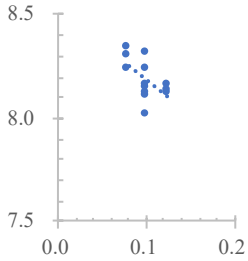
Factor	***RT*** **(s)**	***TR***	***LR*** **(με/s)**
$\ln(S_{mix,0})$	-0.10	0.24	-0.41
	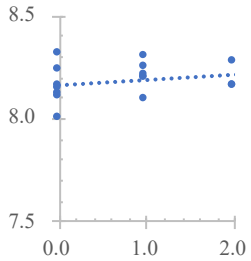	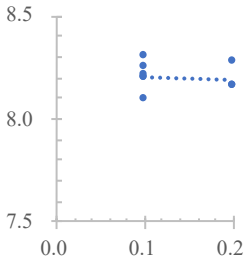	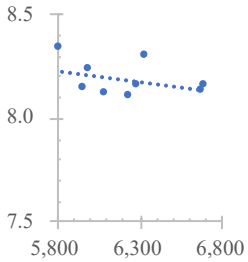

Key observations from this analysis are:

(1) Strain dependence of initial stiffness: Under both tensile fatigue loading modes, a negative correlation exists between $S_{\mathrm{mix},0}$ and ε_0, indicating strain dependency in initial stiffness. Meanwhile, this negative correlation reflects that, at the same composition/temperature, larger imposed initial strain implies larger effective compliance and thus a smaller apparent initial stiffness.

(2) Significance of loading frequency and duration: In both modes, f and LT show a highly significant correlation with $S_{\mathrm{mix},0}$. However, since LT is the inverse of f, their influences on $S_{\mathrm{mix},0}$ are not independent. Meanwhile, the impact of f on $S_{\mathrm{mix},0}$ in stress-controlled tests is stronger than that in strain-controlled tests because viscoelastic stiffening is recorded directly when the load is prescribed; under strain control, the prescribed strain history limits how much the frequency-induced modulus shift alters the observed initial stiffness. Meanwhile, this variation in influence is attributed to the limited range of loading frequencies (8, 10, and 12.5 Hz) used in the strain-controlled tests. Consistent with findings from Tian et al. [21] and Ge et al. [7], when the variation in loading frequency is narrow, its impact on the fatigue characteristics of asphalt mixtures is not pronounced.

(3) Weaker influence of rest time and the ratio of rest time to loading time: Both RT and TR have a relatively weaker impact on $S_{\mathrm{mix},0}$, as recovery windows are shot in early cycles, where $S_{\mathrm{mix},0}$ is measured and damage has not yet accumulated substantially.

(4) Correlation with loading rate: There exists a certain correlation between $S_{\mathrm{mix},0}$ and LR. However, the influence of LR varies between controlled-stress and controlled-strain modes, primarily due to the differing dependencies of $S_{\mathrm{mix},0}$ on ε_0 in these modes.

In summary, regardless of the method employed to measure the modulus of asphalt mixtures or layers, it is imperative to consider the magnitude and duration of the load, or the loading rate, and to apply corrections to align modulus values under a unified standard.

Subsequently, the focus is on establishing a mathematical expression to discern the intricate relationships between the selected load factors and the initial stiffness of the asphalt mixtures. The approach employed is stepwise regression analysis, a technique that incrementally introduces variables into the regression model. This method allows for the inclusion of the most significant

loading factors affecting $S_{\mathrm{mix},0}$ while simultaneously testing and eliminating variables that do not significantly contribute to the model, ensuring that multicollinearity is minimized.

The final expressions for $S_{\mathrm{mix},0}$ obtained through stepwise regression, are as follows:

For stress-controlled tests:

$$\ln(S_{\mathrm{mix},0}) = 8.653 - 0.078\ln(\varepsilon_0) + 0.041f \quad 4\text{-}8$$

For strain-controlled tests:

$$\ln(S_{\mathrm{mix},0}) = 9.640 - 0.239\ln(\varepsilon_0) + 0.007f \quad 4\text{-}9$$

Notably, the expressions do not include LR as it is dependent of f and ε_0. The stepwise regression-derived expression for $S_{\mathrm{mix},0}$ should include only the most significant loading factor from these three. Moreover, Table 4-8 present the variance analysis for these equations. The high values of R indicate a strong regression relationship between the independent variables and $S_{\mathrm{mix},0}$, and the significance test results (p-values) for each variable are less than 0.01, validating the appropriateness and necessity of the chosen variables. Consequently, Equations 4-8 and 4-9 hold statistical significance, confirming that the formulated expressions for $S_{\mathrm{mix},0}$ are both reasonable and empirically valid.

Table 4-8 Regression coefficients and variance analysis for Equations 4-8 and 4-9

No.	Coefficient	Value	t-Value	p-Value	R	R^2	F-value	Sig.
Eq. 4-8	Constant	8.653	34.412	0.000	0.795	0.633	37.037	0.000
	$\ln(\varepsilon_0)$	-0.078	7.072	0.000				
	f	0.041	-3.439	0.008				
Eq. 4-9	Constant	9.640	14.849	0.000	0.860	0.740	24.228	0.000
	$\ln(\varepsilon_0)$	-0.239	-3.808	0.001				
	f	0.007	3.505	0.006				

4.2.3 Impacts of Loading Factors on Fatigue Life

This research also utilized the Pearson correlation coefficient method to analyze the impacts of six selected loading factors on the fatigue life of asphalt mixtures. The outcomes of these analyses, derived from both stress-controlled (ITFT) and strain-controlled (4PB) tests, are systematically presented in Table 4-9 and Table 4-10. These tables detail how N_{f50} varies with initial strain amplitude (ε_0), loading frequency (f), loading time (LT), rest time (RT), the ratio of rest time to loading time (TR), and loading rate (LR). The tables also feature Pearson correlation coefficients,

indicating the degree of correlation between the initial stiffness modulus N_{f50} and each loading factor. In these tables, red highlights positive correlations, and blue signifies negative correlations, with the intensity of the color correlating to the strength of the relationship.

The analysis yields several noteworthy findings:

(1) Significant impact of initial strain amplitude: Across all loading modes, a strong negative correlation exists between N_{f50} and ε_0, suggesting that an increase in the initial strain amplitude leads to a reduction in the fatigue life of the specimen.

(2) Correlation with loading frequency and loading time: Both these factors exhibit a certain degree of correlation with N_{f50}. Consistent with findings by Huang et al. [12], higher loading frequencies and shorter loading times tend to prolong fatigue life. However, since loading frequency is inversely related to loading time, these factors are not independent in their impact on fatigue life, and their correlation with N_{f50} is weaker compared to their relationship with $S_{\mathrm{mix},0}$.

(3) Rest time and ratio of rest time to loading time effects: Both RT and TR positively correlate with N_{f50}, with TR showing a stronger correlation. This implies that the fatigue life of asphalt mixtures not only increases with longer rest periods but is more significantly influenced by the proportion of rest time to loading time. This finding aligns with research by Bonnaure et al. [2], Hsu and Tseng [11], and Guo [9].

(4) Weaker loading rate Correlation: There is a discernible but relatively weaker correlation between loading rate and N_{f50} compared to other factors.

(5) In summary, it's crucial to account for both the magnitude and the proportion of rest time to loading time when assessing the fatigue life of asphalt mixtures, regardless of the testing method.

Table 4-9 Analysis results of the fatigue life from stress-controlled tests

Factor	$\ln(\varepsilon_0)$	f (Hz)	LT(s)
	-0.82	0.53	-0.50
$\ln(N_{f50})$	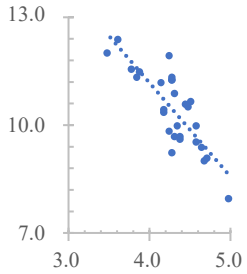	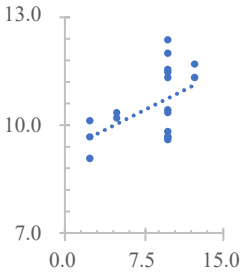	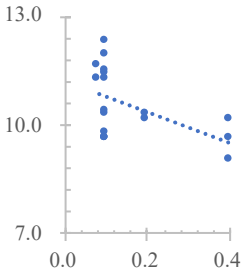
Factor	RT (s)	TR	LR (με/s)
	0.19	0.60	-0.21
$\ln(N_{f50})$	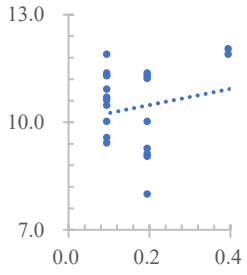	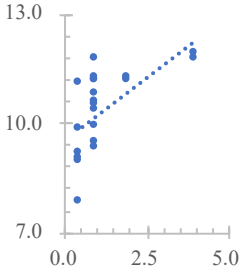	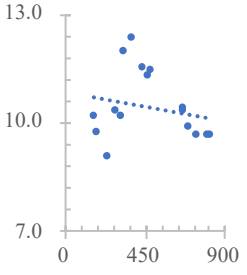

Table 4-10 Analysis results of the fatigue life from strain-controlled tests

Factor	$\ln(\varepsilon_0)$	f (Hz)	LT(s)
	-0.98	0.65	-0.66
$\ln(N_{f50})$	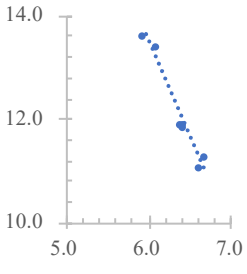	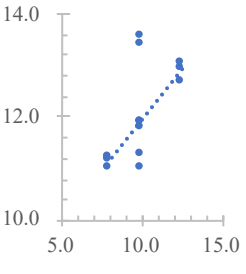	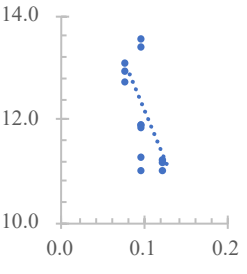
Factor	RT (s)	TR	LR (με/s)
	0.40	0.78	-0.67
$\ln(N_{f50})$	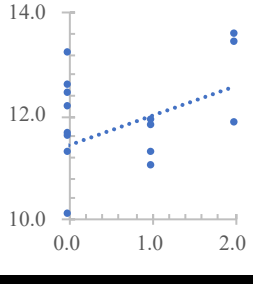	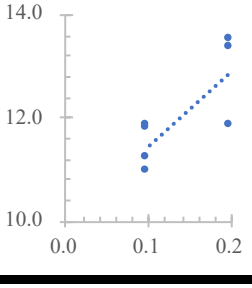	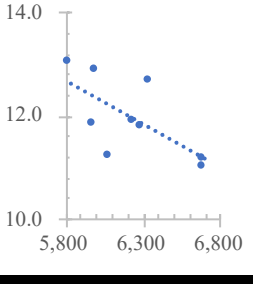

Furthermore, a mathematical expression to discern the intricate relationships between the selected load factors and the fatigue life of the asphalt mixtures was established by employing stepwise regression analysis. The final expressions for N_{f50} are as follows:

For stress-controlled tests:

$$\ln(N_{f50}) = 24.018 - 3.265\ln(\varepsilon_0) + 0.804TR \quad 4\text{-}10$$

For strain-controlled tests:

$$\ln(N_{f50}) = 33.508 - 3.434\ln(\varepsilon_0) + 0.316TR \quad 4\text{-}11$$

The variance analysis for these expressions is given in Table 4-11. These tables demonstrate high R values, indicating a close regression relationship between the independent variables and N_{f50}. The significance tests for the independent variables (p-values) are all below 0.01, affirming the rational and necessary selection of these variables. Thus, the formulated expressions for N_{f50} are both statistically robust and theoretically sound.

Table 4-11 Regression coefficients and variance analysis for Equations 4-10 and 4-11

No.	Coefficient	Value	t-Value	p-Value	R	R^2	F-value	Sig.
Eq. 4-10	Constant	24.018	23.468	0.000	0.907	0.824	107.348	0.000
	$\ln(\varepsilon_0)$	-3.265	-13.699	0.000				
	TR	0.804	9.402	0.000				
Eq. 4-11	Constant	33.508	23.095	0.000	0.979	0.958	126.597	0.000
	$\ln(\varepsilon_0)$	-3.434	-15.412	0.000				
	TR	0.316	3.225	0.008				

4.2.4 Analysis of the Impact of Tensile Fatigue Loading Modes

§4.2.3 reveals significant differences in fatigue life predictions of asphalt mixtures under the stress-controlled and strain-controlled modes. This variability underscores the need for a comprehensive analysis of the last, yet most crucial, influential factor affecting fatigue characteristics of asphalt mixtures: the tensile fatigue loading mode. The objective is to propose a unified approach to predict fatigue life across these different tensile fatigue loading modes.

4.2.4.1 Conversion Equation Method

For this purpose, this research adopts the conversion equation method, originally proposed by Monismith [21] and advanced by Witczak and Mirza [13]. Based on the laboratory-derived fatigue

life equations under stress-controlled and strain-controlled modes, they identified the quantitative relationship between the fatigue lives under these two modes, as shown by F:

$$F = \frac{N_{f\varepsilon}}{N_{f\sigma}} = 6.74^{5}E^{-0.4} = 13909E^{-0.4} \quad 4\text{-}12$$

where $N_{f\varepsilon}$ and $N_{f\sigma}$ represent the fatigue life of asphalt mixtures under strain-controlled and stress-controlled modes, respectively, while E denotes the initial stiffness modulus (MPa). Subsequently, the researchers employed a Sigmoidal model to develop a fatigue life conversion equation F''. Since they considered the strain-controlled mode applicable to thin asphalt layers (less than 5.08 cm) while stress-controlled mode applicable to thick layers (more than 20.32 cm), they utilized the thickness of the asphalt layer instead of the fatigue loading mode as the variable in this fatigue life conversion equation. Building on this foundation, they formulated a unified fatigue life equation, as illustrated in Equation 4-14.

$$F'' = 1 + \frac{F}{1 + \exp^{(1.354h_{ac} - 5.408)}} = 1 + \frac{13909E^{-0.4}}{1 + \exp^{(1.354h_{ac} - 5.408)}} \quad 4\text{-}13$$

$$N_f = F''N_{f\sigma} \quad 4\text{-}14$$

where h_{ac} is the thickness of the asphalt layer.

However, it is obvious that this existing method overlooked the nonlinearity in the fatigue damage progressions, particularly how F varies in this nonlinear process. They also simplistically linked the fatigue loading mode of an asphalt layer to its thickness. As Zhu's [29] research indicates, even within the same pavement structure, asphalt mixtures at different depths may correspond to different fatigue loading modes. Therefore, the use of asphalt layer thickness instead of the loading mode factor as the variable in the conversion equation warrants further discussion.

This study seeks to refine the existing methodology by thoroughly analyzing results from laboratory fatigue tests. It addresses the nonlinear progression of fatigue damage by modifying fatigue life equations to correlate with damage variables. In doing so, the adjusted F varies nonlinearly with the development of damage. Furthermore, the study introduces a conversion function rooted in the Mode Factor (MF), as initially proposed by Monismith and Deacon [17,18], instead of the thickness of the asphalt layer. Incorporating an S-shaped function, this approach endeavors to establish a unified fatigue life equation, adaptable to various tensile fatigue loading modes and states of damage.

4.2.4.2 Modified Fatigue Life Equations

To accurately and coherently capture the nonlinearity in the progression of fatigue damage within asphalt mixtures, this study embarks on a crucial preliminary task of defining the damage variables. Following an extensive review of existing definitions of fatigue damage in asphalt mixtures, the stiffness reduction rate (SRR) is selected as the primary damage variable. This selection is grounded in a detailed analysis of indoor fatigue test results, which provide comprehensive data on both the initial stiffness of each specimen ($S_{\mathrm{mix},0}$) and the stiffness at any given loading cycle ($S_{\mathrm{mix},n}$). These results are encapsulated in Equation 4-15, a key mathematical tool for quantifying fatigue damage in asphalt mixtures. The evolution of this damage is visually depicted in Figure 4-3, offering an intuitive understanding of the damage process.

$$D = \mathrm{SRR} = 1 - \frac{S_{\mathrm{mix},n}}{S_{\mathrm{mix},0}} \qquad 4\text{-}15$$

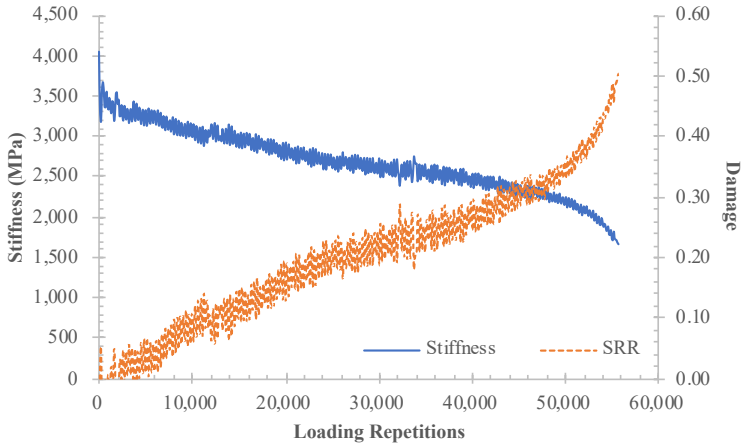

Figure 4-3 Stiffness deterioration processes and fatigue damage progressions of asphalt mixtures

The subsequent phase of the study involves establishing a correlation between fatigue life and the defined damage variable. In this context, N_{al} represents the number of load applications the asphalt mixture undergoes until reaching a predetermined damage level. The residual fatigue life, N_{rf}, is then conceptualized as the difference between the standard fatigue life at 50% stiffness reduction (N_{f50}) and N_{al}. This framework facilitates the use of ITFT and 4PB test results to analyze the residual fatigue life of asphalt mixtures under various damage states. The ultimate goal is to develop predictive equations for N_{rf} under both controlled-stress and controlled-strain loading modes.

Figure 4-4 and Figure 4-5 present the correlation between the residual fatigue life of asphalt mixtures in different damage states, the initial tensile strain level (ε_0), and the temperature ratio (TR). In these figures, the damage variable D is represented by SRR.

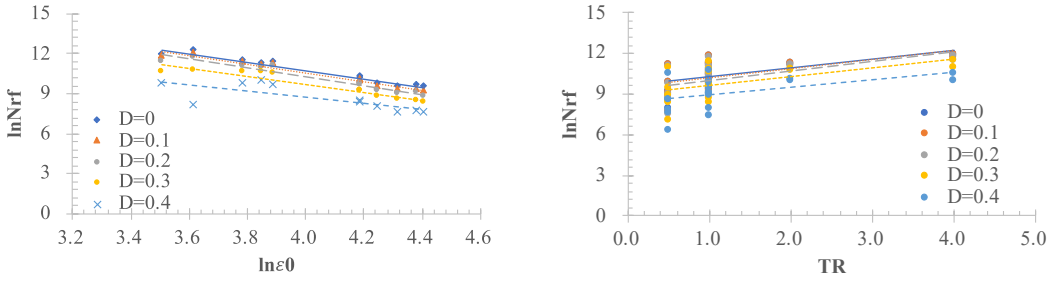

(a) $\ln(N_{rf})$ vs. $\ln(\varepsilon_0)$ (b) $\ln(N_{rf})$ vs. TR

Figure 4-4 N_{rf} under stress-controlled modes: (a) $\ln(N_{rf})$ vs. $\ln(\varepsilon_0)$ and (b) $\ln(N_{rf})$ vs. TR

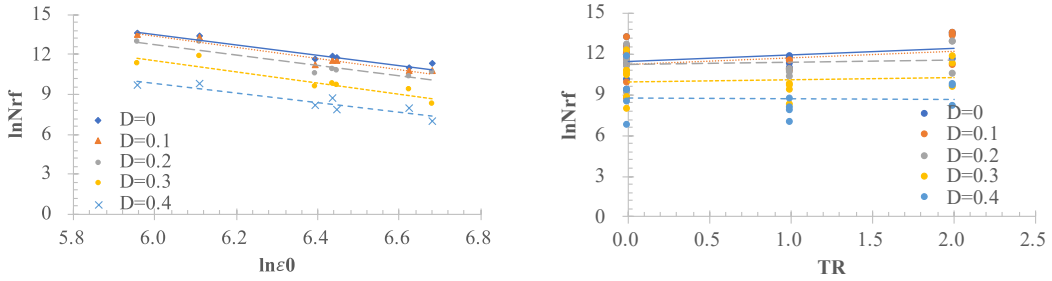

(a) $\ln(N_{rf})$ vs. $\ln(\varepsilon_0)$ (b) $\ln(N_{rf})$ vs. TR

Figure 4-5 N_{rf} under strain-controlled modes: (a) $\ln(N_{rf})$ vs. $\ln(\varepsilon_0)$ and (b) $\ln(N_{rf})$ vs. TR

These graphs demonstrate a robust linear relationship in logarithmic coordinates between N_{rf} and ε_0, as well as TR in half logarithmic coordinates. It is noteworthy that at a fixed initial strain or TR level, the residual fatigue life, N_{rf}, diminishes with an increase in the D. Consequently, N_{rf} can be aptly described as a function of ε_0 and the damage variable D. Moreover, Furthermore, despite the progression of damage, the slopes of the relationships between N_{rf} and ε_0, as well as between N_{rf} and TR, are observed to remain relatively stable, underscoring the consistency of these relationships.

Expanding on the insights gained from the seminal works of Ma [16] and Castro et al. [3], this investigation integrates the damage variable into the fatigue life prediction framework outlined in § 4.2.3. This strategic incorporation culminates in the formulation of Equations 4-16 and 4-17, designed to predict the residual fatigue life of asphalt mixtures under controlled-stress and controlled-strain modes, respectively.

For stress-controlled tests:

$$\ln(N_{rf-\sigma}) = 24.018 - 3.265\ln(\varepsilon_0) + 0.804TR + 2.458\ln(1-D) \quad 4\text{-}16$$

For strain-controlled tests:

$$\ln(N_{rf-\varepsilon}) = 33.508 - 3.434\ln(\varepsilon_0) + 0.316TR + 5.503\ln(1-D) \quad 4\text{-}17$$

The robustness and statistical reliability of these newly developed equations are thoroughly examined and presented in Table 4-12. A key observation is the statistical significance of these equations, as evidenced by the high values of the multiple correlation coefficient R and the coefficient of determination R^2. These metrics highlight a tight and meaningful regression relationship between the independent variables and the residual fatigue life, underscoring the predictive strength and fitting accuracy of the model. Moreover, the significance tests conducted on the independent variables, as indicated by the p-values, all register values below 0.01. This statistically significant outcome not only reinforces the distinct influence of each variable within the model but also validates the overall rationality and appropriateness of the model's form. Such a level of statistical significance implies a very low probability of these results occurring by chance, thereby bolstering confidence in the model's utility for predicting residual fatigue life in asphalt mixtures under varied loading conditions.

Table 4-12 Regression coefficients and variance analysis for Equations 4-16 and 4-17

No.	Coefficient	Value	t-Value	p-Value	R	R^2	F-value	Sig.
Eq.4-16	$\ln(1-D)$	2.458	19.874	0.000	0.890	0.792	394.989	0.000
Eq.4-17	$\ln(1-D)$	5.503	18.623	0.000	0.871	0.759	346.815	0.000

4.2.4.3 Unified Fatigue Life Equation

Refining the foundational work presented in Equations 4-16 and 4-17, which estimate the residual fatigue life of asphalt mixtures, this study further investigates the intricate nonlinear relationship between the residual fatigue life ratios in controlled-stress and controlled-strain loading modes and the damage variable D. By adeptly integrating Equations 4-16 and 4-17 into Equation 4-12, this study derive a ratio, F, as formulated in Equation 4-18. Intriguingly, this ratio F demonstrates a power function relationship with the damage variable D, indicating a complex interplay between these variables.

$$F = \frac{N_{rf-\varepsilon}}{N_{rf-\sigma}} = e^{9.490} \cdot {\varepsilon_0}^{-0.169} \cdot e^{-0.488TR} \cdot (1-D)^{3.045} \quad 4\text{-}18$$

Delving deeper, based on the insights from Equation 4-18, F for varying levels of damage is calculated. Capitalizing on these findings, the study introduces an S-shaped function to develop a continuous transition function, denoted as F'. This innovative function is pivotal in determining the

ratio of residual fatigue life of asphalt mixtures under any fatigue loading mode (N_{rf}) to that under a controlled-stress mode ($N_{rf-\sigma}$), as elucidated in Equation 4-19.

$$F' = 1 + \frac{F-1}{1+e^{k\cdot \mathrm{MF}}} = 1 + \frac{e^{9.490}\cdot {\varepsilon_0}^{-0.169}\cdot e^{-0.488TR}\cdot (1-D)^{3.045}-1}{1+e^{k\cdot \mathrm{MF}}} \quad 4\text{-}19$$

Here, k represents the regression parameter, and MF, initially proposed by Monismith and Deacon [17,18], is detailed in Equation 4-20.

$$\mathrm{MF} = \text{Mode Factor} = \frac{|A|-|B|}{|A|+|B|} \quad 4\text{-}20$$

A and B signify the respective percentage changes in tensile stress and strain within the asphalt layer, corresponding to a given percentage reduction C in its average stiffness. Notably, the MF value adopts -1 under a controlled stress mode and +1 under a controlled strain mode. In scenarios where both stress and strain undergo variations during repeated loading, the MF value intriguingly oscillates between -1 and +1, reflecting the dynamic nature of the loading conditions.

Figure 4-6 elucidates the behavior of the transition function, F', in relation to the MF under varied ε_0 and TR conditions. This figure provides a clear indication that, within identical damage states, the value of F' escalates with an increase in MF. This trend implies a significant insight: as the fatigue loading mode shifts closer to the controlled-stress mode, the residual fatigue life N_{rf} tends to converge towards $N_{rf-\sigma}$. In contrast, as the loading mode veers towards the controlled-strain mode, the disparity between N_{rf} and $N_{rf-\sigma}$ becomes more pronounced. Moreover, it is observed that for any given MF, an increase in the damage variable D correlates with a decrease in F', suggesting a convergence in the residual fatigue lives across various loading modes as the extent of damage intensifies.

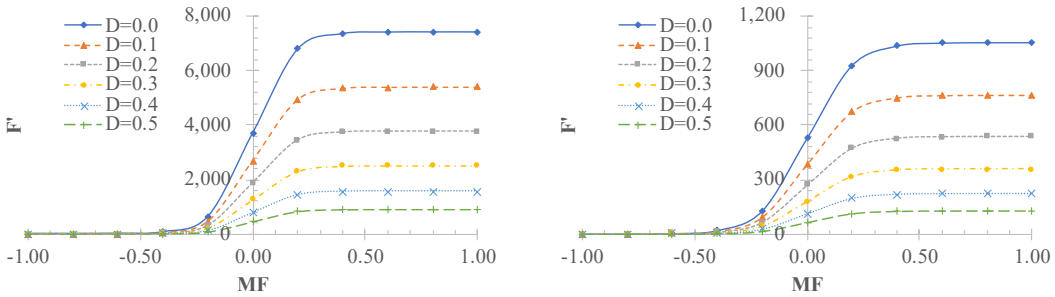

(a) $\varepsilon_0 = 30\mu\varepsilon,\ TR = 0$ (b) $\varepsilon_0 = 30\mu\varepsilon,\ TR = 4$

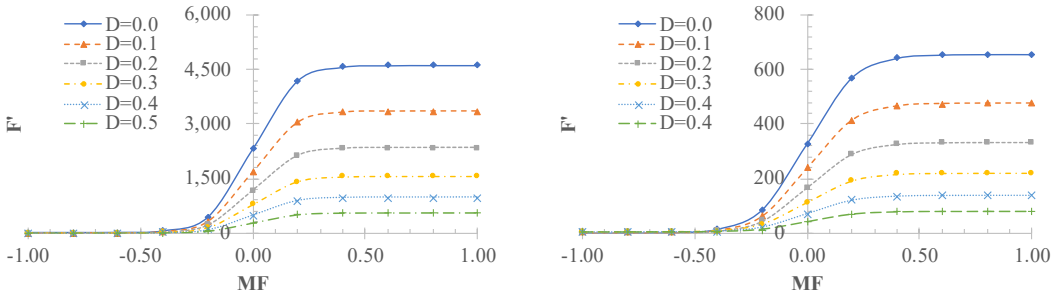

(c) $\varepsilon_0 = 500\mu\varepsilon,\ TR = 0$ (d) $\varepsilon_0 = 500\mu\varepsilon,\ TR = 4$

Figure 4-6 The proposed S-shaped function of F'

Table 4-13 plays an integral part in this analysis by presenting the values of k, revealing a distinct pattern of change correlated with diverse ε_0 and TR. This pattern necessitates a more in-depth examination of the k values. To address this, Figure 4-7 showcases how k varies with ε_0 and TR, uncovering a robust linear relationship between k values and $\ln(\varepsilon_0)$, as well as with TR.

Table 4-13 Regression results of the coefficient k

ε_0	TR	k	ε_0	TR	k	ε_0	TR	k	ε_0	TR	k	ε_0	TR	k
30	0	-11.91	50	0	-11.83	100	0	-11.71	300	0	-11.52	500	0	-11.44
	0.5	-11.67		0.5	-11.58		0.5	-11.46		0.5	-11.28		0.5	-11.19
	1	-11.42		1	-11.34		1	-11.22		1	-11.03		1	-10.95
	2	-10.94		2	-10.85		2	-10.73		2	-10.55		2	-10.46
	4	-9.96		4	-9.87		4	-9.76		4	-9.57		4	-9.48

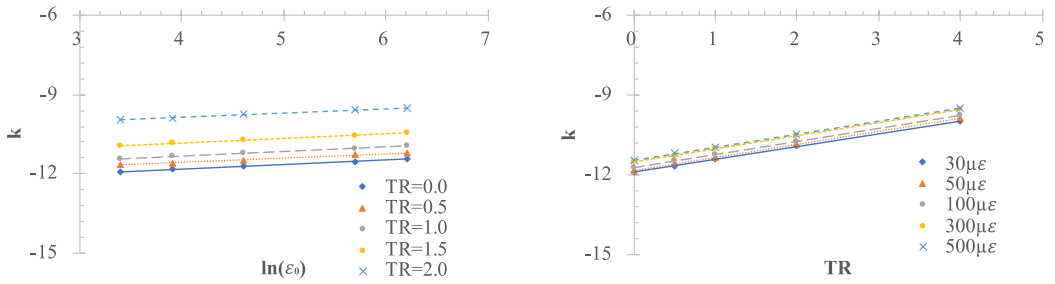

(a) k vs. $\ln(\varepsilon_0)$ (b) k vs. TR

Figure 4-7 Regression results of k vs.: (a) $\ln(\varepsilon_0)$ and (b) TR

Capitalizing on these findings, this study successfully derives an expression for k through meticulous regression analysis, as delineated in Equation 4-21. The empirical robustness of this expression is further bolstered by the statistical parameters detailed in Table 4-14. These parameters affirm the statistical significance and the robust fit of the model. Notably, the p-values for the independent variables being less than 0.01 is a testament to the highly significant differences observed, underscoring the validity and appropriateness of the formulated model for k values.

$$k = -12.489 + 0.170\ln(\varepsilon_0) + 0.488TR \quad 4\text{-}21$$

Table 4-14 Regression coefficients and variance analysis for Equations 4-21

No.	Coefficient	Value	t-Value	p-Value	R	R^2	F-value	Sig.
Eq.4-21	Constant	-12.489	-5557.157	0.000	1.000	1.000	1129848.790	0.000
	$\ln(\varepsilon_0)$	0.170	377.919	0.000				
	TR	0.488	1454.948	0.000				

Therefore, the refined and final expression for F' is presented in Equation 4-22. Moreover, the unified equation for estimating the residual fatigue life of asphalt mixtures under any fatigue loading mode is encapsulated in Equation 4-23.

$$F' = 1 + \frac{F-1}{1+e^{k\cdot \mathrm{MF}}} = 1 + \frac{e^{9.490}\cdot {\varepsilon_0}^{-0.169}\cdot e^{-0.488TR}\cdot (1-D)^{3.045}-1}{1+e^{(-12.489+0.170\ln(\varepsilon_0)+0.488TR)\cdot \mathrm{MF}}} \quad 4\text{-}22$$

$$N_{rf} = F' \cdot N_{rf-\sigma} \quad 4\text{-}23$$

This innovative approach marks a significant advancement over traditional conversion function methods by incorporating the nonlinearity inherent in the fatigue damage process of asphalt mixtures. It also accounts for the nonlinear relationship between the ratios of residual fatigue life under varying fatigue loading modes and the damage variable. Moving beyond the conventional practice of applying a singular fatigue loading mode to a specific pavement structure, this study introduces a conversion function grounded in the MF. This advancement significantly enhances both the rationality and the wider applicability of the conversion function method, offering a more nuanced understanding of fatigue damage in asphalt mixtures.

4.3 Predictions of Laboratory Fatigue Damage Processes

In the ever-evolving landscape of asphalt fatigue research, the realm of study has expanded considerably. The focus has shifted from a rather simplistic assessment of the fatigue life of asphalt layers and mixtures to a more intricate and nuanced understanding of the fatigue damage process. This progression in the field necessitates a comprehensive approach to effectively analyze and monitor the evolution of fatigue damage. To this end, this study embarks on utilizing the SSR as a pivotal metric to identify and predict the progression of fatigue damage in asphalt mixtures. By leveraging SSR, the study aims to provide a detailed portrayal of how fatigue damage develops and progresses under various loading conditions.

4.3.1 The Selected Nonlinear Damage Evolution Models

Recognizing the need for a robust model that can accurately characterize the fatigue damage process and fulfill the criteria set forth in §3.1.2, this research undertook a comprehensive comparison of seven nonlinear models as demonstrated in Table 4-15. The comparative study of these models is systematically presented in the following sub-sections, elucidating the distinctive features, strengths, and limitations. Through the comparative analysis, the research aims to identify the most suitable model that not only aligns with the theoretical framework of asphalt fatigue but also effectively addresses the practical aspects of predicting fatigue damage progressions in laboratory settings.

Table 4-15 The selected nonlinear damage evolution models

No.	Author(s)	Model	Parameters	Loading Mode
①	Weibull [24]	$D = 1 - \exp(-\lambda N^{\gamma})$	λ, γ	Any
②	Sun [16]	$D = \exp\left[-\left(\frac{\alpha}{N}\right)^{\beta}\right]$	α, β	Any
③	Chaboche [4]	$D = 1 - \left(1 - \frac{N}{N_f}\right)^{m}$	m	Controlled stress
④	Yang [27]	$D = a_1 \ln\left[b_1\left(\frac{N}{N_f}\right) + 1\right]$	a_1, b_1	Controlled stress
⑤	Luan &Tian [15]	$D = 2A\left(1 - e^{-\frac{N/N_f}{t}}\right)$	A, t	Controlled stress
⑥	Wu & Zhang [26]	$D = 1 - ae^{\frac{-N/N_f}{b}} + c$	a, b, c	Controlled strain
⑦	Wu [25]	$D = \left(1 - \frac{E_f}{E_0}\right)\left(\frac{N}{N_f}\right)^{k}$	k	Controlled strain

Note: D is the damage variable. N and N_f are the loading repetitions and the material fatigue life, respectively. E_0 and E_f are the material initial stiffness and the stiffness at the fatigue failure, respectively.

4.3.1.1 Weibull Survival Function (WSF)

The Weibull Survival Function (WSF), as depicted in Table 4-15 (identifier ①), plays a crucial role in the domain of asphalt fatigue research. Originally introduced by Weibull [24] in the 1930s, WSF gained early application in pavement cracking prediction by Little et al. [14], and over time, it has been increasingly adopted in road engineering research. Significantly, Tsai [22] in 2001 implemented this model to characterize the fatigue damage development in laboratory asphalt mixtures. Later in 2018, Ma [16] applied the WSF in his research for regression analysis of fatigue damage in asphalt layers.

Upon detailed analysis of WSF, several salient points emerge:

(1) Versatility in damage process representation: The WSF can adapt to various damage progression scenarios depending on the values of the model parameters λ and γ. This versatility is exemplified in Figure 4-8, where: curve 'a' (convex) indicates a damage progression that accelerates initially and then decelerates; curve 'b' (S-shaped) suggests a slow-starting, accelerating, then decelerating damage process; curve 'c' (linear) shows a steady, linear increase in damage with loading cycles; curve 'd' (concave) portrays a slow-beginning damage process that accelerates over time.

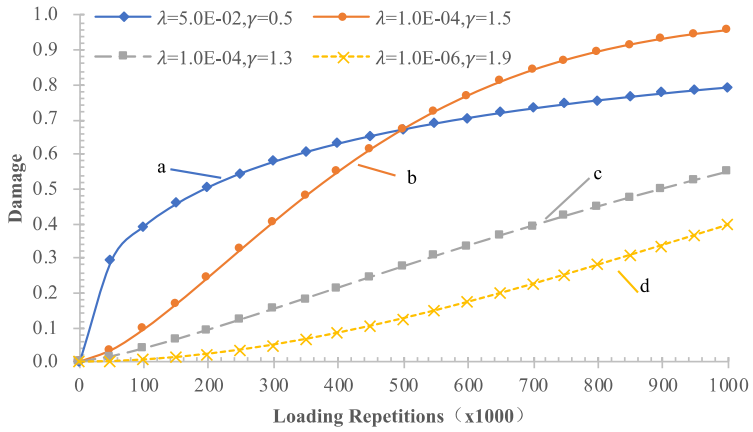

Figure 4-8 Different damage progressions simulated by WSF

(2) Monotonic increase of damage variable: With λ and γ set above 0, the model ensures a monotonic increase in the damage variable D as the number of load applications N rises.

(3) Boundary conditions compliance: The WSF aptly aligns with critical boundary conditions. Specifically, as N approaches zero, D also approaches zero, and conversely, as N trends towards infinity, D asymptotically approaches one.

(4) Model simplicity and parameter significance: The simplicity of the WSF facilitates regression analysis. Meanwhile, the parameters λ and γ are not just mathematical constructs but carry significant interpretative value. Through the transformation of WSF, this study derives the Weibull curve equation, as articulated in Equation 4-24, where $\ln(\lambda)$ is the intercept and γ denotes the slope of the Weibull curve. The influence of variations in λ and γ on the WSF and the Weibull curve is elucidated in Figure 4-9 and Figure 4-10.

a) Shape Factor (γ): The consistency in the shape of the damage progression curves with a

constant γ, as evidenced by the uniform slope of the Weibull curves, underscores γ's role in defining the shape of the damage curve. γ is aptly termed the 'shape factor' in this context.

b) Scale Factor (λ): The scenarios where λ varies, yet the damage progression pattern remains consistent, signify λ's influence in modulating the magnitude of damage for a given load application count. This characteristic positions λ as a 'scale factor', indicating its proportionality to the rate of damage progression.

$$\ln[-\ln(1-D)] = \ln(\lambda) + \gamma \ln(N) \qquad 4\text{-}24$$

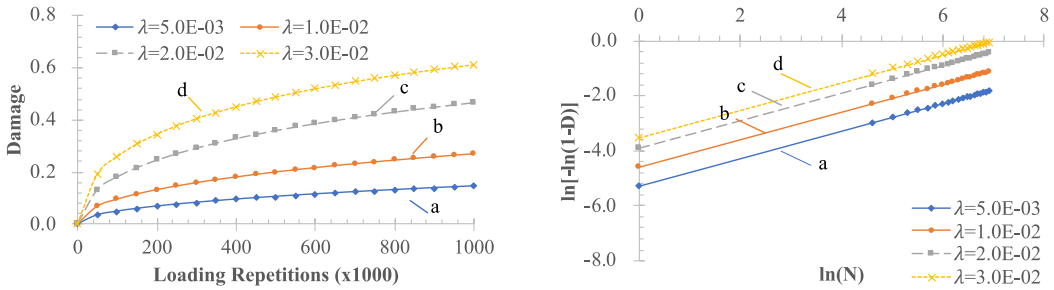

(a) Effect of λ on damage progressions (b) Effect of λ on Weibull curves

Figure 4-9 Effects of λ ($\gamma = 0.5$): (a) on damage progressions and (b) on Weibull curves

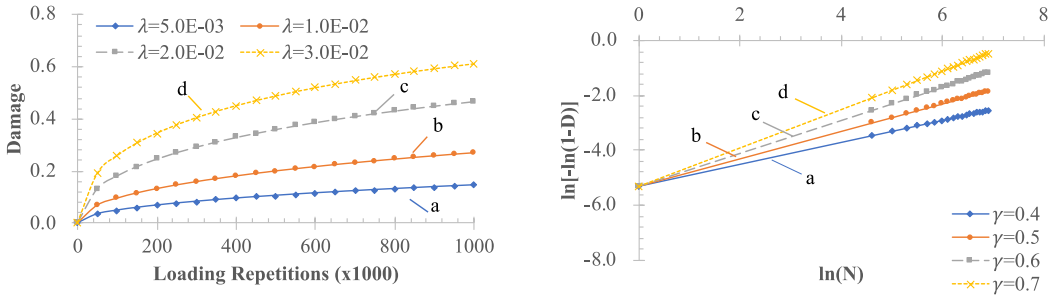

(a) Effect of γ on damage progressions (b) Effect of γ on Weibull curves

Figure 4-10 Effects of γ ($\lambda = 0.005$): (a) on damage progressions and (b) on Weibull curves

In summary, the WSF, with its adaptable model parameters, offers a robust and flexible approach to understanding and predicting fatigue damage progression in asphalt mixtures. Its ability to represent a range of damage scenarios through simple yet meaningful parameters make it an invaluable tool in asphalt fatigue damage analysis.

4.3.1.2 Structural Behavior Function (SBF)

In Table 4-15, identifier ② refers to a variant of the Structural Behavior Function (SBF). Initially proposed by Sun in 1991, SBF was originally used to describe the decay pattern of the Pavement

Condition Index (PCI). In the following research, Ma [16] utilized a modified form of SBF (identifier ②) to conduct regression analysis on the seismic modulus of asphalt layers, thereby testing the feasibility of it for damage evolution analysis.

A thorough analysis of model form ② reveals several key insights:

(1) Adaptability to damage progression scenarios: This damage evolution model, with different values for the parameters α and β, can fit four typical damage development processes as shown in Figure 4-11. The curves a, b, c, and d in the figure correspond to different progression patterns: initially fast then slow (convex curve), initially slow then fast and again slow (S-shaped curve), linear increase (straight line), and initially slow then fast (concave curve).

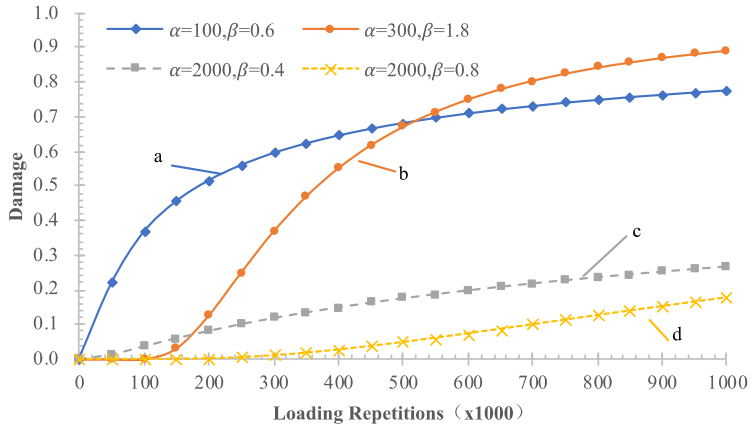

Figure 4-11 Different damage progressions simulated by SBF

(2) Monotonic increase of damage variable: When α and β are greater than 0, the damage variable D increases monotonically with the number of load applications N.

(3) Boundary conditions compliance: This model form aligns well with essential boundary conditions. Specifically, as N approaches zero, D tends towards zero, and as N approaches infinity, D converges to one.

(5) Model simplicity and parameter significance: The simplicity of the SBF facilitates regression analysis. Meanwhile, the parameters α and β are not just mathematical constructs but carry significant interpretative value. The influence of variations in α and β on the SBF is elucidated in Figure 4-12.

a) Impact of α (Lifetime Factor): When N equals α, regardless of β, D always equals 0.368. This means that the model's fitted curve invariably passes through the point (α, 0.368), as illustrated in Figure 4-12. Hence, α can be interpreted as the number of load

applications required for the damage variable D to reach 0.368, or equivalently, for the stiffness of the asphalt mixture to decay to 63.2% of its initial value. Additionally, as observed in Figure 4-12, variations in α alone do not significantly alter the shape of the model curve, leading to the designation of α as the 'Lifetime Factor' in this study.

b) Influence of β (Shape Factor): As shown in Figure 4-12, when α remains constant and β increases, the model's fitted curve transitions from convex through linear to concave or S-shaped forms. Therefore, β predominantly dictates the curve's shape and the mode of damage development, justifying its identification as the 'Shape Factor' in this research.

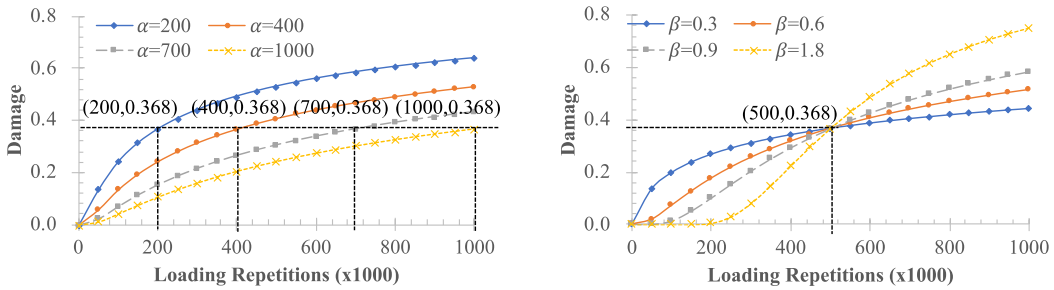

(a) Effect of α ($\beta = 0.5$) (b) Effect of β ($\alpha = 500$)

Figure 4-12 Effects of (a) α and (b) β on SBF

Overall, the SBF, with its capacity to model a diverse range of damage development processes and its clearly defined model parameters, presents a powerful tool in the analysis of asphalt mixture fatigue. Its simplicity and the meaningful interpretation of its parameters contribute significantly to its utility in predicting and understanding the evolution of fatigue damage in asphalt structures.

4.3.1.3 Other Four Models

In the context of contemporary research on asphalt fatigue, Table 4-15 (identifiers ③ to ⑦) introduces four additional typical nonlinear models for fatigue damage evolution. These models encompass a range of approaches: identifier ③ represents a model based on continuum damage mechanics, while identifiers ④ to ⑦ are models grounded in the concept of modulus reduction rate. Each of these models is tailored for different fatigue loading modes, showcasing the diversity in current modeling approaches.

Upon analyzing these five model forms, several important characteristics emerge:

(1) Boundary conditions and monotonic damage increase: All models satisfactorily meet the essential boundary conditions, with the damage variable D demonstrating a monotonic

increase as the number of load applications N rises.

(2) Limitations in damage progression representation: However, it is notable that these models have limitations in the range of damage progression processes they can effectively represent. Specifically, none of these models can accurately fit the S-shaped curve (curve b in Figure 4-8 and Figure 4-11), which typifies a damage progression that starts slowly, accelerates, and then decelerates again. This limitation points to a gap in their ability to capture more complex damage evolution scenarios.

(3) Comparative drawbacks in parameter significance: While these models are straightforward and conducive to regression analysis, a critical observation is that their parameters do not possess clear mathematical or physical interpretations. The parameters function merely as regression coefficients, lacking the interpretative depth found in models WSF and SBF.

In summary, while models ③ to ⑦ contribute to the field of asphalt fatigue damage modeling by offering alternative approaches and simplicity for regression analysis, they fall short in versatility and depth of interpretation compared to more robust models.

4.3.2 Comparative Analysis of Different Models

In this section, this study delves into a comparative analysis of the seven models outlined in Table 4-15, applied to the fatigue damage evolution process of laboratory asphalt mixtures. The regression results for each model's parameters and their R^2 are detailed in Table 4-16 and Table 4-17.

It reveals that under controlled-stress mode, models ①, ②, ④, and ⑤ demonstrate higher R^2 values, indicating a more effective fit to the fatigue damage evolution process of asphalt mixtures. Conversely, model ③ exhibits a lower R^2, signaling a comparatively poorer fit. Figure 4-13, showcasing a typical fit from model ③, illustrates this model's tendency to overestimate the rate of fatigue damage development towards the end of the test, resulting in suboptimal fitting accuracy.

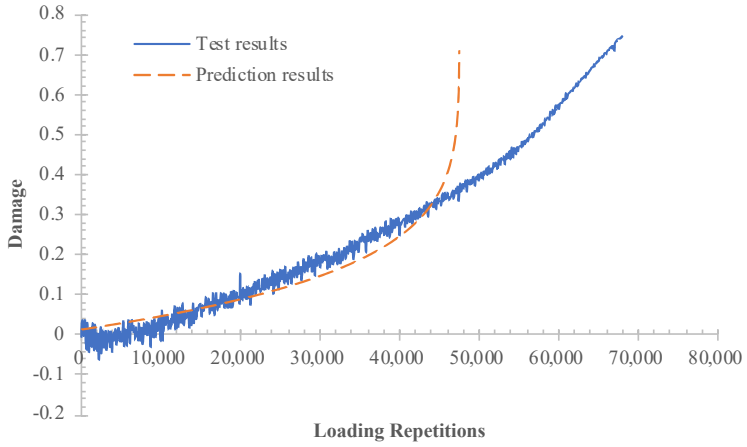

Figure 4-13 Typical prediciton results of Model ③

Similarly, an analysis of Table 4-17 indicates that under controlled-strain mode, models ①, ②, and ⑥ outperform model ⑦ in fitting the fatigue damage development process of asphalt mixtures. The effectiveness of model ⑦ fluctuates with changes in the criteria for fatigue failure determination, casting doubts on its reliability.

Table 4-16 The regression results of stress-controlled tests

Group	No.	Data Points	① $D = 1 - \exp(-\lambda N^{\gamma})$			② $D = \exp\left[-\left(\frac{\alpha}{N}\right)^{\beta}\right]$			③ $D = 1 - \left(1 - \frac{N}{N_f}\right)^{m}$		④ $D = a_1 \ln\left[b_1\left(\frac{N}{N_f}\right) + 1\right]$			⑤ $D = 2A\left(1 - e^{-\frac{N/N_f}{t}}\right)$		
			λ	γ	R^2	α	β	R^2	m	R^2	a_1	b_1	R^2	A	t	R^2
①	1	156335	2.05E-07	1.23	0.95	152142.09	0.72	0.92	0.18	0.89	4.38	0.10	0.95	116.45	541.81	0.95
	2	216458	2.98E-05	0.79	0.98	218683.73	0.51	0.97	0.18	0.85	0.32	2.38	0.98	0.29	0.92	0.98
②	3	98661	8.20E-06	0.98	0.98	77061.68	0.67	0.97	0.21	0.85	0.91	0.68	0.98	0.63	2.13	0.98
	4	77365	4.27E-04	0.66	0.99	47324.42	0.52	0.99	0.21	0.74	0.26	5.53	0.99	0.28	0.56	0.99
	5	88419	2.48E-05	0.89	0.99	67152.86	0.62	0.98	0.21	0.83	0.56	1.30	0.99	0.45	1.36	0.99
③	6	31351	7.95E-07	1.31	0.99	25245.34	0.87	0.98	0.23	0.90	11.11	0.05	0.99	32.61	132.54	0.99
	7	29018	1.30E-06	1.28	0.99	23232.50	0.85	0.98	0.23	0.89	3.53	0.15	0.99	5.84	23.42	0.99
	8	18276	5.51E-06	1.19	0.99	13952.75	0.85	0.98	0.24	0.87	3.12	0.18	0.99	7.64	29.66	0.99
④	9	14901	2.51E-06	1.29	0.99	12645.54	0.83	0.98	0.22	0.90	3.68	0.14	0.99	10.12	42.28	0.99
	10	15526	1.66E-06	1.33	0.99	13104.22	0.86	0.97	0.22	0.90	5.22	0.09	0.99	16.03	66.82	0.99
	11	14701	3.21E-07	1.51	0.99	12166.44	0.98	0.98	0.23	0.92	8.83	0.06	0.99	291.23	1188.26	0.99
⑤	12	24876	3.54E-05	0.97	0.99	18686.02	0.67	0.98	0.22	0.85	0.76	0.89	0.99	0.56	1.77	0.99
	13	15764	1.96E-05	1.07	0.99	12511.02	0.72	0.98	0.22	0.86	1.28	0.45	0.99	1.00	3.69	0.99
	14	8476	9.66E-06	1.22	0.99	7159.06	0.90	0.98	0.22	0.91	6.64	0.07	0.99	63.00	262.82	0.99
⑥	15	29690	7.45E-06	1.09	0.96	22670.24	0.79	0.98	0.24	0.88	2.24	0.25	0.99	2.85	10.85	0.99
	16	26097	1.87E-05	1.03	0.99	20329.82	0.70	0.98	0.22	0.85	0.94	0.66	0.99	0.63	2.12	0.99
⑦	17	111404	1.13E-05	0.94	0.97	84746.18	0.65	0.96	0.22	0.82	0.68	1.00	0.97	0.51	1.61	0.97
	18	78501	7.02E-06	1.01	0.97	63738.92	0.68	0.96	0.21	0.84	0.95	0.62	0.97	0.69	2.46	0.97
⑧	19	138143	1.06E-03	0.54	0.99	88503.81	0.43	0.98	0.18	0.72	0.20	8.59	0.99	0.25	0.53	0.98
	20	78429	7.96E-04	0.60	0.99	53464.52	0.46	0.98	0.19	0.74	0.23	6.20	0.99	0.27	0.59	0.98
	21	72904	1.95E-04	0.72	0.99	60104.70	0.52	0.97	0.18	0.78	0.33	2.71	0.98	0.31	0.88	0.98

Group	No.	Data Points	① $D = 1 - \exp(-\lambda N^{\gamma})$			② $D = \exp\left[-\left(\frac{\alpha}{N}\right)^{\beta}\right]$			③ $D = 1 - \left(1 - \frac{N}{N_f}\right)^{m}$		④ $D = a_1 \ln\left[b_1\left(\frac{N}{N_f}\right) + 1\right]$			⑤ $D = 2A\left(1 - e^{-\frac{N/N_f}{t}}\right)$		
			λ	γ	R^2	α	β	R^2	m	R^2	a_1	b_1	R^2	A	t	R^2
	22	75001	1.24E-03	0.55	0.99	56545.42	0.42	0.99	0.16	0.72	0.20	7.59	0.99	0.24	0.54	0.98
	23	49281	2.99E-03	0.47	0.98	67339.86	0.34	0.97	0.11	0.80	0.15	9.94	0.98	0.18	0.44	0.97
	24	21100	9.66E-03	0.43	0.99	11641.95	0.38	0.98	0.17	0.68	0.16	16.36	0.98	0.24	0.45	0.97
⑨	25	38597	6.99E-05	0.86	0.99	29122.05	0.61	0.98	0.21	0.83	0.51	1.50	0.99	0.42	1.24	0.99
	26	33796	1.13E-03	0.61	0.97	22629.05	0.50	0.95	0.20	0.74	0.26	5.02	0.96	0.28	0.63	0.96
	27	40219	6.32E-05	0.86	0.98	33195.96	0.60	0.97	0.19	0.82	0.59	1.14	0.98	0.45	1.47	0.98
	28	12894	7.15E-06	1.19	0.96	11733.44	0.75	0.94	0.19	0.86	3.02	0.16	0.96	112.24	504.35	0.96
	29	11329	2.07E-03	0.62	0.97	7716.07	0.52	0.95	0.20	0.75	0.29	3.97	0.96	0.31	0.75	0.96
⑩	30	73333	2.45E-04	0.70	0.99	53861.28	0.52	0.98	0.19	0.77	0.30	3.54	0.99	0.30	0.75	0.99
	31	81798	6.54E-04	0.61	0.99	58754.24	0.46	0.97	0.15	0.75	0.24	5.24	0.98	0.28	0.70	0.98
⑪	32	157238	1.61E-04	0.68	0.98	138730.10	0.47	0.96	0.14	0.79	0.33	2.46	0.97	0.34	1.13	0.97
	33	132847	1.54E-05	0.89	0.98	118163.82	0.59	0.96	0.16	0.83	0.71	0.82	0.98	0.63	2.46	0.98
⑫	34	68438	2.03E-02	0.33	1.00	25933.33	0.33	0.99	0.15	0.58	0.13	48.91	0.99	0.22	0.31	0.98
	35	9608	1.48E-02	0.43	0.99	4260.41	0.41	0.99	0.19	0.60	0.16	21.64	0.99	0.24	0.32	0.99
⑬	36	20068	1.84E-03	0.60	0.99	12383.05	0.47	0.99	0.19	0.72	0.22	7.85	0.99	0.26	0.49	0.98
	37	7839	8.55E-04	0.75	0.99	5286.22	0.57	0.98	0.22	0.79	0.34	3.10	0.99	0.32	0.77	0.99
	38	8428	1.50E-03	0.68	0.99	5430.45	0.55	0.99	0.22	0.76	0.29	4.39	0.99	0.29	0.63	0.99
⑭	39	2691	4.34E-04	0.93	0.98	1982.78	0.70	0.97	0.23	0.83	0.71	0.99	0.98	0.76	2.61	1.00

Table 4-17 The regression results of strain-controlled tests

Group	No.	Data Points	① $D = 1 - \exp(-\lambda N^{\gamma})$			② $D = \exp\left[-\left(\frac{\alpha}{N}\right)^{\beta}\right]$			⑥ $D = 1 - ae^{\frac{-N/N_f}{b}} + c$				⑦ $D = \left(1 - \frac{E_f}{E_0}\right)\left(\frac{N}{N_f}\right)^{k}$	
			λ	γ	R^2	α	β	R^2	a	b	c	R^2	k	R^2
①	1	763005	2.88E-06	0.85	0.85	1467249.45	0.66	0.84	0.97	1.51	1.00	0.80	0.88	0.39
	2	649789	2.32E-06	0.90	0.90	1018543.28	0.51	0.88	0.97	2.70	1.00	0.90	2.69	0.73
②	3	139951	2.44E-08	1.41	0.92	146179.30	1.20	0.92	1.05	2.22	1.00	0.88	3.14	0.89
	4	143376	7.24E-07	1.12	0.89	160478.10	0.91	0.88	1.02	2.24	1.00	0.88	3.14	0.85
	5	130676	3.41E-07	1.18	0.89	173681.53	0.69	0.86	1.00	2.51	1.00	0.88	3.52	0.76
③	6	59784	1.70E-05	0.93	0.92	66299.49	0.56	0.90	1.00	2.12	1.00	0.96	1.82	0.92
	7	76426	1.63E-07	1.20	0.92	83039.30	4.04	0.86	0.92	10.62	1.01	0.80	15.15	0.45
④	8	458647	1.60E-06	0.93	0.86	795329.91	0.74	0.83	0.94	3.50	1.00	0.76	6.45	0.66
	9	396651	7.01E-07	1.00	0.92	720426.92	0.69	0.90	1.00	3.55	1.00	0.92	7.68	0.53
	10	316315	2.95E-07	1.07	0.91	505727.08	1.07	0.93	0.94	4.53	1.00	0.90	11.42	0.68
⑤	11	72476	7.96E-07	1.17	0.89	93529.26	0.79	0.86	0.99	2.55	1.00	0.89	3.58	0.83
	12	69114	1.74E-05	0.92	0.97	73193.74	0.57	0.94	0.95	2.03	1.01	0.97	1.34	0.93
	13	58665	7.34E-05	0.80	0.95	61309.00	0.49	0.93	0.95	2.06	1.01	0.95	1.43	0.89
⑥	14	523015	8.92E-03	0.24	0.83	2636880.27	0.06	0.84	0.92	9.61	1.01	0.82	0.02	0.73
	15	238719	1.14E-02	0.35	0.94	93556.89	0.36	0.95	0.80	0.23	1.88	0.95	0.21	0.93
	16	113901	1.13E-05	0.89	0.93	179109.19	0.50	0.91	0.94	2.71	1.00	0.93	2.71	0.74
	17	106492	2.29E-07	1.25	0.93	116823.25	0.95	0.91	0.96	2.19	1.00	0.92	1.95	0.93
	18	184478	5.71E-07	1.11	0.92	220131.62	0.90	0.91	0.97	2.42	1.00	0.92	2.53	0.89
	19	22851	1.52E-07	1.46	0.86	29594.48	0.93	0.83	0.98	2.74	1.00	0.83	4.31	0.81
⑦	20	75815	7.87E-03	0.36	0.87	130538.63	0.28	0.89	0.95	1.90	1.19	0.83	0.11	0.73
	21	288453	7.40E-03	0.32	0.87	498720.10	0.28	0.90	0.97	1.25	1.00	0.89	0.66	0.90

Group	No.	Data Points	① $D = 1 - \exp(-\lambda N^{\gamma})$			② $D = \exp\left[-\left(\frac{\alpha}{N}\right)^{\beta}\right]$			⑥ $D = 1 - ae^{\frac{-N/N_f}{b}} + c$				⑦ $D = \left(1 - \frac{E_f}{E_0}\right)\left(\frac{N}{N_f}\right)^{k}$	
			$\boldsymbol{\lambda}$	$\boldsymbol{\gamma}$	$\boldsymbol{R^2}$	$\boldsymbol{\alpha}$	$\boldsymbol{\beta}$	$\boldsymbol{R^2}$	$\boldsymbol{a}$	$\boldsymbol{b}$	$\boldsymbol{c}$	$\boldsymbol{R^2}$	$\boldsymbol{k}$	$\boldsymbol{R^2}$
	22	10808	8.65E-03	0.30	0.91	141547.28	0.34	0.93	0.97	9.77	1.01	0.92	0.86	0.41

Synthesizing the results from § 4.3.2, a comprehensive comparison of the seven nonlinear damage evolution models in terms of their forms and fitting effectiveness is summarized in Table 4-18.

Table 4-18 Comparisons between the selected nonlinear damage evolution models

No.		①	②	③	④	⑤	⑥	⑦
Applicability to different loading modes		✓	✓	×	×	×	×	×
Fitness to various damage progressions		✓	✓	×	×	×	×	×
Monotonicity		✓	✓	✓	✓	✓	✓	✓
Adaptability to boundary conditions		✓	✓	✓	×	×	×	✓
Interpretability of model parameters		×	✓	×	×	×	×	×
Average of R^2	**Stress-controlled tests**	0.98	0.97	0.81	0.98	0.98	-	-
	Strain-controlled tests	0.90	0.89	-	-	-	0.88	0.77

Upon comparison, it becomes evident that models ① (WSF) and ② (SBF) hold certain advantages over the others. Both families reproduce convex/S-shape/linear SRR progressions, satisfying monotonicity and boundary conditions, and also demonstrate superior fitting effectiveness under both controlled-stress and controlled-strain modes. To further understand the applicability of these two models, the following sections will conduct an analysis of the correlation between their model parameters and various loading factors.

4.4 Influential Factors of Fatigue Damage Progressions

Building upon the regression analysis results of the WSF and SBF, this section conducts a thorough quantitative analysis focused on several key aspects: the independency of model parameters, the correlation between model parameters and two critical mixture properties - the initial stiffness modulus ($S_{\mathrm{mix},0}$) and the fatigue life (N_{f50}). Additionally, it delves into the impacts of six loading factors on the model parameters. These loading factors include the initial strain amplitude (ε_0), loading frequency (f), loading time (LT), rest time (RT), the ratio of rest time to loading time (TR), and loading rate (LR). This comprehensive analysis is crucial for understanding the dynamics of fatigue damage progression in asphalt mixtures. It aims to elucidate how these factors individually and collectively influence the model parameters, thereby shaping the fatigue damage process. Such an understanding is pivotal for accurately predicting and effectively managing fatigue damage in asphalt mixtures, ensuring their longevity and structural integrity.

4.4.1 Interpretation of Parameter λ

The analysis of parameter λ is meticulously carried out based on its regression results, with a particular focus on employing Pearson correlation coefficients to methodically assess the three key aspects. The outcomes from both stress-controlled and strain-controlled tests are systematically compiled in Table 4-19 and Table 4-20. These tables utilize color coding - red and blue - to indicate positive and negative correlations, respectively, with more intense shades denoting stronger correlation intensities.

Table 4-19 Analysis results of the parameter λ from stress-controlled tests

Factor	$\ln(\gamma)$	$\ln(S_{mix,0})$	$\ln(N_{f50})$
	-0.95	-0.24	-0.10
$\ln(\lambda)$	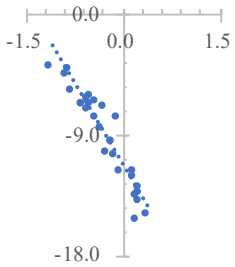	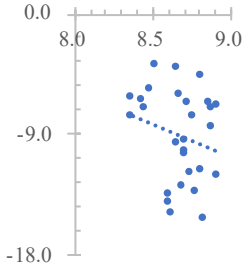	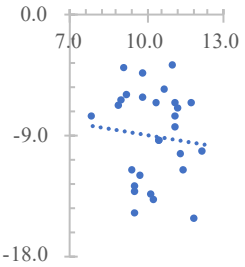
Factor	$\ln(\varepsilon_0)$	f (Hz)	LT(s)
	0.35	-0.28	0.30
$\ln(\lambda)$	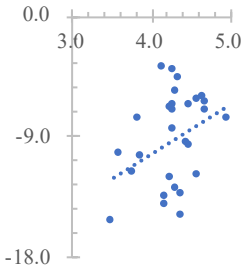	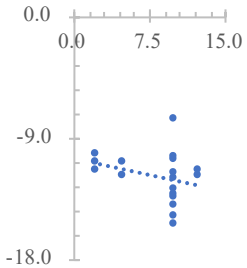	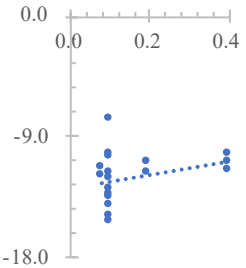
Factor	RT (s)	TR	LR (με/s)
	-0.20	-0.49	-0.50
$\ln(\lambda)$	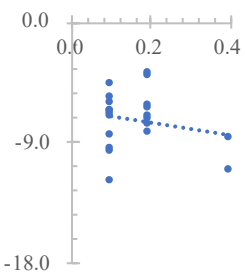	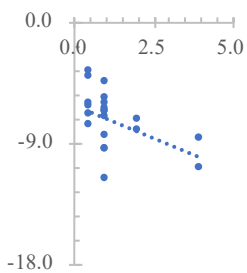	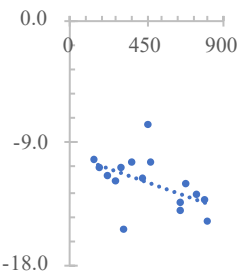

Table 4-20 Analysis results of the parameter λ from strain-controlled tests

Factor	$\ln(\gamma)$	$\ln(S_{mix,0})$	$\ln(N_{f50})$
$\ln(\lambda)$	-0.90	0.37	0.19
	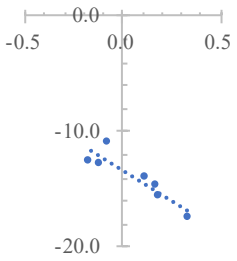	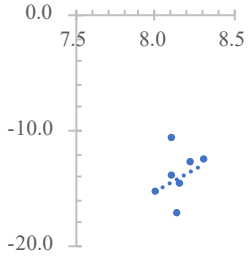	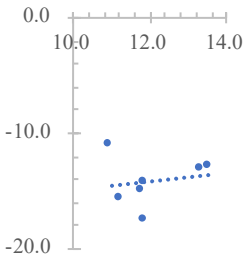
Factor	$\ln(\varepsilon_0)$	f (Hz)	LT(s)
$\ln(\lambda)$	-0.20	-0.41	0.46
	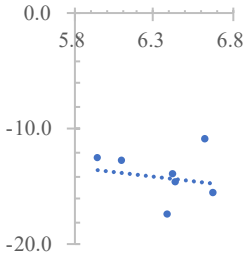	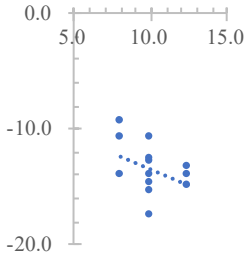	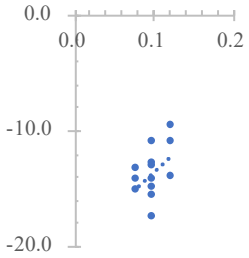
Factor	RT (s)	TR	LR (με/s)
$\ln(\lambda)$	-0.52	-0.13	0.70
	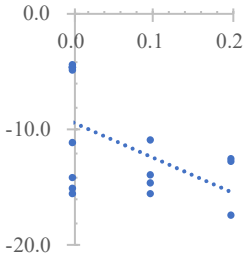	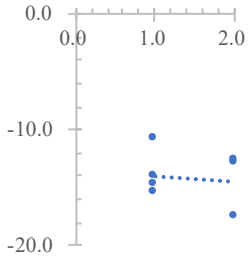	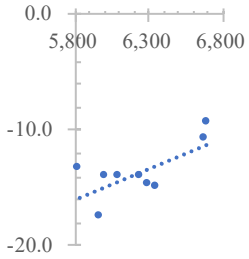

A crucial observation from these tables is the strong negative correlation between the parameters λ and γ in the WSF, with correlation coefficients ranging between -0.90 to -0.95. This finding indicates that λ and γ are not independent entities; rather, they interact and jointly characterize the fatigue decay rate and damage evolution pattern in asphalt mixtures. Moreover, the correlation of λ with $S_{\mathrm{mix},0}$ and N_{f50} is relatively weak. Furthermore, the correlation between λ and various loading factors displays inconsistent results across different tests and loading modes, exhibiting a lack of clear, consistent patterns.

4.4.2 Interpretation of Parameter γ

In the WSF, a parallel analysis is conducted for parameter γ, utilizing Pearson correlation coefficients to evaluate the same three aspects. The results of this analysis, derived from both stress-controlled and strain-controlled tests, are organized in Table 4-21 and Table 4-22.

Table 4-21 Analysis results of the parameter γ from stress-controlled tests

Factor	$\ln(\lambda)$	$\ln(S_{mix,0})$	$\ln(N_{f50})$
	-0.95	0.11	-0.16
$\ln(\gamma)$	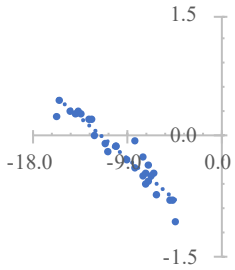	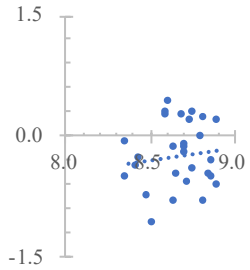	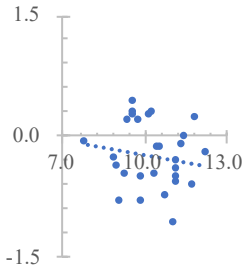
Factor	$\ln(\varepsilon_0)$	f (Hz)	LT(s)
	-0.10	-0.03	0.01
$\ln(\gamma)$	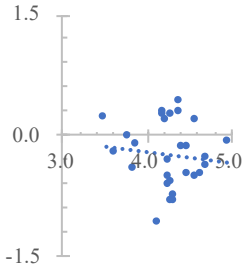	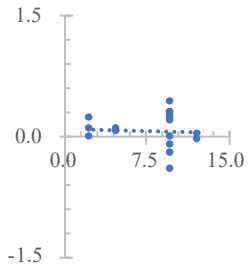	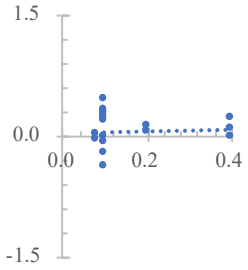
Factor	RT (s)	TR	LR (με/s)
	0.12	0.24	0.48
$\ln(\gamma)$	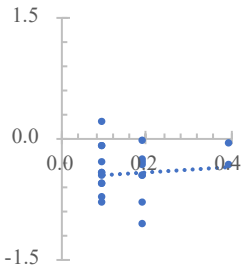	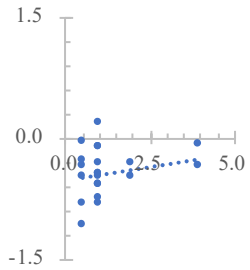	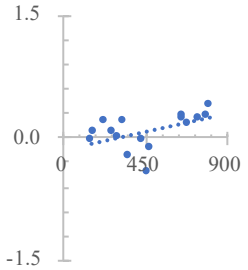

Table 4-22 Analysis results of the parameter γ from strain-controlled tests

Factor	$\ln(\lambda)$	$\ln(S_{mix,0})$	$\ln(N_{f50})$
	-0.90	-0.63	-0.56
$\ln(\gamma)$	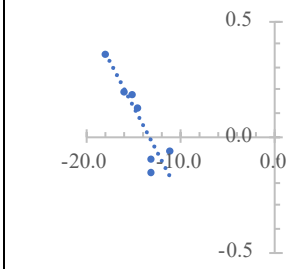	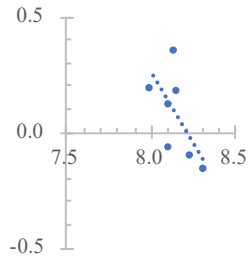	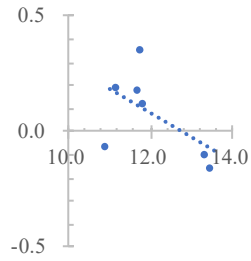
Factor	$\ln(\varepsilon_0)$	f (Hz)	LT(s)
	0.55	0.07	-0.12
$\ln(\gamma)$	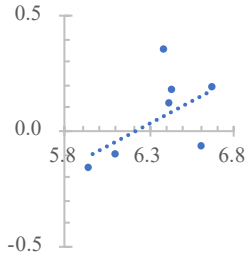	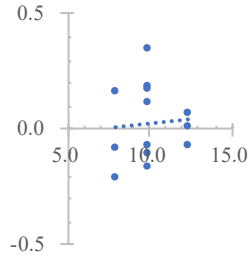	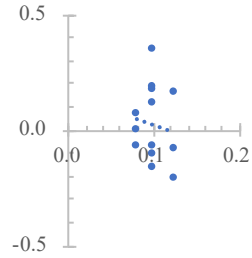
Factor	RT (s)	TR	LR (με/s)
	0.46	-0.22	-0.50
$\ln(\gamma)$	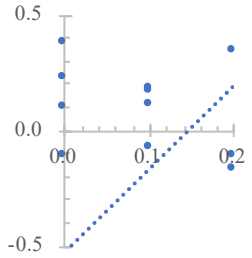	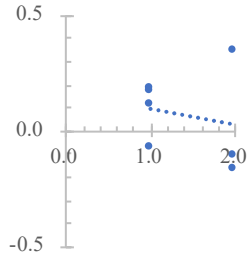	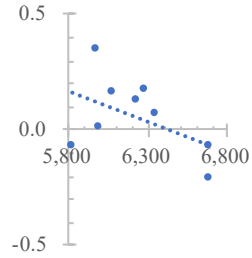

The analysis of parameter γ reveals patterns like those observed for λ. Specifically, the correlation between γ and both $S_{\mathrm{mix},0}$ and N_{f50} is found to be relatively weak. Additionally, the correlation between γ and the loading factors exhibits inconsistent results across different experimental setups and loading modes, indicating a lack of uniformity and predictability in these relationships.

When considering the findings from § 4.4.1, it becomes apparent that despite the WSF demonstrating commendable fitting results, the interpretability of its model parameters, particularly λ and γ, is limited. This highlights a critical aspect of the WSF: while it is effective in fitting the fatigue damage progression, the underlying parameters driving this fit have complex relationships with key aspects of the asphalt mixture's behavior, making their direct interpretation challenging.

4.4.3 Interpretation of Parameter α

For the SBF, the interpretation of parameter α is based on its regression results, using Pearson correlation coefficients to systematically evaluate its relationship with three aspects: the other model parameter β, mixture properties including $S_{\mathrm{mix},0}$ and N_{f50}, and six loading factors. The findings from both stress-controlled and strain-controlled tests are compiled in Table 4-23 and Table 4-24.

Table 4-23 Analysis results of the parameter α from stress-controlled tests

Factor	$\ln(\beta)$	$\ln(S_{mix,0})$	$\ln(N_{f50})$
$\ln(\alpha)$	-0.53	0.52	0.98
	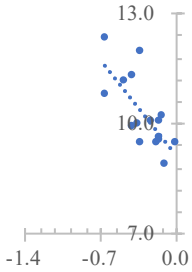	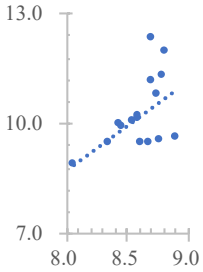	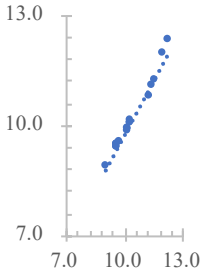
Factor	$\ln(\varepsilon_0)$	f (Hz)	LT(s)
$\ln(\alpha)$	-0.80	0.53	-0.50
	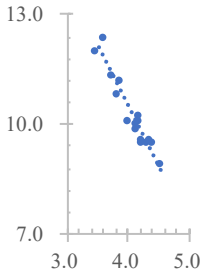	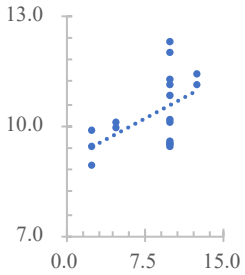	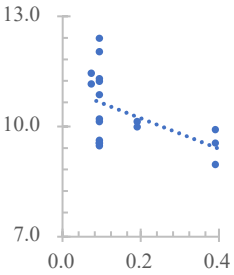
Factor	RT (s)	TR	LR (με/s)
$\ln(\alpha)$	0.18	0.65	-0.20
	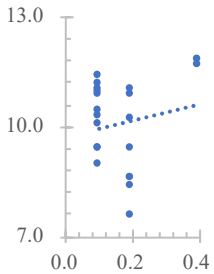	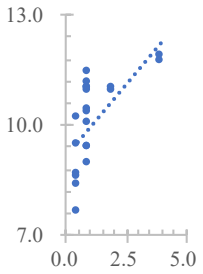	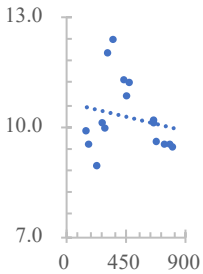

Table 4-24 Analysis results of the parameter α from strain-controlled tests

Factor	$\ln(\beta)$	$\ln(S_{mix,0})$	$\ln(N_{f50})$
	-0.47	0.80	1.00
$\ln(\alpha)$	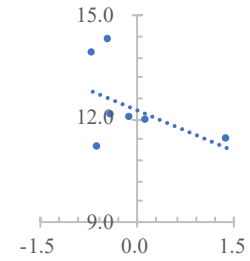	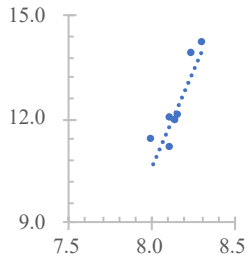	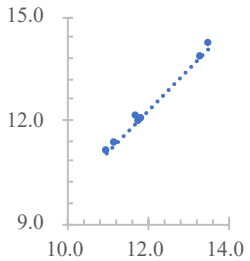
Factor	$\ln(\varepsilon_0)$	f (Hz)	LT(s)
	-0.98	0.66	-0.67
$\ln(\alpha)$	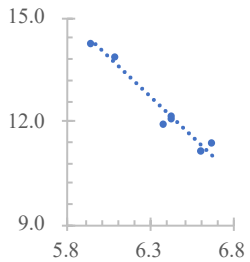	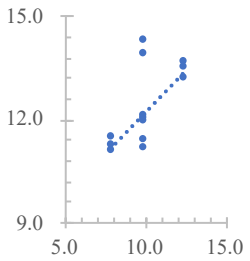	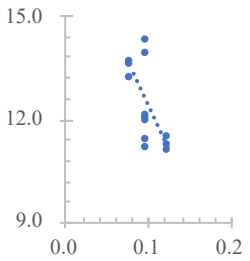
Factor	RT (s)	TR	LR (με/s)
	0.28	0.75	-0.46
$\ln(\alpha)$	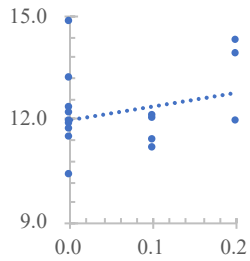	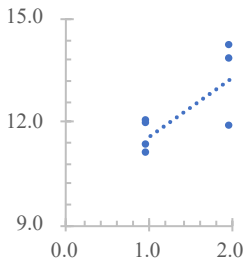	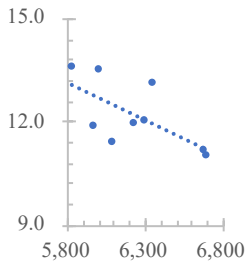

The analysis reveals no significant correlation between the SBF model parameters α and β. However, α shows a strong positive correlation with N_{f50} across different testing methods and fatigue loading modes. This correlation is expected since α, as the SBF's lifetime factor, represents the number of load applications required for the damage variable D to reach 0.368. In line with this, α's correlation with various loading factors appears consistent across different test methods and loading modes: it exhibits a strong negative correlation with the initial strain amplitude (ε_0), positive correlation with loading frequency (f), and negative correlation with loading time (LT). Notably, α is positively correlated with rest time (RT) or the ratio of rest time to loading time (TR), with a stronger correlation observed with TR than with RT. There is no significant correlation between α and loading rate (LR).

These findings suggest that α, as a fatigue life factor, not only reflects the fatigue life of asphalt mixtures but also serves as a function of various loading factors. Therefore, this study employs stepwise regression to develop an expression for α, as expressed by Equations 4-25 and 4-26. Since stepwise regression methodically eliminates variables causing multicollinearity and given the significant correlation between RT and TR, the expression for α includes only TR, which has a more pronounced effect. The absence of loading frequency or loading time in the expression is due to their non-significant partial regression sum of squares.

For stress-controlled tests:

$$\ln(\alpha_{L-\sigma}) = 24.086 - 3.365\ln(\varepsilon_0) + 0.859TR \quad 4\text{-}25$$

For strain-controlled tests:

$$\ln(\alpha_{L-\varepsilon}) = 43.591 - 4.926\ln(\varepsilon_0) + 0.076TR \quad 4\text{-}26$$

Table 4-25 presents the statistical parameters of this expression. It shows high values of the multiple correlation coefficient R and the coefficient of determination R^2, indicating a close regression relationship between the independent variables and α, as well as a good fit of the model. The significance of the independent variables (p-values) being less than 0.01 validates the rational and necessary selection of these variables. Therefore, the form of the expression for the model parameter α is deemed reasonable and robust under various loading conditions.

Table 4-25 Regression coefficients and variance analysis for Equations 4-25 and 4-26

No.	Coefficient	Value	t-Value	p-Value	R	R^2	F-value	Sig.
Eq. 4-25	Constant	24.086	19.633	0.000	0.882	0.778	80.79	0.000
	$\ln(\varepsilon_0)$	-3.365	-11.777	0.000				
	TR	0.859	8.378	0.000				
Eq. 4-26	Constant	43.591	15.454	0.000	0.762	0.681	9.028	0.003
	$\ln(\varepsilon_0)$	-4.926	-8.958	0.000				
	TR	0.076	3.273	0.007				

However, this study identifies significant variations in the expressions of parameter α under stress-controlled and strain-controlled modes, as depicted in Equations 4-25 and 4-26. This variation highlights the necessity to thoroughly examine how tensile fatigue loading modes crucially affect α. The ultimate goal is to formulate a universal method for predicting α across diverse tensile fatigue loading conditions.

To achieve this, the study employs the conversion equation method, previously utilized for developing versatile fatigue life equations in § 4.2.4. This approach begins with a detailed investigation into the relative ratios of α under controlled-stress and controlled-strain loading modes. By integrating Equations 4-25 and 4-26 into Equation 4-12, the study derives a ratio, $F_{\alpha L}$, as outlined in Equation 4-27.

$$F_{\alpha L} = \frac{\alpha_{L-\varepsilon}}{\alpha_{L-\sigma}} = e^{19.509} \cdot {\varepsilon_0}^{-1.561} \cdot e^{-0.783TR} \qquad 4\text{-}27$$

Building on this foundation, an S-shaped function is introduced to create a continuous transition function, $F'_{\alpha L}$, as detailed in Equation 4-28. It is crucial for establishing the ratio of α_L under any fatigue loading mode compared to that ($\alpha_{L-\sigma}$) under a controlled-stress mode. Further exploration, informed by Figure 4-14, illustrates the calculation of $F'_{\alpha L}$ across various levels of ε_0 and TR. It indicates that $F'_{\alpha L}$ increases with the MF within the same ε_0 or TR level. This increase implies that as the fatigue loading mode approaches stress-controlled, α_L tends to align more closely with $\alpha_{L-\sigma}$. Conversely, as it shifts towards strain-controlled, the gap between the general α_L and $\alpha_{L-\sigma}$ widens. Furthermore, an increase in ε_0 or TR levels is observed to correlate with a decrease in $F'_{\alpha L}$.

$$F'_{\alpha L} = 1 + \frac{F_{\alpha L} - 1}{1 + e^{k_{\alpha L} \cdot \mathrm{MF}}} = 1 + \frac{e^{19.509} \cdot {\varepsilon_0}^{-1.561} \cdot e^{-0.783TR} - 1}{1 + e^{k_{\alpha L} \cdot \mathrm{MF}}} \qquad 4\text{-}28$$

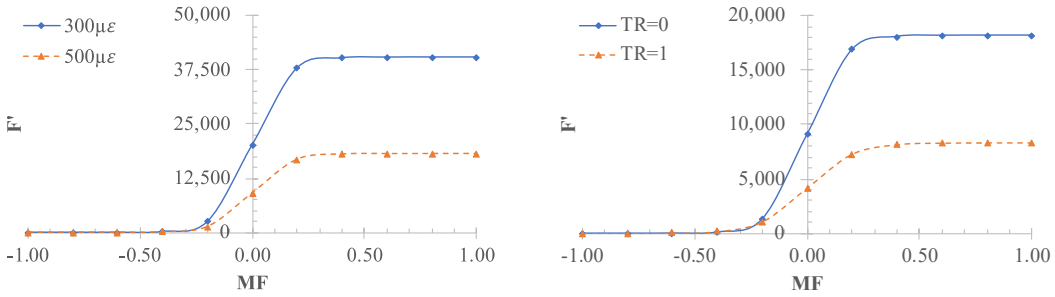

(a) $TR = 0$ (b) $\varepsilon_0 = 500\mu\varepsilon$

Figure 4-14 The proposed S-shaped function of $F'_{\alpha L}$

The analysis is further enriched by the data presented in Table 4-26, which delineates the values of $k_{\alpha L}$ and their patterned changes with various ε_0 and TR levels. This pattern calls for a deeper exploration of $k_{\alpha L}$, as illustrated in Figure 4-15. This figure reveals a strong linear relationship between $k_{\alpha L}$ values and both $\ln(\varepsilon_0)$ and TR.

Table 4-26 Regression results of the coefficient $k_{\alpha L}$

ε_0	TR	$k_{\alpha L}$	ε_0	TR	$k_{\alpha L}$	ε_0	TR	$k_{\alpha L}$	ε_0	TR	$k_{\alpha L}$	ε_0	TR	$k_{\alpha L}$
30	0	-17.20	50	0	-16.40	100	0	-15.32	300	0	-13.60	500	0	-12.80
	0.5	-16.80		0.5	-16.01		0.5	-14.93		0.5	-13.21		0.5	-12.41
	1	-16.41		1	-15.62		1	-14.53		1	-12.82		1	-12.02
	2	-15.63		2	-14.83		2	-13.75		2	-12.04		2	-11.24
	4	-14.06		4	-13.27		4	-12.18		4	-10.47		4	-9.67

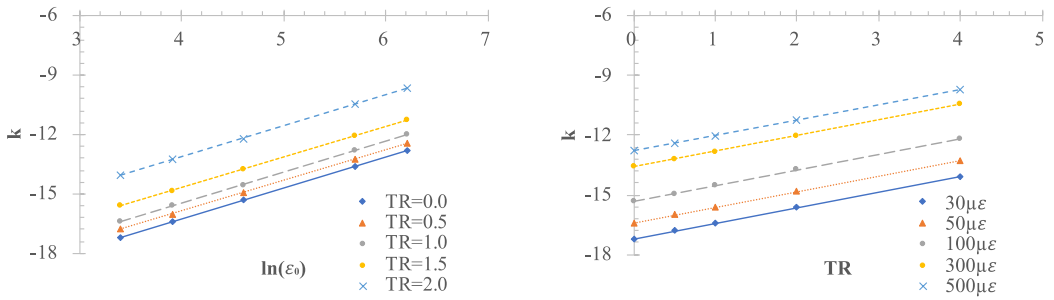

(a) $k_{\alpha L}$ vs. $\ln(\varepsilon_0)$ (b) $k_{\alpha L}$ vs. TR

Figure 4-15 Regression results of $k_{\alpha L}$ vs.: (a) $\ln(\varepsilon_0)$ and (b) TR

Leveraging these insights, the study formulates an expression for $k_{\alpha L}$ through rigorous regression analysis, as presented in Equation 4-29. The statistical robustness of this expression is underscored by the parameters in Table 4-27, confirming its statistical significance and strong model fit. The p-values for the independent variables, being less than 0.01, validate the rational and necessary selection of these variables.

$$k_{\alpha L} = -22.507 + 1.561\ln(\varepsilon_0) + 0.783TR \quad 4\text{-}29$$

Table 4-27 Regression coefficients and variance analysis for Equations 4-1

No.	Coefficient	Value	t-Value	p-Value	R	R^2	F-value	Sig.
Eq.4-29	Constant	-22.507	-7373.647	0.000	1.000	1.000	4761824.360	0.000
	$\ln(\varepsilon_0)$	1.561	2562.854	0.000				
	TR	0.783	1719.136	0.000				

Consequently, the refined and conclusive expression for $F'_{\alpha L}$ is given in Equation 4-30. Furthermore, a unified equation for estimating α under any fatigue loading mode is encapsulated in Equation 4-31.

$$F'_{\alpha L} = 1 + \frac{F_{\alpha L} - 1}{1 + e^{k_{\alpha L}\cdot \mathrm{MF}}} = 1 + \frac{e^{19.509} \cdot {\varepsilon_0}^{-1.561} \cdot e^{-0.783TR} - 1}{1 + e^{(-22.507 + 1.561\ln(\varepsilon_0) + 0.783TR)\cdot \mathrm{MF}}} \quad 4\text{-}30$$

$$\alpha_L = F'_{\alpha L} \cdot \alpha_{L-\sigma} \quad 4\text{-}31$$

4.4.4 Interpretation of Parameter β

Investigating the second model parameter, β, within the SBF, the study leverages analysis results from Table 4-28 and Table 4-29.

Table 4-28 Analysis results of the parameter β from stress-controlled tests

Factor	$\ln(\alpha)$	$\ln(S_{mix,0})$	$\ln(N_{f50})$
	-0.53	-0.24	-0.77
$\ln(\beta)$	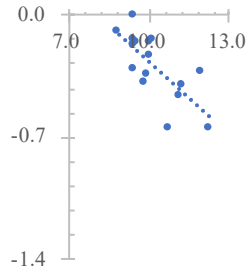	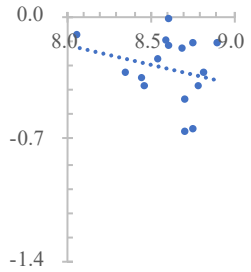	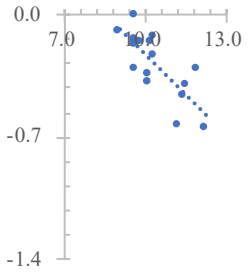
Factor	$\ln(\varepsilon_0)$	f (Hz)	LT(s)
	0.75	-0.14	0.11
$\ln(\beta)$	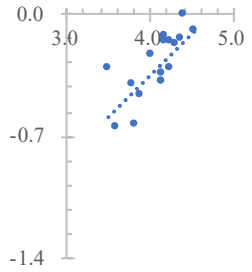	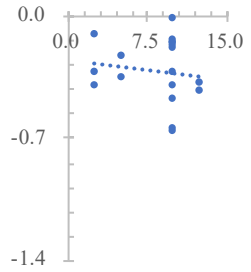	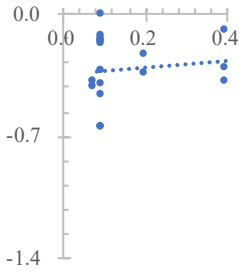
Factor	RT (s)	TR	LR (με/s)
	0.08	0.09	0.46
$\ln(\beta)$	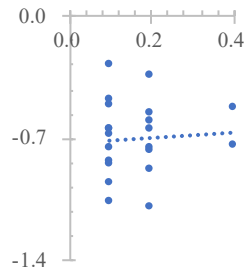	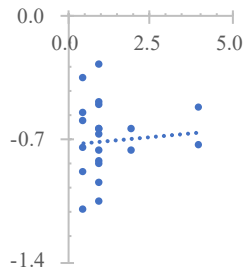	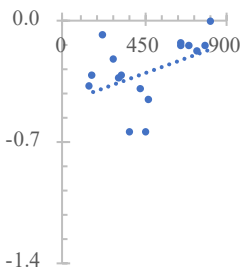

Table 4-29 Analysis results of the parameter β from strain-controlled tests

Factor	$\ln(\alpha)$	$\ln(S_{mix,0})$	$\ln(N_{f50})$
	-0.47	-0.73	-0.45
$\ln(\beta)$	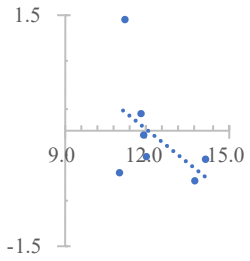	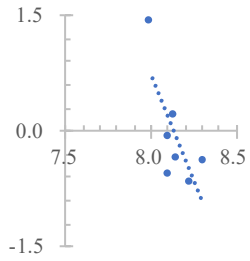	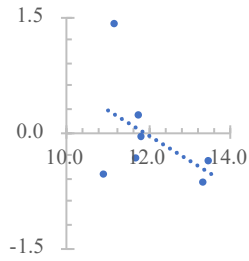
Factor	$\ln(\varepsilon_0)$	f (Hz)	LT(s)
	0.54	0.17	-0.21
$\ln(\beta)$	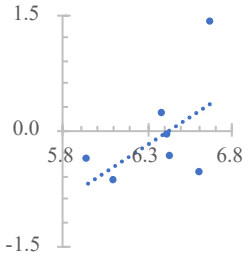	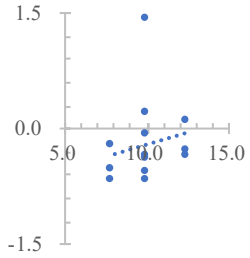	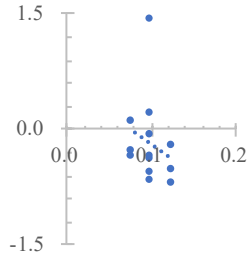
Factor	RT (s)	TR	LR (με/s)
	0.38	-0.29	-0.56
$\ln(\beta)$	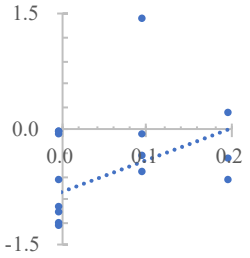	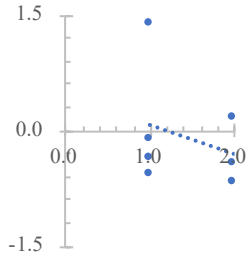	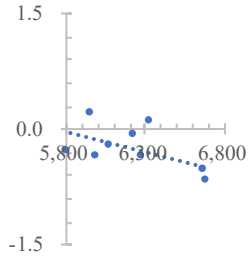

A critical observation is the lack of significant correlation between β and both $S_{\text{mix},0}$ and N_{f50}. However, a noteworthy pattern emerges across various testing methods and fatigue loading modes: β exhibits a strong positive correlation with the initial strain amplitude (ε_0). Besides, while β does not significantly correlate with loading frequency (f), loading time (LT), rest time (RT), and the ratio of rest time to loading time (TR), a discernible relationship is identified with the loading rate (LR). This relationship notably shifts in opposite directions under controlled-stress and controlled-strain loading modes.

These findings indicate that the shaping of the fatigue damage progressions of asphalt mixtures is principally governed by ε_0 and LR. As a result, β essentially acts as a function of these specific

loading factors. In response to this, the study has formulated regression-based expressions for it, shown in Equations 4-32 and 4-33.

For stress-controlled tests:

$$\ln(\beta_{L-\sigma}) = -2.717 + 0.462\ln(\varepsilon_0) + 0.087\ln(LR) \quad 4\text{-}32$$

For strain-controlled tests:

$$\ln(\beta_{L-\varepsilon}) = -5.367 + 0.972\ln(\varepsilon_0) - 0.008\ln(LR) \quad 4\text{-}33$$

Table 4-30 presents the statistical parameters for this expression. The data reveal substantial values for both the multiple correlation coefficient R and the coefficient of determination R^2. This demonstrates a tightly knit and robust regression relationship between the independent variables and β, enhancing the model's overall fitting effectiveness. Furthermore, the significance of the independent variables is validated by p-values less than 0.01, confirming the judicious selection of these variables for inclusion in the model. Consequently, the constructed expression for β is affirmed as both logical and applicable, providing a deeper insight into the influence of various loading factors on the fatigue damage process in asphalt mixtures.

Table 4-30 Regression coefficients and variance analysis for Equations 4-32 and 4-33

No.	Coefficient	Value	t-Value	p-Value	R	R^2	F-value	Sig.
Eq.4-32	Constant	-2.717	-5.049	0.000	0.793	0.628	10.993	0.002
	$\ln(\varepsilon_0)$	0.462	4.198	0.001				
	$\ln(LR)$	0.087	3.431	0.006				
Eq.4-33	Constant	-5.367	-5.860	0.000	0.756	0.608	9.307	0.008
	$\ln(\varepsilon_0)$	0.972	4.963	0.003				
	$\ln(LR)$	-0.008	3.110	0.009				

Adopting a methodology akin to that used for parameter α, this study ventures to establish a unified equation for parameter β. The initial step involves examining the relative ratios of β in controlled-stress and controlled-strain loading scenarios. This is achieved by integrating Equations 4-32 and 4-33 into Equation 4-12, resulting in the derivation of a ratio $F_{\beta L}$, as defined in Equation 4-34.

$$F_{\beta L} = \frac{\beta_{L-\varepsilon}}{\beta_{L-\sigma}} = e^{-2.650} \cdot {\varepsilon_0}^{0.510} \cdot (LR)^{-0.095} \quad 4\text{-}34$$

Building on the foundation laid by Equation 4-34, the study introduces a pivotal S-shaped function, leading to the development of a continuous transition function, denoted as $F'_{\beta L}$ in Equation 4-35.

$$F'_{\beta L} = 1 + \frac{F_{\beta L} - 1}{1 + e^{k_{\beta L} \cdot \mathrm{MF}}} = 1 + \frac{e^{-2.650} \cdot {\varepsilon_0}^{0.510} \cdot (LR)^{-0.095} - 1}{1 + e^{k_{\beta L} \cdot \mathrm{MF}}} \quad 4\text{-}35$$

Further analysis, informed by Equation 4-35, utilizes Table 4-31, which is instrumental in revealing patterns of change in the values of $k_{\beta L}$ in relation to diverse ε_0 and LR. This observed pattern prompts a comprehensive examination of the $k_{\beta L}$ values. Figure 4-16 illustrates how $k_{\beta L}$ varies with ε_0 and LR, revealing a strong linear relationship between $k_{\beta L}$ values and $\ln(\varepsilon_0)$, while highlighting a lack of significant correlation with LR.

Table 4-31 Regression results of the coefficient $k_{\beta L}$

ε_0	LR	$k_{\beta L}$	ε_0	LR	$k_{\beta L}$	ε_0	LR	$k_{\alpha L}$
100	800	-4.79	300	800	-4.13	500	800	-3.037
	1000	-4.81		1000	-4.17		1000	-3.20
	1250	-4.82		1250	-4.211		1250	-3.34

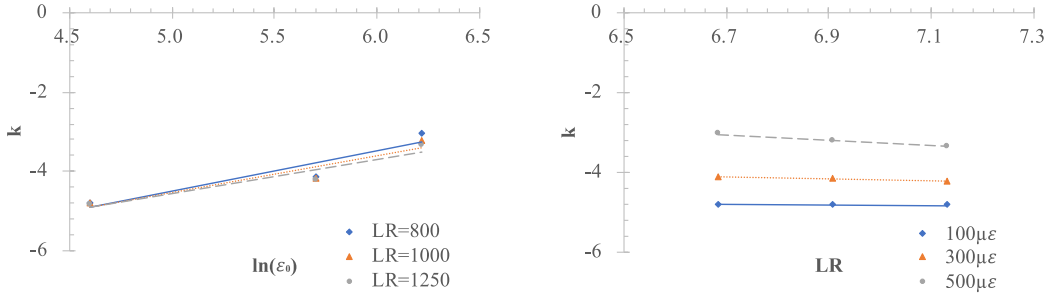

(a) $k_{\beta L}$ vs. $\ln(\varepsilon_0)$ (b) $k_{\beta L}$ vs. LR

Figure 4-16 Regression results of $k_{\beta L}$ vs.: (a) $\ln(\varepsilon_0)$ and (b) LR

Leveraging these insights, the study successfully formulates an expression for $k_{\beta L}$ through a detailed regression analysis, encapsulated in Equation 4-36. The robustness of this expression is reinforced by the statistical parameters presented in Table 4-32, underscoring its statistical significance and the model's precise fit. The p-values for the independent variables, being less than 0.01, validate the model's significance and the judicious choice of variables.

$$k_{\beta L} = -9.210 + 0.936\ln(\varepsilon_0) \quad 4\text{-}36$$

Table 4-32 Regression coefficients and variance analysis for Equations 4-36

No.	Coefficient	Value	t-Value	p-Value	R	R^2	F-value	Sig.
Eq.4-36	Constant	-9.210	-12.975	0.000	0.940	0.884	53.489	0.000
	$\ln(\varepsilon_0)$	0.936	7.310	0.000				

Thus, the refined and conclusive expression for $F'_{\beta L}$ is presented in Equation 4-37. Additionally, this study presents a unified equation, outlined in Equation 4-38, for estimating the parameter β of asphalt mixtures under various fatigue loading modes.

$$F'_{\beta L} = 1 + \frac{F_{\beta L} - 1}{1 + e^{k_{\beta L} \cdot \mathrm{MF}}} = 1 + \frac{e^{-2.650} \cdot {\varepsilon_0}^{0.510} \cdot (LR)^{-0.095} - 1}{1 + e^{(-9.210 + 0.936 \ln(\varepsilon_0)) \cdot \mathrm{MF}}} \quad 4\text{-}37$$

$$\beta_L = F'_{\beta L} \cdot \beta_{L-\sigma} \quad 4\text{-}38$$

The approach used in §4.4.3 and §4.4.4 marks a significant stride in understanding and predicting the impact of different tensile fatigue loading modes on the parameters of SBF, emphasizing a nuanced and comprehensive methodological approach to incorporate the various influential factors of fatigue damage progressions into the SBF.

4.5 Summary

In this chapter, efforts were made to fill the significant knowledge gap in understanding the detailed process of fatigue damage evolution in asphalt mixtures, a gap identified in Chapter 2. Key tasks included performing ITFT and 4PB tests, which are essential for assessing the fatigue behavior of asphalt mixtures under diverse loading conditions. The chapter also engaged in an in-depth analysis of the impact of crucial loading factors on initial stiffness and fatigue life. Another major undertaking was applying and comparing various nonlinear models to represent the fatigue damage evolution observed in laboratory settings accurately. This comparative analysis was instrumental in identifying the model that best encapsulates the multifaceted fatigue damage development process, considering the influence of diverse factors. The chapter also focused on enhancing the interpretability of model parameters, particularly in their response to different types of tensile fatigue loading. This was aimed at providing deeper insights into the fatigue damage mechanisms within asphalt mixtures.

The main findings of this chapter are as follows:

(1) Mixture stiffness: It is vital to consider the load's magnitude and duration, or the loading rate, when measuring the stiffness of asphalt mixtures. Corrections are necessary to align stiffness values under a unified standard.

(2) Fatigue life: The fatigue life assessment of asphalt mixtures should account for both the magnitude and the proportion of rest time to loading time, irrespective of the testing method. The fatigue loading mode significantly impacts fatigue life. The study proposes an innovative, versatile fatigue life prediction approach that transcends traditional conversion function methods. This approach embraces the nonlinearity in asphalt mixtures' fatigue damage process

and the nonlinear relationship between residual fatigue life ratios under various loading modes.

(3) Fatigue damage evolution models: All seven analyzed damage evolution models met boundary conditions and showed a monotonic increase in the damage variable with load applications. Notably, the WSF and SBF models could fit any damage evolution process, were simple in form, and performed well under both controlled-stress and controlled-strain modes.

(4) Influential factors of fatigue damage progressions: The SBF is found to be more rational than the WSF. In the SBF, parameters α and β independently reflect the fatigue life and the shape of the fatigue damage evolution curve of asphalt mixtures. They demonstrate clear correlations with various loading factors, suggesting that any complex damage progression in asphalt mixtures is correspondingly related to α and β. Thus, this study recommends using SBF to describe the fatigue damage progression of asphalt mixtures under the combined effect of multiple factors.

References

[1] Benedetto, H. D., Roche, C. D. L., Baaj, H., et al. Fatigue of bituminous mixtures. *Materials & Structures*, 2004, 37(267):202-216.

[2] Bonnaure, F. P., Huibers, A., & Boonders, A. A laboratory investigation of the influence of rest periods on the fatigue characteristics of bituminous mixes. *Journal of the Association of Asphalt Paving Technologists*, 1982, 51:104-128.

[3] Castro, M., & Sánchez, J. A. Estimation of asphalt concrete fatigue curves–a damage theory approach. *Construction and Building Materials*, 2008, 22(6):1232-1238.

[4] Chaboche, J. L. Continuous damage mechanics - a tool to describe phenomena before crack initiation. *Nuclear Engineering & Design*, 1981, 64(2):233-247.

[5] Deacon, J. A. *Fatigue of Asphalt Concrete*. Berkeley: University of California, Berkeley, 1965.

[6] Deacon, J. A., Tayebali, A., Coplantz, J., et al. *Fatigue response of asphalt aggregate mixes*. Washington, D.C.: National Research Council, 1994.

[7] Ge, Z., Huang, Z., & Huang, S. Study on effect factors of asphalt mixes fatigue properties. *Journal of Highway and Transportation Research and Development*, 2002, 06:1-4.

[8] Ghuzlan, K. A. *Fatigue damage analysis in asphalt concrete mixtures based upon dissipated*

energy concepts. Urbana: University of Illinois at Urbana-Champaign, 2001.

[9] Guo, R. *Predicting in-service fatigue life of flexible pavements based on accelerated pavement testing*. Austin: The University of Texas at Austin, 2007.

[10] Hopman, P. C., Kunst, P. A. J. C., & Pronk, A. C. A renewed interpretation method for fatigue measurement, verification of Miner's Rule. In *Proceedings of the 4th Eurobitume Symposium*. Madrid: European Bitumen Association, 1989:557-561.

[11] Hsu, T. W., & Tseng, K. H. Effect of rest periods on fatigue response of asphalt concrete mixtures. *Journal of Transportation Engineering*, 1996, 122(4):316-322.

[12] Huang, C., Gao, D., & Zhu, H. Influence of loading frequency on fatigue performance of fiber reinforced asphalt concrete. *Journal of North China Institute of Water Conservancy and Hydroelectric Power*, 2012, 33(06):106-111.

[13] Li, B. *Fatigue characteristic of various modified asphalt mixture*. Shanghai: Tongji University, 2016.

[14] Little, D. N., Lytton, R. L., Williams, D., et al. Propagation and healing of microcracks in asphalt concrete and their contributions to fatigue. *Asphalt Science and Technology*, 1997:149-195.

[15] Luan, L., & Tian, X. Non-linear analysis of fatigue damage of asphalt mixture. *Journal of Building Materials*, 2012, 15(4):508-512.

[16] Ma, Z. *Research on the fatigue performance and the method for estimation of remaining fatigue life of in-service asphalt mixture*. Shanghai: Tongji University, 2018.

[17] Monismith, C. L., & Deacon, J. A. Fatigue of asphalt paving mixtures. *Transportation Engineering Journal of ASCE*, 1969, 95(2):317-346.

[18] Monismith, C. L., Secor, K. E., & Blackmer, E. W. Asphalt mixture behaviour in repeated flexure. *Journal of the Association of Asphalt Paving Technologists*, 1961, 30:188-222.

[19] Rowe, G. M. Performance of asphalt mixtures in the trapezoidal fatigue test. *Journal of Asphalt Paving Technologists*, 1993, 62:344-384.

[20] Tangella, S. C., Craus, J., Deacon, J. A., et al. *Summary report on fatigue response of asphalt mixtures*. Washington, D.C.: Strategic Highway Research Program, 1990.

[21] Tian, X., Zheng, J., Xu, Z., et al. Fatigue response of asphalt concrete at low loading frequency. *China Journal of Highway and Transport*, 2002, 15(1):19-19.

[22] Tsai, B. W. *High-temperature fatigue and fatigue damage process of aggregate-asphalt mixes*. Berkeley: University of California, Berkeley, 2003.

[23] Van Dijk, W., & Visser, W. The energy approach to fatigue for pavement design. *Journal of Asphalt Paving Technologists*, 1977, 46:1-40.

[24] Weibull, W. A statistical theory of strength of materials. *Ingenjörs Vetenskaps Akademien Handlingar*, 1939, 151:1-45.

[25] Wu, Z. *Research on cumulative fatigue damage of asphalt mixture and asphalt layer based on multi-level amplitude loading*. Guangdong: South China University of Technology, 2014.

[26] Wu, K., & Zhang, X. Experimental research on uniform model for nonlinear evolution equation of fatigue damage of asphalt mixture. *Highway*, 2007, 05:125-129.

[27] Yang, Y. *Research on fatigue damage of asphalt mixture under different loading frequencies*. Changsha: Changsha University of Science and Technology, 2009.

[28] Yu, J. *Study on fatigue characteristics of asphalt mixture*. Guangdong: South China University of Technology, 2005.

[29] Zhu, J. *Evaluation and critical damage position for fatigue behavior of asphalt pavement considering the full temperature profile*. Shanghai: Tongji University, 2016.

5 ANALYSIS OF FATIGUE DAMAGE IN IN-SITU ASPHALT LAYERS

In this chapter, Full-scale Accelerated Pavement Testings (F-sAPTs) are implemented on the newly constructed asphalt layers laid on semi-rigid and granular bases. The Falling Weight Deflectometer (FWD), Portable Seismic Pavement Analyzer (PSPA), and uniaxial compression tests are utilized to assess the modulus of these asphalt layers. This process involves refining temperature and frequency adjustment factors for the modulus values obtained in situ. Then, taking stiffness reduction ratio (SSR) as the damage variable, a detailed investigation into the fatigue damage progressions across various pavement sections is conducted, focusing on different depths, locations, and orientations. Subsequently, two key models, the Weibull survival function (WSF) and the structural behavior function (SBF), are applied to fitting the damage progressions. The chapter concludes with a comparative study of these models, evaluating their logical consistency, fitting efficiency, and interpretability. The aim is to identify and recommend the most suitable model for characterizing the development of fatigue damage in in-situ asphalt layers, providing valuable insights for pavement engineering and maintenance.

5.1 In-situ Fatigue Tests

5.1.1 Asphalt Pavement Structures and Materials

Delving into the impact of different structural types of the fatigue damage processes of asphalt layers, this research conducted F-sAPTs on newly constructed asphalt pavements with semi-rigid and flexible base layers. The structural configurations of these two types of asphalt pavements are illustrated in Figure 5-1.

Both pavement types consist of a similar structure: a 30 cm AC-13 asphalt layer, a 35 cm base layer, and a 20 cm granular sub-base. However, the base materials differ between the two. Section I employs a cement stablized base, while Section II uses a granular base. Additonally, to minimize the influence of material characteristics on the fatigue damage process, both sections use a uniform

AC-13 asphalt mixture in the asphalt layer. This mixture is consistent with the one used in laboratory fatigue tests. The Marshall parameters and aggregate gradation of this asphalt mixture are detailed in Table 4-1 and Figure 4-1, respectively.

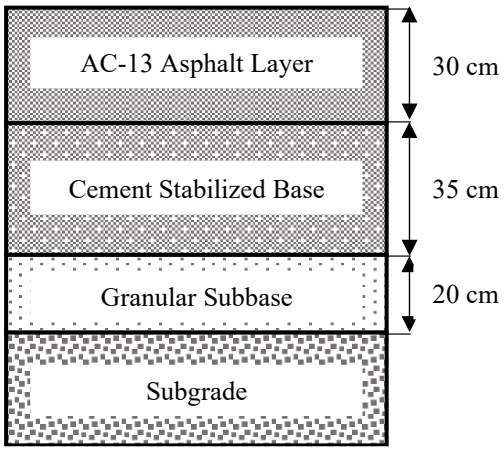

(a) Asphalt pavement with a semi-rigid base (Section I)

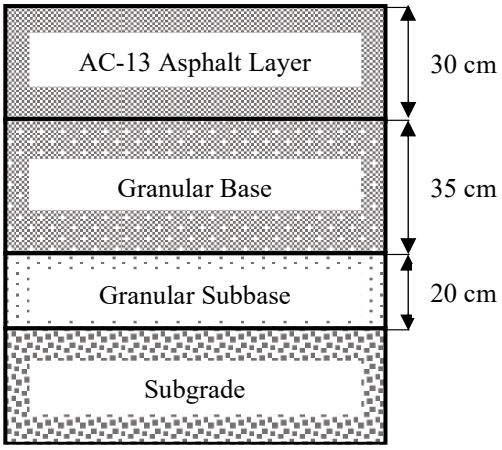

(b) Asphalt pavement with a granular base (Section II)

Figure 5-1 Asphalt pavement structures and materials: (a) Section I and (b) Section II

5.1.2 Layout of Sensors

To track temperature fluctuations within the asphalt layers, PT-100 temperature sensors were embedded in the two test sections. The temperature data of the asphalt layers was collected using a data logger, as illustrated in Figure 5-2.

The temperature sensors, with a measurement range of -50°C to +200°C and an accuracy of 0.1°C, were installed using a core sample embedding method. This involved drilling cores from the asphalt layer, inserting the sensors into holes drilled at specific depths on the side of the core samples, then replacing the core samples and sealing them with hot asphalt, as depicted in Figure 5-3. The

sensors were placed at depths of 8 cm, 15 cm, 21 cm, and 27 cm. The data logger collected data every five minutes, providing continuous 24-hour monitoring.

(a) PT-100 temperature sensor

(b) Data logger

Figure 5-2 The temperature sensor (left) and the data logger (right)

(a) Coring and drilling

(b) Embedding sensors

(c) Reburial of cores

(d) Grouting completion

Figure 5-3 The embedment process of temperature sensors

Additionally, strain gauges (model KMS-100), as shown in Figure 5-4, were embedded in the asphalt layers of the two sections to detect strain responses under load. These strain gauges have a range of ±500 microstrains (με) and an accuracy of 1 με, with an operational temperature range of -20°C to +180°C, adequately meeting the requirements for strain response detection in asphalt layers.

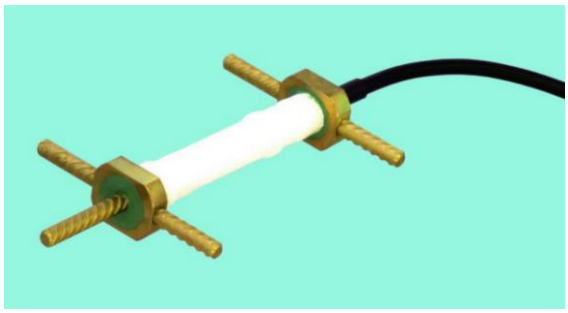

Figure 5-4 KMS-100 strain gauge

These strain gauges were installed using a direct embedding method. During the asphalt layer paving process, the strain gauges were positioned and fixed at the respective layers, and then the asphalt

mixture was uniformly spread over them using a paver. This ensured that the gauges were covered before the next layer was laid and compacted, as shown in Figure 5-5.

(a) Sensor positioning (b) Sensor fixation (c) Mixture spreading (d) Mixture compaction

Figure 5-5 The embedment process of strain gauges

To observe strain responses at various depths and orientations within the asphalt layers, four strain gauges were embedded at specific depths in each of Sections I and II. In Section I, gauges were placed at depths of 12 cm and 24 cm, while in Section II, they were located at 6 cm and 30 cm (the bottom of the asphalt layer). These included two transverse and two longitudinal strain gauges, with the transverse direction being perpendicular to the direction of axle load movement, and the longitudinal direction parallel to it. The four gauges at each depth were arranged sequentially along the direction of axle load movement, spaced 50 cm apart.

5.1.3 Full-scale Accelerated Pavement Tests (F-sAPTs)

5.1.3.1 Loading Equipment

The F-sAPT can effectively simulate real-world pavement structures, traffic, and environmental conditions, accelerating the damage process for study. The research utilizes F-sAPT to investigate the evolution of fatigue damage within asphalt layers.

The primary equipment used for the accelerated loading tests is the MLS66, as illustrated in Figure 5-6. The MLS66 is a linear-type loading device with an effective operational length of 6.6 meters. This equipment, equipped with six sets of loading wheels, is capable of reaching a maximum loading frequency of 6000 passes per hour, equivalent to approximately 6 meters per second or 22 kilometers per hour.

(a) The appearance of MLS66

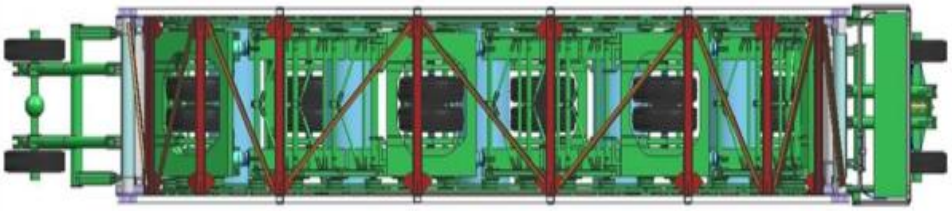

(b) The load settings of MLS66

Figure 5-6 The MLS66 at Tongji University: (a) The appearance and (b) The load settings

In the experiments conducted on both Sections I and II, the research employs a specific loading configuration: a dual-wheel load with no lateral movement. This setup involves a half-axle load of 50 kN and a loading frequency of 5000 cycles per hour, which equates to a speed of about 5 meters per second. Additionally, the study includes an assessment of the tire contact area under the selected axle load, crucial for calculating tire contact pressure. This measurement, depicted in Figure 5-7, reveals that the load's contact shape with the ground is nearly rectangular. The detailed load profile parameters and the resultant contact pressures are systematically documented in Table 5-1.

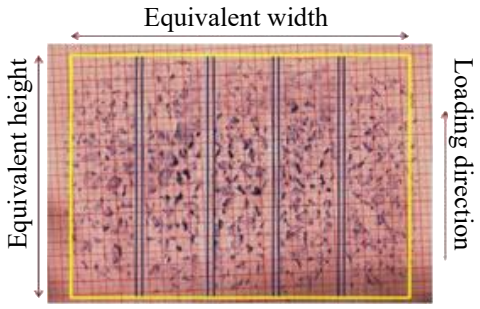

Figure 5-7 The measured tire contact area

Table 5-1 Load profile parameters and tire contact pressure

Load (kN)	Load Profile Parameters (cm)			Contact pressure (MPa)
	Equivalent Width	Equivalent Height	Dual Wheel Base	
50	22	17.8	36	0.64

5.1.3.2 Implementation of F-sAPT on Section I

The following subsections provide a detailed overview of the experimental process and its outcomes. The study conducted F-sAPT on Test Section I from November 9, 2018, to June 14, 2019, administering a total of 3 million load cycles. Notably, during this testing period, there was no significant cracking observed on the surface of the asphalt layer.

In Figure 5-8, the temperature variations within the asphalt layer of Section II during the F-sAPT are displayed. Given the indoor setting of the experiment, the influence of solar radiation was minimal, leading to negligible temperature disparities and gradients across different depths of the asphalt layer. As a result, the study employs the average temperature of the asphalt layer within the pavement structure for further analytical purposes.

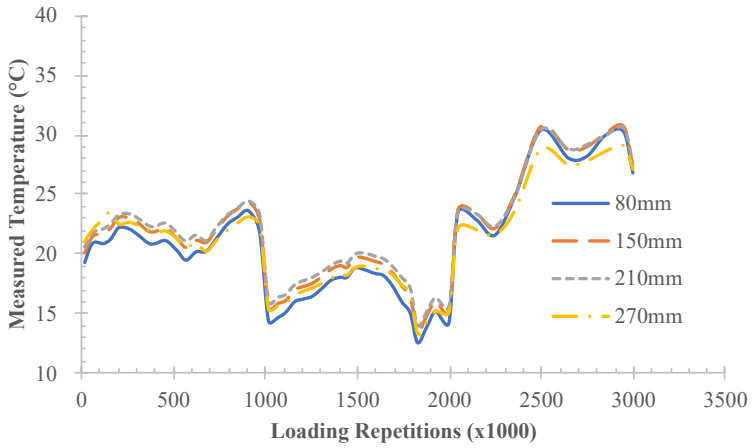

Figure 5-8 Temperature variations at various depths of the asphalt layer in Section I

Additionally, Figure 5-9 illustrates the typical strain response in the asphalt layer of Section II under the MLS66 load. A notable feature in this data is the pronounced asymmetry in the longitudinal strain curve of the asphalt layer, characterized by a "compression-tension-compression" cycle. This indicates that the asphalt layer undergoes compressive strain when the wheel load approaches and recedes, and tensile strain when directly under the wheel load. Conversely, the transverse strain predominantly displays tensile properties, with its curve exhibiting a more symmetrical pattern of change.

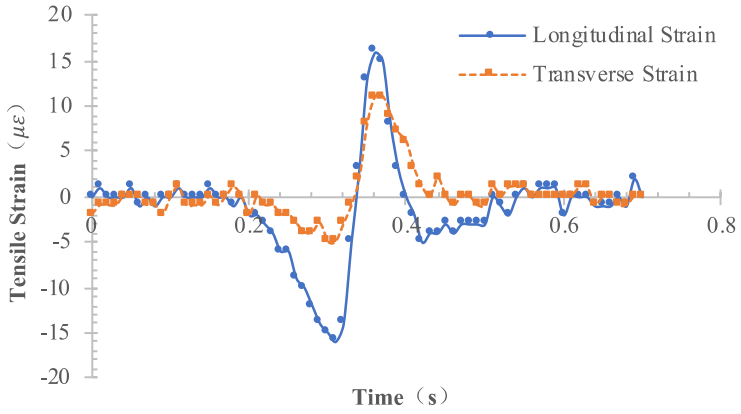

Figure 5-9 Typical profiles of tensile strain in the asphalt layer of Section I

Figure 5-10 presents a comprehensive view of how the peak strain values, recorded by the strain gauges during the F-sAPT, correlate with the average temperature of the asphalt layer and the number of load cycles. It is important to note the absence of data from the transverse strain gauge at a depth of 12 cm due to its failure. The data indicates that the peak strain values generally fluctuate in tandem with the average temperature of the asphalt layer. This consistency in strain gauge readings throughout the loading process confirms their reliability and proper adhesion to the asphalt layer. Furthermore, the consistent data implies that there were no significant internal cracks within the asphalt layer, underscoring the resilience of the material under test conditions.

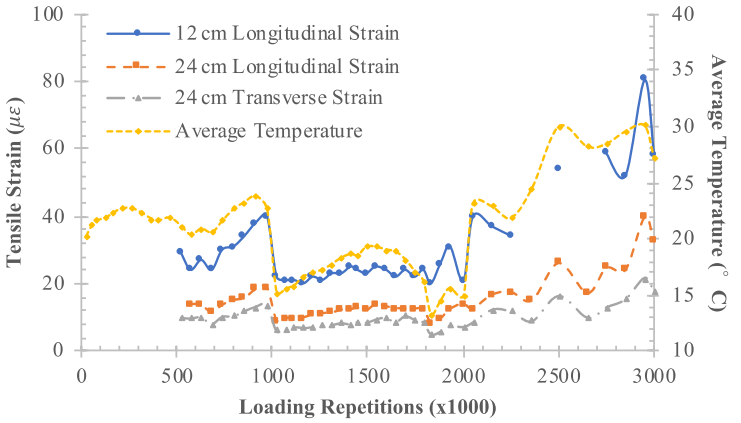

Figure 5-10 Variation of peak tensile strain values in the asphalt layer of Section I

5.1.3.3 Implementation of F-sAPT on Section II

This subsection delves into the F-sAPT carried out on Section III, a segment constructed indoors. The testing period spanned from January 6, 2020, to June 29, 2020, during which the section was

subjected to 2.5 million load cycles. A key observation from this phase was the absence of significant cracking on the asphalt layer's surface, indicating its resilience under repeated loading.

Temperature variations within the asphalt layer are meticulously documented in Figure 5-11, showing changes at various depths in relation to the number of load cycles. Echoing observations from Sections I, this section also exhibited minimal temperature differences and gradients across different depths. Consequently, the study prudently opts to use the average temperature of the asphalt layer for more in-depth analysis, ensuring consistency across different test sections.

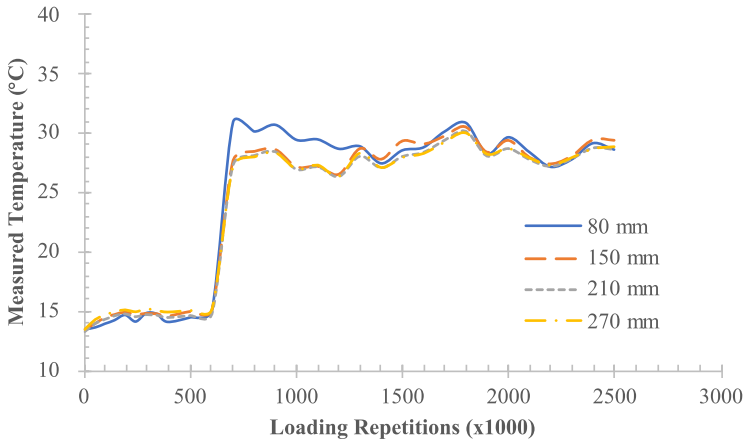

Figure 5-11 Temperature variations at various depths of the asphalt layer in Section II

Regarding strain measurement, it is noted that the strain gauges embedded at the 6 cm depth and at the base of the asphalt layer in Section II did not function throughout the test duration, leading to a lack of viable strain data from these locations.

5.2 Detection of Fatigue Damage of Asphalt Layer

This section delineates the techniques and procedures employed in the F-sAPTs to evaluate the modulus of asphalt layers, which are pivotal for the analysis of fatigue damage progressions in these layers. The following subsections systematically details the detection methods and experimental approaches utilized across the two test sections.

5.2.1 In-situ Detection Methods and Experimental Scheme

5.2.1.1 Coring and Laboratory Dynamic Modulus Test

Coring and laboratory testing is one of the conventional methods to detect asphalt layer modulus. Many researchers cored specimens from the asphalt layer for laboratory resilient modulus test [21], uniaxial dynamic modulus test [9,17], indirect dynamic modulus test [9,23], flexural dynamic modulus test [8,9,23], and ultrasonic test [33]. The uniaxial compression dynamic modulus test is notably prevalent in current research methodologies, as indicated by its integration into the MEPDG and China's latest highway asphalt pavement design standards (JTG D50-2017).

For this study, coring and laboratory uniaxial compression dynamic modulus tests were conducted in the non-loaded areas of Sections I and II. Cores with a 101.6 mm ± 1 mm diameter were extracted and sawed at depths of 70 mm and 220 mm to make the specimens with a height of 150 mm ± 1 mm. Following AASHTO TP 62-03 standards [1], the dynamic modulus tests were executed without confining pressures and conducted with a stress-controlled half-sine waveform. Test temperatures were varied across -10°C, 4.4°C, 21.1°C, 37.8°C, and 54.4°C, and the loading frequencies were set at 25 Hz, 10 Hz, 5 Hz, 1 Hz, 0.5 Hz, and 0.1 Hz. The experimental setup and process are illustrated in Figure 5-12.

(a) In-situ coring

(b) Uniaxial compressive dynamic modulus test

Figure 5-12 Coring (left) and laboratory dynamic modulus test (right)

5.2.1.2 Falling Weight Deflectometer (FWD) Test

While the coring method is widely used, it has significant limitations: it can damage the pavement, and the results from core samples may not comprehensively reflect the condition of the entire pavement. Consequently, non-destructive testing methods, such as the FWD test, are increasingly favored for their minimal damage to the asphalt layer, rapid and efficient testing process, and broader coverage.

The FWD method has gained widespread application in pavement analysis. In 2017, the AASHTO conducted a detailed study on FWD [5,28,33]. This research reviewed FWD testing

methods, deflection basin shape parameters, various back-calculation theories, and software tools since 1955. The study presented a guideline for FWD testing and analysis through six field case studies, demonstrating its broad applicability. Furthermore, research by Chen [8] and Sebaaly et al. [32] involved back-calculation analysis of FWD data from F-sAPTs. They successfully tracked the decay process of asphalt layer modulus under load, validating the effectiveness of FWD in F-sAPTs.

Based on these insights, this study employs FWD test as the second method to assess the average modulus of the asphalt layers in the non-loaded areas of Sections I and II. It was conducted using the truck-mounted FWD as shown in Figure 5-13. This equipment can apply different load levels by adjusting the height of the falling weight. During the test, it simultaneously records the road surface temperature, the duration of the load application, and the deflection values at distances of 0, 20 cm, 30 cm, 45 cm, 60 cm, 90 cm, 120 cm, 150 cm, 180 cm, and 210 cm from the load center.

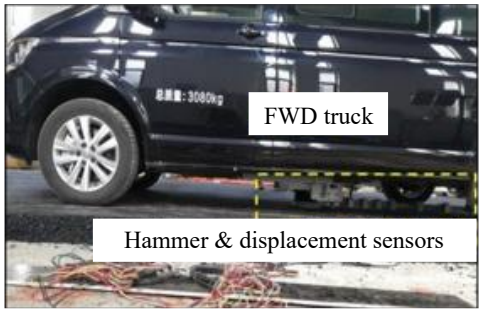

Figure 5-13 FWD Equipment

5.2.1.3 Portable Seismic Pavement Analyzer (PSPA) Test

PSPA is another non-destructive method for evaluating the modulus of asphalt layers [17,19]. It is recognized for its cost-effectiveness, portability, and ease of use, making it a popular tool in road engineering [7,14]. Unlike the traditional FWD testing, PSPA can determine the modulus of asphalt layers at various depths without the need for complex back-calculation analysis, providing unique and direct results. Studies, including those by Oh et al. [27], highlight the practicality and operability of PSPA, noting an average variability of 9.2% in its results, which underscores its effectiveness. As a result, PSPA is utilized in this research to measure the seismic modulus of asphalt layers during the F-sAPTs.

The PSPA equipment, developed by Baker et al. [4] in 1995, is depicted in Figure 5-14. It comprises one source and two receivers. The source includes a 500 g rubber hammer and a pressure

sensor, and a laptop will connect to this device to give commands and store the signals collected by the receivers [12,23].

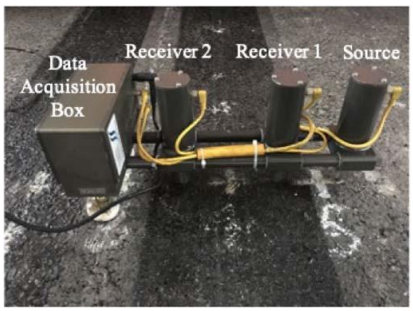

Figure 5-14 PSPA Equipment

The PSPA device functions by generating high-frequency impulse to detect short-wavelength surface waves within the pavement layer. Utilizing the surface wave method (SWM) [4], the surface wave velocity is assumed constant across wavelengths that are equal to or shorter than the thickness of the uppermost layer. However, if the properties of the asphalt layer vary with depth, a corresponding change in surface wave velocity across different wavelengths is observed.

The PSPA device determines the relationship between surface wave velocity and wavelength using time measurements recorded by the two receivers. From these measurements, the seismic modulus of the asphalt layer is directly calculated using the equation [6,26]:

$$E_s = 2\rho[(1.13 - 0.16\upsilon)V_R]^2(1+\upsilon) \quad 5\text{-}1$$

where E_s is the seismic modulus (Pa), V_R is the Rayleigh wave speed (m/s), ρ means the density of the asphalt layer (2090 kg/m^3), and υ means Poisson's ratio (0.35). It is crucial to note the limitations imposed by the source's loading frequency and the fixed distance between the receivers. Consequently, the PSPA equipment in this study is restricted to measuring the asphalt layer's modulus only within a depth range of 7 cm to 28 cm. For thorough analysis, this depth range is further subdivided into 1 cm thick layers, allowing for a more granular examination of the seismic modulus at varying depths of the asphalt layer.

5.2.1.4 Experimental Scheme

This study adopted the aforementioned three methods (FWD, PSPA, and uniaxial compression dynamic modulus tests) to detect the modulus of asphalt layers during the F-sAPTs. The spatial arrangement of the test points and the overall testing plan are illustrated in Figure 5-15 and summarized in Table 5-2.

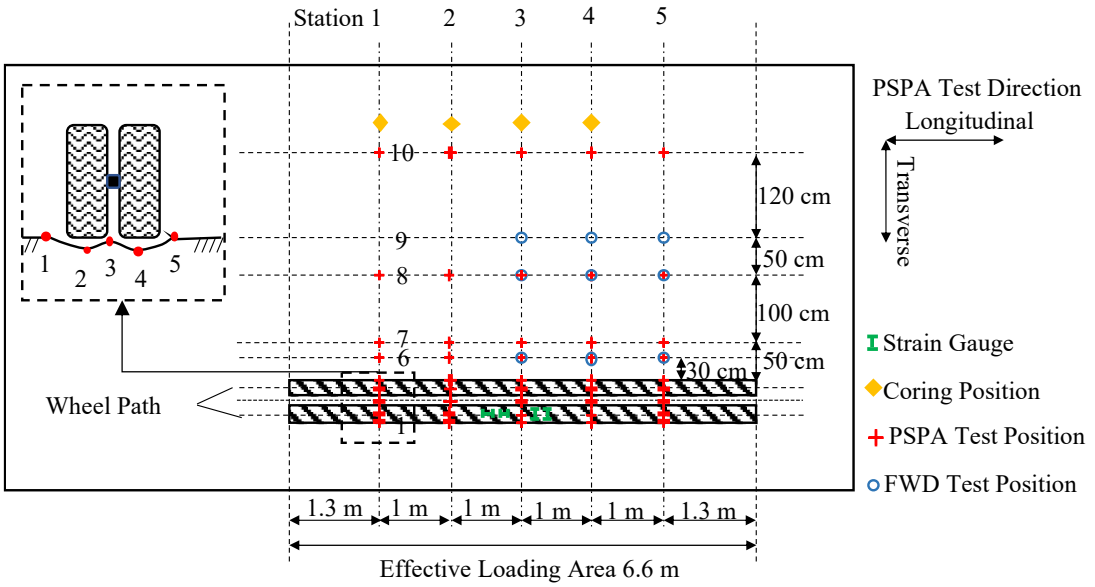

Figure 5-15 Layout of fatigue damage detection points

Table 5-2 Asphalt Layer fatigue damage detection scheme

Detection Method		**Section I**	**Section II**
Coring and Laboratory Test		Randomly selected four cores	Randomly selected four cores
FWD	Points in Non-Loaded Area	No. 6, 7, 9	No. 6, 7, 9
	Inspections in Non-Loaded Area	26	9
PSPA	Points in Non-Loaded Area	No. 6, 7, 8, 10	No. 6, 7, 8, 10
	Inspections in Non-Loaded Area	43	30
	Points in Loaded Area	No. 1, 2, 3, 4, 5	No. 1, 2, 3, 4, 5
	Inspections in Loaded Area	51	30

As Figure 5-15 indicates, five testing stations were strategically chosen within the effective length of loading, each spaced one meter apart. These stations were carefully positioned to be far from the location where the wheel landed and lifted off the pavement. Each stations encompasses ten distinct test points: Points 1 to 5 are within the loaded zone, heavily influenced by the load, whereas Points 6 to 10 lie in the non-loaded zone, experiencing relatively less wheel load impact. Specifically, Points 1 and 5 align with the outer edges of the wheel paths; Points 2 and 4 are at the center of the wheel paths; Point 3 is at the center of the wheels' gap; and Points 6 to 10 are located progressively farther from the right wheel path's outer edge, at intervals of 30 cm, 50 cm, 150 cm, 200 cm, and 320 cm.

Given the potential for uneven contact between the FWD loading plate and the wheel paths, FWD assessments were exclusively performed at Points 6, 7, and 9 in the non-loaded areas. Sections I and II underwent 26 and 9 FWD tests, respectively, utilizing load levels of 40 kN, 50 kN, and 60

kN. Each load level was accompanied by two parallel trials. This approach resulted in Test Sections I and II producing 1404 and 486 sets of deflection basin data, respectively.

To evaluate the seismic modulus of the asphalt layer in the non-loaded areas, PSPA tests were conducted at Points 6, 7, 8, and 10 in Sections I and II, as outlined in Table 5-2. Each test direction—longitudinal (parallel to axle load movement) and transverse (perpendicular to axle load movement)—underwent ten parallel tests. Consequently, Sections I and II accumulated 17,200 and 12,000 sets of seismic modulus data from the non-loaded areas, respectively, during the F-sAPTs.

Furthermore, to analyze the seismic modulus of the asphalt layer under various damage conditions, PSPA testing was executed at Points 1 to 5 within the loaded zones of both test sections. Each test point, in both test directions, was subjected to ten parallel tests. Therefore, Test Sections I and II generated 25,500, and 15,000 data sets of seismic modulus under different damage conditions, respectively. This rigorous and structured testing scheme ensures an in-depth and nuanced understanding of the asphalt layers' modulus under various stress and damage scenarios.

5.2.2 Temperature Correction of the Detection Results

Asphalt mixtures are known for their temperature-sensitive properties, with their modulus varying significantly in response to temperature changes. In this study, a crucial aspect was the temperature correction of the asphalt layer's modulus measurements to eliminate the influence of temperature variations on the results. This approach is particularly relevant for non-loaded areas, where the modulus variations are predominantly influenced by temperature rather than load. The study focuses on analyzing the modulus in these areas, proposing temperature correction methodologies for both inversion results from the FWD test and the PSPA test outcomes, subsequently applying these methods to the results from loaded area.

5.2.2.1 Temperature correction of FWD Inversion Results

The MODULUS 7.0 software was employed for back-calculating the FWD test results, providing the average modulus of the asphalt layer in the non-loaded areas. This software utilizes a static database search-matching approach, based on a method introduced in 1988 [34]. It involves calculating possible deflection basins within a defined modulus range for each material layer, creating a database, and then identifying the layer modulus values that minimize the error between

theoretical and actual deflection basins [28]. This process has been refined and optimized over the years [20,24,29-31], enhancing its applicability in such analyses.

The temperature correction of the FWD inversion results was conducted using a model previously applied in various studies [13,15,22]:

$$\log E_{T_m} = b + nT_m \quad 5\text{-}2$$

$$E_{T_m} = 10^{b+nT_m} \quad 5\text{-}3$$

$$\omega = \frac{E_{T_0}}{E_{T_m}} = 10^{n(T_0 - T_m)} \quad 5\text{-}4$$

where E_{T_m} is the asphalt modulus at the measured temperature of T_m, E_{T_0} is the asphalt modulus at the targeted temperature of T_0, ω means the temperature correction factor, and b and n are regression coefficients. This model assumes a linear relationship between the asphalt layer's modulus and temperature on a semi-logarithmic scale. Notably, the regression coefficient n in this model is independent of load levels and the target temperature [15], which simplifies the determination of the temperature correction factor.

By aggregating the FWD test results from two test sections, the study back-calculated 1890 average modulus values. Regression analysis with corresponding average asphalt layer temperatures yielded a regression coefficient n of -0.0236, with the model exhibiting an R^2 value of 0.66.

Setting the target temperature T_0 at 20°C, the FWD inversion results for both test sections were corrected to this standard temperature, as illustrated in Figure 5-16. The analysis showed that the load level did not significantly affect the temperature correction outcomes. Summarizing and averaging across all three load levels, the average modulus of the asphalt layer in the non-loaded area was found to be 9130 MPa, with a standard deviation of 876 MPa. The majority of the temperature-corrected modulus values fell within one standard deviation from the mean, underscoring the validity and effectiveness of the employed back-calculation method and temperature correction model.

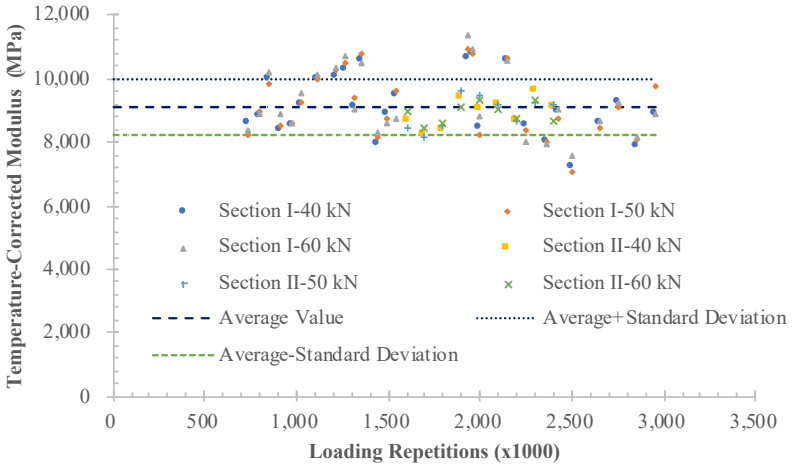

Figure 5-16 Temperature-corrected inverse modulus of non-loading areas

5.2.2.2 Temperature correction of PSPA Results

This study also addressed the need for temperature correction of the PSPA test results, particularly in assessing the seismic modulus of asphalt layers. A temperature correction model, represented by Equation 5-5 and widely utilized in previous research [2,7,16], was considered.

$$\frac{1}{\omega} = \frac{E_{T_m}}{E_{T_0}} = s + kT_m \qquad 5\text{-}5$$

where s and k are regression coefficients. This model, though straightforward, presumes a linear relationship between the seismic modulus ratios at different temperatures and the temperature itself. It's important to note, however, that this linear assumption is not always valid, especially at very high or low temperatures. Li and Nazarian's research highlighted that this model's optimal temperature range is between 25°C and 60°C, and its accuracy diminishes at higher temperatures. In this study, the asphalt layer temperatures varied between 10°C and 40°C, as illustrated in Figure 5-8 and Figure 5-11, rendering Equation 5-5 unsuitable for temperature correction of the PSPA results.

Given the broader applicability of the models in Equations 5-2 to 5-4, this study adopted these models to adjust the seismic modulus of asphalt layers. Aggregating the PSPA test results from non-loaded areas resulted in 29,200 measurements of the average seismic modulus. Regression analysis, using Equation 5-2, correlated these values with corresponding average asphalt layer temperatures, yielding a regression coefficient n of -0.0058 and an R^2 value of 0.61.

The average seismic modulus of the asphalt layers in the non-loaded areas of Sections I and II was then corrected to a standard temperature of 20°C (T_0=20°C). This correction yielded an average

modulus of 14.42 GPa, with a standard deviation of 0.77 GPa. Figure 5-17 showcases these temperature-corrected results, indicating a uniform average seismic modulus across the asphalt layer, with most values falling within one standard deviation. This uniformity attests to the effectiveness of the temperature correction model implemented in this study.

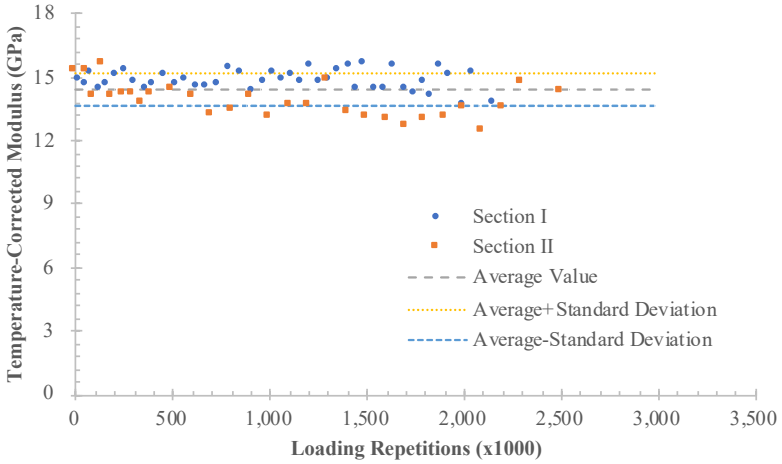

Figure 5-17 Temperature-corrected seismic modulus of non-loading areas

Further, with the derived analysis parameters (n=-0.0058, T_0=20°C), this study applied temperature corrections to the PSPA test results at various depths within the loaded areas. The corrected data across the five stations were then compiled and averaged, taking into account the test point, depth, and direction. The outcomes, presented as contour plots in Figure 5-18 and Figure 5-19, depict the results for the two test sections.

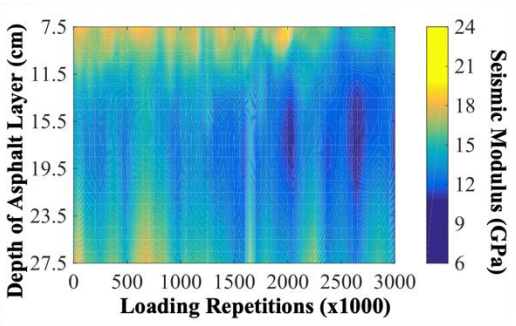

(a) Transverse direction - Point 1

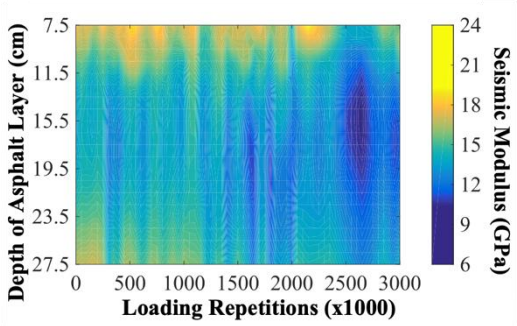

(b) Longitudinal direction - Point 1

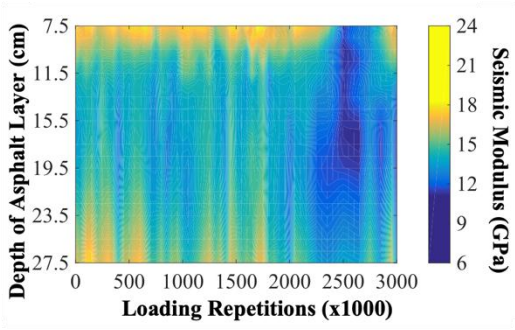

(c) Transverse direction - Point 2

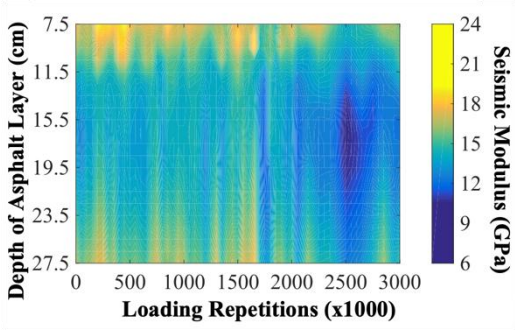

(d) Longitudinal direction - Point 2

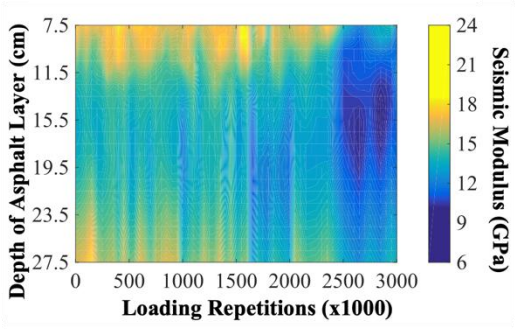

(e) Transverse direction - Point 3

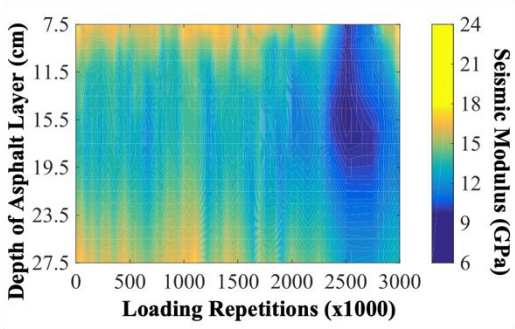

(f) Longitudinal direction - Point 3

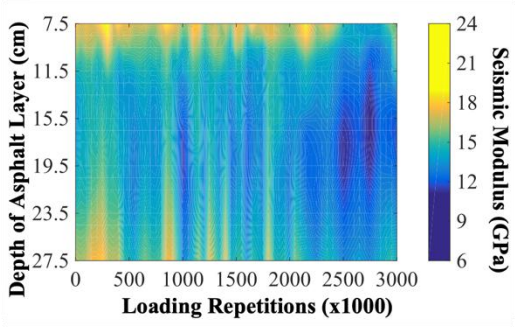

(g) Transverse direction - Point 4

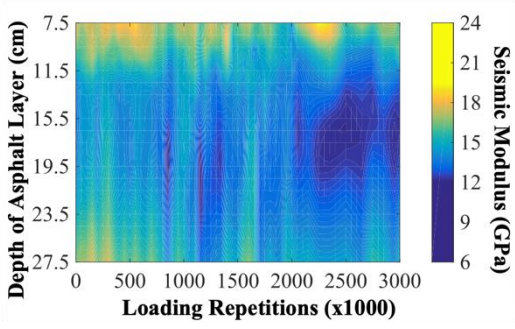

(h) Longitudinal direction - Point 4

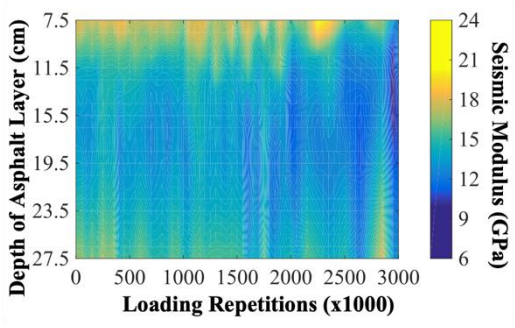

(i) Transverse direction - Point 5

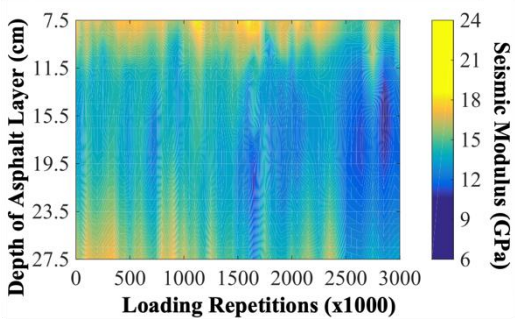

(j) Longitudinal direction - Point 5

Figure 5-18 Temperature-corrected seismic modulus in loading areas of Section I

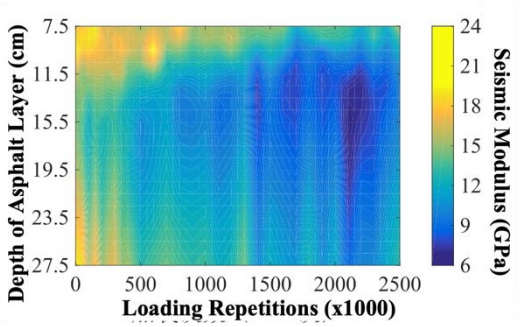

(a) Transverse direction - Point 1

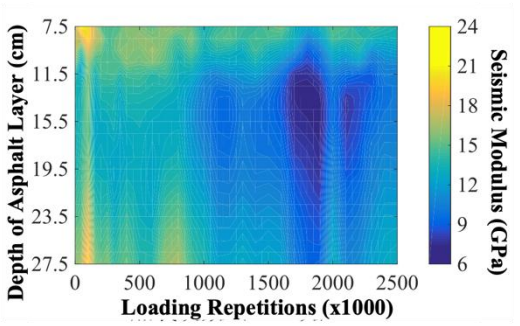

(b) Longitudinal direction - Point 1

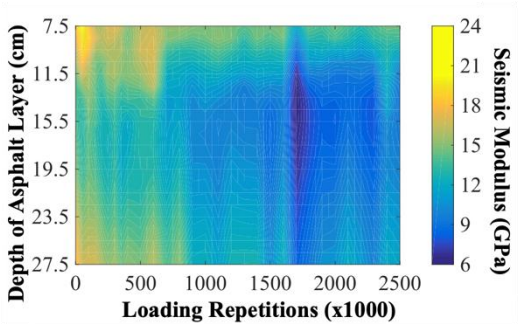

(c) Transverse direction - Point 2

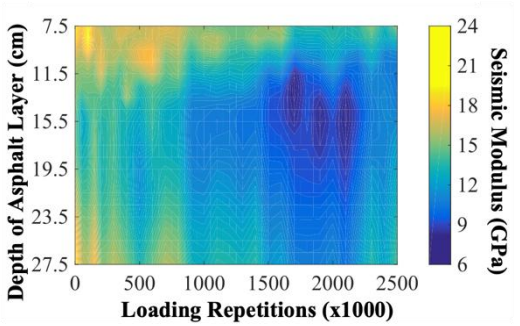

(d) Longitudinal direction - Point 2

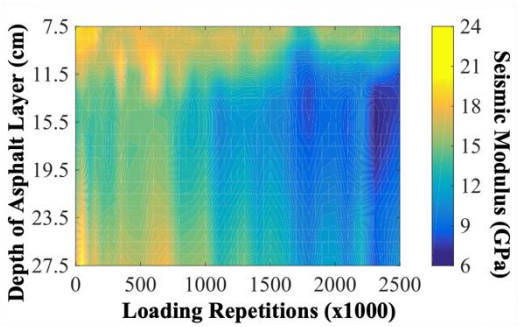

(e) Transverse direction - Point 3

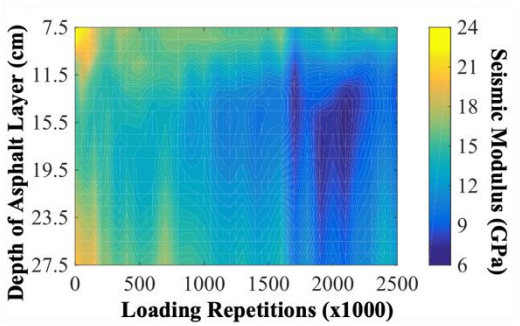

(f) Longitudinal direction - Point 3

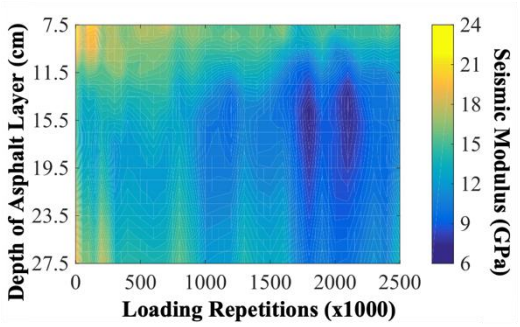

(g) Transverse direction - Point 4

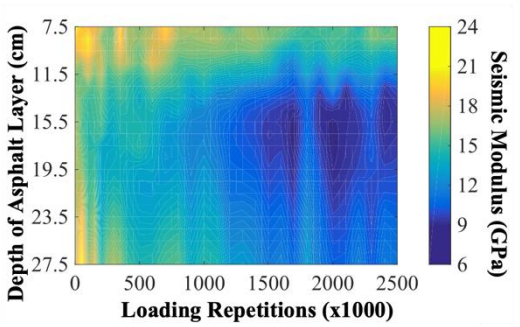

(h) Longitudinal direction - Point 4

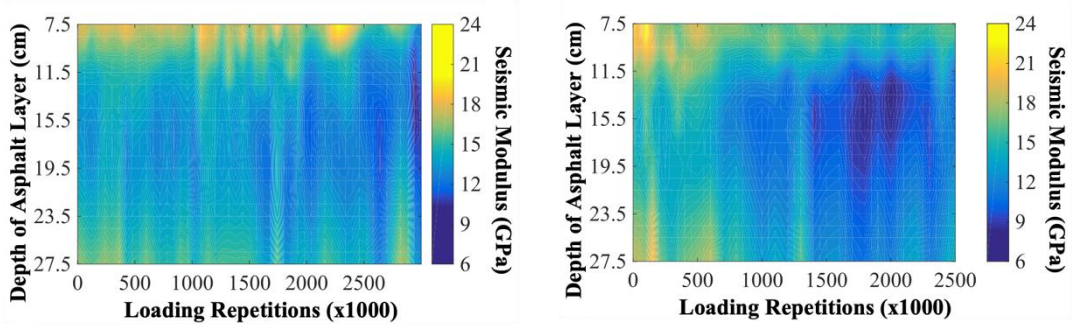

(i) Transverse direction - Point 5

(j) Longitudinal direction - Point 5

Figure 5-19 Temperature-corrected seismic modulus in loading areas of Section II

Analysis of Figure 5-18 and Figure 5-19 reveals that the modulus of the asphalt layers in Sections I and II decreased markedly with an increase in the number of load applications. The distribution of the modulus contours, however, was complex, indicating varied modulus change patterns depending on the test location, depth, and direction. This complexity necessitates a more in-depth analysis. Moreover, the comparison of the contour distributions, using identical contour intervals, shows that Section II, with its flexible base, exhibited a denser contour distribution. This suggests that the asphalt layer modulus in this section was more significantly affected by the loading, experiencing greater attenuation compared to the other section.

5.2.3 Frequency Adjustment of In-situ Seismic Moduli

Asphalt mixtures, being viscoelastic materials, exhibit time-temperature equivalence, meaning their modulus is significantly affected not only by temperature but also by variations in load application time and frequency. An analysis comparing temperature-corrected modulus results from FWD tests (Figure 5-16) and PSPA tests (Figure 5-17) showed that the PSPA's higher load application frequency led to a greater modulus in the asphalt layer compared to the FWD results. Consequently, it's necessary to adjust for frequency as well as temperature to accurately represent the modulus of asphalt layers.

Addressing this need, the study developed frequency adjustment methods for both undamaged and damaged asphalt layers. These methods aimed to align seismic modulus values to a modulus value corresponding to a designated design frequency.

5.2.3.1 Relationship between Seismic Moduli and Other Detection Results

For undamaged asphalt layers in non-loaded areas, this study used master curve analysis, inspired by methods from Bai [3] and Lin et al. [18], to propose a frequency correction coefficient for the seismic modulus.

Table 5-3 presents the uniaxial compression dynamic modulus test results for the asphalt coring samples in the non-loaded area. The results indicated a clear time-temperature equivalence for the asphalt mixtures, with a notable decrease in dynamic modulus at higher temperatures and lower load frequencies.

Table 5-3 Average results from the laboratory dynamic modulus tests (MPa)

Temperature (°C)	**Frequency (Hz)**					
	25	**10**	**5**	**1**	**0.5**	**0.1**
-10	24137	22965	21909	19662	18405	14754
4.4	17555	15826	14504	11452	10197	7393
21.1	8508	6932	5919	3541	2958	1657
37.8	3203	2224	1529	708	561	299
54.4	1009	714	520	196	158	97

Following the research by Witczak and Kaloush [35], this study represented the relationship between the dynamic modulus of asphalt mixtures and load frequency at a constant temperature using a master curve. This curve utilizes a Sigmoidal function proposed by Ferry in 1970 [25]:

$$\log(E^*) = \delta + \frac{\alpha}{1 + e^{[\beta + \gamma \log(f_r)]}} \quad 5\text{-}6$$

where E^* denotes the dynamic modulus (Pa), f_r the load application frequency (Hz), δ the low-frequency asymptote, α the difference between high- and low-frequency asymptotes, and β and γ shape parameters. Regression analysis of the data in Table 5-3 yielded parameters for the modulus master curve at different temperatures (Table 5-4). Remarkably, the parameters δ, α, and γ were largely unaffected by temperature variations, indicating that the asphalt mixtures' modulus remains stable across temperature changes under low and high-frequency loading.

Table 5-4 Model parameters of the master curve at different temperatures

Temperature (°C)	$\boldsymbol{\delta}$	$\boldsymbol{\alpha}$	$\boldsymbol{\beta}$	$\boldsymbol{\gamma}$
-10	6.8076	3.6425	-3.0628	-0.5010
4.4	6.7937	3.6598	-2.1295	-0.4988
21.1	6.8001	3.6529	-1.1368	-0.4999
37.8	6.8006	3.6526	-0.3011	-0.4999
54.4	6.7994	3.6538	0.2858	-0.4997

With the Sigmoidal model in Equation 5-6, the modulus master curve can reflect the modulus of asphalt mixtures across all frequencies and help determine the modulus values corresponding to the design frequency. Hence, the study attempted to unify the FWD inversion results, PSPA test outcomes, and uniaxial compression dynamic modulus using the master curve.

The study first identified the load frequencies for the FWD and PSPA tests. The average load frequency for FWD, based on the 1,890 tests in the non-loaded areas of Sections I and II, was calculated at 33.07 Hz, while the PSPA load frequency was set at 10 kHz, following the findings of Daniel and Kim [11], Celaya and Nazarian [6], and Oh et al. [27].

The FWD and PSPA results for the undamaged asphalt layers were then temperature-corrected to the values in Table 5-4 and plotted on the modulus master curve relative to their respective load frequencies, as depicted in Figure 5-20. It can be observed that despite the variations in testing methodologies, load frequencies, and modulus analysis approaches, there was a good correlation between the results from the FWD, PSPA, and uniaxial compression dynamic modulus tests, aligning well with the master curve predictions.

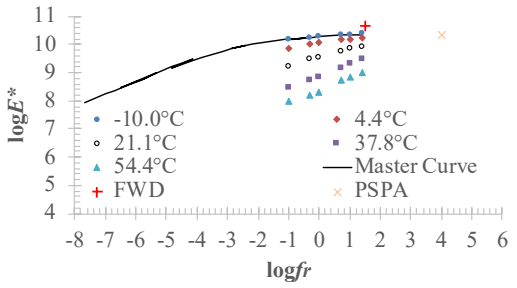

(a) -10 °C

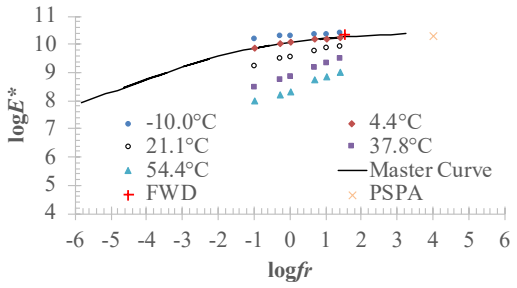

(b) -10 °C

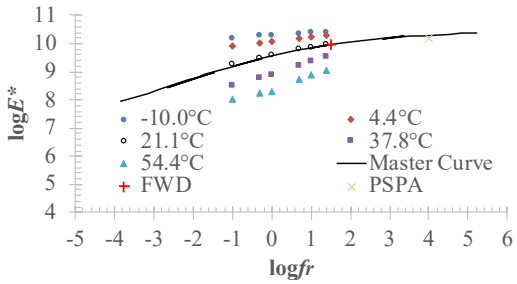

(c) -10 °C

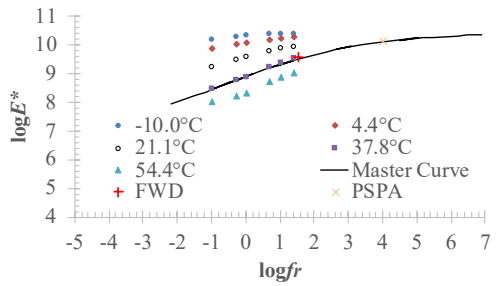

(d) -10 °C

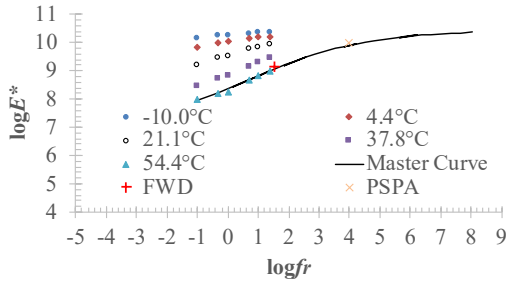

(e) -10 °C

Figure 5-20 Master curves at different temperatures

Leveraging the relationship between PSPA results and dynamic modulus shown in Figure 5-20, the study introduced a frequency correction coefficient K for the seismic modulus of undamaged asphalt layers:

$$K = \frac{E_S}{E_D^*} \tag{5-7}$$

where E_S represents the seismic modulus at temperature T_R, E_D^* is the modulus corresponding to the design frequency on the master curve at the same temperature, and T_R refers to the test temperatures from Table 5-4.

5.2.3.2 Modified Frequency Adjustment Factor

In addressing the challenge of accurately assessing the modulus of asphalt layers, particularly when damage occurs due to loading, this study identified a need to refine the frequency correction coefficient K, initially derived from PSPA test results and dynamic modulus analysis for undamaged layers. The key insight was that the modulus of asphalt layers decreases upon damage, altering the modulus master curve and thus affecting the relationship between PSPA test results and dynamic modulus. This change renders the initial frequency correction coefficient K unsuitable for modulus frequency adjustment in damaged asphalt layers within the loaded area.

To overcome this challenge, the study adapted the modulus master curve model from the CalME design method [10], as specified in Equation 5-8. This model effectively describes the dynamic modulus of damaged asphalt layers across a full frequency range.

$$\log(E^*) = \delta + \frac{\alpha(1-\omega)}{1+e^{[\beta+\gamma\log(f_r)]}} \tag{5-8}$$

This model incorporates a damage variable, ω. When ω=0, $E^*=E_0$, making Equation 5-8 analogous to Equation 5-6. When $E^*=E_{\min}=10^{\delta}$ representing the low-frequency asymptotic value

of the asphalt mixture's dynamic modulus. From this model, this study derived a new frequency correction coefficient, K_ω, for the seismic modulus of damaged asphalt layers:

$$K = E_S/E_D^* = 10^{\frac{\alpha}{1+e^{[\beta+\gamma\log(f_{r1})]}} - \frac{\alpha}{1+e^{[\beta+\gamma\log(f_{r2})]}}} \quad 5\text{-}9$$

$$K_\omega = E_S'/E_D^{*\prime} = 10^{(1-\omega)\left[\frac{\alpha}{1+e^{[\beta+\gamma\log(f_{r1})]}} - \frac{\alpha}{1+e^{[\beta+\gamma\log(f_{r2})]}}\right]} = K^{(1-\omega)} \quad 5\text{-}10$$

and

$$\omega = \frac{\ln\left(E_0/E_S'\right)}{\ln\left(E_0/E_{\min}\right)} \quad 5\text{-}11$$

where E_S' is the seismic modulus of the damaged asphalt layer at the target temperature; E_0 is the seismic modulus of the undamaged asphalt layer at the target temperature; $E_D^{*\prime}$ is the modulus value at the design frequency on the damaged layer's modulus master curve at the same temperature; and $E_{\min}$ is the low-frequency asymptotic value of the modulus master curve at the same temperature.

The proposed frequency correction method for the seismic modulus of damaged asphalt layers involves a multi-step process:

(1) Establish the modulus master curve for undamaged asphalt mixtures at different test temperatures T_R, ranging from -10 °C to 54.4 °C, using results from laboratory uniaxial compression dynamic modulus tests.

(2) Use the modulus master curve to calculate $E_{\min}$ and E_D^*, the modulus value of undamaged asphalt layers at temperature T_R corresponding to the design frequency.

(3) Adjust the measured seismic modulus of undamaged asphalt layers to temperature T_R, yielding E_S.

(4) Apply E_S and E_D^* in Equation 5-7 to compute the frequency correction coefficient K at temperature T_R.

(5) Formulate the relationship between K and test temperature T_R to ascertain the frequency correction coefficient K at the target temperature.

(6) Correct the measured seismic moduli of both undamaged and damaged asphalt layers to the target temperature, obtaining E_0 and E_S'.

(7) Utilize Equation 5-11 to calculate the damage variable ω.

(8) Employ Equation 5-10 to determine the frequency correction coefficient K_ω for the damaged asphalt layer.

(9) Divide the corrected seismic modulus of the damaged asphalt layer E_S' at the target temperature by K_ω to determine the modulus value at the design frequency.

This approach enables a precise adjustment of asphalt layer modulus values, considering both undamaged and damaged conditions, across varying frequencies and temperatures.

5.2.3.3 Validation of the Modified Frequency Adjustment Factor

In this phase of the research, the developed seismic modulus correction method was applied to the PSPA test results at the center of the wheel paths in Section I. These corrected moduli were then used in a finite element model to calculate theoretical values of strain response within the asphalt layer. This calculation aimed to validate the method's effectiveness by comparing the calculated theoretical strain responses within the asphalt layer with actual measurements.

The first step involved obtaining real strain response values. During the F-sAPTs, strain data were collected at depths of 12 cm and 24 cm in the longitudinal direction (aligned with axle load movement) and at 24 cm in the transverse direction (perpendicular to axle load movement) in Section I. Table 5-5 presents the variations in the measured tensile strain peaks.

Table 5-5 Variation in peak tensile strain and axial load frequency

Load (x1000)	Temp. (°C)	Longitudinal (12 cm)		Longitudinal (24 cm)		Transverse (24 cm)	
		ε_t (με)	f (Hz)	ε_t (με)	f (Hz)	ε_t (με)	f (Hz)
520	21.25	29.00	2.65	-	-	10.17	3.73
570	20.94	24.00	2.86	13.83	5.00	9.92	5.00
625	21.03	27.00	2.63	13.75	4.55	10.33	5.56
680	20.71	24.00	2.78	11.33	4.55	8.33	5.00
735	21.75	30.00	2.78	13.67	4.55	10.42	5.00
795	22.83	31.00	2.94	15.17	4.55	10.58	5.00
850	23.42	34.00	2.50	15.67	4.17	12.00	5.56
910	24.00	38.00	2.63	18.33	4.17	13.33	5.00
970	22.79	40.00	2.38	19.00	4.17	13.80	5.00
1020	15.32	22.00	2.38	9.00	4.17	6.33	5.00
1070	15.70	21.00	2.50	9.67	4.17	6.67	4.55
1112	15.96	21.00	2.50	9.83	4.17	7.50	4.17
1162	16.81	20.00	2.38	9.83	4.17	7.17	4.17
1210	17.11	22.00	2.50	10.83	4.17	7.50	5.00
1260	17.38	21.00	2.17	11.17	3.85	7.83	4.55
1310	17.89	23.00	2.50	11.33	3.85	8.00	4.17
1360	18.47	23.00	2.50	12.17	3.57	8.67	3.85
1410	18.80	25.00	2.50	12.33	3.33	8.17	3.85

Load (x1000)	Temp. (°C)	Longitudinal (12 cm)		Longitudinal (24 cm)		Transverse (24 cm)	
		ε_t (με)	f (Hz)	ε_t (με)	f (Hz)	ε_t (με)	f (Hz)
1445	18.66	24.00	2.50	12.83	3.85	9.00	4.55
1490	19.44	23.00	2.38	12.00	3.85	8.67	4.55
1540	19.44	25.00	2.27	13.83	4.17	9.67	4.55
1595	19.16	24.00	2.38	13.17	3.57	10.17	4.17
1645	18.99	22.00	2.50	12.67	3.13	8.83	4.17
1695	18.29	24.00	2.50	12.50	3.85	10.67	3.85
1745	17.22	22.00	2.50	12.50	3.33	9.50	3.33
1790	16.37	24.00	2.63	12.33	3.13	8.83	3.13
1830	13.41	20.00	2.27	8.33	2.94	5.33	3.13
1880	14.62	26.00	2.50	9.50	3.13	6.17	2.94
1930	15.79	31.00	2.63	12.50	3.13	7.83	2.94
2000	15.01	20.65	2.22	14.00	2.26	7.50	2.26
2050	23.35	39.97	3.13	12.50	3.13	8.83	3.57
2150	23.03	36.94	2.50	16.83	2.94	12.50	4.17
2250	21.96	34.11	2.50	17.50	3.13	12.00	4.17
2360	24.68	-	-	15.00	3.13	9.17	4.17
2500	30.23	53.83	2.78	26.33	3.57	16.50	4.17
2650	28.38	-	-	17.17	3.33	10.17	3.33
2750	28.66	58.65	2.63	24.83	3.33	13.17	3.33
2850	29.75	52.13	2.50	24.17	2.94	15.50	3.33
2950	30.30	80.50	2.94	40.17	3.57	21.67	3.33
3000	27.27	58.50	2.63	32.83	3.33	17.67	2.63

The study then focused on determining the design frequency. Based on the approach outlined in Figure 5-21 and Equation 5-12, the variation in axle load frequency during the testing phase was calculated, as shown in Table 5-5.

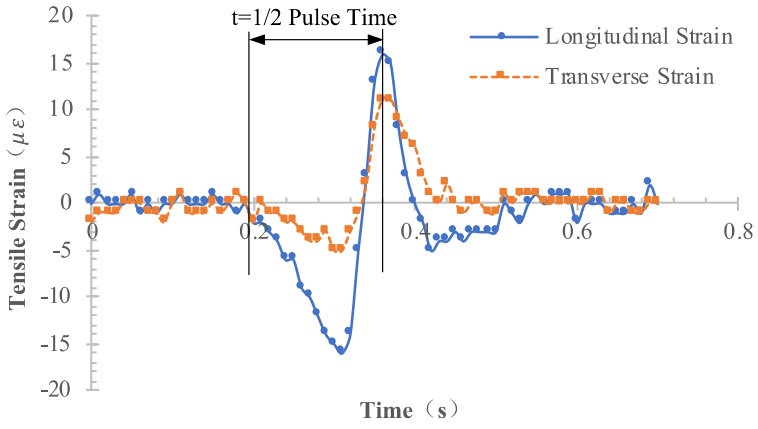

Figure 5-21 Determination of axial load frequency

$$f_{\text{axle}} = \frac{1}{2t} \quad 5\text{-}12$$

where f_{axle} represents axle load frequency (Hz), and t is half the pulse time (s). This approach was designed to address issues arising from asymmetric strain waveforms. The axle load frequency during the test ranged between 2.17 Hz and 5.56 Hz, with the study adopting an average value of 3.22 Hz as the design frequency for the frequency correction of the seismic modulus in damaged asphalt layers.

Subsequent steps involved frequency correction of PSPA test results from the center of the wheel paths in Section I:

(1) Establish the modulus master curve for the undamaged asphalt mixture at different test temperatures T_R, as shown in Equation 5-6 and Table 5-4.

(2) Using these modulus master curves, $E_{\min}$ (6.32 MPa) and the modulus value E_D^* corresponding to the design frequency of 3.22 Hz at different temperatures T_R were calculated.

(3) The measured average seismic modulus of undamaged asphalt layers in non-loaded areas was adjusted to each test temperature T_R, resulting in E_S.

(4) E_S and E_D^* were inserted into Equation 5-7 to calculate the frequency correction coefficient K at each temperature T_R, detailed in Table 5-6.

Table 5-6 Frequency adjustment factor K at various temperatures

Targeted Temperature (°C)	K
-10.0	1.2724
4.4	1.7823
21.1	3.7667
37.8	9.9894
54.4	19.8608

(5) The relationship between K and temperature T_R, was established, as shown in Figure 5-22 and Equation 5-11. The study selected the average asphalt layer temperature during each strain measurement in Table 5-5 as the target temperatures and computed 40 frequency correction factors K for each target temperature.

(6) The seismic moduli of both undamaged and damaged asphalt layers were corrected to the target temperatures, yielding 40 sets of E_0 and $E_S{}'$.

(7) The damage variable ω was calculated for each strain measurement using Equation 5-11.

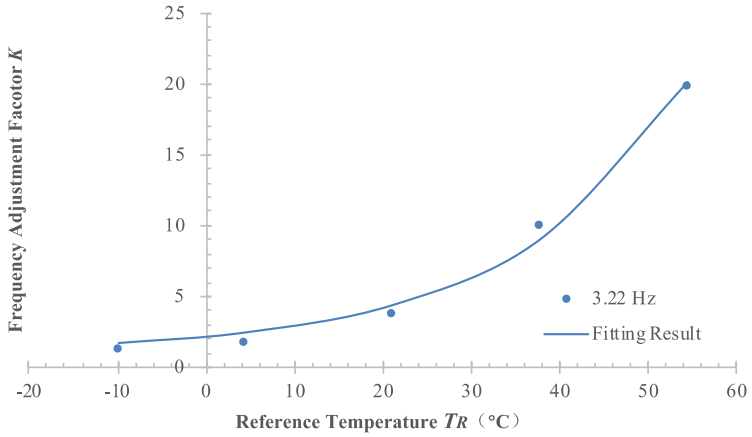

Figure 5-22 Relationship between K and reference temperature

$$K = 1 + 1.1186 * e^{0.0522T_R} \quad 5\text{-}13$$

(8) The frequency correction coefficient K_ω for damaged asphalt layers was determined for each strain measurement using Equation 5-10.

(9) The temperature-adjusted seismic wave modulus of damaged asphalt layers $E_S{}'$ was divided by the corresponding K_ω to obtain the modulus value at the design frequency.

Finally, the corrected seismic modulus results for damaged asphalt layers at the center of the wheel paths of Section I were integrated into a finite element model to analyze the variations in tensile strain within the asphalt layer. The model, based on ABAQUS software and illustrated in Figure 5-23, was meticulously designed. To ensure a balance between accuracy and computational efficiency, the model dimensions were set to 6.37 m in depth, 6 m in width, and 9 m in length. To minimize boundary effects and oscillations in results, a 0.5 m thick layer of infinite elements was implemented around and beneath the model, resulting in final dimensions of 6.85 m deep, 7 m wide, and 10 m long.

In the planar direction of the model, the length of the wheel load's loading area was set to 4 m. The contact area and pressure of the load were set according to the parameters in Table 5-1. A denser mesh was used in the loading area, with mesh sizes of 0.044 m × 0.015 m × 0.088 m, and the mesh density was gradually reduced in directions away from the loading zone to improve computational efficiency. Then, a dynamic implicit solution was used with a distributed tire-contact pressure applied over a translating footprint equivalent, yielding a quasi-moving passage within the trimmed domain. Inertial terms were retained; explicit rolling contact was not modeled.

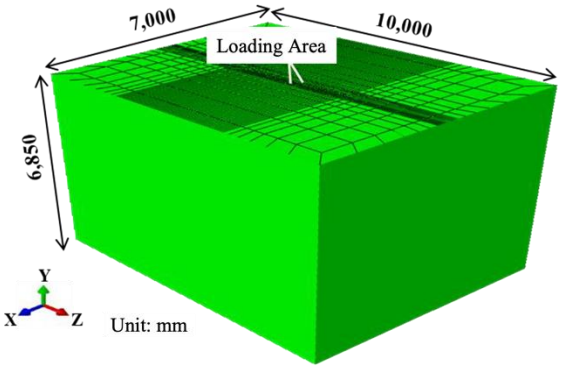

(a) 3D model

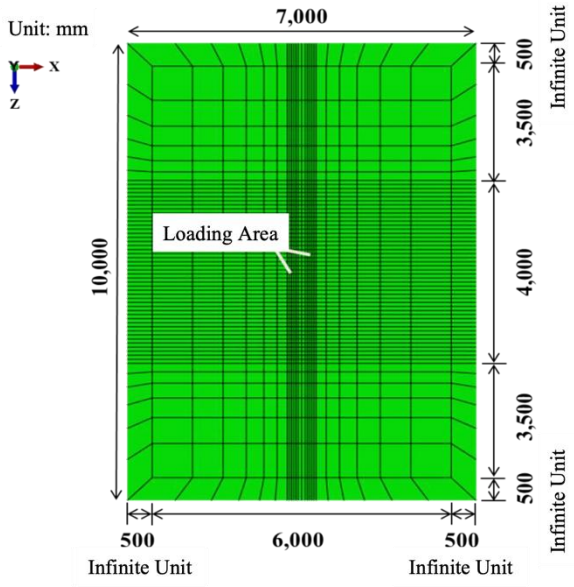

(b) Plan view of the model

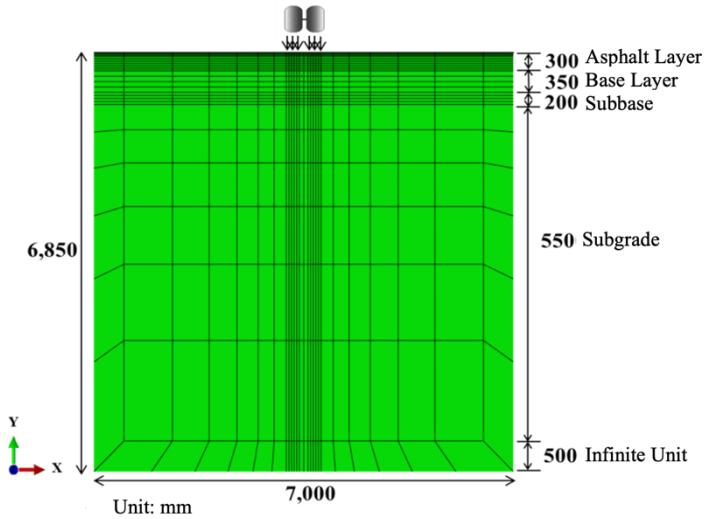

(c) Cross-sectional view of the model

Figure 5-23 Configuration of the finite element model

For the model's depth, the subgrade was set to a thickness of 5.5 m, matching the actual structural layer thicknesses in Sections I and II and assuming full continuity between layers. The asphalt layer was divided into 30 sub-layers of 1 cm each, the base layer into 5 sub-layers of 7 cm each, the sub-base layer into 4 sub-layers of 5 cm each, and the subgrade into 6 progressively thicker sub-layers. The model used C3D8J finite elements, CIN3D8 infinite elements, and a dynamic implicit algorithm.

Regarding mechanical parameters, the asphalt layer modulus was based on the corrected seismic modulus results for damaged layers at the center of the wheel paths of Section II, while the base layer and subgrade modulus values were taken from inversion analysis of FWD test results on the base layer surface.

Using this finite element model, this study calculated peak tensile strains at 12 cm and 24 cm depths in the longitudinal direction and at 24 cm depth in the transverse direction. These theoretical values were compared with the uncorrected measured peak tensile strains from Table 5-5, as displayed in Figure 5-24.

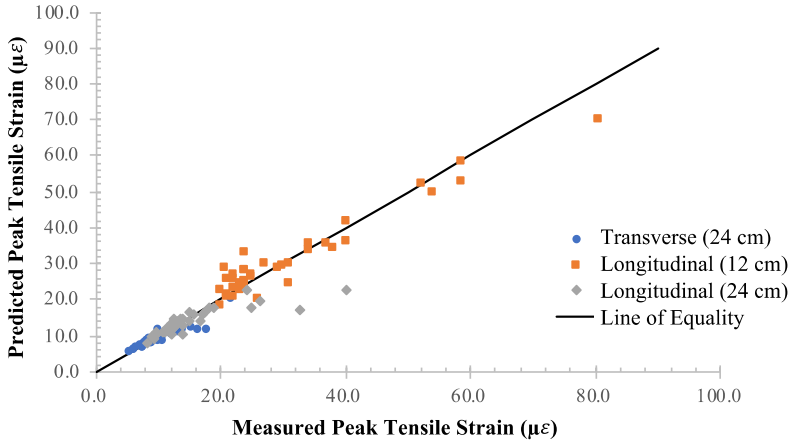

Figure 5-24 Comparisons between predicted and measured peak tensile strains

The finite element model results closely aligned with the measured peak tensile strains. The percentage differences between these theoretical and measured peak strains were calculated using Equation 5-14, with an average difference of 9.39% across different depths.

$$PV = \frac{|\varepsilon_c - \varepsilon_M|}{\varepsilon_M} \times 100\% \qquad 5\text{-}14$$

where PV (%) represents the percentage difference, ε_c is the peak tensile strain calculated by the finite element model (με), and ε_M is the measured peak tensile strain in the pavement structure (με).

This study also conducted calculations using the finite element model with uncorrected seismic modulus values. The average percentage difference between these calculations and the measured peak strains was a significant 84.04%. This substantial difference further affirmed the rationality of the frequency correction method and coefficient K_ω for the modulus of damaged asphalt layers.

5.3 Predictions of In-situ Fatigue Damage Processes

5.3.1 Fatigue Damage Progressions of Asphalt Layer

Building upon the insights gained in § 5.2, this research successfully acquired both the initial seismic moduli (representative of undamaged asphalt layers) and the seismic moduli under various damage states (representative of damaged asphalt layers) for each test section. By adjusting these moduli to a standard temperature of 20 °C and utilizing the stiffness reduction rate SRR defined in Equation 4-15, the study was able to effectively trace the fatigue damage evolution within the asphalt layers.

Taking Point 2, located at the center of the wheel paths, as an example, Figure 5-25 and Figure 5-26 graphically depict the degradation of the seismic modulus and the progression of fatigue damage in the asphalt layers during the F-sAPTs.

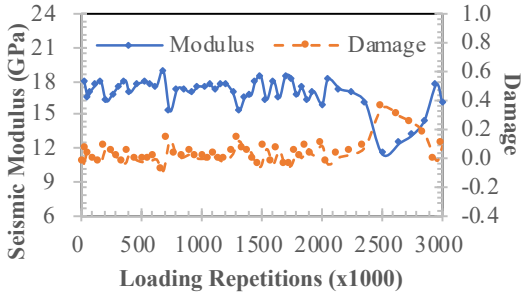

(a) Transverse direction - 7.5 cm

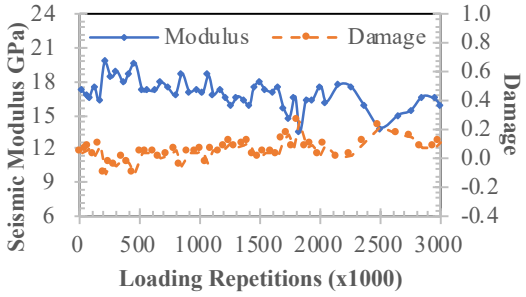

(b) Longitudinal direction – 7.5 cm

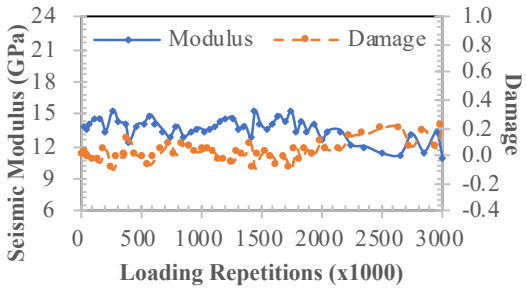

(c) Transverse direction - 17.5 cm

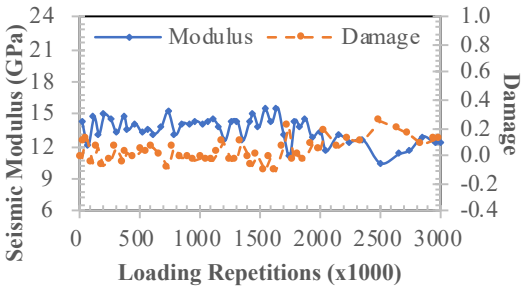

(d) Longitudinal direction – 17.5 cm

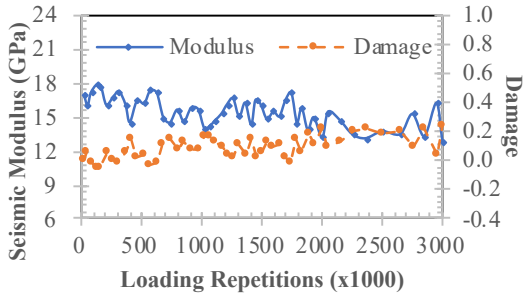

(e) Transverse direction - 27.5 cm

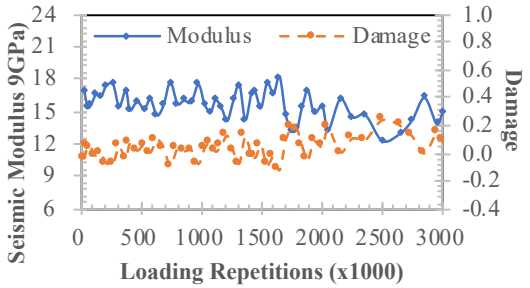

(f) Longitudinal direction – 27.5 cm

Figure 5-25 Fatigue damage progressions of asphalt layers in Section I

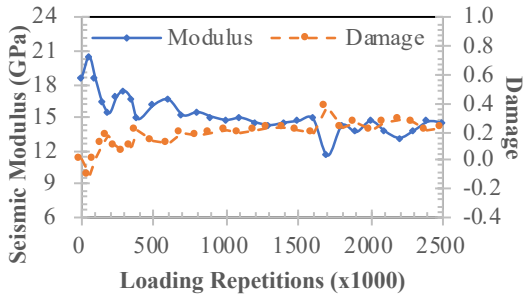

(a) Transverse direction - 7.5 cm

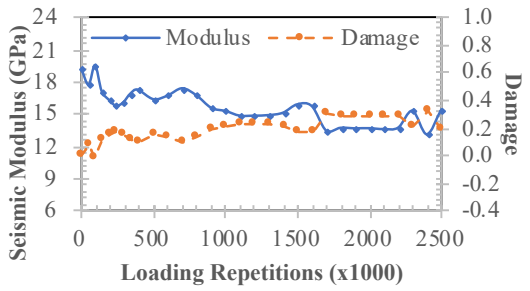

(b) Longitudinal direction – 7.5 cm

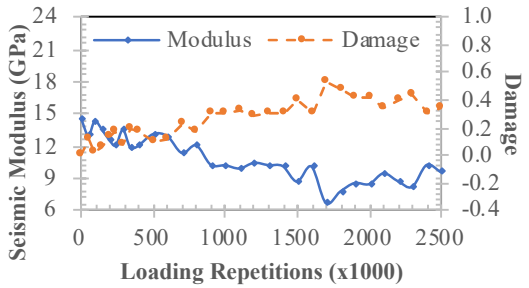

(c) Transverse direction - 17.5 cm

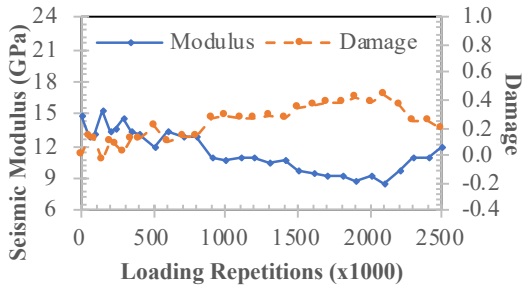

(d) Longitudinal direction – 17.5 cm

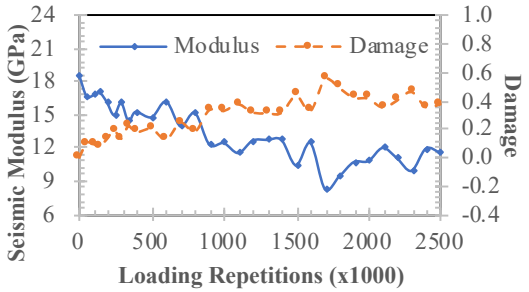

(e) Transverse direction - 27.5 cm

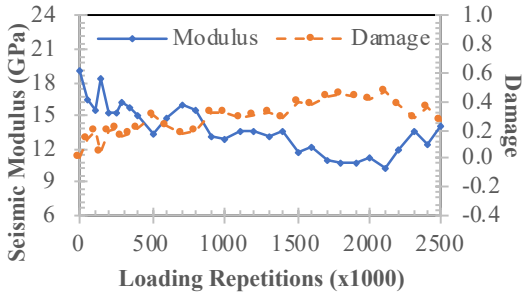

(f) Longitudinal direction – 27.5 cm

Figure 5-26 Fatigue damage progressions of asphalt layers in Section II

These figures reveal that the evolution of damage within the asphalt layers exhibit a distinctly nonlinear character. Notably, the patterns of damage progression are found to vary significantly across different depths, positions, and orientations within the pavement structure, highlighting the necessity for a more nuanced and comprehensive analysis.

Further, Figure 5-27 and Figure 5-28 provides a visual representation of the depth-wise distribution of damage within the asphalt layers at the conclusion of the F-sAPTs. The observed distribution patterns of damage quantity within the asphalt layers proved to be intricate and varied, negating the possibility of making broad generalizations. This observation underscores the need for additional research focused on understanding the depth-wise distribution patterns of damage in asphalt layers and identifying the key factors influencing these patterns.

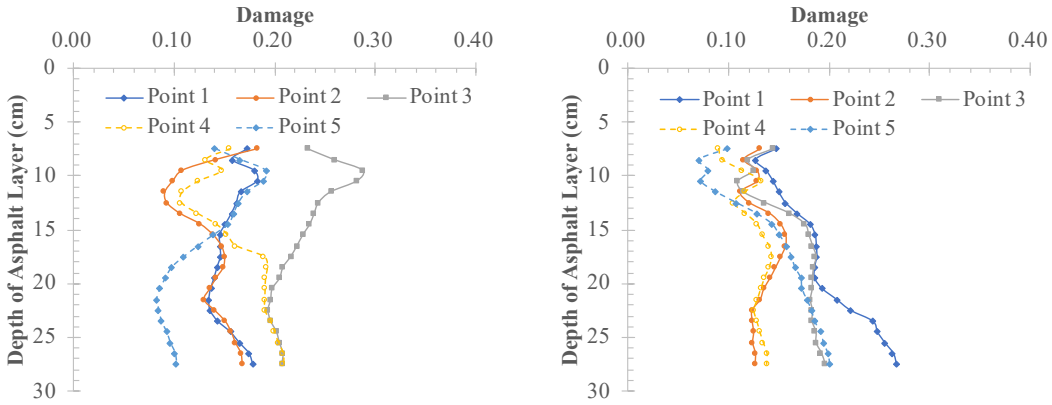

(a) Transverse direction (b) Longitudinal direction

Figure 5-27 Accumulated fatigue damage of asphalt layers in Section I

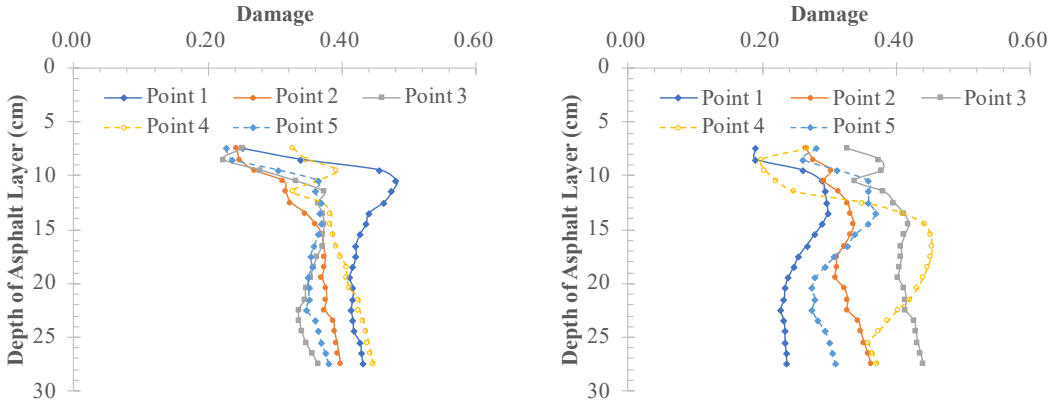

(a) Transverse direction (b) Longitudinal direction

Figure 5-28 Accumulated fatigue damage of asphalt layers in Section II

5.3.2 Comparative Analysis of Different Models

Based on the analysis in §4.3, which compared seven nonlinear damage evolution models, it was determined that only the Weibull survival function (WSF) and the structural behavior function (SBF) adequately met all the criteria set out in §3.1.2. Furthermore, these models were found to be

applicable across different fatigue loading patterns. Consequently, this research focused on utilizing these two models to model the fatigue damage evolution in the asphalt layers. The aim was to assess their feasibility and perform a comparative analysis of their rationality and effectiveness in fitting the data. This analysis was crucial in identifying the most appropriate model for accurately describing the fatigue damage progression in the asphalt layers.

5.3.2.1 Fitting Results of WSF

The WSF is defined as shown in Equation 5-15.

$$D = \mathrm{SRR} = 1 - \exp(-\lambda N^{\gamma}) \quad \text{5-15}$$

where N is the loading repetitions (x1000), λ and γ are model parameters.

Utilizing this model, this study carried out a comprehensive fitting analysis of the damage progression at various depths, testing points, and directions in the asphalt layers of Sections I and II. This extensive analysis resulted in the creation of 420 regression models. The outcomes of these regression analyses, including the regression results for each parameter and the coefficient of determination (R^2), are detailed in Table 5-7 to Table 5-12.

Table 5-7 Derived λ of Section I

Depth (cm)	Point 1		Point 2		Point 3		Point 4		Point 5	
	Transverse	Longitudinal	Transverse	Longitudinal	Transverse	Longitudinal	Transverse	Longitudinal	Transverse	Longitudinal
7.5	1.58E-05	2.55E-05	3.51E-10	8.18E-08	1.52E-08	8.69E-09	5.43E-09	3.46E-03	1.88E-09	1.54E-09
8.5	8.58E-06	3.16E-05	2.49E-09	5.23E-08	1.88E-09	6.30E-09	1.82E-08	4.79E-04	1.77E-09	5.84E-10
9.5	1.38E-05	1.94E-05	6.52E-05	1.92E-08	1.05E-09	1.22E-09	2.01E-05	1.09E-03	1.39E-09	8.19E-10
10.5	3.63E-05	9.34E-06	9.06E-05	3.45E-08	2.13E-08	8.67E-09	4.32E-06	7.55E-04	1.94E-09	1.81E-09
11.5	4.67E-05	3.32E-05	9.15E-06	1.54E-08	3.55E-09	8.78E-09	4.65E-07	1.43E-05	8.49E-10	1.94E-09
12.5	1.81E-05	1.98E-05	2.70E-06	5.79E-09	2.65E-09	2.51E-09	3.20E-08	1.05E-08	1.05E-09	1.55E-09
13.5	3.92E-05	5.26E-05	3.41E-09	5.73E-09	2.77E-09	2.01E-09	9.66E-09	1.28E-07	1.15E-09	2.89E-09
14.5	6.45E-05	2.88E-05	8.91E-10	4.56E-09	2.30E-09	8.03E-09	9.34E-09	3.86E-07	1.41E-09	3.29E-09
15.5	7.47E-05	2.57E-05	3.27E-08	1.73E-08	1.58E-09	7.53E-09	4.64E-08	6.83E-07	1.77E-09	3.64E-09
16.5	1.65E-04	1.33E-04	2.27E-09	2.99E-09	7.20E-09	4.44E-09	2.75E-07	3.51E-06	2.67E-09	3.91E-09
17.5	1.45E-04	6.04E-05	5.26E-09	2.10E-09	2.06E-08	5.53E-09	1.31E-05	3.23E-05	5.90E-09	1.65E-08
18.5	4.88E-04	4.69E-04	5.53E-09	3.28E-09	6.35E-08	5.05E-09	6.96E-05	1.23E-04	1.39E-08	1.53E-07
19.5	1.12E-04	7.20E-05	4.06E-08	5.26E-08	4.85E-07	4.80E-09	2.17E-04	4.30E-04	1.60E-07	5.69E-07
20.5	1.35E-06	6.44E-04	3.61E-08	5.76E-09	3.60E-06	6.70E-09	6.27E-04	9.94E-04	1.22E-06	3.05E-06
21.5	2.48E-04	5.04E-04	7.95E-07	8.69E-08	1.05E-05	7.16E-09	9.81E-04	1.64E-03	9.19E-06	8.24E-06
22.5	3.94E-04	4.81E-03	1.35E-05	5.74E-08	2.44E-05	1.07E-08	1.55E-03	3.90E-03	2.98E-05	1.64E-05
23.5	8.81E-04	3.65E-04	6.32E-05	3.17E-08	7.43E-05	3.26E-08	3.13E-03	5.02E-03	5.63E-05	3.85E-05
24.5	4.15E-03	1.04E-02	1.22E-04	8.03E-08	1.03E-04	9.42E-09	4.35E-03	6.57E-03	7.70E-05	5.13E-05
25.5	3.67E-03	1.88E-02	3.71E-04	2.64E-07	1.57E-04	9.64E-08	5.31E-03	1.01E-02	1.25E-04	7.96E-05
26.5	5.04E-03	1.86E-02	3.51E-04	2.69E-07	2.32E-04	1.13E-07	7.17E-03	1.13E-02	1.34E-04	1.09E-04
27.5	5.77E-03	2.06E-02	6.38E-04	3.80E-07	2.08E-04	9.73E-08	7.94E-03	1.07E-02	1.39E-04	1.21E-04

Table 5-8 Derived γ of Section I

Depth (cm)	Point 1		Point 2		Point 3		Point 4		Point 5	
	Transverse	Longitudinal	Transverse	Longitudinal	Transverse	Longitudinal	Transverse	Longitudinal	Transverse	Longitudinal
7.5	1.17	1.06	2.51	1.42	2.07	2.06	2.15	0.43	2.27	2.24
8.5	1.20	1.01	2.22	1.46	2.35	1.33	1.97	0.68	2.30	2.27
9.5	1.18	1.09	1.51	1.59	2.45	1.27	1.11	0.61	2.05	2.28
10.5	1.08	1.19	1.46	1.43	1.97	1.10	1.28	0.67	2.31	1.80
11.5	1.03	0.84	1.63	1.70	2.28	1.77	1.55	1.14	2.39	2.22
12.5	1.16	1.11	1.80	2.11	2.31	1.95	1.88	2.03	2.37	2.27
13.5	1.06	1.09	2.16	2.33	2.30	2.31	2.05	1.73	2.36	2.52
14.5	0.99	1.10	2.35	2.17	2.32	2.04	2.08	1.61	2.33	2.22
15.5	0.97	1.01	2.01	2.01	2.36	2.05	1.89	1.54	2.29	2.21
16.5	0.88	0.92	2.17	2.03	2.17	2.01	1.68	1.34	2.23	2.21
17.5	0.90	0.93	1.96	2.08	2.04	1.99	1.20	1.07	2.12	2.04
18.5	0.75	0.77	1.96	2.02	1.90	1.80	0.99	0.90	2.00	1.76
19.5	0.83	0.71	1.70	1.87	1.64	1.81	0.85	0.74	1.69	1.59
20.5	0.70	0.74	1.62	1.94	1.38	1.76	0.72	0.64	1.43	1.38
21.5	0.55	0.67	1.44	1.89	1.25	1.76	0.67	0.58	1.17	1.26
22.5	0.57	0.50	1.18	1.84	1.14	1.60	0.61	0.48	1.03	1.18
23.5	0.57	0.52	0.99	1.81	1.00	1.56	0.53	0.45	0.96	1.07
24.5	0.59	0.42	0.91	1.70	0.97	1.42	0.50	0.43	0.92	1.04
25.5	0.51	0.36	0.78	1.65	0.92	1.32	0.48	0.38	0.87	0.99
26.5	0.48	0.36	0.79	1.55	0.87	1.20	0.44	0.37	0.86	0.95
27.5	0.46	0.35	0.72	1.51	0.88	1.12	0.43	0.38	0.86	0.94

Table 5-9 Derived R^2 of Section I

Depth (cm)	Point 1		Point 2		Point 3		Point 4		Point 5	
	Transverse	Longitudinal	Transverse	Longitudinal	Transverse	Longitudinal	Transverse	Longitudinal	Transverse	Longitudinal
7.5	0.66	0.64	0.61	0.71	0.79	0.64	0.62	0.66	0.64	0.64
8.5	0.60	0.69	0.63	0.61	0.80	0.64	0.64	0.62	0.60	0.66
9.5	0.79	0.66	0.63	0.63	0.89	0.68	0.69	0.75	0.75	0.69
10.5	0.89	0.66	0.63	0.70	0.92	0.66	0.60	0.84	0.77	0.61
11.5	0.85	0.66	0.66	0.69	0.97	0.60	0.68	0.81	0.70	0.69
12.5	0.82	0.71	0.65	0.74	0.98	0.70	0.59	0.84	0.72	0.70
13.5	0.81	0.72	0.63	0.79	0.99	0.81	0.63	0.90	0.76	0.79
14.5	0.77	0.76	0.69	0.79	0.95	0.86	0.66	0.91	0.73	0.84
15.5	0.72	0.78	0.67	0.74	0.90	0.88	0.66	0.86	0.67	0.84
16.5	0.72	0.78	0.68	0.72	0.86	0.89	0.65	0.83	0.61	0.85
17.5	0.72	0.81	0.69	0.70	0.84	0.91	0.65	0.81	0.67	0.86
18.5	0.70	0.83	0.69	0.69	0.82	0.93	0.64	0.78	0.63	0.84
19.5	0.68	0.85	0.67	0.67	0.80	0.94	0.62	0.77	0.61	0.83
20.5	0.73	0.87	0.67	0.66	0.79	0.95	0.61	0.76	0.60	0.84
21.5	0.64	0.89	0.65	0.64	0.78	0.94	0.60	0.75	0.59	0.84
22.5	0.64	0.91	0.66	0.62	0.78	0.95	0.60	0.76	0.60	0.85
23.5	0.64	0.92	0.67	0.62	0.79	0.94	0.60	0.77	0.61	0.86
24.5	0.65	0.95	0.68	0.63	0.79	0.94	0.60	0.77	0.62	0.87
25.5	0.65	0.96	0.69	0.62	0.79	0.94	0.61	0.78	0.63	0.87
26.5	0.66	0.97	0.70	0.63	0.80	0.94	0.62	0.79	0.64	0.88
27.5	0.65	0.97	0.70	0.62	0.79	0.94	0.62	0.78	0.65	0.88

Table 5-10 Derived λ of Section II

Depth (cm)	Point 1		Point 2		Point 3		Point 4		Point 5	
	Transverse	Longitudinal	Transverse	Longitudinal	Transverse	Longitudinal	Transverse	Longitudinal	Transverse	Longitudinal
7.5	9.22E-04	5.39E-03	1.55E-02	1.09E-02	1.50E-05	9.74E-03	4.98E-02	3.31E-02	6.46E-03	2.69E-02
8.5	6.58E-04	4.70E-03	5.74E-03	1.03E-03	1.44E-05	9.53E-03	4.84E-02	5.81E-03	3.91E-04	1.42E-02
9.5	8.80E-04	2.63E-04	2.59E-03	5.29E-05	7.16E-06	9.78E-03	1.55E-02	1.92E-03	2.98E-04	1.04E-02
10.5	8.83E-04	4.99E-05	1.01E-03	2.76E-05	1.39E-06	1.61E-04	6.47E-04	2.07E-04	6.43E-04	3.04E-03
11.5	1.08E-03	6.42E-05	4.97E-04	8.44E-05	7.50E-07	4.55E-05	6.50E-05	1.35E-04	5.96E-04	1.17E-03
12.5	2.28E-03	1.79E-04	6.50E-04	5.80E-04	7.78E-07	4.32E-05	1.38E-04	2.27E-04	7.99E-04	1.46E-03
13.5	3.58E-03	4.44E-04	1.15E-03	1.10E-03	2.89E-06	1.18E-04	2.51E-04	8.00E-04	1.03E-03	2.32E-03
14.5	5.94E-03	7.55E-04	1.82E-03	2.08E-03	4.04E-06	1.66E-04	5.61E-04	1.84E-03	1.73E-03	2.59E-03
15.5	8.11E-03	1.01E-03	2.42E-03	2.61E-03	3.89E-06	2.94E-04	1.09E-03	2.99E-03	2.42E-03	2.81E-03
16.5	9.21E-03	1.21E-03	2.75E-03	3.22E-03	3.67E-06	3.32E-04	2.77E-03	4.96E-03	3.40E-03	2.93E-03
17.5	1.09E-02	1.59E-03	3.77E-03	3.96E-03	4.29E-06	5.48E-04	6.75E-03	7.98E-03	3.41E-03	3.83E-03
18.5	1.28E-02	2.11E-03	4.80E-03	4.64E-03	5.38E-06	7.92E-04	1.33E-02	9.73E-03	3.92E-03	4.02E-03
19.5	1.24E-02	2.14E-03	5.30E-03	5.27E-03	3.55E-06	1.03E-03	1.69E-02	1.07E-02	3.02E-03	3.53E-03
20.5	1.64E-02	2.38E-03	7.19E-03	6.99E-03	6.65E-06	2.23E-03	2.27E-02	1.11E-02	3.00E-03	3.60E-03
21.5	1.78E-02	2.60E-03	7.29E-03	7.88E-03	8.84E-06	2.95E-03	3.03E-02	9.03E-03	3.31E-03	4.07E-03
22.5	1.74E-02	2.34E-03	7.72E-03	7.99E-03	1.22E-05	3.49E-03	3.32E-02	9.88E-03	3.70E-03	4.32E-03
23.5	1.86E-02	2.52E-03	9.14E-03	7.41E-03	1.29E-05	5.78E-03	3.45E-02	1.05E-02	3.78E-03	5.47E-03
24.5	1.64E-02	2.24E-03	8.09E-03	8.12E-03	1.32E-05	5.68E-03	3.17E-02	1.36E-02	3.38E-03	5.35E-03
25.5	1.86E-02	2.27E-03	8.28E-03	8.15E-03	1.81E-05	6.12E-03	3.23E-02	1.49E-02	3.26E-03	5.52E-03
26.5	1.80E-02	2.22E-03	7.89E-03	8.30E-03	1.81E-05	6.23E-03	3.22E-02	1.48E-02	3.13E-03	5.42E-03
27.5	1.73E-02	2.18E-03	7.59E-03	8.50E-03	1.68E-05	6.29E-03	3.22E-02	1.52E-02	3.53E-03	5.35E-03

Table 5-11 Derived γ of Section II

Depth (cm)	Point 1		Point 2		Point 3		Point 4		Point 5	
	Transverse	Longitudinal	Transverse	Longitudinal	Transverse	Longitudinal	Transverse	Longitudinal	Transverse	Longitudinal
7.5	0.76	0.41	0.40	0.46	0.37	0.30	0.27	0.29	0.48	0.34
8.5	0.85	0.55	0.54	0.74	0.45	0.28	0.28	0.49	0.85	0.41
9.5	0.85	0.93	0.67	1.15	1.40	0.51	0.44	0.65	0.94	0.48
10.5	0.87	1.16	0.80	1.25	1.65	1.04	0.84	0.95	0.86	0.65
11.5	0.85	1.16	0.91	1.12	1.75	1.22	1.14	1.02	0.89	0.79
12.5	0.75	1.04	0.88	0.87	1.76	1.23	1.06	0.99	0.86	0.77
13.5	0.68	0.92	0.81	0.79	1.59	1.11	0.98	0.85	0.83	0.71
14.5	0.60	0.85	0.74	0.71	1.44	1.07	0.88	0.75	0.75	0.69
15.5	0.55	0.81	0.70	0.67	1.45	0.99	0.79	0.69	0.70	0.68
16.5	0.53	0.78	0.68	0.64	1.35	0.97	0.66	0.63	0.65	0.67
17.5	0.51	0.73	0.64	0.61	1.32	0.90	0.54	0.56	0.64	0.62
18.5	0.49	0.69	0.61	0.56	1.39	0.85	0.46	0.53	0.63	0.61
19.5	0.49	0.69	0.59	0.53	1.24	0.81	0.43	0.52	0.66	0.62
20.5	0.45	0.67	0.56	0.47	1.16	0.71	0.40	0.51	0.66	0.62
21.5	0.44	0.66	0.55	0.44	1.12	0.68	0.37	0.54	0.69	0.60
22.5	0.45	0.67	0.55	0.43	1.17	0.66	0.36	0.57	0.72	0.59
23.5	0.44	0.66	0.53	0.39	1.16	0.60	0.35	0.60	0.72	0.57
24.5	0.46	0.68	0.55	0.40	1.12	0.60	0.37	0.65	0.75	0.57
25.5	0.45	0.68	0.54	0.40	1.16	0.59	0.37	0.69	0.77	0.57
26.5	0.45	0.68	0.55	0.41	1.15	0.59	0.37	0.70	0.79	0.58
27.5	0.46	0.69	0.56	0.41	1.16	0.59	0.37	0.70	0.80	0.58

Table 5-12 Derived R^2 of Section II

Depth (cm)	Point 1		Point 2		Point 3		Point 4		Point 5	
	Transverse	Longitudinal	Transverse	Longitudinal	Transverse	Longitudinal	Transverse	Longitudinal	Transverse	Longitudinal
7.5	0.69	0.69	0.73	0.73	0.68	0.74	0.71	0.60	0.67	0.65
8.5	0.84	0.65	0.74	0.75	0.66	0.78	0.81	0.67	0.69	0.68
9.5	0.85	0.67	0.74	0.85	0.71	0.81	0.84	0.73	0.79	0.78
10.5	0.87	0.69	0.75	0.80	0.74	0.81	0.80	0.75	0.80	0.78
11.5	0.89	0.74	0.75	0.79	0.75	0.86	0.78	0.79	0.77	0.79
12.5	0.90	0.76	0.74	0.79	0.78	0.88	0.78	0.87	0.75	0.78
13.5	0.88	0.76	0.78	0.77	0.85	0.90	0.76	0.91	0.75	0.77
14.5	0.86	0.75	0.79	0.76	0.89	0.90	0.74	0.93	0.73	0.74
15.5	0.83	0.73	0.80	0.73	0.88	0.88	0.74	0.93	0.71	0.70
16.5	0.80	0.72	0.81	0.72	0.86	0.86	0.73	0.92	0.69	0.72
17.5	0.78	0.70	0.80	0.72	0.85	0.85	0.71	0.91	0.68	0.73
18.5	0.77	0.69	0.80	0.71	0.85	0.83	0.71	0.92	0.67	0.73
19.5	0.76	0.68	0.79	0.71	0.85	0.82	0.70	0.92	0.64	0.71
20.5	0.76	0.67	0.80	0.71	0.84	0.82	0.71	0.90	0.64	0.69
21.5	0.76	0.66	0.80	0.72	0.84	0.81	0.72	0.89	0.63	0.67
22.5	0.75	0.65	0.80	0.72	0.83	0.81	0.72	0.87	0.63	0.67
23.5	0.75	0.65	0.81	0.73	0.82	0.81	0.72	0.84	0.62	0.67
24.5	0.76	0.66	0.81	0.73	0.82	0.81	0.73	0.83	0.63	0.66
25.5	0.77	0.66	0.81	0.73	0.82	0.81	0.74	0.82	0.63	0.66
26.5	0.78	0.66	0.82	0.74	0.81	0.82	0.75	0.83	0.64	0.67
27.5	0.79	0.65	0.82	0.73	0.81	0.81	0.75	0.83	0.64	0.66

The analysis of R^2, as shown in Table 5-9 and Table 5-12, indicates that the WSF exhibits good fitting effectiveness for modeling the fatigue damage evolution process in the asphalt layers. However, during the study, it was observed that the regression analysis results for the model parameters λ and γ exhibited some instability.

For instance, focusing on the regression analysis results for Point 2 in Section I, it was noted that the damage progression processes at depths of 14.5 cm and 15.5 cm in the direction perpendicular to axle load movement were very similar. Yet, when fitted with the WSF, there was a considerable disparity in the regression results of the model parameters: at a depth of 14.5 cm, λ was calculated as 8.91E-10 and γ as 2.35, whereas at 15.5 cm, λ was 3.27E-08 and γ was 2.01.

5.3.2.2 Fitting Results of SBF

The SBF can be expressed by Equation 5-16:

$$D = \mathrm{SRR} = \exp\left[-\left(\frac{\alpha}{N}\right)^{\beta}\right] \qquad 5\text{-}16$$

where N is the number of loading repetitions (x1000), α is the life factor indicating the number of loading repetitions needed for the damage variable D to reach 0.368, and β is the shape factor primarily influencing the pattern of damage development.

This research utilized the SBF to fit the fatigue damage progression in the asphalt layers, resulting in the creation of 420 regression models. The outcomes of these regression analyses, including the results for each parameter and the coefficient of determination R^2, are detailed in Table 5-13 through Table 5-18.

Table 5-13 Derived α of Section I

Depth (cm)	Point 1		Point 2		Point 3		Point 4		Point 5	
	Transverse	Longitudinal	Transverse	Longitudinal	Transverse	Longitudinal	Transverse	Longitudinal	Transverse	Longitudinal
7.5	3863.71	7586.18	4487.31	13461.62	3507.16	6176.92	4435.91	218607.88	3030.25	4301.79
8.5	4265.38	9180.01	5355.51	13504.39	3260.48	11504.46	4679.72	59696.93	3250.61	5277.00
9.5	5051.16	7684.65	9313.98	9709.61	3158.96	9499.21	17677.21	36857.29	3701.50	6155.87
10.5	5141.20	6654.34	10541.46	12814.62	3209.18	10545.23	12884.59	30356.88	3690.79	7860.02
11.5	5610.26	5238.28	8170.83	8337.31	3385.70	7463.89	10979.56	17170.86	3738.51	6709.30
12.5	6059.58	4854.20	7565.02	6166.60	3470.28	6052.32	6757.16	7114.04	3895.17	5903.53
13.5	6829.00	4848.87	5484.79	5239.39	3535.52	5163.51	5095.33	7929.14	4282.06	5446.96
14.5	7204.27	4956.68	4649.36	4817.65	3609.35	4724.16	4506.30	8644.81	4544.62	5132.61
15.5	7807.90	5164.83	4393.26	4632.15	3774.63	4521.40	4513.53	8812.22	4943.08	5144.70
16.5	8280.23	5448.67	4252.17	4589.76	4026.57	4396.38	5287.51	10840.95	5446.40	5278.12
17.5	8772.12	5792.36	4190.15	4716.46	4453.37	4376.13	12358.23	15037.20	6341.48	5711.93
18.5	9449.56	6503.77	4231.42	4974.42	5015.59	4491.57	14525.76	19778.23	8146.57	6370.06
19.5	10318.89	7611.02	4419.71	5291.75	5556.30	4563.67	17021.33	25936.09	10869.57	6902.84
20.5	11767.14	10341.97	4665.98	5618.39	6345.31	4652.45	19554.52	30351.67	15484.27	7898.44
21.5	12752.65	13274.48	5143.20	5862.55	6939.55	4725.42	20950.69	34638.72	20437.90	8571.59
22.5	15730.79	15374.81	9605.99	6560.27	7721.99	4793.17	22904.83	42036.97	25594.80	9160.62
23.5	19827.96	15608.70	15298.93	6762.53	8635.43	4887.30	22788.21	41047.50	27674.76	9386.34
24.5	22276.77	13746.99	17606.23	6968.19	8797.02	4771.28	23223.52	43192.51	27837.99	9351.41
25.5	26859.12	13173.47	19404.68	7293.77	9524.60	4796.47	23142.08	41501.45	30192.16	9577.79
26.5	28587.17	12178.15	19772.48	7372.37	9746.45	4708.44	22528.89	41086.67	29896.18	9559.45
27.5	30334.04	11917.56	19919.16	7539.13	9977.93	4642.27	22793.40	42063.06	29241.44	9577.31

Table 5-14 Derived β of Section I

Depth (cm)	Point 1		Point 2		Point 3		Point 4		Point 5	
	Transverse	Longitudinal	Transverse	Longitudinal	Transverse	Longitudinal	Transverse	Longitudinal	Transverse	Longitudinal
7.5	1.84	0.78	1.38	0.47	1.97	1.00	1.54	0.20	16.81	1.07
8.5	1.57	0.68	1.21	0.52	2.33	0.58	1.55	0.28	4.38	0.95
9.5	0.99	0.62	0.77	0.62	2.15	0.62	0.42	0.29	1.93	0.74
10.5	0.91	0.84	0.72	0.50	1.98	0.62	0.54	0.30	1.91	0.54
11.5	0.87	1.13	0.89	0.75	1.86	0.81	0.64	0.45	2.00	0.92
12.5	0.81	1.24	0.93	0.99	1.83	0.92	1.00	0.90	1.84	1.08
13.5	0.70	1.18	1.26	1.13	1.76	1.00	1.34	0.76	1.47	1.10
14.5	0.67	1.07	1.49	1.22	1.68	1.07	1.52	0.66	1.31	1.12
15.5	0.63	0.96	1.55	1.27	1.51	1.13	1.42	0.63	1.20	1.07
16.5	0.58	0.86	1.58	1.29	1.29	1.18	1.04	0.52	1.09	1.00
17.5	0.55	0.76	1.57	1.25	1.06	1.18	0.43	0.42	0.94	0.87
18.5	0.51	0.65	1.52	1.16	0.88	1.13	0.37	0.36	0.76	0.75
19.5	0.48	0.55	1.41	1.08	0.76	1.11	0.34	0.31	0.62	0.68
20.5	0.44	0.41	1.29	1.01	0.66	1.07	0.31	0.29	0.50	0.59
21.5	0.42	0.32	1.12	0.98	0.60	1.05	0.29	0.27	0.43	0.54
22.5	0.37	0.26	0.57	0.89	0.54	1.02	0.27	0.25	0.38	0.50
23.5	0.32	0.22	0.40	0.86	0.48	0.99	0.26	0.24	0.36	0.48
24.5	0.29	0.23	0.35	0.83	0.46	1.02	0.25	0.23	0.35	0.47
25.5	0.25	0.22	0.32	0.79	0.42	1.01	0.24	0.23	0.34	0.45
26.5	0.24	0.22	0.31	0.78	0.41	1.02	0.24	0.22	0.33	0.44
27.5	0.23	0.21	0.30	0.76	0.40	1.04	0.24	0.22	0.33	0.43

Table 5-15 Derived R^2 of Section I

Depth (cm)	Point 1		Point 2		Point 3		Point 4		Point 5	
	Transverse	Longitudinal	Transverse	Longitudinal	Transverse	Longitudinal	Transverse	Longitudinal	Transverse	Longitudinal
7.5	0.76	0.82	0.74	0.76	0.86	0.72	0.84	0.79	0.77	0.87
8.5	0.76	0.81	0.71	0.67	0.85	0.67	0.80	0.81	0.76	0.86
9.5	0.89	0.86	0.65	0.63	0.88	0.71	0.85	0.87	0.87	0.76
10.5	0.88	0.80	0.65	0.69	0.88	0.71	0.84	0.90	0.82	0.76
11.5	0.79	0.77	0.70	0.70	0.95	0.81	0.82	0.86	0.80	0.79
12.5	0.79	0.84	0.73	0.77	0.94	0.86	0.82	0.83	0.86	0.85
13.5	0.87	0.83	0.77	0.79	0.91	0.88	0.82	0.79	0.88	0.86
14.5	0.84	0.83	0.77	0.79	0.89	0.89	0.80	0.80	0.90	0.85
15.5	0.81	0.83	0.76	0.79	0.87	0.87	0.78	0.82	0.87	0.85
16.5	0.78	0.82	0.76	0.76	0.85	0.87	0.77	0.82	0.83	0.84
17.5	0.79	0.83	0.77	0.75	0.84	0.87	0.77	0.84	0.81	0.84
18.5	0.77	0.85	0.76	0.74	0.85	0.86	0.75	0.84	0.80	0.82
19.5	0.75	0.87	0.76	0.72	0.86	0.85	0.75	0.83	0.80	0.81
20.5	0.73	0.87	0.75	0.71	0.86	0.84	0.74	0.82	0.80	0.80
21.5	0.72	0.88	0.75	0.69	0.87	0.84	0.74	0.80	0.81	0.81
22.5	0.72	0.88	0.76	0.67	0.87	0.85	0.73	0.80	0.81	0.81
23.5	0.72	0.88	0.76	0.67	0.86	0.84	0.73	0.80	0.82	0.82
24.5	0.73	0.89	0.77	0.67	0.86	0.84	0.73	0.81	0.82	0.83
25.5	0.73	0.89	0.77	0.67	0.86	0.83	0.72	0.81	0.82	0.83
26.5	0.73	0.89	0.77	0.67	0.86	0.83	0.72	0.82	0.83	0.84
27.5	0.73	0.89	0.77	0.67	0.86	0.83	0.72	0.81	0.83	0.84

Table 5-16 Derived α of Section II

Depth (cm)	Point 1		Point 2		Point 3		Point 4		Point 5	
	Transverse	Longitudinal	Transverse	Longitudinal	Transverse	Longitudinal	Transverse	Longitudinal	Transverse	Longitudinal
7.5	4900.80	5959.29	6005.27	8620.88	15548.72	2275.89	4849.49	16674.91	12507.49	6202.11
8.5	2628.04	6100.09	3985.39	5502.26	14157.06	1709.59	3757.60	15092.36	5016.77	6264.30
9.5	1690.70	3642.37	2692.03	2829.21	2959.40	2035.28	2569.00	6787.46	2713.23	3117.10
10.5	1476.58	2764.60	2354.06	2504.58	2250.21	2241.34	2754.70	4172.04	2261.51	2533.17
11.5	1372.09	2247.86	1967.20	2293.35	2003.87	1978.33	2442.70	3278.90	1896.98	2016.01
12.5	1322.96	2019.05	1853.91	2250.39	1896.58	1884.21	2232.72	2415.05	1668.02	1853.63
13.5	1399.27	1964.98	1822.75	2246.76	1859.96	1812.95	2215.64	2035.68	1734.32	1864.15
14.5	1501.03	2011.58	1843.50	2334.77	1892.35	1774.29	2256.24	1788.55	1898.99	1986.64
15.5	1693.30	2145.01	1918.59	2500.44	1909.22	1813.32	2450.20	1697.26	2089.66	2145.25
16.5	1826.43	2328.35	2050.42	2656.85	1938.96	1896.18	2692.02	1670.13	2237.91	2285.19
17.5	1851.24	2522.17	2093.19	2840.70	1996.20	1974.48	3020.05	1583.94	2319.44	2479.92
18.5	1819.49	2675.16	2125.91	2983.47	2041.32	2018.26	2837.22	1508.39	2355.71	2600.27
19.5	1875.96	2864.79	2165.79	3127.99	2079.42	2046.44	2471.04	1503.43	2498.26	2872.15
20.5	1677.97	3018.65	2114.39	3030.86	2127.87	1959.40	2147.73	1483.23	2550.61	3141.47
21.5	1617.28	3010.66	2055.78	2956.69	2160.16	1895.60	1759.06	1598.48	2604.80	3143.57
22.5	1659.00	3115.98	2087.60	3019.01	2238.53	1866.76	1690.96	1784.47	2667.23	3232.78
23.5	1547.87	3087.47	1953.19	2621.67	2244.64	1663.61	1546.58	1830.74	2572.36	2855.87
24.5	1542.98	3007.57	1933.75	2609.39	2233.03	1656.16	1519.43	1960.11	2530.47	2796.49
25.5	1418.97	2948.32	1891.04	2493.09	2219.38	1592.12	1441.07	2013.73	2472.78	2708.08
26.5	1391.84	2860.02	1860.67	2442.79	2188.46	1550.35	1387.44	1940.47	2406.68	2615.25
27.5	1370.39	2785.33	1832.95	2389.75	2160.61	1511.46	1338.11	1876.84	2348.71	2536.46

Table 5-17 Derived β of Section II

Depth (cm)	Point 1		Point 2		Point 3		Point 4		Point 5	
	Transverse	Longitudinal	Transverse	Longitudinal	Transverse	Longitudinal	Transverse	Longitudinal	Transverse	Longitudinal
7.5	0.40	0.23	0.23	0.24	0.18	0.20	0.16	0.15	0.25	0.20
8.5	0.53	0.29	0.30	0.37	0.21	0.20	0.17	0.23	0.49	0.23
9.5	0.70	0.55	0.39	0.73	0.87	0.31	0.28	0.32	0.61	0.30
10.5	0.72	0.74	0.52	0.80	1.12	0.73	0.57	0.54	0.62	0.44
11.5	0.70	0.78	0.65	0.77	1.35	0.96	0.75	0.59	0.67	0.58
12.5	0.61	0.75	0.65	0.63	1.28	0.97	0.75	0.68	0.70	0.58
13.5	0.54	0.68	0.60	0.59	1.18	0.86	0.73	0.65	0.67	0.56
14.5	0.47	0.62	0.55	0.54	1.08	0.81	0.68	0.60	0.58	0.54
15.5	0.42	0.57	0.52	0.51	1.06	0.75	0.63	0.56	0.50	0.51
16.5	0.39	0.53	0.50	0.48	1.05	0.71	0.59	0.50	0.44	0.49
17.5	0.37	0.48	0.47	0.45	1.04	0.65	0.52	0.41	0.41	0.44
18.5	0.34	0.44	0.44	0.41	1.04	0.60	0.31	0.37	0.40	0.42
19.5	0.34	0.42	0.43	0.37	1.02	0.56	0.26	0.36	0.42	0.42
20.5	0.31	0.41	0.40	0.32	0.99	0.49	0.25	0.34	0.43	0.40
21.5	0.31	0.40	0.39	0.29	0.98	0.46	0.23	0.35	0.45	0.39
22.5	0.31	0.40	0.39	0.28	0.96	0.43	0.23	0.36	0.49	0.38
23.5	0.30	0.39	0.37	0.25	0.95	0.40	0.23	0.38	0.51	0.37
24.5	0.31	0.40	0.39	0.26	0.95	0.40	0.24	0.40	0.54	0.37
25.5	0.31	0.40	0.40	0.26	0.96	0.40	0.24	0.42	0.55	0.37
26.5	0.32	0.41	0.40	0.27	0.98	0.40	0.25	0.43	0.57	0.38
27.5	0.32	0.41	0.41	0.27	0.99	0.41	0.25	0.43	0.58	0.38

Table 5-18 Derived R^2 of Section II

Depth (cm)	Point 1		Point 2		Point 3		Point 4		Point 5	
	Transverse	Longitudinal	Transverse	Longitudinal	Transverse	Longitudinal	Transverse	Longitudinal	Transverse	Longitudinal
7.5	0.68	0.68	0.74	0.72	0.63	0.76	0.69	0.59	0.64	0.65
8.5	0.83	0.63	0.76	0.74	0.61	0.78	0.79	0.67	0.69	0.68
9.5	0.86	0.66	0.76	0.85	0.71	0.80	0.82	0.73	0.81	0.79
10.5	0.88	0.71	0.76	0.82	0.76	0.79	0.80	0.76	0.81	0.79
11.5	0.91	0.77	0.77	0.81	0.77	0.86	0.80	0.79	0.80	0.81
12.5	0.92	0.79	0.77	0.81	0.81	0.89	0.80	0.88	0.78	0.80
13.5	0.89	0.78	0.80	0.79	0.87	0.90	0.79	0.92	0.76	0.79
14.5	0.86	0.77	0.81	0.78	0.91	0.90	0.76	0.93	0.73	0.76
15.5	0.82	0.75	0.82	0.74	0.90	0.88	0.74	0.93	0.70	0.73
16.5	0.79	0.73	0.81	0.73	0.89	0.86	0.73	0.91	0.68	0.74
17.5	0.77	0.71	0.80	0.73	0.88	0.84	0.68	0.90	0.67	0.76
18.5	0.76	0.70	0.80	0.72	0.87	0.81	0.67	0.90	0.66	0.75
19.5	0.75	0.68	0.79	0.71	0.87	0.80	0.66	0.91	0.63	0.73
20.5	0.75	0.67	0.79	0.70	0.86	0.80	0.68	0.90	0.63	0.70
21.5	0.75	0.66	0.80	0.70	0.85	0.79	0.69	0.88	0.62	0.68
22.5	0.75	0.65	0.80	0.71	0.84	0.79	0.69	0.86	0.62	0.67
23.5	0.75	0.65	0.80	0.71	0.82	0.79	0.70	0.84	0.62	0.68
24.5	0.76	0.65	0.80	0.71	0.82	0.79	0.71	0.83	0.62	0.67
25.5	0.77	0.65	0.81	0.72	0.81	0.80	0.72	0.82	0.62	0.67
26.5	0.78	0.66	0.81	0.72	0.81	0.80	0.72	0.82	0.63	0.67
27.5	0.79	0.66	0.82	0.72	0.80	0.81	0.73	0.83	0.64	0.68

An analysis of R^2, as shown in Table 5-15 and Table 5-18, reveals that the SBF effectively fits the fatigue damage evolution in the asphalt layers. Moreover, the regression analysis results for the model parameters α and β were found to be considerably more stable than those for the λ and γ in the WSF. For example, when the SBF was applied to fit the two damage processes at depths of 14.5 cm and 15.5 cm at Point 2 in the transverse direction of Section I, the parameters at a depth of 14.5 cm were found to be α=4649.36 and β=1.49, while at the depth of 15.5 cm, α=4393.26 and β=1.55. These results for α and β were more closely aligned compared to the results for the λ and γ in the WSF.

5.4 Profiles of Model Parameters along Depth

In conducting the regression analysis for the model parameters λ, γ, α, and β, it was observed that the results for these parameters exhibited systematic variations with increasing depth within the asphalt layer. Additionally, since PSPA readings are reliable from approximately 7-28 cm given the source frequency and receiver spacing use, results for 1-6 cm are not reported. As discussed in §4.4, each of these parameters holds specific mathematical or physical significance: $\ln(\lambda)$ represents the intercept of the Weibull curve; γ is the slope of this curve; α is the life factor, indicating the number of load applications required for the damage variable D to reach a value of 0.368; and β predominantly affects the shape of the damage development curve. This section extends the analysis to explore the profiles of these four model parameters along the depth of the asphalt layers.

From Table 5-7 to Table 5-18, it is evident that the regression analysis results vary considerably across different test sections. To enable a comparative analysis of the model parameters across these sections and to identify the trends of λ, γ, α, and β along the depth of the asphalt layers, a normalization procedure was applied to the regression results of these parameters. This normalization approach is detailed as follows:

$$x_n = \frac{x - x_{\min}}{x_{\max} - x_{\min}} \qquad 5\text{-}17$$

Here, x_n denotes the normalized value of a model parameter, x is the actual regression result, and $x_{\max}$ and $x_{\min}$ represent the maximum and minimum values of the parameter for the same testing point and direction across various depths.

This normalization method facilitates a coherent and comparative understanding of the model parameter values across different test sections and depths. By standardizing these values, the approach shows how parameters behave and influence the fatigue damage in asphalt layers.

5.4.1 Profiles of Parameter λ along Depth

Figure 5-29 and Figure 5-30 display the normalized outcomes for the model parameter λ in Sections I and II, respectively. In these figures, 'transverse' refers to the direction perpendicular to axle load movement, while 'longitudinal' pertains to the direction parallel to it.

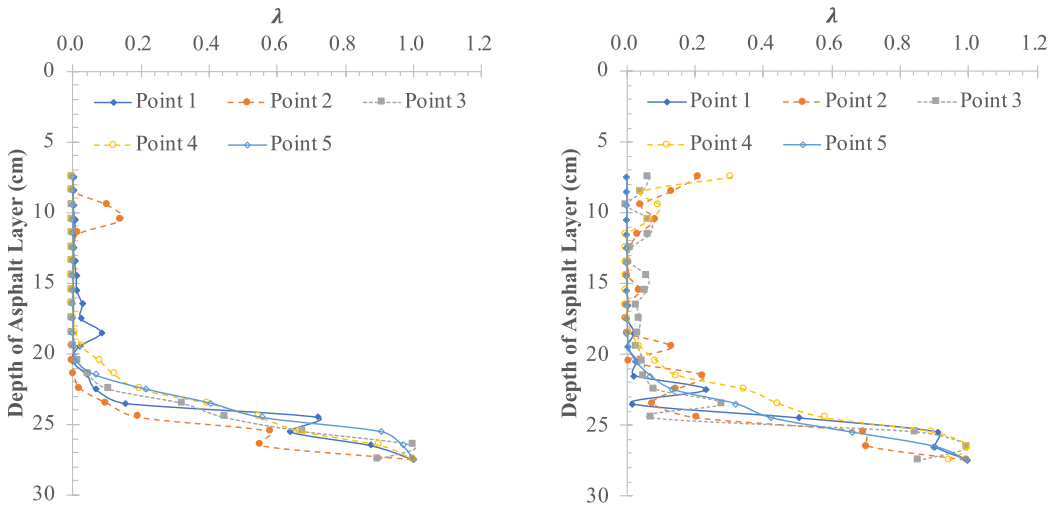

(a) Transverse direction (b) Longitudinal direction

Figure 5-29 The normalized λ of asphalt layers in Section I

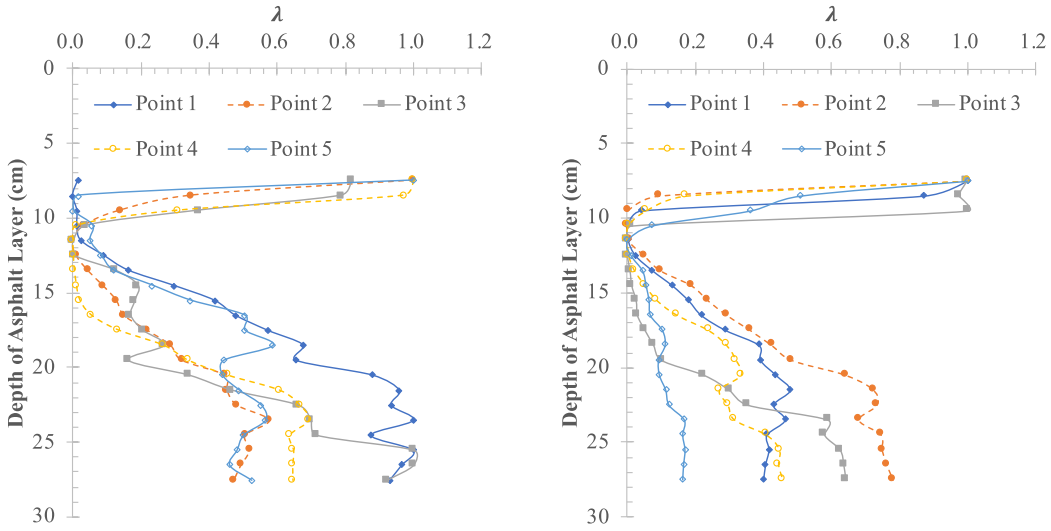

(a) Transverse direction (b) Longitudinal direction

Figure 5-30 The normalized λ of asphalt layers in Section II

Observations from Figure 5-29 indicate that in Section I, below 7.5 cm and within a depth of 20 cm, the value of λ exhibits little change with increasing depth. However, below 20 cm, λ increases rapidly, reaching its highest value at the bottom of the asphalt layer. Conversely, Figure 5-30 for Section II shows that below 7.5 cm, λ first decreases and then increases, reaching its minimum value between depths of 12 cm and 14 cm.

Subsequent to these observations, laboratory indirect tensile fatigue tests were conducted on asphalt samples cored from Sections I and II. These tests aimed to analyze the variation in fatigue life at different depths of the asphalt layers, both before and after the F-sAPTs. These results were then compared to the depth-wise distribution of λ to explore its physical significance. This study took 12 cores in total, three each from the non-loaded and wheel paths of both Sections I and II. These cores were cut into 72 specimens of 40±2.0 mm height, corresponding to various asphalt layer depths as listed in Table 5-19.

These fatigue tests adhered to the European standard EN 12697-24, utilizing a stress-controlled loading mode with a stress amplitude of 250 kPa, a loading frequency of 10 Hz without rest periods, and a test temperature of 20 °C. The study defined the fatigue life of the asphalt mixtures as N_{f50}, allowing for the calculation of average fatigue life at various depths within the asphalt layers before (non-loaded area) and after (wheel path area) loading. The percentage change in fatigue life across these depths was calculated using Equation 5-18:

$$PC = \frac{N_{f0} - N_{fn}}{N_{f0}} \times 100\% \qquad 5\text{-}18$$

Here, PC (%) denotes the percentage change in fatigue life within a specific depth range, N_{f0} is the average fatigue life before loading, and N_{fn} is the average fatigue life after loading at the same depth range. The analysis results of N_{f0}, N_{fn}, and PC are presented in Table 5-19.

Table 5-19 Fatigue life derived from ITFT before and after F-sAPTs

Range of Depth	Section I			Section II		
	N_{f0}	N_{fn}	PC	N_{f0}	N_{fn}	PC
1 cm to 5 cm	49512	48516	2.01%	45230	45118	0.25%
5 cm to 9 cm	77030	22002	71.44%	54690	25004	54.28%
9 cm to 13 cm	98541	15120	84.66%	114268	29006	74.62%
14 cm to 18 cm	80032	15242	80.96%	93574	19705	78.94%
19 cm to 23 cm	76606	20459	73.29%	39376	20395	48.20%
24 cm to 28 cm	24003	20537	14.44%	28002	10645	61.98%

This study then compared the percentage changes in fatigue life at different asphalt layer depths with the average values of λ, as illustrated in Figure 5-31 and Figure 5-32. As established in previous sections, $\ln(\lambda)$ is the intercept of the Weibull curve and changes in λ indicate similar fatigue damage processes but with varying amounts of damage caused by the same number of load applications, where a larger λ value might indicate faster damage development. Therefore, if λ could independently and effectively signify the rate of fatigue damage evolution in pavement structures, larger values of λ should correlate with greater percentage changes in fatigue life at corresponding depths.

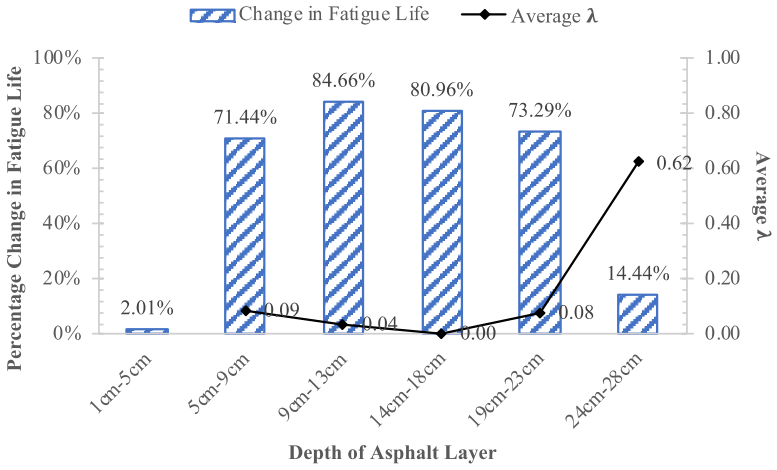

Figure 5-31 The Relationship between λ of Section I and the change in fatigue life

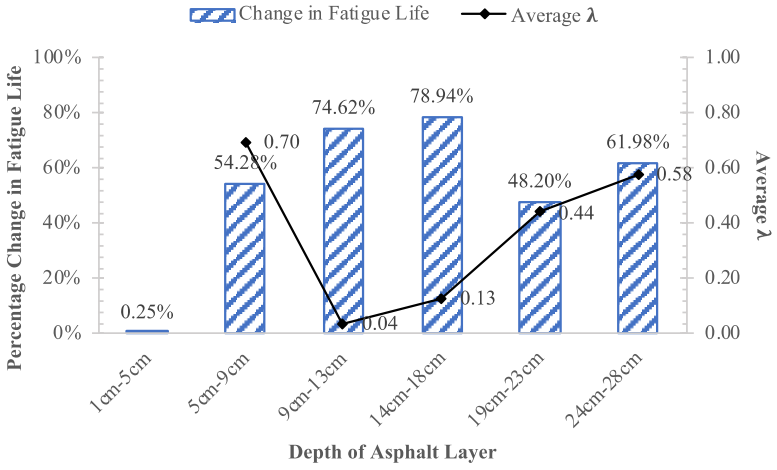

Figure 5-32 The Relationship between λ of Section II and the change in fatigue life

However, as shown in Figure 5-31 and Figure 5-32, the correlation between the average values of λ and the percentage changes in fatigue life along the asphalt layer depth was weak. This lack of

correlation was attributed to the continuous variation in the regression results for the model parameter γ across different depths. Therefore, it was concluded that the WSF's parameter λ cannot independently and effectively represent the fatigue damage evolution rate in pavement structures. Instead, the evolution of fatigue damage is determined by a combination of the parameters λ and γ.

In summary, although the parameter λ from the WSF has a clear mathematical interpretation, its physical meaning along the depth of the asphalt layer remains ambiguous. The evolution of fatigue damage is governed by the interplay of both λ and γ.

5.4.2 Profiles of Parameter γ along Depth

Figure 5-33 and Figure 5-34 present the normalized outcomes of the model parameter γ for Sections I and II, respectively.

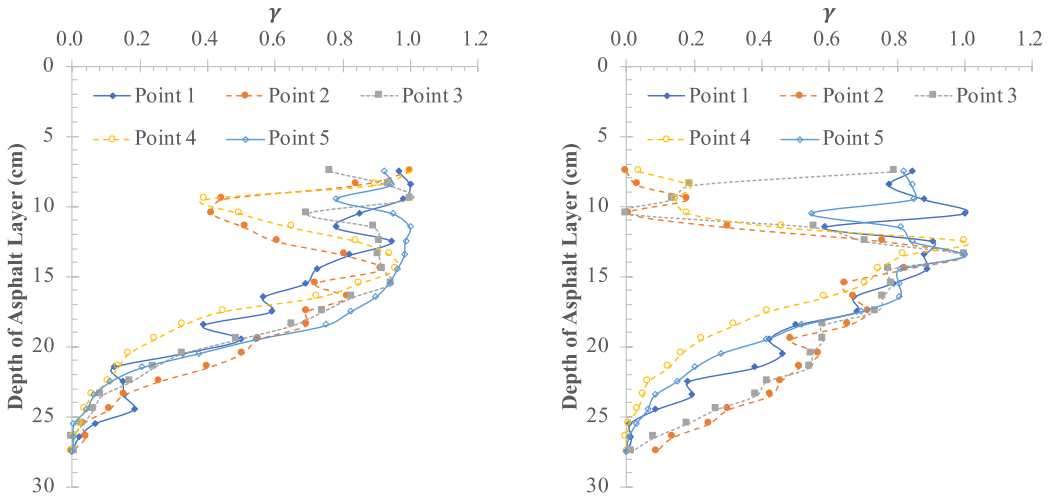

(a) Transverse direction (b) Longitudinal direction

Figure 5-33 The normalized γ of asphalt layers in Section I

In Figure 5-33, pertaining to Section I with a semi-rigid base, the variation of γ with depth below 7.5 cm is notably complex. At the outer edge of the wheel paths (Points 1 and 5), there is a general trend of γ decreasing with increasing depth. In contrast, at the center of the wheel paths (Points 2 and 4) and at the center of the wheels' gap (Point 3), γ first decreases, then increases, and finally decreases again as depth increases.

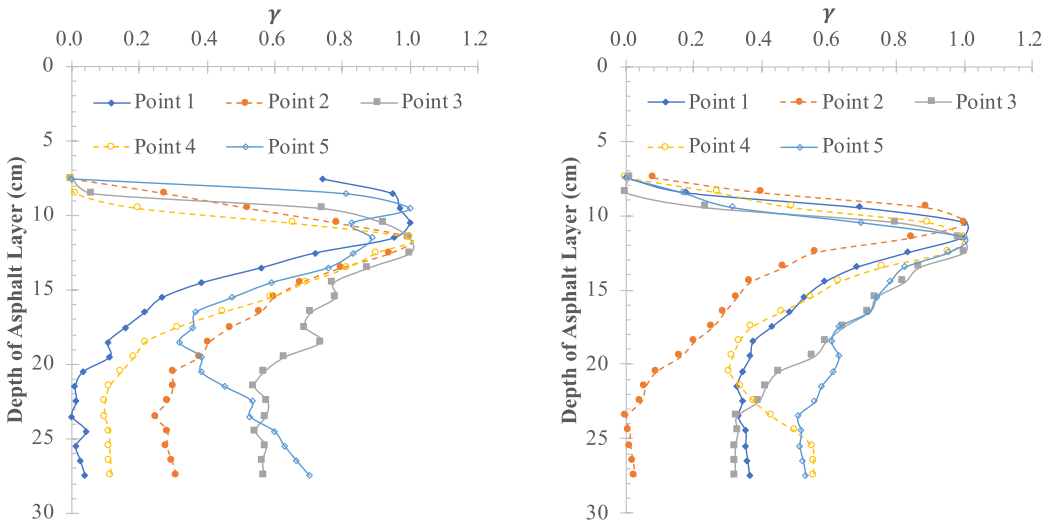

(a) Transverse direction (b) Longitudinal direction

Figure 5-34 The normalized γ of asphalt layers in Section II

Meanwhile, Figure 5-34 illustrates that in Section II, which features a flexible base, γ initially decreases and then increases with depth below 7.5 cm, followed by a slight increase again below 24.5 cm.

Summarizing these observations, it becomes evident that the profile of γ along the depth of the asphalt layer varies considerably across different testing points and directions, consistently changing with depth. As analyzed in §4.3.1, λ can effectively represent the rate of fatigue damage development only when γ remains constant. Hence, while the WSF can achieve a satisfactory fit for engineering applications in modeling the fatigue damage process within asphalt layers, it is the combined influence of both λ and γ that dictates the evolution of the fatigue damage curve. Despite their distinct mathematical identities, the physical interpretations of λ and γ in relation to their distribution with depth are not straightforward.

5.4.3 Profiles of Parameter α along Depth

Figure 5-35 and Figure 5-36 illustrate the normalized results for the model parameter α in Sections I and II, respectively. In these figures, ‘transverse’refers to the direction perpendicular to axle load movement, while ‘longitudinal’ denotes the direction parallel to it.

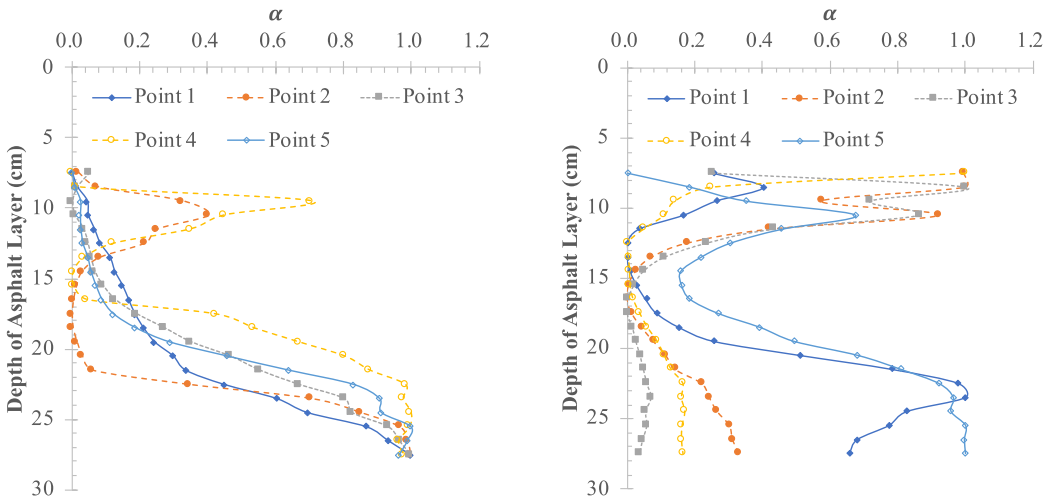

(a) Transverse direction (b) Longitudinal direction

Figure 5-35 The normalized α of asphalt layers in Section I

Figure 5-35 shows that for Section I, which features a semi-rigid base, the pattern of change in α along the depth is complex, particularly below 7.5 cm. At the outer edge of the wheel paths (Points 1 and 5) and at the center of the wheel's gap (Point 3) in the transverse direction, α generally increases with depth, suggesting an increase in the fatigue life of the asphalt layer with depth. Conversely, at other points, α initially decreases then increases with depth, reaching its minimum value between 14 cm and 18 cm.

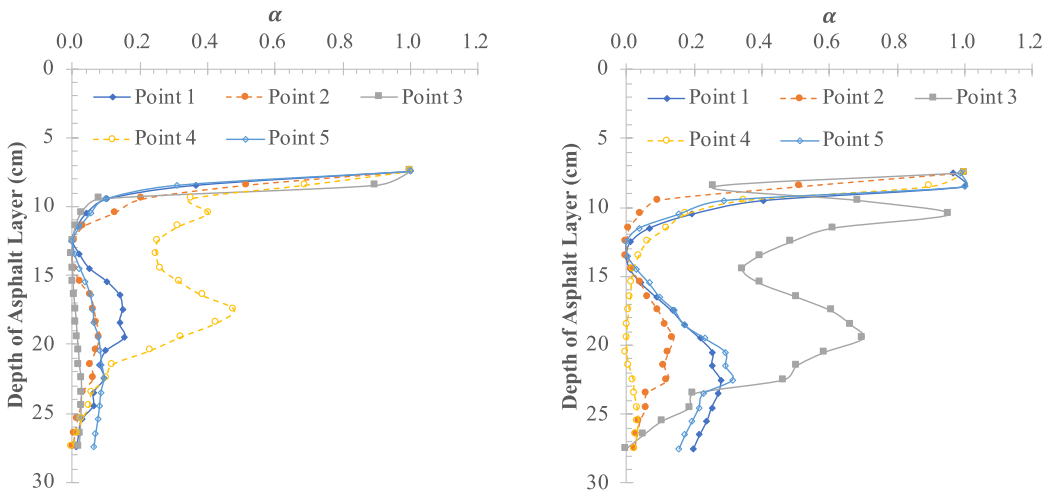

(a) Transverse direction (b) Longitudinal direction

Figure 5-36 The normalized α of asphalt layers in Section II

In Figure 5-36, for Section II with a flexible base, α below 7.5 cm first rapidly decreases, then slightly increases, and finally decreases again, reaching its lowest value either between 12 cm and 15 cm depth or at the asphalt layer's bottom.

The study also compared the laboratory indirect tensile fatigue test results with the profile of α along the depth. Figure 5-37 and Figure 5-38 display the average values of α at various depths within the asphalt layers, along with the percentage change in fatigue life before and after the F-sAPTs. As detailed in §4.3.1, α acts as a life factor, indicating the number of load applications required for the damage variable D to reach 0.368, with a lower α indicating quicker damage development. Therefore, if α effectively represents the fatigue life in pavement structures, smaller α values should correspond to greater percentage changes in fatigue life at those depths.

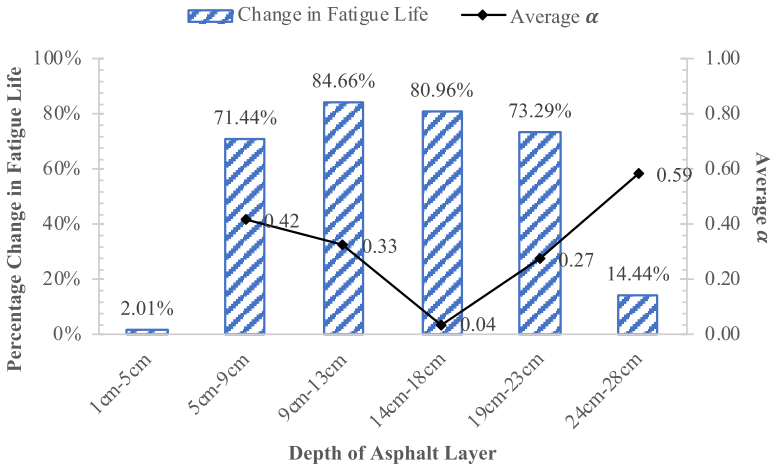

Figure 5-37 The Relationship between α of Section I and the change in fatigue life

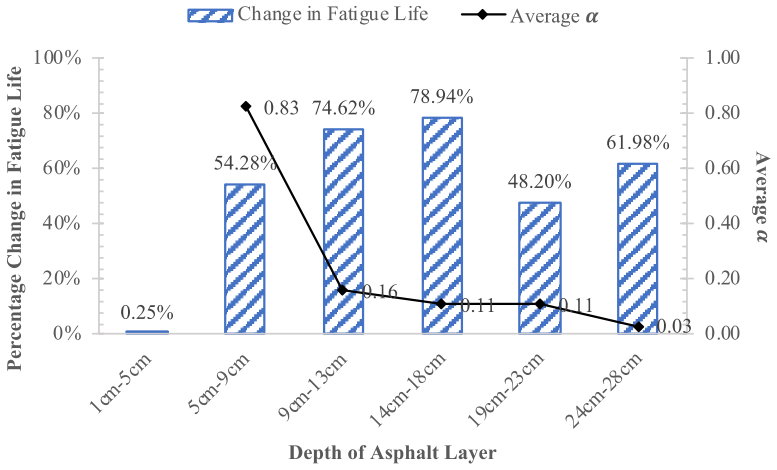

Figure 5-38 The Relationship between α of Section II and the change in fatigue life

The analysis found a strong correlation between the average values of α and the percentage change in fatigue life, showing an inverse relationship in their trends along the depth. Thus, the distribution

of the SBF's model parameter α along the depth effectively mirrors the fatigue life distribution in the asphalt layers.

5.4.4 Profiles of Parameter β along Depth

Figure 5-39 and Figure 5-40provide the normalized results for the model parameter β in Sections I and II.

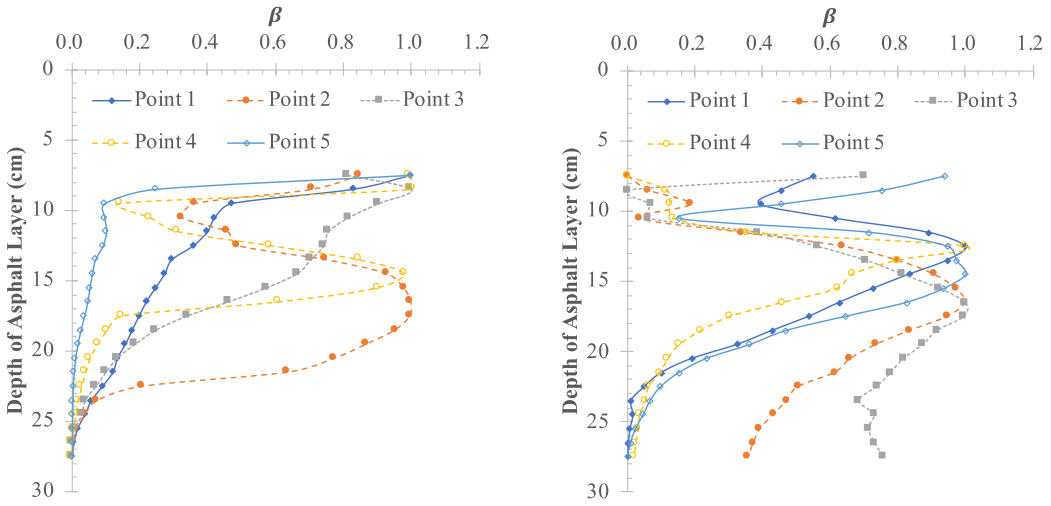

(a) Transverse direction (b) Longitudinal direction

Figure 5-39 The normalized β of asphalt layers in Section I

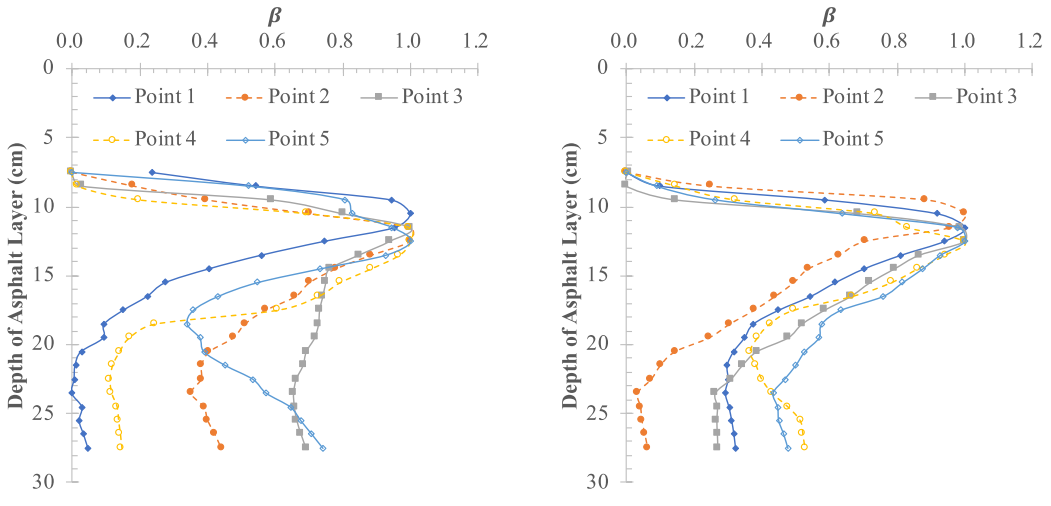

(a) Transverse direction (b) Longitudinal direction

Figure 5-40 The normalized β of asphalt layers in Section II

In Figure 5-39, for Section I, which has a semi-rigid base, it is observed that the distribution of β along the depth varies depending on the testing points and directions. Below 7.5 cm, particularly at the outer edge of the wheel paths (Points 1 and 5) and at the center of the wheel's gap (Point 3) in

the transverse direction, β decreases with increasing depth. At other points, β initially decreases, then increases, and finally decreases again as depth increases.

Figure 5-40 for Section II shows that the pattern of β across different testing points and directions is more uniform: below 7.5 cm and within a depth of 24.5 cm, β initially increases and then decreases with increasing depth; below 24.5 cm, the change in β with increasing depth is minimal or slightly increases.

To summarize, across both test sections, the distribution of the model parameter β along the depth of the asphalt layer is complex and exhibits variations across different testing points and directions. As analyzed in §4.3.1, β significantly influences the shape of the damage development curve. Therefore, the form of these curves varies at different depths within the asphalt layers, as detailed in Figure 5-25 and Figure 5-26.

5.5 Comparisons between WSF and SBF

Integrating the findings from Chapter 4 with the current chapter's analysis, a comparative summary between the WSF and the SBF is presented in Table 5-20.

Table 5-20 Comparisons between WSF and SBF

No.		**WSF**	**SBF**
Applicability to different loading modes		✓	✓
Fitness to various damage progressions		✓	✓
Monotonicity		✓	✓
Adaptability to boundary conditions		✓	✓
Interpretability of model parameters		×	✓
Stability of model parameters		Poor	Good
Asphalt Mixture (Average of R^2)	**Stress-controlled tests**	0.98	0.97
	Strain-controlled tests	0.90	0.89
Asphalt Layer (Average of R^2)	**Section I**	0.74	0.80
	Section II	0.76	0.76
Physical significance of parameter profile with depth			

This table elucidates that both models satisfy four key principles:

(1) Accurately depicting the entire progression of damage development in asphalt layers.

(2) Ensuring that the modeled damage variable D consistently increases with the number of load repetitions.

(3) Adhering to essential boundary conditions: damage amount D approaches zero as the number of load applications nears zero, and conversely, D approaches one as the number of load applications heads towards infinity.

(4) Featuring simple model forms with parameters that are straightforward to derive.

Both models are effective in fitting the fatigue damage evolution process in laboratory-tested asphalt mixtures and in asphalt layers within pavement structures, thus meeting the requirements for engineering applications. However, the SBF is considered to be more rational compared to the WSF for several reasons:

The parameters λ and γ in the WSF, representing the Weibull curve's intercept and slope respectively, influence each other, leading to ambiguous physical meanings. Their stability is also less reliable under minor variations in experimental data. Moreover, their correlation with loading factors lacks consistency and therefore interpretability. Furthermore, when the WSF is employed to fit the fatigue damage process in asphalt layers, the depth-wise distribution of λ and γ lacks clear physical significance.

In contrast, the SBF boasts well-defined physical interpretations for its parameters. α indicates the number of load repetitions needed for the damage variable D to reach 0.368, while β significantly shapes the damage development curve. Notably, α and β exhibit better stability against minor data variations. They also demonstrate a clear correlation with various loading factors, enhancing their interpretability. Using this model to fit the fatigue damage process in asphalt layers, the depth-wise distribution of α clearly reflects the fatigue life distribution in asphalt layers.

To summarize, this study advocates for the use of the SBF as the preferred method for modeling the fatigue damage evolution process in both laboratory asphalt mixtures and in-situ asphalt layers. This recommendation is based on its clearer parameter interpretations, stability, and effective portrayal of fatigue life characteristics.

5.6 Summary

This chapter explores the implementation of F-sAPTs on asphalt layers constructed atop semi-rigid and granular bases. An array of techniques—FWD, PSPA, and uniaxial compression dynamic modulus testing—were utilized to evaluate the modulus of these layers. A significant aspect of the

work involved the calibration of temperature and frequency factors for in situ modulus values. An in-depth analysis centered on understanding the fatigue damage across various pavement sections was conducted, using SSR as the primary variable. This encompassed examining fatigue damage in relation to depth, location, and orientation across pavement sections. The chapter also delves into the application and comparative evaluation of two predominant models: the WSF and the SBF. This comparison focused on their respective abilities to logically and efficiently fit damage progression, with an overarching goal of determining the most applicable model for capturing fatigue damage in in-situ asphalt layers. This comprehensive analysis provides actionable insights beneficial for pavement engineering and maintenance.

The main findings of this chapter are as follows:

(1) Both the FWD inversion analysis and PSPA detection results could be effectively temperature-corrected using a model based on a semi-logarithmic scale relationship between the asphalt layer's modulus and temperature.

(2) The undamaged asphalt mixture's modulus master curve can reflect the modulus across all frequencies, aligning with the predictions for both FWD and PSPA results.

(3) The frequency adjustment coefficients for the seismic modulus of both undamaged and damaged asphalt layers can effectively recalibrate the PSPA detection results to match modulus values at design frequencies.

(4) The significant decrease in the modulus of asphalt layers with increasing load repetitions is influenced by factors such as base type. Additionally, the pattern of modulus decay is not uniform and varies with depth and detection specifics.

(5) Both the WSF and the SBF models were found to be effective in modeling the fatigue damage evolution in asphalt layers. However, the SBF, with its clearer parameter interpretations and stability against minor data variations, is deemed more recommended. In contrast, the WSF's parameters show less stability and clarity in physical significance.

References

[1] AASHTO TP 62-03. *Standard method of rest for determining dynamic modulus of hot mix asphalt concrete mixtures*. Washington, D.C.: American Association of State Highway and

Transportation Officials, 2011.

[2] Aouad, M. F., Stokoe II, K. H. & Briggs, R. C. Stiffness of asphalt concrete surface layer from stress wave measurements. *Journal of Transportation Research Record*, 1993, 1384:29-35.

[3] Bai, X. *Assessment of relationship between dynamic and seismic moduli of asphalt concrete mixtures*. El Paso: The University of Texas at El Paso, 2004.

[4] Baker, M. R., Crain, K. & Nazarian, S. *Determination of pavement thickness with a new ultrasonic device*. El Paso: Texas Department of Transportation, 1995.

[5] Bruinsma, J. E., Vandenbossche, J. M. Chatti, K., et al. *Using falling weight deflectometer data with mechanistic-empirical design and analysis, volume II: case study reports*. McLean: Federal Highway Administration, 2017.

[6] Celaya, M. & Nazarian, S. Seismic testing to determine quality of hot-mix asphalt. *Journal of Transportation Research Record*, 2006, 946:113-122.

[7] Celaya, M. & Nazarian, S. Stripping detection in asphalt pavements with seismic methods. *Journal of Transportation Research Record*, 2007, 2005:64-74.

[8] Chen, S. *Study on fatigue performance of asphalt pavement by accelerated pavement test*. Guangdong: South China University of Technology, 2007.

[9] Chen, S., Yu, J., Li, H., et al. Comparative analysis of different test methods on asphalt mixture moduli. *Journal of Highway and Transportation Research and Development*, 2008, 25(08):6-9,14.

[10] Collop, A. C. *Effects of traffic and temperature on flexible pavement wear*. Cambridge: Cambridge University, 1994.

[11] Daniel, J. S. & Kim, Y. R. Relationship among rate-dependent stiffnesses of asphalt concrete using laboratory and field test methods. *Journal of Transportation Research Board*, 1998, 1630:3-9.

[12] Ding, T. *Micro-damage evaluation of asphalt pavement for preventive maintenance*. Shanghai: Tongji University, 2016.

[13] Johnson, A. M. & Baus, R. L. Alternative method for temperature correction of backcalculated equivalent pavement moduli. *Journal of Transportation Research Record*, 1992, 1355:75-81.

[14] Jurado, M., Gibson, N., Celaya, M., et al. Evaluation of asphalt damage and cracking development with seismic pavement analyzer. *Journal of Transportation Research Record*,

2012, 2304:47-54.

[15] Kim, Y. R., Hibbs, B. O. & Lee, Y. C. Temperature correction of deflections and backcalculated asphalt concrete moduli. *Journal of Transportation Research Record*, 1995, 1473:55-62.

[16] Lee, N. K. J., Hugo, F. & Stokoe, K. H. Detection and monitoring of cracks in asphalt pavement under Texas mobile load simulator testing. *Journal of Transportation Research Record*, 1997, 1570:10-22.

[17] Lin, S., Ashlock, J. C., & Williams, R. C. Nondestructive quality assessment of asphalt pavements based on dynamic modulus. *Construction and Building Materials*, 2016, 112:836-847.

[18] Lin, S., Ashlock, J., Williams, R. C., et al. Evaluation of three nondestructive testing techniques for quality assessment of asphalt pavements. *Nondestructive Testing and Evaluation*, 2018, 33(4):361-375.

[19] Lin, S., Shams, S., Choi, H., et al. Estimation of wave velocity for ultrasonic imaging of concrete based on dispersion analysis. *Journal of Testing and Evaluation*, 2020, 48(2):1095-1107.

[20] Liu, W. & Scullion, T. *MODULUS 6.0 for windows: user's manual*. College Station: Texas Transportation Institute, 2001.

[21] Liu, J., Wang, X., Liu, Z., et al. Experimental study on static and dynamic compressive resilient moduli. *Journal of Highway and Transportation Research and Development*, 2017, 34(06):45-52.

[22] Lukanen, E. O., Stubstad, R., Briggs, R. C., et al. *Temperature predictions and adjustment factors for asphalt pavement.* McLean: Federal Highway Administration, 2000.

[23] Ma, Z. *Research on the fatigue performance and the method for estimation of remaining fatigue life of in-service asphalt mixture*. Shanghai: Tongji University, 2018.

[24] Michalak, C. H. & Scullion, T. *MODULUS 5.0: User's manual*. College Station: Texas Transportation Institute, 1995.

[25] Nazarian, S., Tandon, V. & Yuan, D. Mechanistic quality management of hot mix asphalt layers with seismic methods. *Journal of ASTM International*, 2005, 2(9):1-12.

[26] Nazarian, S., Yuan, D. & Tandon, V. Structural field testing of flexible pavement layers with seismic methods for quality control. *Journal of Transportation Research Record*, 1999,

1654:50-60.

[27] Oh, J. H., Fernando, E. G., Lee, S. I., et al. Correlation of asphalt concrete layer moduli determined from laboratory and nondestructive field tests. *Journal of Transportation Engineering*, 2012, 138(3):361-370.

[28] Pierce, L. M., Bruisma, J. E., Smith, K. D., et al. *Using falling weight deflectometer data with mechanistic-empirical design and analysis, volume III: guidelines for deflection testing, analysis, and interpretation*. McLean: Federal Highway Administration, 2017.

[29] Rohde, G. T. & Scullion, T. *MODULUS 4.0: Expansion and validation of the MODULUS backcalculation system*. College Station: Texas Transportation Institute, 1990.

[30] Scullion, T. & Michalak, C. H. *MODULUS 4.0: User's manual*. College Station: Texas Transportation Institute, 1991.

[31] Scullion, T., Uzan, J. & Paredes, M. MODULUS: A microcomputer-based backcalculation system. *Journal of Transportation Research Record*, 1990, 1260:180-191.

[32] Sebaaly, P., Tabatabaee, N., Bonaquist, R., et al. Evaluating structural damage of flexible pavements using cracking and falling weight deflectometer data. *Journal of Transportation Research Record*, 1989, 1227:64-74.

[33] Smith, K. D., Bruinsma, J. E., Wade, M. J., et al. *Using falling weight deflectometer data with mechanistic-empirical design and analysis, volume I: final report*. McLean: Federal Highway Administration, 2017.

[34] Uzan, J., Scullion, T., Michalek, C. H., et al. *A microcomputer based procedure for backcalculating layer moduli from FWD data*. College Station: Texas Transportation Institute, 1988.

[35] Witczak, M. W. & Kaloush, K. Specimen geometry and aggregate size effects in uniaxial compression and constant height shear tests. *Journal of Association of Asphalt Paving Technologist*, 2000, 69:733-793.

6 FATIGUE LOADING MODES AND CRITICAL DAMAGE LOCATIONS IN ASPHALT LAYERS

An extensive review in Chapter 2 establishes a general agreement that the fatigue loading modes in asphalt layers correlate with the thickness of these layers. However, there is emerging research that challenges this notion, suggesting variability in fatigue loading modes at different depths within the same pavement structure, a topic that has not been exhaustively explored. The chapter also addresses the ambiguity surrounding the critical damage locations and the most applicable fatigue loading modes for semi-rigid base asphalt pavements. Building on the regression analysis of the SBF from the preceding chapter, this chapter embarks on a detailed examination of the mechanical mechanisms contributing to fatigue damage in asphalt layers. It seeks to unravel the intricacies of these mechanisms and their impact on pavement durability. Further, this chapter comprehensively analyzes the critical damage locations in both semi-rigid and flexible asphalt pavements. This investigation is crucial in identifying the zones most prone to fatigue damage, offering a comparative insight into the differing behaviors of semi-rigid and flexible pavements under similar conditions. Lastly, the chapter introduces a novel concept: the tensile-shear loading mode factor. This factor responds to the limitations observed in traditional tensile fatigue loading models, which often fall short in replicating the complex conditions experienced by asphalt layers in real-world scenarios. By incorporating this new factor, the aim is to provide a more accurate representation of the responses of asphalt layers under actual operational conditions, enhancing the understanding of pavement fatigue and its management.

6.1 Mechanical Mechanism Underlying Fatigue Damage in Asphalt Layers

Contemporary studies indicate that fatigue damage within asphalt layers is predominantly initiated by flexural-tensile or shear effects under repetitive loading [2,9]. These effects are integral in understanding the onset of both bottom-up and top-down fatigue cracking in asphalt layers, with a

notable correlation between the prominence of these effects and the reduction in the asphalt layer's fatigue life. Since the parameter α in the SBF is instrumental in effectively depicting the fatigue life and rate of damage progression in asphalt layer, this section is dedicated to establishing a quantitative relationship between α, and the tensile ε_t and shear strains ε_s distributed across the depth of the asphalt layers. This analysis aims to dissect and clarify the complexities surrounding fatigue damage in asphalt layers, highlighting the significant impact of these mechanical mechanisms on the overall durability of pavement.

In pursuit of this goal, the study utilizes a finite element model to calculate ε_t and ε_s at various depths within the asphalt layers for different testing points and directions in both Sections I and II. The finite element model is based on the configuration detailed in Figure 5-23. For the asphalt layer modulus, the study adopts adjusted values derived from seismic modulus results of the damaged asphalt layers in these sections, with a target frequency of 3.22 Hz and a target temperature of 20 °C. The moduli for the semi-rigid base, flexible base, and subgrade are determined from inverse analysis values obtained through FWD testing at the top of the base layer.

This study then proceeds to aggregate and average the results of α regression analysis from test points 1 and 5, along with finite element results for ε_t and ε_s, categorizing them by detection direction and depth within the asphalt layer. Similarly, the distribution of α, ε_t, and ε_s along the depth at the center of the wheel paths in each test section is ascertained through the synthesis of regression analysis and finite element calculation results from test points 2 and 4. This comprehensive approach ensures a thorough and detailed understanding of the spatial variations in mechanical strain and its impact on pavement fatigue.

6.1.1 Outer Edge of the Wheel Path in Section I

6.1.1.1 Longitudinal Direction

In Section I, characterized by a semi-rigid base, Figure 6-1 illustrates the depth-wise distribution of normalized life factor α, alongside tensile strain ε_t, and shear strain ε_s at the edge of the wheel paths, aligned with the axle load movement direction.

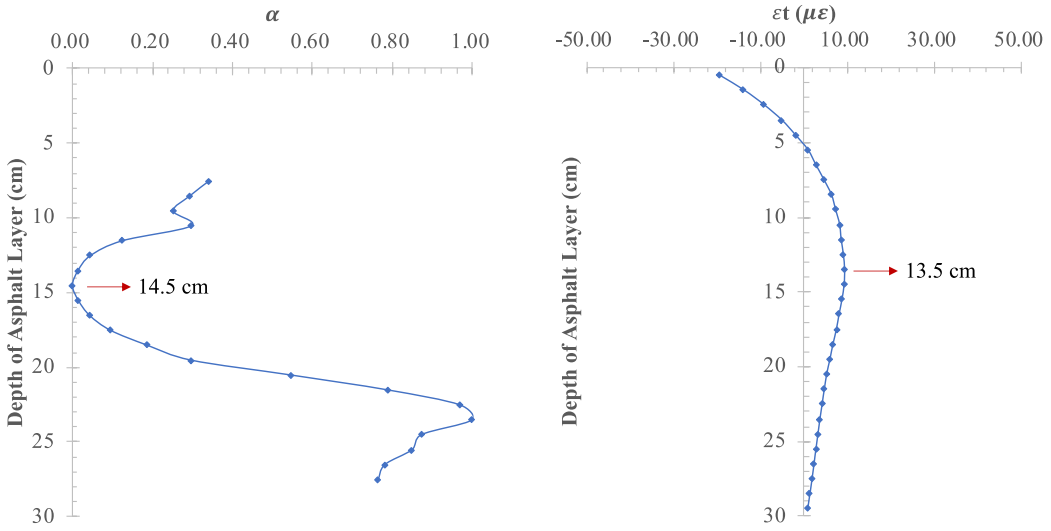

(a) Average normalized α

(b) Average tensile strain ε_t

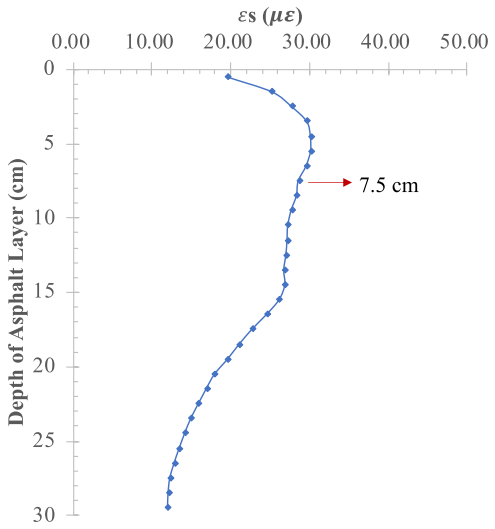

(c) Average shear strain ε_s

Figure 6-1 Longitudinal mechanical responses at the outer edge of the wheel path for Section I

The figure specifically marks the depths at and below 7.5 cm where the maximum values of α, ε_t, and ε_s are located, yielding significant insights:

(1) Life factor α dynamics: Below 7.5 cm, the life factor α exhibits a notable trend, decreasing and then increasing with depth. It reaches its minimum value at 14.5 cm. This trend implies that the fatigue life of the asphalt layer within the pavement structure initially decreases and subsequently increases with depth.

(2) Tensile strain ε_t variations: The tensile strain ε_t increases with depth, turning from negative to positive between the depths of 4 cm and 5 cm, and attains its maximum at 13.5 cm.

(3) Shear strain ε_s fluctuations: Shear strain ε_s initially rises with depth, peaking between 5 cm

and 6 cm, and then decreases as depth continues to increase. Specifically, below 7.5 cm, ε_s diminishes with increased depth.

A critical observation emerges when comparing the depth-wise distributions of α, ε_t, and ε_s below 7.5 cm. The depth at which α is minimal (14.5 cm) does not align with the depths where ε_t or ε_s are maximal (13.5 cm or 7.5 cm). This finding appears to diverge from traditional research perspectives, which typically associate maximal strain with minimal fatigue life at the same depth.

To explore this anomaly, the study involved calculating the cumulative effect of tensile strain ε_t and shear strain ε_s across various depths within the asphalt layer. Figure 6-2 presents a comparative analysis of α in relation to the sum of ε_t and ε_s along the depth, with specific emphasis on depths at and below 7.5 cm where the combined value is highest.

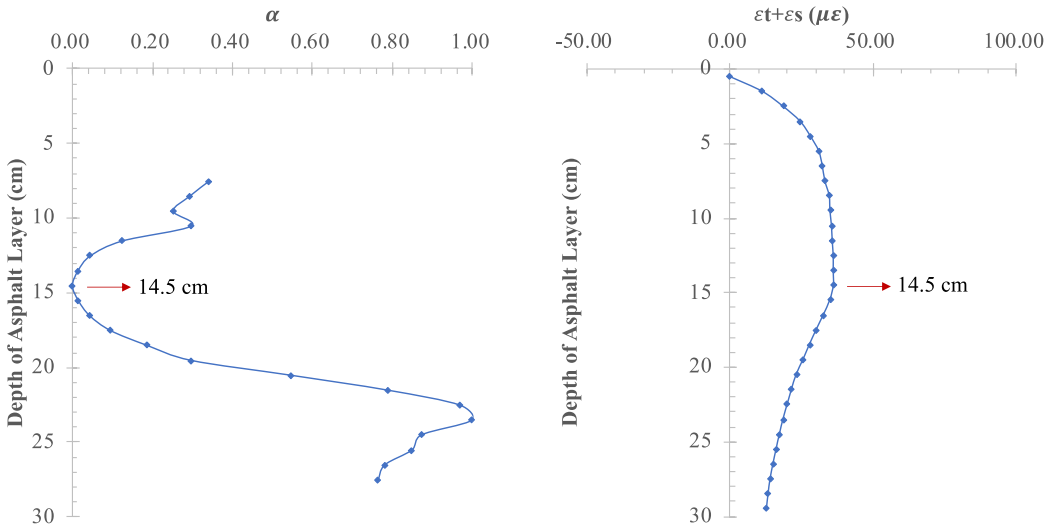

(a) Average normalized α (b) Sum of tensile and shear strains $(\varepsilon_t + \varepsilon_s)$

Figure 6-2 Comparison between average normalized α and the sum of tensile and shear strains

The analysis revealed that the aggregate of ε_t and ε_s initially increases and subsequently decreases with depth, reaching a peak at 14.5 cm. Notably, at this depth, α is also at its lowest, indicating that the asphalt layer's fatigue life is at its shortest when the combined impact of tensile and shear strains is highest. This observation suggests a more complex interplay between the fatigue life of the asphalt layer and the combined effects of flexural-tensile and shear forces, rather than their individual influences.

The subsequent sections will extend this analysis to other test points and directions in Sections I and II, aiming to further corroborate this nuanced understanding of strain impacts on asphalt layer fatigue damage.

6.1.1.2 Transverse Direction

Figure 6-3 in the study provides a detailed analysis of the life factor α, tensile strain ε_t, shear strain ε_s, and the aggregate of ε_t and ε_s along the depth of the asphalt layer. This analysis focuses on the edge of the wheel paths in Section II and is oriented perpendicular to the axle load movement direction.

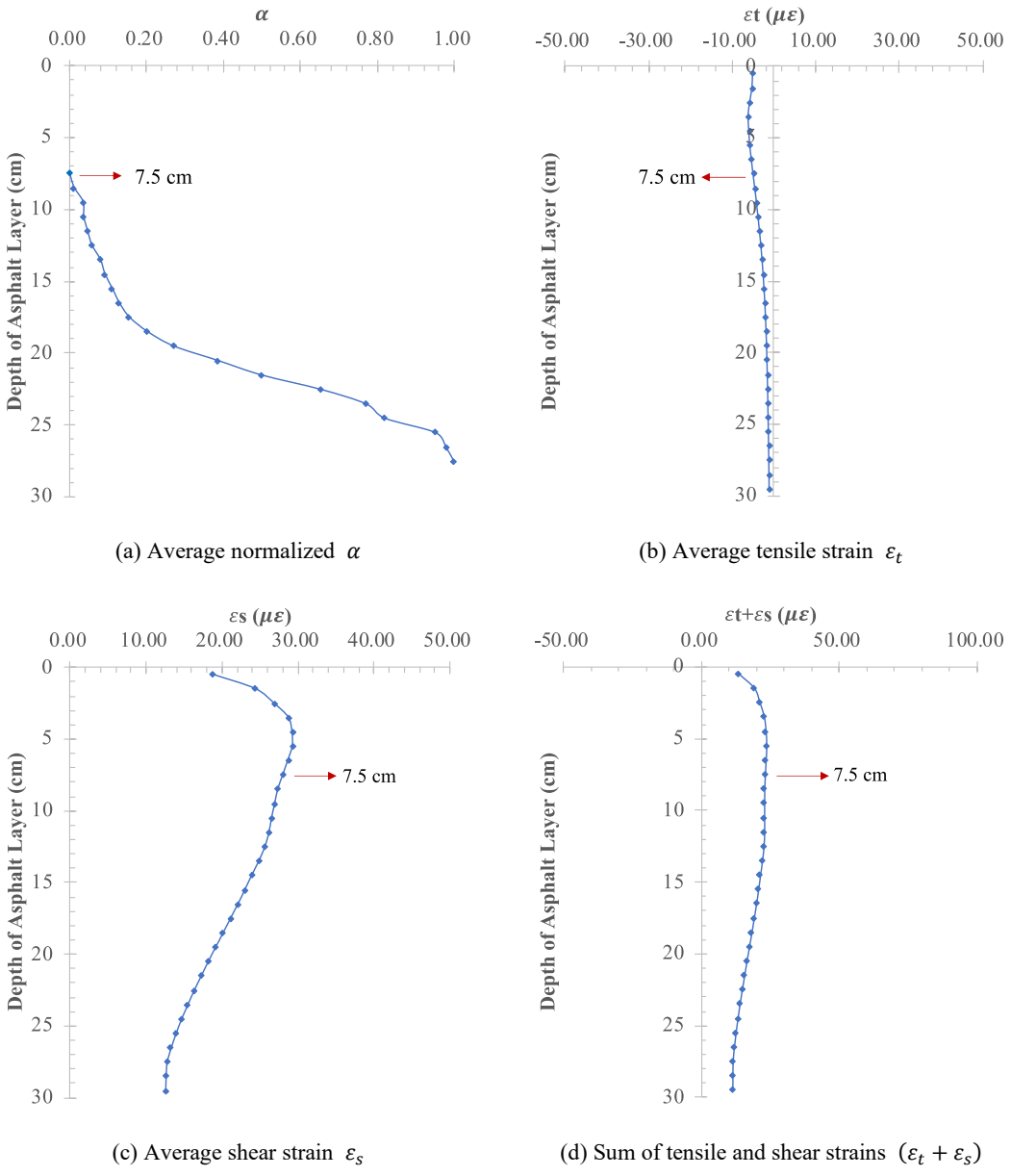

(a) Average normalized α

(b) Average tensile strain ε_t

(c) Average shear strain ε_s

(d) Sum of tensile and shear strains $(\varepsilon_t + \varepsilon_s)$

Figure 6-3 Transverse mechanical responses at the outer edge of the wheel path for Section I

Notably, the figure marks with arrows the depths at and below 7.5 cm where these four parameters attain their maximum values, revealing several critical insights:

(1) Life factor α trends with depth: The life factor α demonstrates a distinctive pattern below 7.5

cm, increasing as the depth increases. The minimum value of α at the depth of 7.5 cm indicates an increase in the fatigue life of the asphalt layer with depth, accompanied by a concurrent decrease in the rate of damage development.

(2) Behavior of tensile strain ε_t: Throughout the measured depths, ε_t maintains negative values, with its absolute magnitude initially increasing and then decreasing with depth. Notably, below 7.5 cm, the absolute value of ε_t diminishes with increasing depth, peaking in magnitude at this depth.

(3) Shear strain ε_s fluctuations: The shear strain ε_s follows a trend of initially increasing and then decreasing with depth. Significantly, below 7.5 cm, ε_s decreases as the depth increases, reaching its maximal value at the depth of 7.5 cm.

(4) Combined effect of ε_t and ε_s: The sum of ε_t and ε_s exhibits a gradual variation with depth. Below the threshold of 7.5 cm, this combined value decreases with increasing depth, achieving its maximum at 7.5 cm.

A comparative analysis of the distributions of α, ε_t, ε_s, and their combined sum below the depth of 7.5 cm reveals a crucial correlation. At this specific depth, where the absolute value of ε_t, ε_s, and their combined sum are at their highest, the value of α is at its lowest. This indicates that the fatigue life of the asphalt mixture within the asphalt layer is shortest at this depth. These observations suggest that the fatigue life of the asphalt layer in pavement structures is not only affected by individual tensile and shear strains but also exhibits a significant correlation with the combined effects of these strains, offering a more nuanced understanding of asphalt layer fatigue dynamics.

6.1.2 Center of the Wheel Path in Section I

6.1.2.1 Longitudinal Direction

In Section I, Figure 6-4 details the distribution of normalized life factor α, tensile strain ε_t, shear strain ε_s, and the sum of ε_t and ε_s along the depth of the asphalt layer at the center of the wheel paths, parallel to the axle load movement direction. The figure uses arrows to highlight the depths at and below 7.5 cm where the maximum values of these factors are recorded, presenting several key observations:

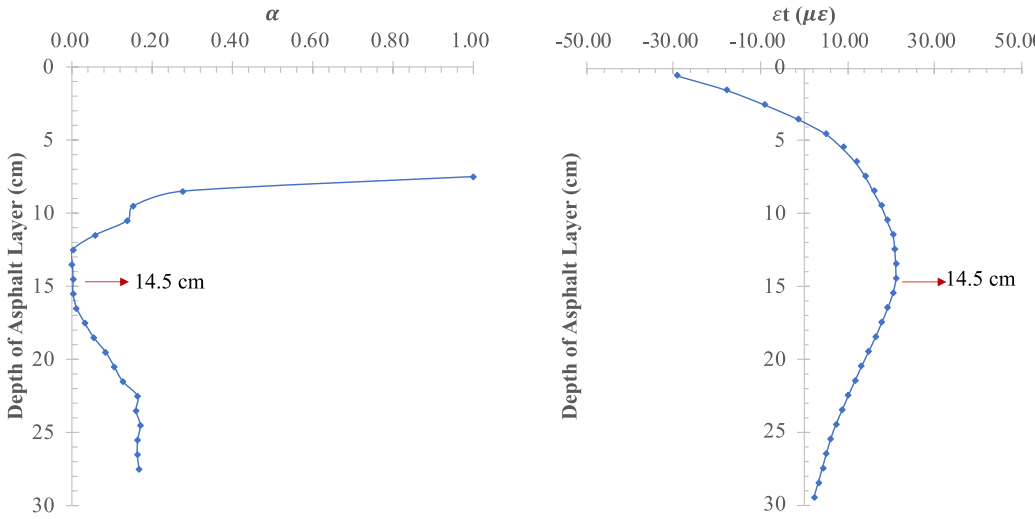

(a) Average normalized α (b) Average tensile strain ε_t

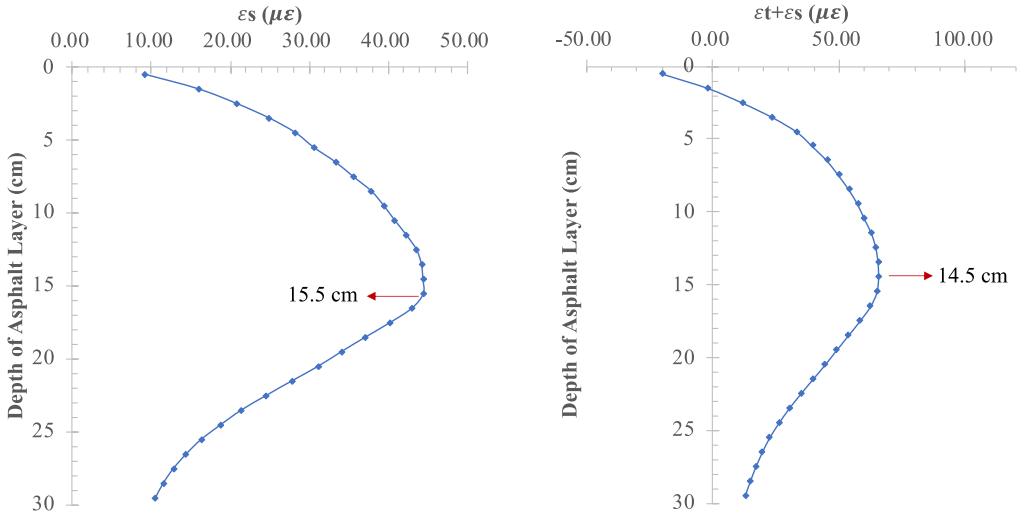

(c) Average shear strain ε_s (d) Sum of tensile and shear strains $(\varepsilon_t + \varepsilon_s)$

Figure 6-4 Longitudinal mechanical responses at the center of the wheel path for Section I

(1) Life factor α and depth correlation: Below 7.5 cm, α shows a marked decrease with increasing depth, reaching its minimum at a depth of 14.5 cm. After this depth, there is a notable increase in α.

(2) Tensile strain ε_t dynamics: The tensile strain ε_t initially increases with depth, then decreases, changing from negative to positive between depths of 3 cm and 4 cm. It reaches its maximum value at a depth of 14.5 cm.

(3) Shear strain ε_s fluctuations: ε_s follows a similar pattern, increasing and then decreasing with depth. Its maximum value is observed at a depth of 15.5 cm.

(4) Combined impact of ε_t and ε_s: The aggregate of ε_t and ε_s initially rises and then falls with

increasing depth, peaking at 14.5 cm.

Comparing the distributions of α, ε_t, ε_s, and their combined sum at depths below 7.5 cm reveals a significant insight. At a depth of 15.5 cm, where ε_s is at its maximum, α does not register its lowest value. Instead, the minimal value of α is identified at a depth of 14.5 cm, aligning with the depths where ε_t and the combined strains are at their maximum. This pattern indicates that the shortest fatigue life within the asphalt layer is at depths where either tensile strain alone or the combined effect of tensile and shear strains reach their maximal values.

6.1.2.2 Transverse Direction

Figure 6-5 in this study illustrates the depth-wise distribution of the life factor α, tensile strain ε_t, shear strain ε_s, and the sum of ε_t and ε_s within the asphalt layer at the center of the wheel paths in Section I. This analysis is conducted perpendicular to the axle load movement direction, with the figure highlighting the depths at and below 7.5 cm where these factors reach their maximum values. Key observations from the figure include:

(1) Life factor α: Below the depth of 7.5 cm, the life factor α is observed to reach its minimum at a depth of 15.5 cm.

(2) Behavior of tensile strain ε_t with depth: ε_t exhibits an increase followed by a decrease as depth increases, transitioning from negative to positive between 4 cm and 5 cm deep. It reaches its peak value at a depth of 14.5 cm.

(3) Dynamics of shear strain ε_s: Similar to ε_t, ε_s initially increases and then decreases with increasing depth, achieving its highest value at 15.5 cm.

(4) Combined effect of ε_t and ε_s: The aggregate of ε_t and ε_s shows a pattern of increasing and then decreasing with depth, peaking at 15.5 cm.

Upon comparing the distributions of α, ε_t, ε_s, and their combined sum below 7.5 cm, it is discerned that the depth where α is at its minimum (15.5 cm) differs from where ε_t is at its maximum (14.5 cm). However, this minimum value of α coincides with the depths where ε_s and the combined sum of ε_t and ε_s are at their highest. This finding suggests that the shortest fatigue life within the asphalt layer occurs at depths where either the shear strain is at its maximum or the combined effects of tensile and shear strains are most pronounced.

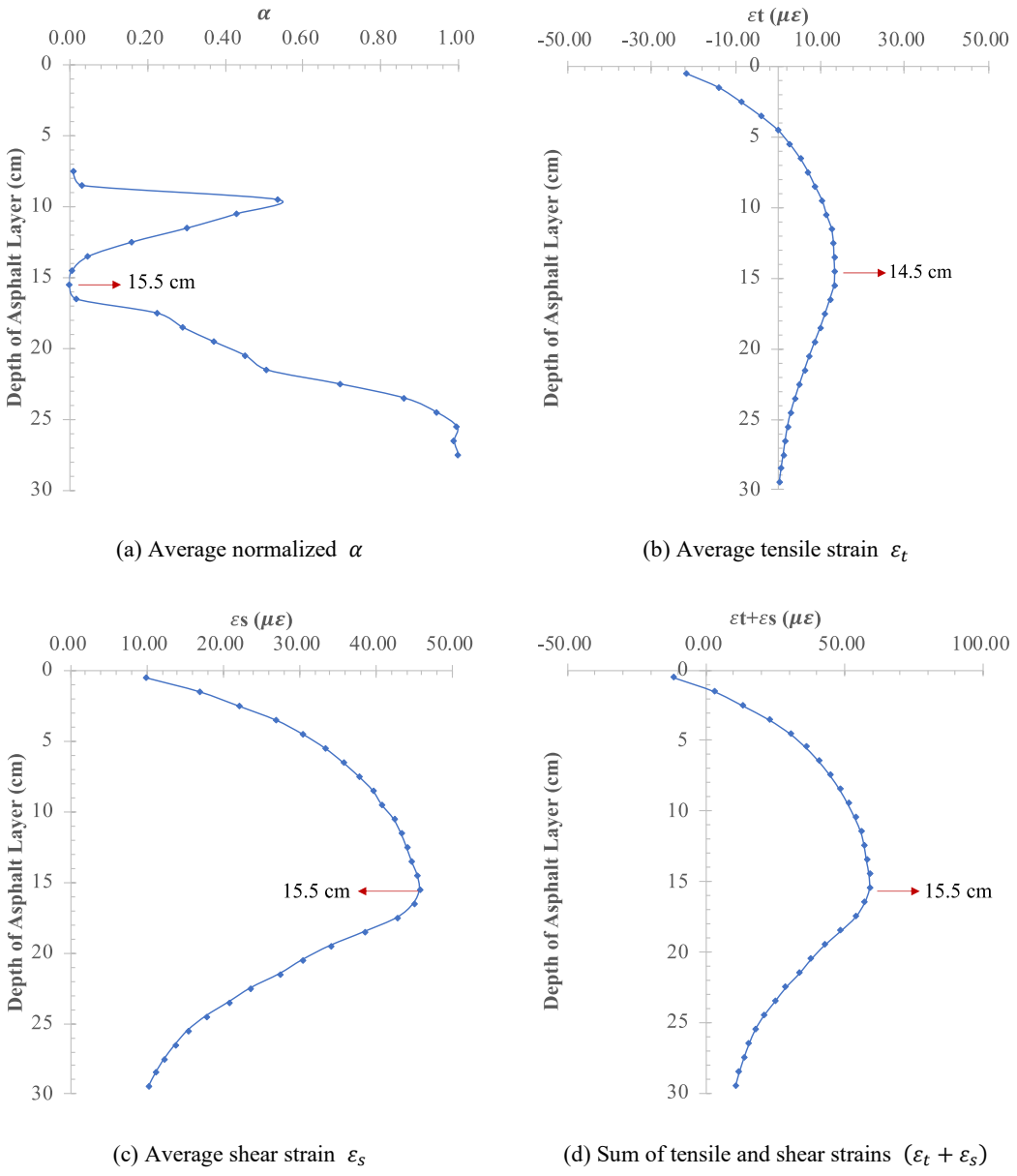

(a) Average normalized α

(b) Average tensile strain ε_t

(c) Average shear strain ε_s

(d) Sum of tensile and shear strains $(\varepsilon_t + \varepsilon_s)$

Figure 6-5 Transverse mechanical responses at the center of the wheel path for Section I

6.1.3 Outer Edge of the Wheel Path in Section II

6.1.3.1 Longitudinal Direction

Figure 6-6 of Section II, which focuses on a flexible base, details the distribution of normalized life factor α, tensile strain ε_t, shear strain ε_s, and the combined sum of ε_t and ε_s along the depth of the asphalt layer at the outer edge of the wheel paths, parallel to the axle load movement direction. The figure marks with arrows the depths at and below 7.5 cm where these factors reach their maximum values, either on a global or local scale. The analysis reveals the following key insights:

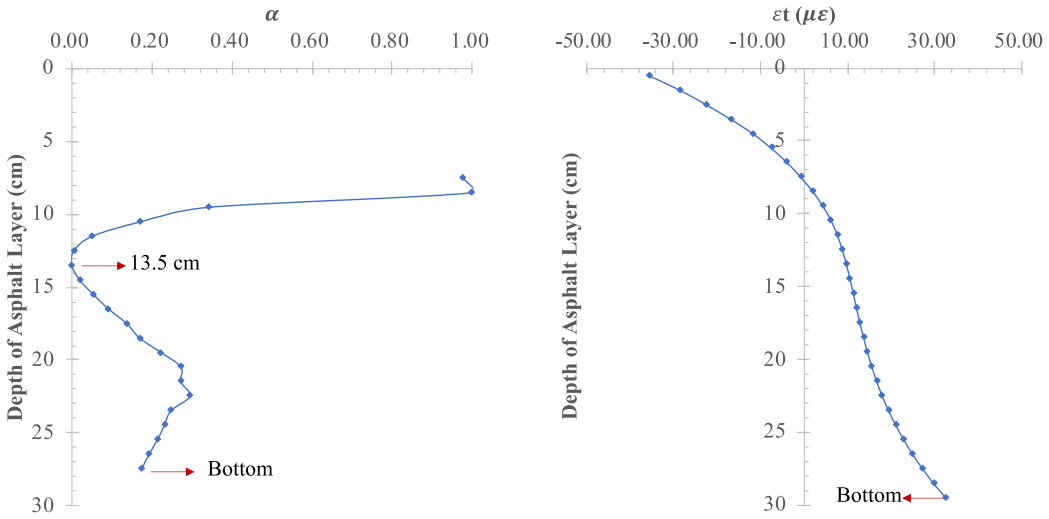

(a) Average normalized α (b) Average tensile strain ε_t

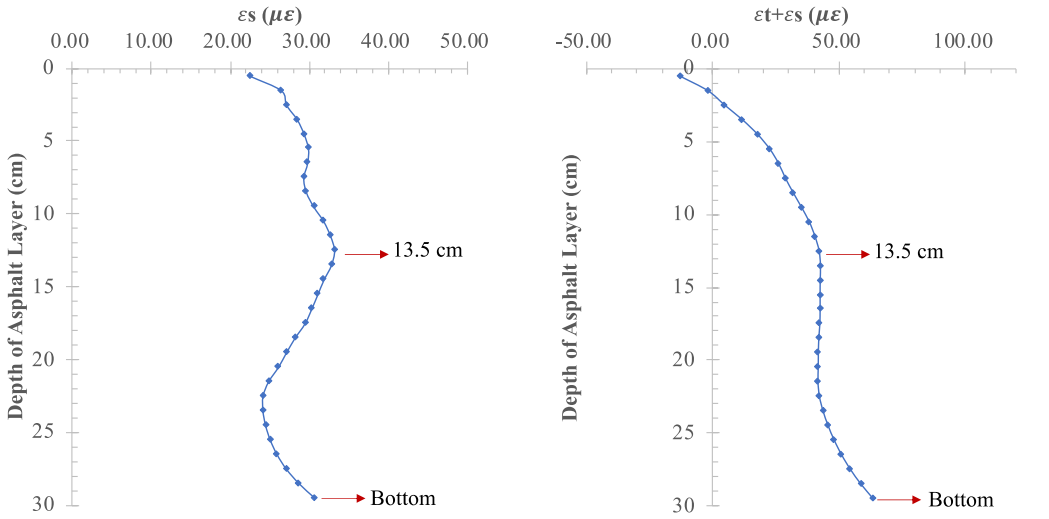

(c) Average shear strain ε_s (d) Sum of tensile and shear strains $(\varepsilon_t + \varepsilon_s)$

Figure 6-6 Longitudinal mechanical responses at the outer edge of the wheel path for Section II

(1) Depth-dependent behavior of life factor α: The value of α initially decreases rapidly with increasing depth, achieving its global minimum at 13.5 cm. Beyond this depth, there is an initial increase followed by a decrease in α, resulting in a local minimum at the base of the asphalt layer.

(2) Tensile strain ε_t trends: The tensile strain ε_t consistently increases with depth, reaching its highest value at the bottom of the asphalt layer.

(3) Shear strain ε_s variations: ε_s shows an initial increase with depth, peaking at its global maximum at 13.5 cm. Subsequently, it decreases and then increases again, culminating in a local maximum at the bottom of the asphalt layer.

(4) Combined ε_t and ε_s dynamics: The aggregate of ε_t and ε_s progressively increases with depth, achieving a local peak at 13.5 cm. Following this, there is a slight decrease before it increases again, reaching the global maximum at the asphalt layer's bottom.

A comparative analysis of the depth-wise distributions of α, ε_t, ε_s, and their combined sum below 7.5 cm depth demonstrates that at 13.5 cm, ε_s and the sum of ε_t and ε_s attain their respective global and local maxima, while α records its global minimum. As depth increases, both ε_t and the combined sum of ε_t and ε_s reach their global maximum values at the layer's base, where ε_s achieves a local maximum. In this context, α also registers a local minimum. This complex interplay highlights the significant influence of both tensile and shear strains, and their cumulative effect, on determining the fatigue life of the asphalt layer in a flexible base asphalt pavement structure.

6.1.3.2 Transverse Direction

Figure 6-7 of Test Section II provides a comprehensive depiction of the distribution of the life factor α, tensile strain ε_t, shear strain ε_s, and the sum of ε_t and ε_s along the depth of the asphalt layer at the edge of the wheel paths, aligned perpendicularly to the axle load movement direction. The figure specifically identifies, with arrows, the depths at and below 7.5 cm where these factors achieve their maximum values, either on a global or local scale. The key findings from this analysis include:

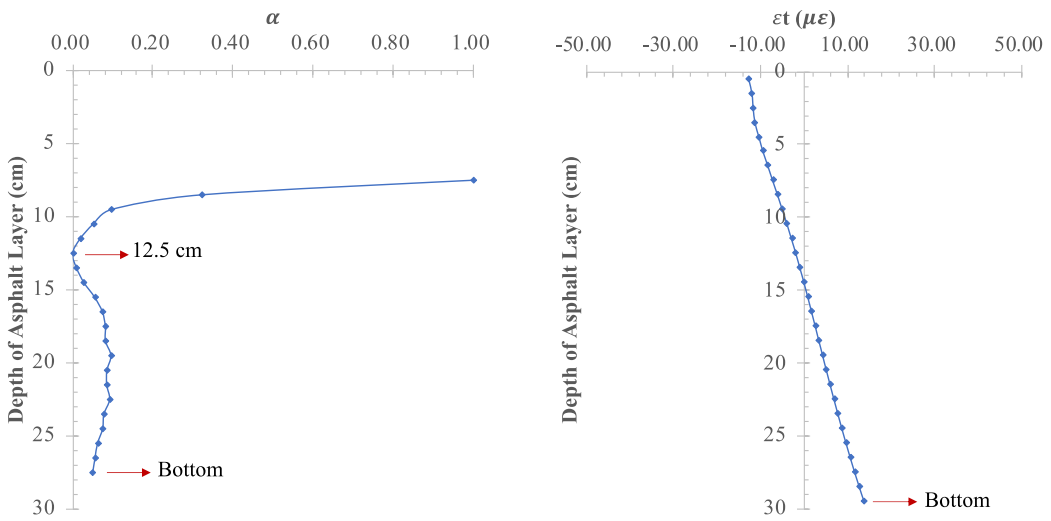

(a) Average normalized α

(b) Average tensile strain ε_t

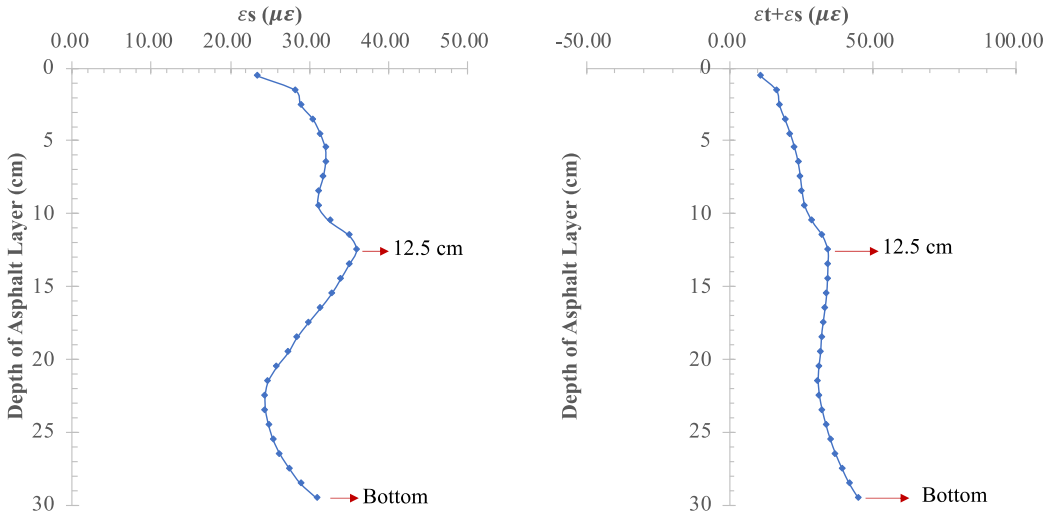

(c) Average shear strain ε_s (d) Sum of tensile and shear strains $(\varepsilon_t + \varepsilon_s)$

Figure 6-7 Transverse mechanical responses at the outer edge of the wheel path for Section II

(1) Depth-dependent behavior of life factor α: The value of α exhibits a rapid decrease with increased depth, reaching its overall minimum at 12.5 cm. Beyond this depth, α shows a slight increase followed by a decrease, culminating in a local minimum at the asphalt layer's bottom.

(2) Tensile strain ε_t trends with depth: ε_t consistently increases as the depth increases, achieving its maximum value at the bottom of the asphalt layer.

(3) Shear strain ε_s distribution complexity: The distribution of ε_s is intricate; initially decreasing and then increasing with depth, ε_s reaches its overall maximum at 12.5 cm. Following this peak, ε_s experiences a decrease and then an increase, culminating in a local maximum at the layer's base.

(4) Combined ε_t and ε_s variation with depth: The sum of ε_t and ε_s undergoes a gradual change with increasing depth. Below 7.5 cm, this combined value first decreases and then increases, reaching a local maximum at 12.5 cm. It then follows a similar pattern of decrease and increase, achieving its overall maximum at the asphalt layer's bottom.

Comparative analysis of the depth-wise distributions of α, ε_t, ε_s, and their combined sum below 7.5 cm reveals a distinct pattern. The distribution of α inversely mirrors the trends of ε_s and the sum of ε_t and ε_s. Notably, at the depth of 12.5 cm, where ε_s and the combined sum of ε_t and ε_s reach their respective overall and local maxima, α attains its overall minimum value. As depth increases, both ε_t and the combined sum of ε_t and ε_s reach their overall maximum at the

layer's bottom, where ε_s also achieves a local maximum. Correspondingly, at this depth, α is observed to reach a local minimum.

6.1.4 Center of the Wheel Path in Section II

6.1.4.1 Longitudinal Direction

Figure 6-8, pertaining to Section II, presents a detailed distribution of the life factor α, tensile strain ε_t, shear strain ε_s, and the combined sum of ε_t and ε_s along the depth of the asphalt layer at the center of the wheel paths, parallel to the axle load movement direction.

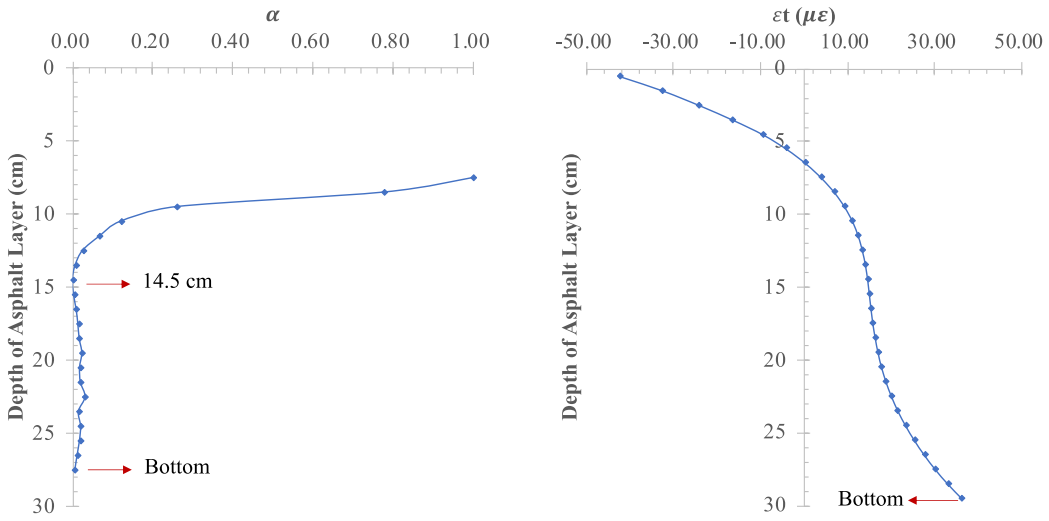

(a) Average normalized α (b) Average tensile strain ε_t

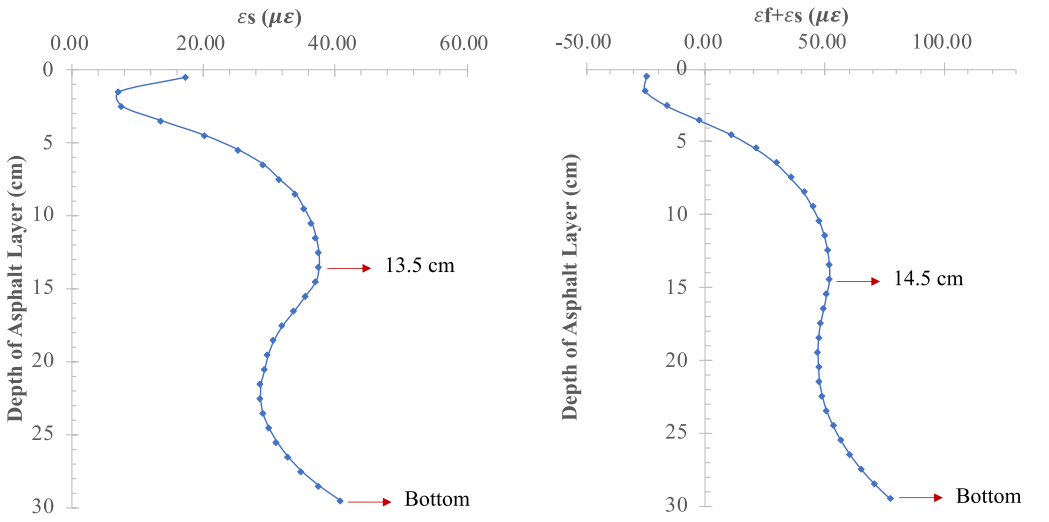

(c) Average shear strain ε_s (d) Sum of tensile and shear strains $(\varepsilon_t + \varepsilon_s)$

Figure 6-8 Longitudinal mechanical responses at the center of the wheel path for Section II

This analysis marks the depths at and below 7.5 cm where the maximum values of these variables are observed, either globally or locally. The key findings from this figure include:

(1) Life factor α trends: α demonstrates a notable decrease with increasing depth, reaching its overall minimum at a depth of 14.5 cm. Following this depth, there is a slight rise in α, followed by a decrease, resulting in a local minimum at the asphalt layer's bottom.

(2) Dynamics of tensile strain ε_t with depth: ε_t shows a consistent increase with depth, achieving its highest value at the bottom of the asphalt layer.

(3) Shear strain ε_s variations below 7.5 cm: Initially, ε_s increases with depth, peaking at a local maximum at 13.5 cm. Beyond this peak, it decreases and then increases again, reaching its global maximum at the layer's bottom.

(4) Combined ε_t and ε_s behavior with depth: The aggregate of ε_t and ε_s first rises with increasing depth, attaining a local maximum at 14.5 cm. Then, it exhibits a slight decrease followed by an increase, culminating in its global maximum at the base of the asphalt layer.

A comparative analysis of the distributions of α, ε_t, ε_s, and their combined sum below 7.5 cm depth reveals crucial insights: At the base of the asphalt layer, where ε_t, ε_s, and their combined sum all reach their maximum values, α is observed to be at its minimum. Notably, at a depth of 14.5 cm, α reaches its overall minimum; however, at this specific depth, neither ε_t nor ε_s individually are at their maximum, only the combined sum of ε_t and ε_s is. This pattern suggests that the fatigue life of the asphalt layer in pavement structures is not solely influenced by individual tensile or shear strains but is significantly affected by the combined impact of flexural-tensile and shear forces.

6.1.4.2 Transverse Direction

Figure 6-9, focusing on Test Section II with a flexible base, presents an in-depth analysis of the life factor α, tensile strain ε_t, shear strain ε_s, and the sum of ε_t and ε_s along the depth of the asphalt layer at the center of the wheel paths, oriented perpendicular to the axle load movement direction. The figure highlights with arrows the depths at and below 7.5 cm where the maximum values of these parameters, whether they are global or local maxima, are located. The key findings from the figure include:

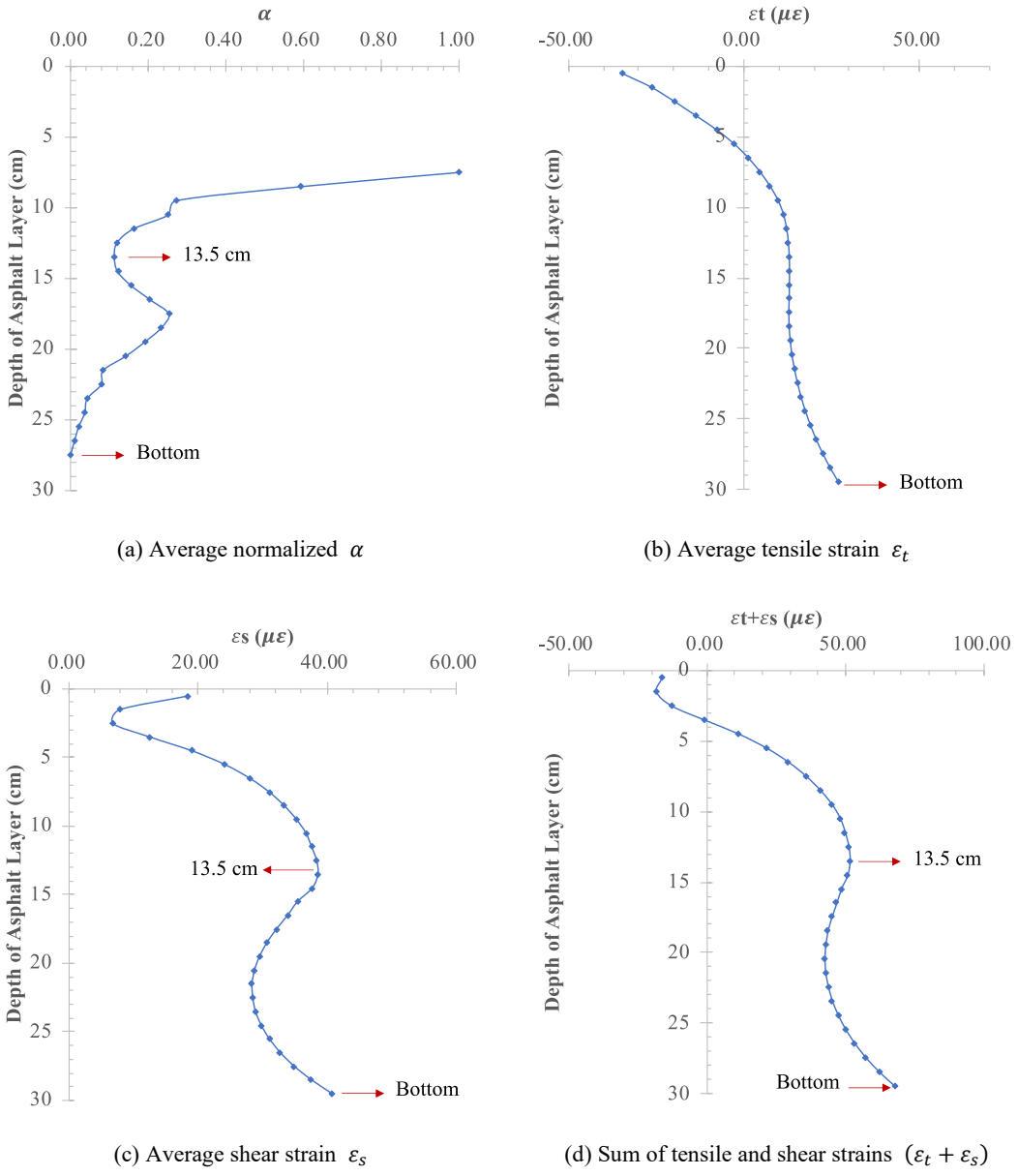

(a) Average normalized α (b) Average tensile strain ε_t

(c) Average shear strain ε_s (d) Sum of tensile and shear strains $(\varepsilon_t + \varepsilon_s)$

Figure 6-9 Transverse mechanical responses at the center of the wheel path for Section II

(1) Life factor α depth-dependent dynamics: Below 7.5 cm: α exhibits a rapid decrease with increasing depth, reaching a local minimum at 13.5 cm. After this point, α undergoes an increase followed by a decrease, culminating in its overall minimum at the asphalt layer's base.

(2) Tensile strain ε_t behavior with depth: ε_t shows a steady increase as depth increases, achieving its highest value at the base of the asphalt layer.

(3) Shear strain ε_s distribution complexity: The pattern of ε_s is intricate; it first increases with depth, reaching a local maximum at 13.5 cm. Following this, ε_s decreases and then increases again, ultimately achieving its global maximum at the base of the asphalt layer.

(4) Combined ε_t and ε_s variations: The sum of ε_t and ε_s initially rises with depth, attaining a

local maximum at 13.5 cm. It then experiences a slight decrease before increasing again, reaching its overall maximum at the asphalt layer's base.

A comparison of the depth-wise distributions of α, ε_t, ε_s, and their combined sum below 7.5 cm reveals that the local minimum value of α at 13.5 cm aligns with the local maximum values of ε_s and the sum of ε_t and ε_s. Additionally, the overall minimum value of α, observed at the base of the asphalt layer, corresponds with the overall maximum values of all three strain measurements. This alignment underscores a significant correlation between the fatigue life of the asphalt layer, as indicated by α, and the combined impacts of tensile and shear strains. It highlights the complexity of the factors influencing the asphalt layer's fatigue life and the importance of considering both individual and combined strain effects in pavement structural analysis.

6.2 Critical Fatigue Damage Locations in Asphalt Layer

The comprehensive analysis encompassing §6.1 has led to a detailed compilation of data concerning the depths where the life factor α exhibits its local or overall minimum values below 7.5 cm in Sections I and II. This data is juxtaposed against the depths where the tensile strain ε_t, shear strain ε_s, and their combined sum reach their respective local or overall maximum values. This comparative information is systematically presented in Table 6-1.

Table 6-1 Depths corresponding to extreme values of α and mechanical responses

Test Position		Direction	α	ε_{t0}	ε_{s0}	$\varepsilon_{t0}+\varepsilon_{s0}$
Section I	Outer Edge of Wheel Path	Transverse	14.5 cm[a]	13.5 cm[a]	7.5 cm[a]	14.5 cm[a]
		Longitudinal	7.5 cm[a]	7.5 cm[a]	7.5 cm[a]	7.5 cm[a]
	Center of Wheel Path	Transverse	14.5 cm[a]	14.5 cm[a]	15.5 cm[a]	14.5 cm[a]
		Longitudinal	15.5 cm[a]	14.5 cm[a]	15.5 cm[a]	15.5 cm[a]
Section II	Outer Edge of Wheel Path	Transverse	13.5 cm[a]	-	13.5 cm[a]	13.5 cm[b]
			Bottom[b]	Bottom[a]	Bottom[b]	Bottom[a]
		Longitudinal	12.5 cm[a]	-	12.5 cm[a]	12.5 cm[b]
			Bottom[b]	Bottom[a]	Bottom[b]	Bottom[a]
	Center of Wheel Path	Transverse	14.5 cm[b]	-	13.5 cm[b]	14.5 cm[b]
			Bottom[a]	Bottom[a]	Bottom[a]	Bottom[a]
		Longitudinal	13.5 cm[b]	-	13.5 cm[b]	13.5 cm[b]
			Bottom[a]	Bottom[a]	Bottom[a]	Bottom[a]

Note: a represents the global maximum or minimum, and b represents the local maximum or minimum.

The insights gleaned from the table are quite revealing:

(1) Complex depth correlation of life factor α and strains: There is an observable disparity between the depths at which α attains its local or overall minimum and the depths at which ε_t or ε_s reach their respective maximums. For example, in Section I, along the edge of the wheel paths, α's minimum occurs at a depth of 14.5 cm. However, the maximum for shear strain ε_s is noted at a significantly different depth of 7.5 cm. Moreover, the distribution pattern of α in Section II demonstrates complexities, with local or overall minimum values being found at various depths within the asphalt layer, including the middle and bottom. Conversely, tensile strain ε_t increases consistently with depth, peaking only at the layer's base, indicating a lack of direct correspondence with the depths of minimum α values.

(2) Consistency of life factor α with combined strain values: A more consistent pattern emerges when comparing the depths of α's minimum values with those where the combined sum of ε_t and ε_s reaches its maximum. This consistency challenges prior research, suggesting that the fatigue damage of asphalt layers is not solely dictated by individual flexural-tensile or shear effects but is more significantly influenced by their combined action.

Consequently, this study defines critical damage locations within the asphalt layer as those depths where the combined strains ε_t and ε_s reach their maximum, and correspondingly, where α attains its minimum, whether locally or overall. This approach revises the understanding of critical damage locations in asphalt pavements with semi-rigid base, which are identified not just at the bottom but potentially within the middle of the layer. Similarly, for asphalt pavements with flexible base, multiple critical damage locations are recognized, both in the middle and at the bottom of the layer. This finding underlines the inadequacy of previous studies that singularly focused on the bottom of the asphalt layer for fatigue damage analysis. It highlights the necessity of considering multiple potential critical damage points within the asphalt layer of pavement structures, factoring in the material properties of the asphalt mixture at these critical locations to accurately predict the initiation of fatigue cracking.

6.3 Fatigue Loading Mode of Asphalt Layer

The analysis conducted in this study reveals a multifaceted understanding of the mechanical mechanism underlying the fatigue damage progressions of asphalt layers within pavement structures.

It is clear that the fatigue damage progressions are not solely affected by either tensile strain or shear strain individually. Rather, it is the result of the combined impact of both flexural-tensile and shear effects. To translate these findings into practical application, the study has established a quantitative analysis between the life factor α and the initial tensile strain ε_{t0} and initial shear strain ε_{s0}.

During this analytical process, the research firstly focused on assessing the Pearson correlation coefficients between α and the initial strains ε_{t0} and ε_{s0}, as well as their combined sum. The outcomes of this correlation analysis are detailed in Table 6-2.

Table 6-2 Correlation analysis between α and mechanical responses of asphalt layer

Test Position		Direction	Parameter	ε_{t0}	ε_{s0}	$\varepsilon_{t0}+\varepsilon_{s0}$
Section I	Outer Edge of Wheel Path	Transverse	Correlation Coefficient	0.755	-0.924	-0.944
			Sig. (Two-tailed)	0.000	0.000	0.000
			No. of Cases	42	42	42
		Longitudinal	Correlation Coefficient	-0.783	-0.732	-0.795
			Sig. (Two-tailed)	0.000	0.000	0.000
			No. of Cases	42	42	42
	Center of Wheel Path	Transverse	Correlation Coefficient	-0.675	-0.666	-0.677
			Sig. (Two-tailed)	0.000	0.000	0.000
			No. of Cases	42	42	42
		Longitudinal	Correlation Coefficient	-0.642	-0.538	-0.641
			Sig. (Two-tailed)	0.007	0.009	0.002
			No. of Cases	42	42	42
Section II	Outer Edge of Wheel Path	Transverse	Correlation Coefficient	-0.548	0.171	-0.627
			Sig. (Two-tailed)	0.003	0.279	0.000
			No. of Cases	42	42	42
		Longitudinal	Correlation Coefficient	-0.516	-0.230	-0.689
			Sig. (Two-tailed)	0.006	0.411	0.000
			No. of Cases	42	42	42
	Center of Wheel Path	Transverse	Correlation Coefficient	-0.663	-0.080	-0.764
			Sig. (Two-tailed)	0.000	0.613	0.000
			No. of Cases	42	42	42
		Longitudinal	Correlation Coefficient	-0.626	0.036	-0.672
			Sig. (Two-tailed)	0.007	0.821	0.000
			No. of Cases	42	42	42

From the data presented in the table, it is observed that in pavements with a semi-rigid base asphalt layer, α exhibits a relatively similar correlation with both the initial tensile strain ε_{t0} and the initial shear strain ε_{s0}. This finding indicates that the fatigue life of the asphalt layer is concurrently influenced by both tensile and shear strains. In contrast, pavements with a flexible base asphalt layer

show a more significant correlation between α and the initial tensile strain ε_{t0} than with the initial shear strain ε_{s0}. This trend suggests a predominant influence of tensile strain on the asphalt layer's fatigue life in such pavement structures.

Moreover, irrespective of whether the pavement structure features a semi-rigid or flexible base, the strongest correlation was consistently observed between the life factor α and the sum of the initial tensile strain ε_{t0} and initial shear strain ε_{s0}. Consequently, it is deduced that the life factor α should be functionally related to the combined sum of the initial tensile strain ε_{t0} and initial shear strain ε_{s0}, highlighting a more comprehensive approach to understanding and predicting asphalt layer fatigue in pavement engineering.

However, a closer examination of the correlation analysis results reveals that most correlation coefficients between the life factor α and the sum of the initial strains hover around 0.7. This observation suggests that the fatigue damage of asphalt layers within pavement structures cannot be solely attributed to the initial tensile strain ε_{t0} and initial shear strain ε_{s0}. Extensive research, as cited in references[3,5-8], corroborates that the fatigue life of asphalt mixtures is also contingent upon the fatigue loading mode. Consequently, it becomes clear that the life factor α is not just a function of the combined values of ε_{t0} and ε_{s0}, but it must also be understood and defined in relation to the fatigue loading mode. This section of the study therefore advances the exploration into the fatigue loading modes present within the asphalt layers, aiming to integrate these modes into the overall understanding of asphalt layer's fatigue damage.

6.3.1 Analysis of Traditional Tensile Fatigue Loading Mode

In prior studies, the fatigue loading mode of asphalt layers has been defined as the method of variation in tensile stress and strain during repeated loading processes [6]. Building on this foundation, the current study initially employs the Mode Factor (MF), as conceptualized by Monismith and Deacon [1], to quantitatively analyze the tensile fatigue loading mode at different depths in the asphalt layers. This analysis is encapsulated in Equation 6-1.

$$\mathrm{MF} = \frac{|A| - |B|}{|A| + |B|} \qquad 6\text{-}1$$

According to this approach, if the modulus at a particular depth in the asphalt layer decays by C%, A represents the percentage change in tensile stress at that depth, while B denotes the percentage

change in tensile strain. Therefore, in scenarios where tensile stress is controlled, the MF value is -1; in cases where tensile strain is controlled, MF is +1. For other tensile fatigue loading modes, where both tensile stress and strain vary, the MF value ranges between -1 and +1.

To ascertain the MF at various depths within the asphalt layers of Sections I and II during the F-sAPT testing, the finite element model shown in Figure 5-23 was utilized. This model computed the tensile stress and strain at different depths within the asphalt layers at both the initial and final stages of loading, denoted as σ_{t0} and ε_{t0} for initial loading, and σ_{tN} and ε_{tN} for final loading. For the initial asphalt layer modulus, this study used the corrected seismic modulus from undamaged areas in these test sections (targeting a frequency of 3.22 Hz and temperature of 20 °C), while for the final modulus, it utilized the corrected results from damaged areas. The moduli for the semi-rigid base, flexible base, and subgrade were derived from inverse analysis values based on FWD testing at the base layer's top.

Subsequently, by analyzing the σ_{t0}, ε_{t0}, σ_{tN} and ε_{tN}, the study determined the corresponding percentage changes in tensile stress (A) and tensile strain (B). These results were then inserted into Equation 6-1 to calculate the MF at various depths within the asphalt layers in different test points and directions throughout the F-sAPT test process in each test section.

6.3.1.1 Section I

Figure 6-10 provides an insightful analysis of the tensile fatigue loading mode MF along the depth at the edge of the wheel paths (Points 1 and 5) in Section I, which consists of a semi-rigid base.

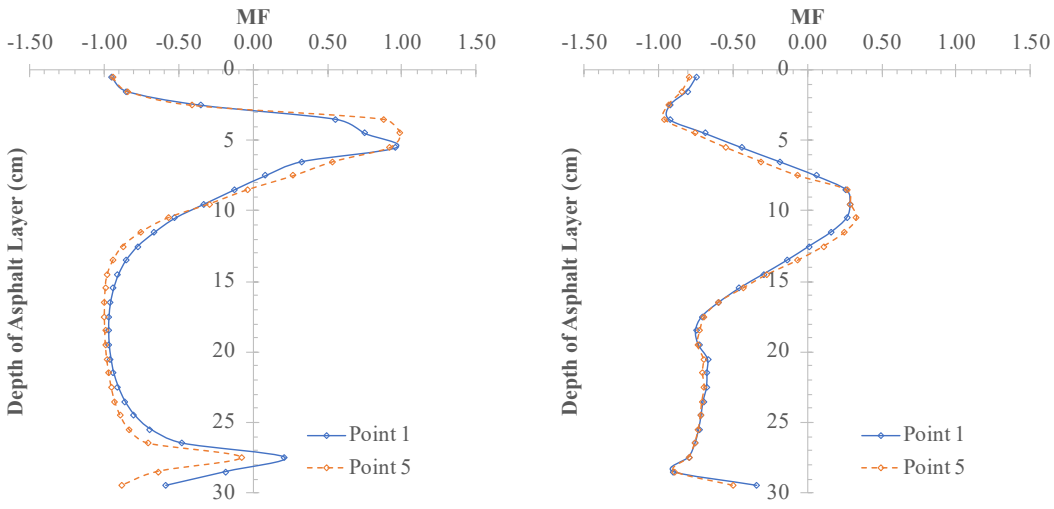

(a) Transverse direction (b) Longitudinal direction

Figure 6-10 The calculated MF at the outer edge of wheel path in Section I

Key observations for the transverse direction (perpendicular to the wheel load direction):

(1) 0.5 cm to 5.5 cm: Within this depth range, MF increases with depth, reaching a value close to +1. This indicates a transition from a tensile stress-controlled fatigue loading mode to a tensile strain-controlled mode.

(2) Below 5.5 cm: MF rapidly decreases with increasing depth, approaching -1. This shift signifies a change back to a tensile stress-controlled fatigue loading mode.

(3) 14.5 cm to 24.5 cm: In this zone, MF remains near -1 and relatively stable, suggesting that the fatigue loading mode predominantly aligns with a tensile stress-controlled mode.

(4) Below 24.5 cm: MF shows a slight increase and then decreases, with the maximum value not exceeding 0.5. This pattern points to a transition towards other fatigue loading modes where both tensile stress and strain are variable.

For the longitudinal direction (parallel to the wheel load direction):

(1) 0.5 cm to 9.5 cm: MF initially decreases and then increases with depth, with the maximum not surpassing 0.5. This indicates a shift from a tensile stress-controlled mode to other fatigue loading modes involving changes in both stress and strain.

(2) Below 9.5 cm: Here, MF generally decreases with depth, approaching -1 at its minimum, signifying a return to a tensile stress-controlled mode.

(3) At the bottom of the asphalt layer: MF ranges between -0.5 and 0, indicative of fatigue loading modes where both tensile stress and strain undergo variations.

Meanwhile, Figure 6-11 presents the analysis of the tensile fatigue loading mode along the depth within the asphalt layer at the center of the wheel paths (Points 2 and 4) in Section I.

Key observations for the transverse direction (perpendicular to the wheel load direction):

(1) 0.5 cm to 11.5 cm: Within this depth range, MF increases with depth, with the maximum value nearing 0. This indicates a transition from a tensile stress-controlled fatigue loading mode to other fatigue loading modes where both tensile stress and strain vary.

(2) Below 11.5 cm: MF rapidly decreases with increasing depth, approaching -1. This shift signifies a change back to a tensile stress-controlled fatigue loading mode.

(3) 16.5 cm to 29.5 cm: In this zone, MF remains close to -1 and relatively constant, suggesting that the fatigue loading mode predominantly aligns with a tensile stress-controlled mode.

(4) At the bottom of the asphalt layer: Here, MF ranges between -0.5 and 0, indicative of other

fatigue loading modes where both tensile stress and strain change.

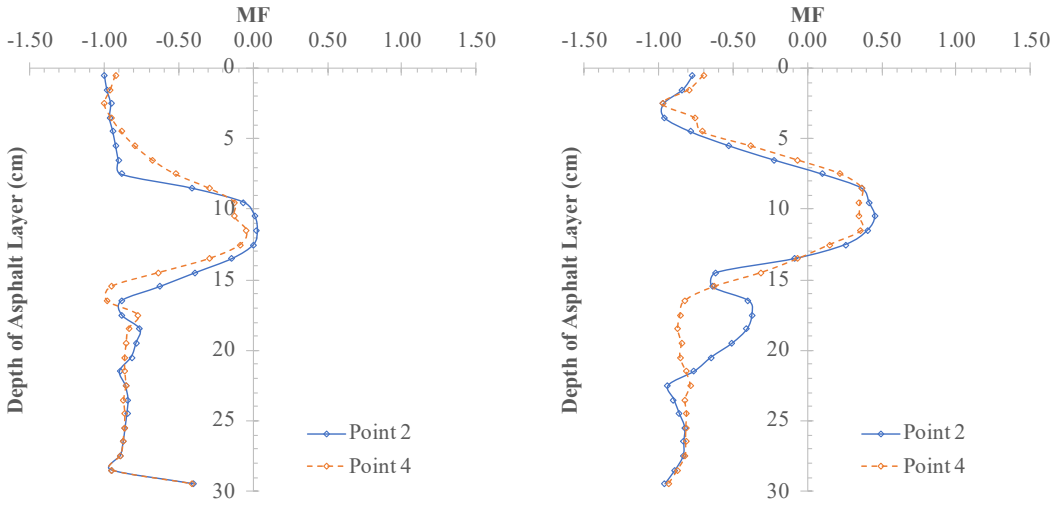

(a) Transverse direction (b) Longitudinal direction

Figure 6-11 The calculated MF at the center of wheel path in Section I

For the longitudinal direction (parallel to the wheel load direction):

(1) 0.5 cm to 10.5 cm: MF initially decreases slightly and then increases with depth, with the maximum not surpassing +0.5. This pattern indicates a shift from a tensile stress-controlled mode to other fatigue loading modes involving changes in both stress and strain.

(2) Below 10.5 cm: MF generally decreases with increasing depth, approaching -1 at its minimum, signifying a return to a tensile stress-controlled mode.

6.3.1.2 Section II

Figure 6-12 presents the analysis of the fatigue loading mode MF along the depth at the edge of the wheel paths (Test Points 1 and 5) in Section II, which features a flexible base.

Key observations for the transverse direction (perpendicular to the wheel load direction):

(1) 0.5 cm to approximately 11.5 cm: Within this depth range, MF initially decreases slightly and then increases, with the maximum value approaching +1. This indicates a transition from a tensile stress-controlled fatigue loading mode to a tensile strain-controlled mode.

(2) 11.5 cm to 24.5 cm: Here, MF generally decreases with increasing depth, nearing -1. This shift signifies a change from a tensile strain-controlled mode back to a tensile stress-controlled fatigue loading mode.

(3) Below 24.5 cm: MF slightly increases with depth, but the maximum value remains less than -0.5, suggesting a persistent inclination towards a tensile stress-controlled mode.

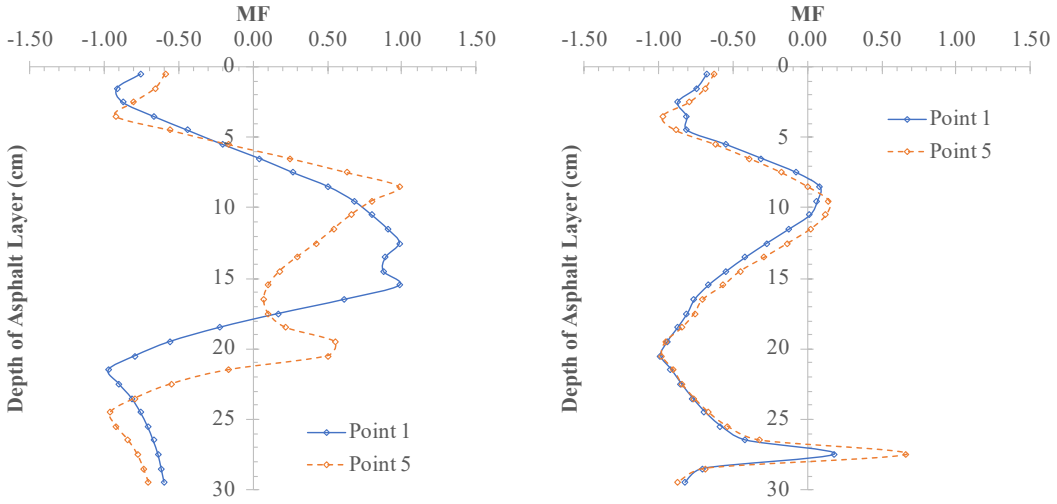

(a) Transverse direction (b) Longitudinal direction

Figure 6-12 The calculated MF at the outer edge of wheel path in Section II

For the longitudinal direction (parallel to the wheel load direction):

(1) 0.5 cm to 9.5 cm: MF initially decreases slightly and then increases with depth, with the maximum value near 0. This pattern indicates a shift from a tensile stress-controlled mode to other fatigue loading modes involving changes in both tensile stress and strain.

(2) 9.5 cm to 20.5 cm: In this depth range, MF decreases with increasing depth, approaching -1 at its minimum. This suggests a transition from other fatigue loading modes back to a tensile stress-controlled mode.

(3) Below 20.5 cm: Here, MF first increases and then decreases with depth. The fatigue loading mode transitions from a tensile stress-controlled mode to other modes, before shifting back to a tensile stress-controlled mode at the base of the asphalt layer.

Figure 6-13 presents the distribution of the MF along the depth at the center of the wheel paths (Points 2 and 4) in Section II. The findings indicate that the distribution of MF perpendicular to the direction of wheel load is similar to the results analyzed parallel to the direction of wheel load. Key observations include:

(1) 0.5 cm to 9.5 cm: Within this range, MF initially decreases slightly and then increases with depth. The maximum value does not exceed +0.5, indicating a transition from a tensile stress-controlled fatigue loading mode to other fatigue loading modes where both tensile stress and strain change.

(2) 9.5 cm to 17.5 cm: In this depth range, MF decreases with increasing depth, approaching -1.

This suggests a shift from other fatigue loading modes to a tensile stress-controlled mode.

(3) Below 17.5 cm: Below this depth, MF first increases and then decreases, with the maximum value not exceeding 0.3. The fatigue loading mode initially transitions from a tensile stress-controlled mode to other modes and then shifts back to a tensile stress-controlled mode at the base of the asphalt layer.

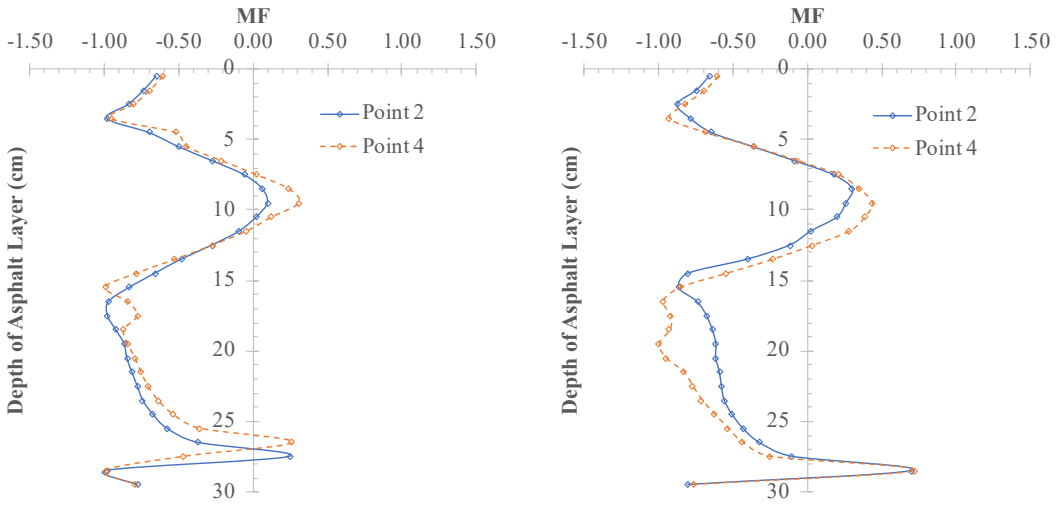

(a) Transverse direction – Section II (b) Longitudinal direction– Section II

Figure 6-13 The calculated MF at the center of wheel path in Section II

Summarizing the aforementioned results, it is evident that there is a dynamic pattern in the tensile fatigue loading mode of the asphalt layer. The Mode Factor (MF) values exhibit variability with depth, signifying shifts between tensile stress-controlled and tensile strain-controlled modes. These findings underscore the complexity of fatigue behavior in asphalt layers under varying stress and strain conditions within pavement structures. This nuanced understanding of fatigue loading modes, as reflected in the changing MF values at different depths, emphasizes the multifaceted nature of fatigue responses in pavement materials, highlighting the need for comprehensive analysis in pavement design and maintenance.

6.3.2 Propose of Composite Fatigue Loading Mode

This study's analysis reveals that MF primarily reflects changes in flexural-tensile stress and strain. Consequently, a relationship between the life factor α and MF would predominantly address the influence of flexural-tensile effects on the fatigue damage process and the asphalt layer's fatigue life. However, as detailed in §6.1 and §6.2, it's clear that the fatigue of asphalt layers is influenced

not only by flexural-tensile effects but also significantly by the combined impact of both flexural-tensile and shear effects.

To address this broader spectrum of influences, this study introduces a new composite fatigue loading mode factor, designated as CMF, as expressed by Equation 6-2. CMF is devised to quantitatively analyze the variations in the combined tensile and shear stresses and strains at various depths within the asphalt layers.

$$\mathrm{CMF} = \frac{|A'| - |B'|}{|A'| + |B'|} \qquad 6\text{-}2$$

where A' represents the percentage change in the sum of tensile and shear stresses, and B' the percentage change in the sum of tensile and shear strains at a given depth. Under this framework, CMF equals -1 when the sum of stresses is controlled, and +1 when the sum of strains is controlled. For other fatigue loading modes involving changes in both the sums of stresses and strains, the value of CMF ranges between -1 and +1.

In alignment with the analysis method used for MF, the study employs the finite element model illustrated in Figure 5-23. This model is used to calculate the tensile stress, tensile strain, shear stress, and shear strain at various depths within the asphalt layer at different test points and orientations, both at the initial and final stages of loading. The initial loading results, including tensile and shear stresses and strains, are denoted as σ_{t0}, ε_{t0}, σ_{s0}, and ε_{s0}, while the final loading results are $\sigma_{t\mathrm{N}}$, $\varepsilon_{t\mathrm{N}}$, $\sigma_{s\mathrm{N}}$, and $\varepsilon_{s\mathrm{N}}$. These measurements consider the initial and final moduli of the asphalt layer, reflecting the states of the undamaged and damaged areas within the test sections, respectively.

By analyzing these loading results, the study calculates the corresponding percentage changes in the sum of tensile and shear stresses (A') and the sum of tensile and shear strains (B'). These calculations are then integrated into Equation 6-2 to determine the composite fatigue loading mode CMF at various depths across different test points and directions during the F-sAPTs in each test section. This approach offers a more comprehensive understanding of the fatigue behavior under varied stress and strain conditions within the asphalt layers of pavement structures.

6.3.2.1 Section I

Figure 6-14 presents the analysis of the CMF along the depth at the edge of the wheel paths (Test Points 1 and 5) in Section I, which has a semi-rigid base.

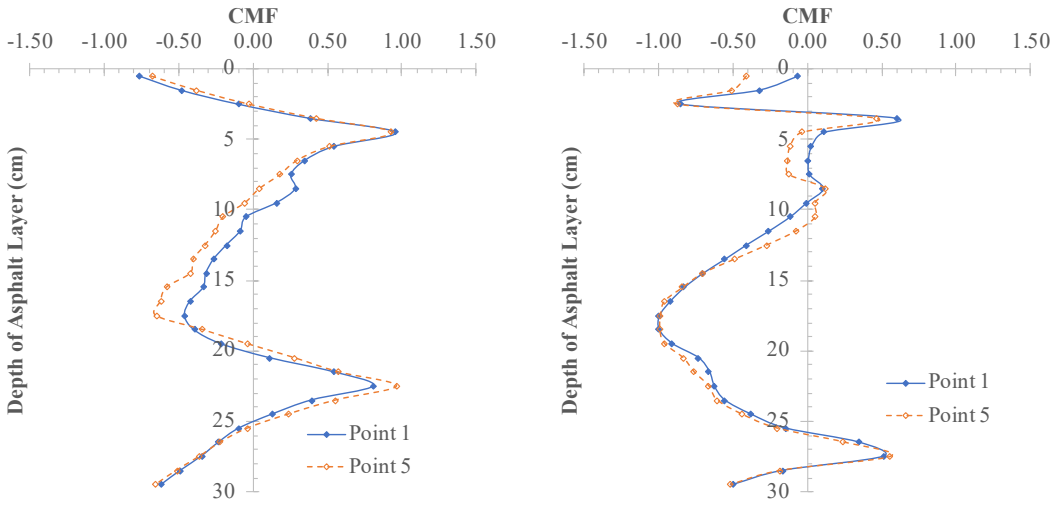

(a) Transverse direction (b) Longitudinal direction

Figure 6-14 The calculated CMF at the outer edge of wheel path in Section I

Key observations for the transverse direction (perpendicular to the wheel load direction):

(1) 0.5 cm to 5.5 cm: Within this depth range, CMF increases with depth, with the maximum value nearing +1. This indicates a shift in the fatigue loading mode from a stress sum-controlled mode to a strain sum-controlled mode.

(2) 5.5 cm to 17.5 cm: CMF rapidly decreases with increasing depth, approaching -1. This suggests a transition from a strain sum-controlled mode back to a stress sum-controlled mode.

(3) 17.5 cm to 22.5 cm: Here, CMF quickly increases with depth, nearing +1, indicating a shift again from a stress sum-controlled mode to a strain sum-controlled mode.

(4) Below 22.5 cm: CMF decreases with depth, with the minimum value being less than -0.6, suggesting a return to a stress sum-controlled fatigue loading mode.

For the longitudinal direction (parallel to the wheel load direction):

(1) 0.5 cm to 2.5 cm: In this range, CMF decreases with depth, with the minimum value approaching -1. This transition indicates a shift from other fatigue loading modes involving changes in both stress and strain sums to a stress sum-controlled mode.

(2) 2.5 cm to 8.5 cm: CMF exhibits a complex distribution along this depth range, with the maximum value near +0.5, suggesting a shift back to other fatigue loading modes from a stress sum-controlled mode.

(3) 8.5 cm to 18.5 cm: Here, CMF rapidly decreases with increasing depth, nearing -1, indicating a shift back to a stress sum-controlled mode from other fatigue loading modes.

(4) 18.5 cm to 27.5 cm: CMF quickly increases with depth, nearing +0.5, indicating a transition again to other fatigue loading modes from a stress sum-controlled mode.

(5) Below 27.5 cm: CMF decreases with increasing depth, with the minimum value close to -0.5, suggesting the persistence of other fatigue loading modes involving changes in both stress and strain sums.

Figure 6-15 shows the analysis of the CMF along the depth within the asphalt layer at the center of the wheel paths (Test Points 2 and 4) in Section I.

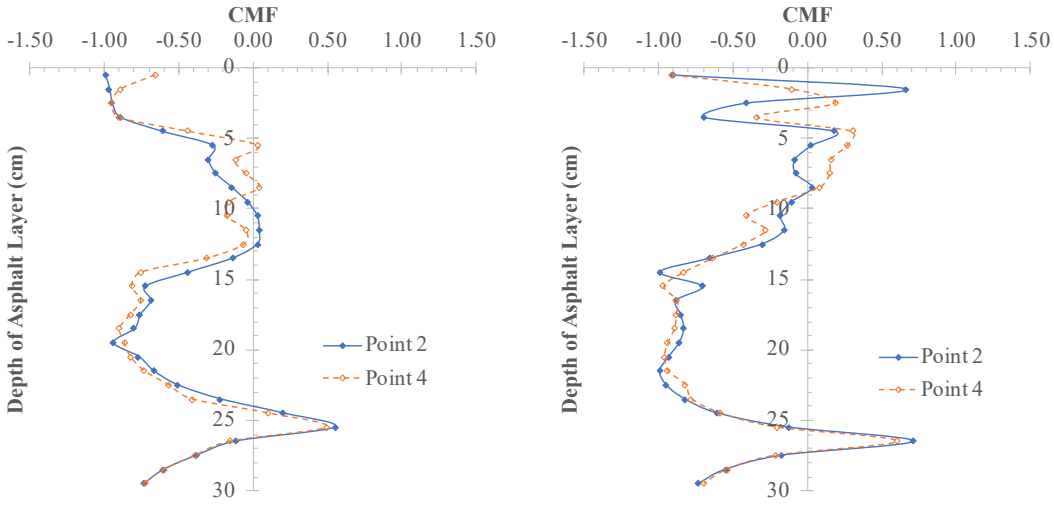

(a) Transverse direction (b) Longitudinal direction

Figure 6-15 The calculated CMF at the center of wheel path in Section I

Key observations for the transverse direction (perpendicular to the wheel load direction):

(1) 0.5 cm to 12.5 cm: In this range, CMF generally increases with depth, with the maximum value nearing 0. This indicates a shift in the fatigue loading mode from a stress sum-controlled mode to other modes involving changes in both the sums of stress and strain.

(2) 12.5 cm to 19.5 cm: Here, CMF decreases with increasing depth, approaching -1. This suggests a transition from other fatigue loading modes to a stress sum-controlled mode.

(3) 19.5 cm to 25.5 cm: In this zone, CMF rapidly increases with depth, with the maximum value close to +0.5. This shift signifies a transition from a stress sum-controlled mode to other fatigue loading modes.

(4) Below 25.5 cm: Below this depth, CMF decreases with increasing depth, and the minimum value is less than -0.7, indicating a shift back to a stress sum-controlled mode.

For the longitudinal direction (parallel to the wheel load direction):

(1) 0.5 cm to 9.5 cm: The variability of CMF along this depth range is complex, with the fatigue loading mode transitioning from a stress sum-controlled mode to other modes involving changes in both stress and strain sums, progressively shifting towards the latter.

(2) 9.5 cm to 21.5 cm: In this range, CMF decreases with depth, nearing -1, indicating a shift from other fatigue loading modes to a stress sum-controlled mode.

(3) 21.5 cm to 26.5 cm: Here, CMF rapidly increases with depth, with the maximum value greater than +0.6, suggesting a transition from a stress sum-controlled mode to a strain sum-controlled mode.

(4) Below 26.5 cm: Below this depth, CMF decreases with increasing depth, and the minimum value is less than -0.7, indicating a shift back from a strain sum-controlled mode to a stress sum-controlled mode.

6.3.2.2 Section II

Figure 6-16 presents the analysis of the CMF along the depth at the edge of the wheel paths (Test Points 1 and 5) in Section II, which features a flexible base.

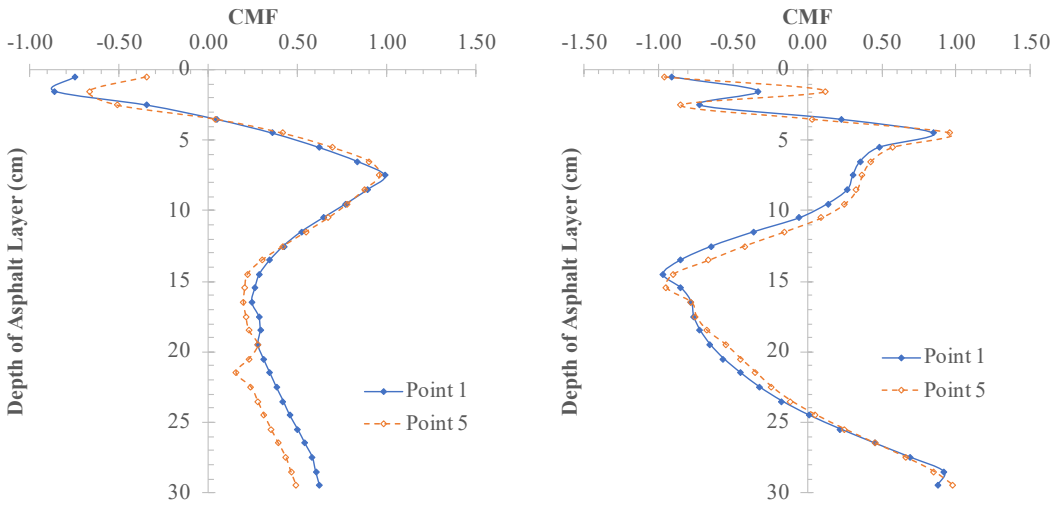

(a) Transverse direction (b) Longitudinal direction

Figure 6-16 The calculated CMF at the outer edge of wheel path in Section II

Key observations for the transverse direction (perpendicular to the wheel load direction):

(1) 0.5 cm to 7.5 cm: In this depth range, CMF initially decreases slightly and then increases with depth. This indicates a shift in the fatigue loading mode from a stress sum-controlled mode to a strain sum-controlled mode.

(2) Below 7.5 cm: CMF first decreases and then increases with depth, signifying a transition from

a strain sum-controlled mode to other fatigue loading modes where both the sums of stress and strain change.

For the longitudinal direction (parallel to the wheel load direction):

(1) 0.5 cm to 4.5 cm: Here, CMF increases with depth, with the maximum value nearing +1. This suggests a transition from a stress sum-controlled mode to a strain sum-controlled mode.

(2) 4.5 cm to 15.5 cm: In this depth range, CMF decreases with increasing depth, approaching -1. This indicates a shift from a strain sum-controlled mode back to a stress sum-controlled mode.

(3) Below 15.5 cm: Below this depth, CMF increases with increasing depth, with the maximum value nearing +1, indicating a transition again from a stress sum-controlled mode to a strain sum-controlled mode.

Figure 6-17 provides the distribution of the CMF along the depth at the center of the wheel paths (Test Points 2 and 4) in Section II. The findings indicate that the distribution of CMF perpendicular to the direction of wheel load is similar to the results analyzed parallel to the direction of wheel load.

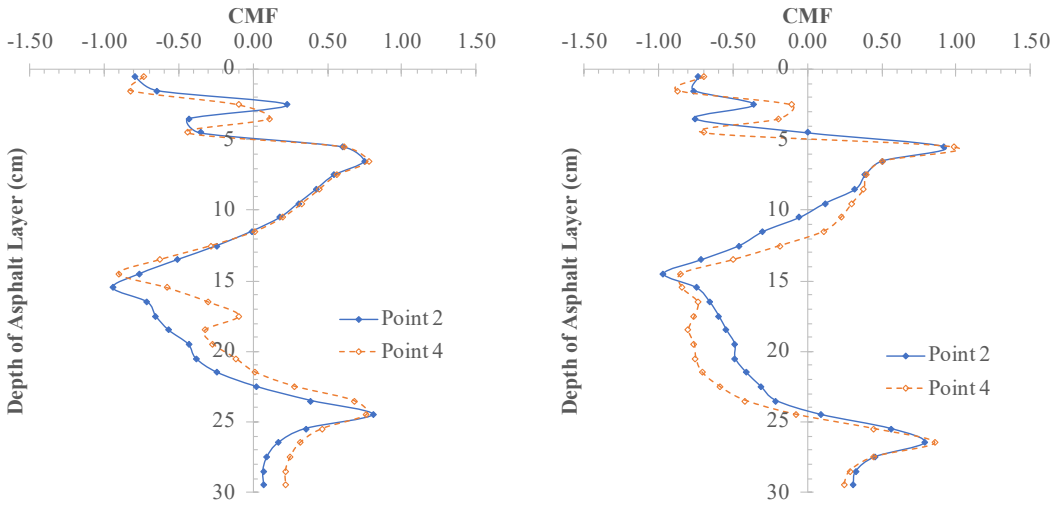

(a) Transverse direction – Section II

(b) Longitudinal direction– Section II

Figure 6-17 The calculated CMF at the center of wheel path in Section II

Key observations include:

(1) 0.5 cm to 6.5 cm: In this depth range, CMF increases with depth, with the maximum value exceeding +1. This indicates a transition from a stress sum-controlled fatigue loading mode to a strain sum-controlled mode.

(2) 6.5 cm to 15.5 cm: Here, CMF decreases with increasing depth, approaching -1. This suggests a shift from a strain sum-controlled mode back to a stress sum-controlled mode.

(3) Below 15.5 cm: Below this depth, CMF first increases and then decreases, with the maximum value nearing +0.8. The fatigue loading mode initially transitions from a stress sum-controlled mode to a strain sum-controlled mode, and then shifts to other fatigue loading modes involving changes in both stress and strain sums at the base of the asphalt layer.

Summarizing the findings from §6.3.2.1 and §6.3.2.2, it is evident that the fatigue loading mode of the asphalt layers within pavement structures varies with the depth of the asphalt layer. These analytical results corroborate the research conclusions of Zhu [9], affirming that even within the same pavement structure, the fatigue loading mode of asphalt mixtures varies at different depths. Further analysis indicates that even at the same depth, the values of MF and CMF differ across various test points and in different directions of measurement. This showcases an extremely complex fatigue evolution process throughout the asphalt layer. It is therefore impractical to generalize a single fatigue loading mode as applicable to an entire asphalt layer, nor is it feasible to directly associate the fatigue loading mode of asphalt layers solely with the thickness of the asphalt layer. These observations highlight the nuanced and intricate nature of fatigue behavior in asphalt layer, necessitating a comprehensive and multi-faceted approach to understanding and addressing fatigue in pavement engineering.

6.4 Summary

This chapter advances from the SBF analysis in the preceding chapter, focusing on the mechanisms responsible for fatigue damage in asphalt layers. It undertakes a meticulous exploration of these mechanisms to understand their role in influencing the longevity and resilience of pavement. The chapter also emphasizes a detailed investigation into the zones within both semi-rigid and flexible asphalt pavements that are most vulnerable to fatigue damage. This comparative study is crucial for understanding the distinct responses of different pavement types under similar operational conditions. Furthermore, the chapter breaks new ground by proposing the concept of the composite loading mode factor, an innovative approach that addresses the inadequacies of traditional tensile fatigue loading modes, which often fail to accurately represent real-world complexities faced by asphalt layers.

The main findings of this chapter are as follows:

(1) The interplay of tensile and shear forces determines the locations of critical damage in asphalt layers within pavement structures. Additionally, these locations are notably distinct in semi-rigid and flexible asphalt pavements. In asphalt pavements with a semi-rigid base, critical damage predominantly occurs in the mid-asphalt layer, whereas asphalt pavements with a flexible base exhibit critical damage both in the mid-asphalt layer and at the bottom of the asphalt layer.

(2) Regarding the life factor α, its strongest correlations are observed with the combined tensile and shear strains, rather than with individual strains. The study also notes that the minimum value of α does not consistently align with the maximum values of individual strains, but rather with the peak of their combined sum.

(3) The fatigue loading mode varies significantly across different depths and even varies at the same depth when comparing different test points and directions. This complexity suggests that fatigue loading modes cannot be universally applied across an asphalt layer and cannot be simplistically linked to its thickness. These findings underscore the complexity of fatigue behavior in pavements and challenge conventional understanding, highlighting the need for nuanced and multifaceted analysis in pavement engineering.

References

[1] Huang, C., Gao, D., & Zhu, H. Influence of loading frequency on fatigue performance of fiber reinforced asphalt concrete. *Journal of North China Institute of Water Conservancy and Hydroelectric Power*, 2012, 33(06):106-111.

[2] Ma, Z. *Research on the fatigue performance and the method for estimation of remaining fatigue life of in-service asphalt mixture*. Shanghai: Tongji University, 2018.

[3] Monismith, C. L. *Fatigue response of asphalt-aggregate mixes*. Washington, D.C.: Strategic Highway Research Program, 1994.

[4] Pell, P. S. Characterization of fatigue behavior. In *Proceedings of 52nd Annual Meeting of the Highway Research Board*. Columbia: Highway Research Board, 1973:49-64.

[5] Rowe, G. M. Performance of asphalt mixtures in the trapezoidal fatigue test. *Journal of the Association of Asphalt Paving Technologists*, 1993, 62:344-384.

[6] Tangella, S. C., Craus, J., Deacon, J. A., et al. *Summary report on fatigue response of asphalt mixtures*. Washington, D.C.: Strategic Highway Research Program, 1990.

[7] Tsai, B. W. *High-temperature fatigue and fatigue damage process of aggregate-asphalt mixes*. Berkeley: University of California, Berkeley, 2003.

[8] Yang, Y. *Research on fatigue damage of asphalt mixture under different loading frequencies*. Changsha: Changsha University of Science and Technology, 2009.

[9] Zhu, J. *Evaluation and critical damage position for fatigue behavior of asphalt pavement considering the full temperature profile*. Shanghai: Tongji University, 2016.

7 RELATIONSHIPS BETWEEN LABORATORY AND IN-SITU FATIGUE DAMAGE PROGRESSIONS

In this study, a meticulous examination of existing research both domestically and internationally reveals that, although numerous researchers have proposed conversion factors and empirical values to elucidate the relationship between fatigue life in laboratory asphalt mixtures and asphalt layers in structural applications, a definitive link concerning the evolution of fatigue damage between these two scenarios remains unestablished. To bridge this gap, this investigation leverages regression analysis findings from the SBF to develop a nuanced model that correlates the life factor α and the shape factor β of SBF parameters in both laboratory and real-world environments.

The methodology commences with the integration of in-situ loading parameters into laboratory-based model parameter interpretation equations. Subsequently, the study introduces a meticulously crafted conversion factor, designed to seamlessly connect model parameters derived from laboratory tests with those obtained from F-sAPTs data. Such an approach is crucial for the accurately transposing laboratory fatigue test outcomes to practical applications in pavement conditions, ensuring that theoretical insights are effectively translated into real-world engineering solutions.

7.1 Comparative Analysis of Parameter α

§ 4.4.3 presents the development of the expression for the life factor α of laboratory asphalt mixtures under varying fatigue loading modes. This development involved the application of the conversion equation method, combined with an S-shaped function, to formulate a unified equation guided by the fatigue loading mode factor. This final unified expression is encapsulated as follows:

$$\alpha_L = F'_{\alpha L} \cdot \alpha_{L-\sigma} \tag{7-1}$$

$$F'_{\alpha L} = 1 + \frac{F_{\alpha L} - 1}{1 + e^{k_{\alpha L} \cdot \mathrm{MF}}} = 1 + \frac{e^{19.509} \cdot {\varepsilon_{t0}}^{-1.561} \cdot e^{-0.783TR} - 1}{1 + e^{(-22.507 + 1.561 \ln(\varepsilon_{t0}) + 0.783TR) \cdot \mathrm{MF}}} \tag{7-2}$$

$$\alpha_{L-\sigma} = e^{24.086 - 3.365 \ln(\varepsilon_{t0}) + 0.859TR} \tag{7-3}$$

where α_L is the life factor of laboratory asphalt mixtures under varying fatigue loading modes. This equation is intricately linked to the initial tensile strain amplitude ε_{t0}, the ratio of rest period to loading time TR, and the tensile fatigue loading mode MF.

In the quest to correlate the life factor α of asphalt mixtures in laboratory conditions with that in structural applications, the study integrates in-situ loading factors into this laboratory-based α interpretation equations. This necessitates the determination of the initial strain at different depths of the asphalt, the TR, and the fatigue loading mode during the F-sAPTs.

Drawing insights from Chapter 6, which establishes that the fatigue damage process in asphalt layers is influenced by both flexural-tensile and shear forces, the initial tensile strain amplitude ε_{t0} in the equation is substituted with the sum of the initial tensile strain ε_{t0} and initial shear strain ε_{s0}. These values are calculated using the finite element model depicted in Figure 5-23. Furthermore, the equation incorporates a combined fatigue loading mode CMF, as proposed in §6.2.3.

Besides, TR during the F-sAPTs is determined through the analysis of strain waveforms within the asphalt layer of Section I, as demonstrated in Figure 7-1 and defined in Equation 7-4, where T represents the total time between two strain amplitudes and t is half the loading time.

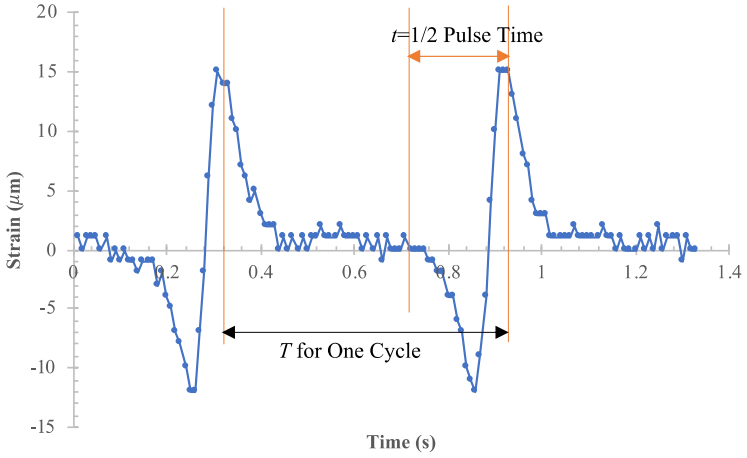

Figure 7-1 Determination of in-situ TR

$$TR = \frac{T - 2t}{2t} = \frac{T}{2t} - 1 \qquad 7\text{-}4$$

The findings conclude that the average TR value during the F-sAPTs is 0.5. All these values, when input into the equation, yields the calculated life factor α_F of the laboratory asphalt mixture under the loading conditions of the F-sAPTs. Then, a conversion factor CF_α, designed to seamlessly

connect model parameters derived from laboratory tests with those obtained from F-sAPTs data, can be expressed by:

$$\mathrm{CF}_{\alpha} = \frac{\alpha_F}{\alpha_L} \qquad 7\text{-}5$$

This CF_{α} indicates that, at a damage level of 0.368, the ratio of load applications the asphalt mixture can endure in the F-sAPT compared to that in a laboratory setting under similar loading conditions. The analytical results for the outer edge and center of the wheel paths in Sections I and II are detailed in Table 7-1 to Table 7-4.

The data analysis reveals that this conversion factor fluctuates with changes in pavement structure and is significantly influenced by the depth of the asphalt layer. It is observed that even within the same pavement structure, CF_{α} values vary at different depths. Further scrutiny shows that at the same depth, CF_{α} values differ across various test points and measurement directions, displaying substantial differences in magnitude.

In the case of Section I, which features a semi-rigid base, the pattern of CF_{α} is characterized by an initial increase, followed by a decrease, and then an increase again towards the bottom of the asphalt layer. This pattern is replicated in the most test points and directions of Section II, which comprises a flexible base. However, CF_{α} on the transverse direction outside the wheel paths of Section II initially exhibits a slight decrease with depth, then consistently increases, peaking at the asphalt layer's bottom.

These findings underscore the complexity of the relationship between the life factor α as derived from laboratory tests and that obtained from F-sAPTs data. Meanwhile, the close association of α with fatigue life explains a wide range of shift factors to adapt the fatigue life from laboratory asphalt mixtures to that of asphalt layers in the literature reviews in Chapter 2.

Table 7-1 The calculated CF_{α} for the outer edge of the wheel paths in Section I

Depth	Transverse direction at Test Point 1			Transverse direction at Test Point 5			Longitudinal direction at Test Point 1			Longitudinal direction at Test Point 5		
	α_F	α_L	CF_{α}	α_F	α_L	CF_{α}	α_F	α_L	CF_{α}	α_F	α_L	CF_{α}
7.5 cm	3.86E+06	1.81E+12	2.14E-06	3.03E+06	1.62E+12	1.88E-06	7.59E+06	1.45E+11	5.22E-05	4.30E+06	2.51E+10	1.72E-04
8.5 cm	4.27E+06	1.88E+12	2.27E-06	3.25E+06	1.22E+12	2.67E-06	9.18E+06	1.97E+11	4.66E-05	5.28E+06	1.73E+11	3.05E-05
9.5 cm	5.05E+06	1.83E+12	2.76E-06	3.70E+06	5.01E+11	7.39E-06	7.68E+06	1.04E+11	7.36E-05	6.16E+06	1.24E+11	4.94E-05
10.5 cm	5.14E+06	6.30E+11	8.16E-06	3.69E+06	5.43E+10	6.80E-05	6.65E+06	2.72E+10	2.44E-04	7.86E+06	1.27E+11	6.20E-05
11.5 cm	5.61E+06	3.69E+11	1.52E-05	3.74E+06	2.38E+10	1.57E-04	5.24E+06	2.99E+09	1.75E-03	6.71E+06	4.07E+10	1.65E-04
12.5 cm	6.06E+06	9.07E+10	6.68E-05	3.90E+06	7.58E+09	5.14E-04	4.85E+06	2.57E+08	1.89E-02	5.90E+06	2.25E+09	2.62E-03
13.5 cm	6.83E+06	2.39E+10	2.86E-04	4.28E+06	2.14E+09	2.00E-03	4.85E+06	2.80E+07	1.73E-01	5.45E+06	7.56E+07	7.21E-02
14.5 cm	7.20E+06	1.11E+10	6.47E-04	4.54E+06	1.75E+09	2.60E-03	4.96E+06	3.13E+06	1.58E+00	5.13E+06	2.98E+06	1.72E+00
15.5 cm	7.81E+06	9.60E+09	8.13E-04	4.94E+06	1.25E+08	3.95E-02	5.16E+06	8.57E+05	6.03E+00	5.14E+06	7.67E+05	6.71E+00
16.5 cm	8.28E+06	2.37E+09	3.50E-03	5.45E+06	7.23E+07	7.54E-02	5.45E+06	6.31E+05	8.63E+00	5.28E+06	5.70E+05	9.25E+00
17.5 cm	8.77E+06	1.55E+09	5.64E-03	6.34E+06	5.09E+07	1.25E-01	5.79E+06	6.79E+05	8.53E+00	5.71E+06	6.61E+05	8.64E+00
18.5 cm	9.45E+06	5.64E+09	1.67E-03	8.15E+06	1.35E+10	6.05E-04	6.50E+06	8.22E+05	7.91E+00	6.37E+06	7.92E+05	8.05E+00
19.5 cm	1.03E+07	1.64E+11	6.31E-05	1.09E+07	2.18E+12	4.99E-06	7.61E+06	1.19E+06	6.39E+00	6.90E+06	1.00E+06	6.88E+00
20.5 cm	1.18E+07	8.72E+12	1.35E-06	1.55E+07	8.49E+12	1.82E-06	1.03E+07	7.14E+06	1.45E+00	7.90E+06	2.07E+06	3.82E+00
21.5 cm	1.28E+07	1.29E+13	9.87E-07	2.04E+07	1.11E+13	1.84E-06	1.33E+07	3.05E+07	4.35E-01	8.57E+06	5.54E+06	1.55E+00
22.5 cm	1.57E+07	1.72E+13	9.17E-07	2.56E+07	1.46E+13	1.75E-06	1.54E+07	7.07E+07	2.17E-01	9.16E+06	3.15E+07	2.91E-01
23.5 cm	1.98E+07	2.29E+13	8.66E-07	2.77E+07	1.87E+13	1.48E-06	1.56E+07	3.30E+08	4.74E-02	9.39E+06	1.03E+08	9.11E-02
24.5 cm	2.23E+07	2.84E+13	7.84E-07	2.78E+07	2.39E+13	1.16E-06	1.37E+07	9.51E+09	1.45E-03	9.35E+06	2.45E+09	3.82E-03
25.5 cm	2.69E+07	6.39E+12	4.21E-06	3.02E+07	1.04E+13	2.90E-06	1.32E+07	7.98E+11	1.65E-05	9.58E+06	2.06E+11	4.66E-05
26.5 cm	2.86E+07	7.85E+11	3.64E-05	2.99E+07	7.00E+11	4.27E-05	1.22E+07	1.71E+13	7.12E-07	9.56E+06	1.16E+13	8.23E-07
27.5 cm	3.03E+07	1.15E+11	2.63E-04	2.92E+07	6.71E+10	4.36E-04	1.19E+07	2.36E+13	5.06E-07	9.58E+06	1.62E+13	5.89E-07

Table 7-2 The calculated CF_α for the center of the wheel paths in Section I

Depth	Transverse direction at Test Point 2			Transverse direction at Test Point 4			Longitudinal direction at Test Point 2			Longitudinal direction at Test Point 4		
	α_F	α_L	CF_α	α_F	α_L	CF_α	α_F	α_L	CF_α	α_F	α_L	CF_α
7.5 cm	4.49E+06	3.74E+08	1.20E-02	4.44E+06	6.46E+09	6.87E-04	1.35E+07	2.78E+09	4.84E-03	2.19E+08	1.28E+10	1.70E-02
8.5 cm	5.36E+06	1.58E+09	3.39E-03	4.68E+06	1.11E+10	4.22E-04	1.35E+07	6.21E+09	2.17E-03	5.97E+07	9.16E+09	6.52E-03
9.5 cm	9.31E+06	5.01E+09	1.86E-03	1.77E+07	1.13E+09	1.56E-02	9.71E+06	1.49E+09	6.49E-03	3.69E+07	4.54E+08	8.12E-02
10.5 cm	1.05E+07	9.16E+09	1.15E-03	1.29E+07	9.33E+08	1.38E-02	1.28E+07	5.43E+08	2.36E-02	3.04E+07	2.01E+07	1.51E+00
11.5 cm	8.17E+06	1.18E+10	6.93E-04	1.10E+07	6.00E+09	1.83E-03	8.34E+06	8.21E+08	1.02E-02	1.72E+07	1.50E+08	1.15E-01
12.5 cm	7.57E+06	1.41E+10	5.35E-04	6.76E+06	6.66E+09	1.02E-03	6.17E+06	1.04E+08	5.93E-02	7.11E+06	1.63E+07	4.35E-01
13.5 cm	5.48E+06	3.11E+09	1.77E-03	5.10E+06	2.37E+08	2.15E-02	5.24E+06	6.28E+05	8.35E+00	7.93E+06	9.04E+05	8.77E+00
14.5 cm	4.65E+06	3.92E+07	1.19E-01	4.51E+06	3.65E+05	1.23E+01	4.82E+06	6.38E+04	7.55E+01	8.64E+06	1.14E+05	7.57E+01
15.5 cm	4.39E+06	6.40E+05	6.87E+00	4.51E+06	2.58E+05	1.75E+01	4.63E+06	4.87E+05	9.51E+00	8.81E+06	9.10E+04	9.68E+01
16.5 cm	4.25E+06	1.42E+06	2.99E+00	5.29E+06	6.64E+05	7.97E+00	4.59E+06	1.29E+05	3.57E+01	1.08E+07	1.47E+05	7.36E+01
17.5 cm	4.19E+06	7.57E+05	5.54E+00	1.24E+07	4.60E+05	2.68E+01	4.72E+06	1.93E+05	2.45E+01	1.50E+07	1.89E+05	7.96E+01
18.5 cm	4.23E+06	6.64E+05	6.37E+00	1.45E+07	4.21E+05	3.45E+01	4.97E+06	2.86E+05	1.74E+01	1.98E+07	2.35E+05	8.42E+01
19.5 cm	4.42E+06	4.26E+05	1.04E+01	1.70E+07	6.58E+05	2.59E+01	5.29E+06	3.12E+05	1.69E+01	2.59E+07	2.76E+05	9.40E+01
20.5 cm	4.67E+06	1.73E+06	2.69E+00	1.96E+07	1.20E+06	1.63E+01	5.62E+06	3.20E+05	1.76E+01	3.04E+07	3.52E+05	8.62E+01
21.5 cm	5.14E+06	1.03E+07	5.01E-01	2.10E+07	4.98E+06	4.21E+00	5.86E+06	3.91E+05	1.50E+01	3.46E+07	4.94E+05	7.01E+01
22.5 cm	9.61E+06	2.33E+08	4.13E-02	2.29E+07	1.01E+08	2.28E-01	6.56E+06	5.59E+05	1.17E+01	4.20E+07	1.21E+06	3.49E+01
23.5 cm	1.53E+07	5.19E+10	2.95E-04	2.28E+07	2.26E+09	1.01E-02	6.76E+06	1.38E+06	4.90E+00	4.10E+07	2.56E+06	1.60E+01
24.5 cm	1.76E+07	4.02E+12	4.38E-06	2.32E+07	4.09E+12	5.67E-06	6.97E+06	4.23E+07	1.65E-01	4.32E+07	7.35E+07	5.88E-01
25.5 cm	1.94E+07	7.11E+12	2.73E-06	2.31E+07	8.14E+12	2.84E-06	7.29E+06	2.12E+11	3.43E-05	4.15E+07	7.52E+10	5.52E-04
26.5 cm	1.98E+07	1.32E+12	1.50E-05	2.25E+07	8.26E+11	2.73E-05	7.37E+06	3.90E+12	1.89E-06	4.11E+07	5.01E+12	8.20E-06
27.5 cm	1.99E+07	2.38E+10	8.37E-04	2.28E+07	2.28E+10	1.00E-03	7.54E+06	3.36E+11	2.24E-05	4.21E+07	2.04E+11	2.06E-04

Table 7-3 The calculated CF_α for the outer edge of the wheel paths in Section II

Depth	Transverse direction at Test Point 1			Transverse direction at Test Point 5			Longitudinal direction at Test Point 1			Longitudinal direction at Test Point 5		
	α_F	α_L	CF_α	α_F	α_L	CF_α	α_F	α_L	CF_α	α_F	α_L	CF_α
7.5 cm	4.90E+06	1.15E+12	4.25E-06	1.25E+07	1.45E+12	8.61E-06	5.96E+06	4.21E+11	1.42E-05	6.20E+06	8.54E+11	7.26E-06
8.5 cm	2.63E+06	1.26E+12	2.09E-06	5.02E+06	1.15E+12	4.38E-06	6.10E+06	2.43E+11	2.51E-05	6.26E+06	5.36E+11	1.17E-05
9.5 cm	1.69E+06	1.12E+12	1.51E-06	2.71E+06	1.10E+12	2.47E-06	3.64E+06	1.17E+11	3.10E-05	3.12E+06	3.95E+11	7.88E-06
10.5 cm	1.48E+06	7.79E+11	1.90E-06	2.26E+06	7.57E+11	2.99E-06	2.76E+06	2.73E+10	1.01E-04	2.53E+06	1.93E+11	1.31E-05
11.5 cm	1.37E+06	5.46E+11	2.52E-06	1.90E+06	5.52E+11	3.44E-06	2.25E+06	2.08E+08	1.08E-02	2.02E+06	1.17E+10	1.73E-04
12.5 cm	1.32E+06	4.37E+11	3.03E-06	1.67E+06	4.47E+11	3.73E-06	2.02E+06	2.33E+06	8.65E-01	1.85E+06	1.23E+08	1.51E-02
13.5 cm	1.40E+06	3.59E+11	3.90E-06	1.73E+06	3.22E+11	5.38E-06	1.96E+06	2.01E+05	9.78E+00	1.86E+06	2.42E+06	7.69E-01
14.5 cm	1.50E+06	3.31E+11	4.54E-06	1.90E+06	2.67E+11	7.12E-06	2.01E+06	1.43E+05	1.40E+01	1.99E+06	2.08E+05	9.56E+00
15.5 cm	1.69E+06	3.14E+11	5.40E-06	2.09E+06	2.59E+11	8.06E-06	2.15E+06	2.12E+05	1.01E+01	2.15E+06	1.87E+05	1.15E+01
16.5 cm	1.83E+06	3.23E+11	5.66E-06	2.24E+06	2.65E+11	8.45E-06	2.33E+06	3.73E+05	6.24E+00	2.29E+06	4.55E+05	5.02E+00
17.5 cm	1.85E+06	3.62E+11	5.12E-06	2.32E+06	2.86E+11	8.11E-06	2.52E+06	4.56E+05	5.53E+00	2.48E+06	6.82E+05	3.64E+00
18.5 cm	1.82E+06	4.03E+11	4.51E-06	2.36E+06	3.09E+11	7.62E-06	2.68E+06	8.22E+05	3.25E+00	2.60E+06	1.89E+06	1.38E+00
19.5 cm	1.88E+06	4.24E+11	4.42E-06	2.50E+06	3.21E+11	7.78E-06	2.86E+06	2.19E+06	1.31E+00	2.87E+06	1.34E+07	2.14E-01
20.5 cm	1.68E+06	4.90E+11	3.42E-06	2.55E+06	3.36E+11	7.59E-06	3.02E+06	9.21E+06	3.28E-01	3.14E+06	6.89E+07	4.56E-02
21.5 cm	1.62E+06	5.23E+11	3.09E-06	2.60E+06	3.26E+11	8.00E-06	3.01E+06	5.75E+07	5.23E-02	3.14E+06	3.82E+08	8.23E-03
22.5 cm	1.66E+06	4.96E+11	3.34E-06	2.67E+06	3.11E+11	8.58E-06	3.12E+06	4.07E+08	7.65E-03	3.23E+06	1.88E+09	1.72E-03
23.5 cm	1.55E+06	4.22E+11	3.67E-06	2.57E+06	2.73E+11	9.43E-06	3.09E+06	3.75E+09	8.24E-04	2.86E+06	1.20E+10	2.39E-04
24.5 cm	1.54E+06	3.41E+11	4.53E-06	2.53E+06	2.28E+11	1.11E-05	3.01E+06	2.81E+10	1.07E-04	2.80E+06	4.96E+10	5.63E-05
25.5 cm	1.42E+06	2.70E+11	5.25E-06	2.47E+06	1.86E+11	1.33E-05	2.95E+06	3.94E+10	7.48E-05	2.71E+06	5.31E+10	5.10E-05
26.5 cm	1.39E+06	2.05E+11	6.79E-06	2.41E+06	1.46E+11	1.65E-05	2.86E+06	3.03E+10	9.43E-05	2.62E+06	4.04E+10	6.48E-05
27.5 cm	1.37E+06	1.51E+11	9.08E-06	2.35E+06	1.11E+11	2.11E-05	2.79E+06	2.20E+10	1.27E-04	2.54E+06	2.91E+10	8.70E-05

Table 7-4 The calculated CF_α for the center of the wheel paths in Section II

Depth	Transverse direction at Test Point 2			Transverse direction at Test Point 4			Longitudinal direction at Test Point 2			Longitudinal direction at Test Point 4		
	α_F	α_L	CF_α	α_F	α_L	CF_α	α_F	α_L	CF_α	α_F	α_L	CF_α
7.5 cm	6.01E+06	1.59E+11	3.77E-05	4.85E+06	2.96E+11	1.64E-05	8.62E+06	8.21E+10	1.05E-04	1.67E+07	6.06E+11	2.75E-05
8.5 cm	3.99E+06	8.40E+10	4.74E-05	3.76E+06	1.46E+11	2.58E-05	5.50E+06	4.23E+10	1.30E-04	1.51E+07	2.47E+11	6.10E-05
9.5 cm	2.69E+06	5.39E+10	4.99E-05	2.57E+06	7.57E+10	3.39E-05	2.83E+06	2.49E+10	1.14E-04	6.79E+06	1.50E+11	4.53E-05
10.5 cm	2.35E+06	3.73E+10	6.31E-05	2.75E+06	4.09E+10	6.74E-05	2.50E+06	7.02E+09	3.57E-04	4.17E+06	9.32E+10	4.48E-05
11.5 cm	1.97E+06	1.61E+10	1.22E-04	2.44E+06	1.93E+10	1.27E-04	2.29E+06	1.90E+08	1.21E-02	3.28E+06	6.53E+10	5.02E-05
12.5 cm	1.85E+06	7.11E+08	2.61E-03	2.23E+06	3.87E+08	5.77E-03	2.25E+06	1.52E+07	1.48E-01	2.42E+06	3.45E+09	6.99E-04
13.5 cm	1.82E+06	1.10E+07	1.66E-01	2.22E+06	1.70E+06	1.30E+00	2.25E+06	3.45E+05	6.52E+00	2.04E+06	2.25E+07	9.04E-02
14.5 cm	1.84E+06	2.84E+05	6.49E+00	2.26E+06	1.09E+05	2.08E+01	2.33E+06	6.68E+04	3.50E+01	1.79E+06	2.16E+05	8.28E+00
15.5 cm	1.92E+06	1.06E+05	1.82E+01	2.45E+06	4.38E+06	5.60E-01	2.50E+06	2.55E+05	9.81E+00	1.70E+06	2.38E+05	7.12E+00
16.5 cm	2.05E+06	6.36E+05	3.23E+00	2.69E+06	3.96E+08	6.79E-03	2.66E+06	9.03E+05	2.94E+00	1.67E+06	6.90E+05	2.42E+00
17.5 cm	2.09E+06	1.65E+06	1.27E+00	3.02E+06	1.18E+10	2.57E-04	2.84E+06	2.53E+06	1.12E+00	1.58E+06	5.50E+05	2.88E+00
18.5 cm	2.13E+06	6.86E+06	3.10E-01	2.84E+06	4.69E+08	6.05E-03	2.98E+06	6.08E+06	4.90E-01	1.51E+06	3.62E+05	4.17E+00
19.5 cm	2.17E+06	6.05E+07	3.58E-02	2.47E+06	1.25E+09	1.98E-03	3.13E+06	1.56E+07	2.01E-01	1.50E+06	5.28E+05	2.85E+00
20.5 cm	2.11E+06	1.40E+08	1.51E-02	2.15E+06	1.33E+10	1.62E-04	3.03E+06	1.64E+07	1.85E-01	1.48E+06	5.57E+05	2.66E+00
21.5 cm	2.06E+06	1.33E+09	1.55E-03	1.76E+06	5.75E+10	3.06E-05	2.96E+06	4.94E+07	5.99E-02	1.60E+06	8.58E+05	1.86E+00
22.5 cm	2.09E+06	3.56E+10	5.87E-05	1.69E+06	8.87E+10	1.91E-05	3.02E+06	2.12E+08	1.42E-02	1.78E+06	4.37E+06	4.09E-01
23.5 cm	1.95E+06	5.24E+10	3.73E-05	1.55E+06	7.51E+10	2.06E-05	2.62E+06	8.75E+08	3.00E-03	1.83E+06	5.84E+07	3.14E-02
24.5 cm	1.93E+06	4.22E+10	4.58E-05	1.52E+06	5.93E+10	2.56E-05	2.61E+06	1.68E+10	1.55E-04	1.96E+06	8.81E+09	2.22E-04
25.5 cm	1.89E+06	3.22E+10	5.86E-05	1.44E+06	4.48E+10	3.22E-05	2.49E+06	1.56E+10	1.60E-04	2.01E+06	2.76E+10	7.29E-05
26.5 cm	1.86E+06	2.23E+10	8.36E-05	1.39E+06	3.22E+10	4.30E-05	2.44E+06	1.11E+10	2.20E-04	1.94E+06	2.01E+10	9.65E-05
27.5 cm	1.83E+06	1.37E+10	1.34E-04	1.34E+06	2.22E+10	6.03E-05	2.39E+06	7.60E+09	3.15E-04	1.88E+06	1.41E+10	1.33E-04

In light of the need for practicality in engineering applications, the study consolidates and averages the conversion factors for various locations and directions within each section, as detailed in Table 7-5. This methodological approach offers a streamlined and efficient application of these insights for real-world engineering scenarios, balancing accuracy with operational feasibility.

Table 7-5 The summarized CF_{α} for both sections

Section	Outer edge of the wheel paths		Center of the wheel paths		Average
	Transverse	Longitudinal	Transverse	Longitudinal	
Section I	6.17E-03	2.11E+00	4.32E+00	2.29E+01	7.32E+00
Section II	6.23E-06	1.99E+00	1.25E+00	2.12E+00	1.34E+00

The data analysis reveals that the conversion factor CF_{α} exhibits its minimum value in the direction perpendicular to the loading direction at the outer edge of the wheel paths, while its maximum is observed in the direction parallel to the loading direction at the center of the wheel paths. This finding indicates a tendency of laboratory fatigue tests to overestimate the fatigue life of asphalt layers at the outer edge of wheel paths in the direction perpendicular to the loading. Such overestimation could lead to inadequate fatigue design in these specific areas, increasing the risk of cracking along the wheel load direction. Conversely, these tests tend to provide conservative estimates of the fatigue life of asphalt layers at the center of the wheel paths in the direction parallel to the loading, potentially resulting in an overly cautious approach in the fatigue design of these areas.

Further comparison between the two sections highlights a notable distinction: CF_{α} for Section I, characterized by a semi-rigid base, is higher than that for Section II, with a flexible base. This disparity suggests that the current methods of laboratory fatigue tests and design are less suitable for semi-rigid pavements when compared to flexible pavements. This observation underscores the necessity for further enhancement and adaptation of these methods, ensuring their effectiveness and applicability in the context of semi-rigid pavement scenarios.

7.2 Comparative Analysis of Parameter β

Employing the conversion equation method and an S-shaped function, §4.4.4 introduces the development of a unified expression for the shape factor β of laboratory asphalt mixtures under various fatigue loading modes:

$$\beta_L = F'_{\beta L} \cdot \beta_{L-\sigma} \quad 7\text{-}6$$

$$F'_{\beta L} = 1 + \frac{F_{\beta L} - 1}{1 + e^{k_{\beta L} \cdot \mathrm{MF}}} = 1 + \frac{e^{-2.650} \cdot {\varepsilon_0}^{0.510} \cdot (LR)^{-0.095} - 1}{1 + e^{(-9.210 + 0.936 \ln(\varepsilon_0)) \cdot \mathrm{MF}}} \quad 7\text{-}7$$

$$\beta_{L-\sigma} = e^{-2.717 + 0.462 \ln(\varepsilon_0) + 0.087 \ln(LR)} \quad 7\text{-}8$$

This expression is formulated to be responsive to the initial tensile strain amplitude ε_{t0}, the loading rate LR, and the tensile fatigue loading mode MF. In the quest to establish a connection between the β of asphalt mixtures in laboratory settings and their counterparts in structural applications, the study incorporates in-situ loading factors into this laboratory-derived β interpretation equation. This requires assessing the initial strain at different depths of the asphalt, the LR, and the fatigue loading mode during the F-sAPTs.

In a process analogous to the analysis of α, the initial tensile strain amplitude ε_{t0} in the equation is replaced with the combined total of the initial tensile strain ε_{t0} and initial shear strain ε_{s0}, as calculated from the finite element model illustrated in Figure 5-23. By summing these strains and utilizing the average loading frequency of 3.22 Hz, the LR is determined. The equation also integrates a combined fatigue loading mode CMF, as suggested in §6.2.3.

With these variables incorporated into the equation, the resulting calculation provides the shape factor β_F of the laboratory asphalt mixture under the loading conditions in the F-sAPTs. Consequently, a conversion factor CF_β is established, bridging the gap between model parameters derived from laboratory tests and those from F-sAPTs data. This factor is formulated as follows:

$$\mathrm{CF}_\beta = \frac{\beta_F}{\beta_L} \quad 7\text{-}9$$

The results of this analytical process, including the values for Sections I and II, are comprehensively presented in Table 7-6 to Table 7-9.

Table 7-6 The calculated CF_β for the outer edge of the wheel paths in Section I

Depth	Transverse direction at Test Point 1			Transverse direction at Test Point 5			Longitudinal direction at Test Point 1			Longitudinal direction at Test Point 5		
	β_F	β_L	CF_β	β_F	β_L	CF_β	β_F	β_L	CF_β	β_F	β_L	CF_β
7.5 cm	1.84	0.15	12.60	16.81	0.17	97.37	0.78	0.31	2.48	1.07	0.39	2.73
8.5 cm	1.57	0.14	11.33	4.38	0.23	19.02	0.68	0.27	2.51	0.95	0.27	3.52
9.5 cm	0.99	0.18	5.60	1.93	0.28	6.94	0.62	0.33	1.86	0.74	0.31	2.39
10.5 cm	0.91	0.27	3.37	1.91	0.34	5.64	0.84	0.39	2.16	0.54	0.31	1.74
11.5 cm	0.87	0.29	3.03	2.00	0.35	5.66	1.13	0.45	2.52	0.92	0.38	2.44
12.5 cm	0.81	0.33	2.48	1.84	0.37	4.99	1.24	0.48	2.58	1.08	0.45	2.38
13.5 cm	0.70	0.35	2.02	1.47	0.38	3.89	1.18	0.49	2.43	1.10	0.49	2.26
14.5 cm	0.67	0.35	1.89	1.31	0.37	3.53	1.07	0.48	2.21	1.12	0.49	2.30
15.5 cm	0.63	0.35	1.78	1.20	0.38	3.16	0.96	0.47	2.02	1.07	0.48	2.25
16.5 cm	0.58	0.36	1.63	1.09	0.37	2.92	0.86	0.46	1.85	1.00	0.47	2.14
17.5 cm	0.55	0.35	1.55	0.94	0.37	2.57	0.76	0.45	1.70	0.87	0.45	1.93
18.5 cm	0.51	0.34	1.53	0.76	0.33	2.29	0.65	0.44	1.50	0.75	0.44	1.72
19.5 cm	0.48	0.29	1.65	0.62	0.23	2.67	0.55	0.42	1.30	0.68	0.42	1.61
20.5 cm	0.44	0.16	2.87	0.50	0.11	4.66	0.41	0.40	1.02	0.59	0.41	1.45
21.5 cm	0.42	0.07	5.94	0.43	0.07	6.00	0.32	0.38	0.82	0.54	0.39	1.36
22.5 cm	0.37	0.06	6.03	0.38	0.06	6.05	0.26	0.37	0.72	0.50	0.38	1.32
23.5 cm	0.32	0.07	4.37	0.36	0.07	5.52	0.22	0.35	0.64	0.48	0.36	1.32
24.5 cm	0.29	0.12	2.33	0.35	0.10	3.60	0.23	0.32	0.71	0.47	0.34	1.37
25.5 cm	0.25	0.21	1.24	0.34	0.19	1.76	0.22	0.26	0.86	0.45	0.29	1.56
26.5 cm	0.24	0.24	0.99	0.33	0.25	1.33	0.22	0.08	2.58	0.44	0.11	4.02
27.5 cm	0.23	0.25	0.90	0.33	0.27	1.24	0.21	0.06	3.30	0.43	0.07	6.44

Table 7-7 The calculated CF_β for the center of the wheel paths in Section I

Depth	Transverse direction at Test Point 2			Transverse direction at Test Point 4			Longitudinal direction at Test Point 2			Longitudinal direction at Test Point 4		
	β_F	β_L	CF_β	β_F	β_L	CF_β	β_F	β_L	CF_β	β_F	β_L	CF_β
7.5 cm	1.38	0.58	2.37	1.54	0.48	3.22	0.47	0.53	0.89	0.20	0.38	0.53
8.5 cm	1.21	0.55	2.21	1.55	0.44	3.55	0.52	0.48	1.09	0.28	0.44	0.65
9.5 cm	0.77	0.49	1.55	0.42	0.56	0.76	0.62	0.56	1.11	0.29	0.60	0.49
10.5 cm	0.72	0.45	1.59	0.54	0.56	0.96	0.50	0.60	0.83	0.30	0.67	0.45
11.5 cm	0.89	0.43	2.05	0.64	0.48	1.33	0.75	0.58	1.28	0.45	0.63	0.72
12.5 cm	0.93	0.42	2.19	1.00	0.48	2.10	0.99	0.63	1.57	0.90	0.66	1.36
13.5 cm	1.26	0.50	2.50	1.34	0.57	2.36	1.13	0.67	1.68	0.76	0.66	1.14
14.5 cm	1.49	0.58	2.56	1.52	0.60	2.52	1.22	0.66	1.84	0.66	0.65	1.03
15.5 cm	1.55	0.58	2.66	1.42	0.58	2.44	1.27	0.63	2.02	0.63	0.63	1.01
16.5 cm	1.58	0.56	2.83	1.04	0.55	1.88	1.29	0.61	2.12	0.52	0.60	0.87
17.5 cm	1.57	0.54	2.94	0.43	0.52	0.82	1.25	0.59	2.13	0.42	0.57	0.72
18.5 cm	1.52	0.51	2.96	0.37	0.50	0.75	1.16	0.56	2.06	0.36	0.55	0.65
19.5 cm	1.41	0.49	2.88	0.34	0.48	0.71	1.08	0.54	2.00	0.31	0.53	0.59
20.5 cm	1.29	0.46	2.78	0.31	0.45	0.68	1.01	0.52	1.97	0.29	0.50	0.57
21.5 cm	1.12	0.44	2.54	0.29	0.43	0.68	0.98	0.49	1.98	0.27	0.48	0.57
22.5 cm	0.57	0.41	1.40	0.27	0.40	0.68	0.89	0.47	1.89	0.25	0.45	0.55
23.5 cm	0.40	0.33	1.19	0.26	0.37	0.71	0.86	0.44	1.93	0.24	0.43	0.56
24.5 cm	0.35	0.14	2.47	0.25	0.18	1.42	0.83	0.41	1.99	0.23	0.40	0.57
25.5 cm	0.32	0.08	4.06	0.24	0.08	3.02	0.79	0.30	2.60	0.23	0.32	0.70
26.5 cm	0.31	0.25	1.26	0.24	0.26	0.93	0.78	0.08	9.21	0.22	0.08	2.67
27.5 cm	0.30	0.29	1.05	0.24	0.29	0.82	0.76	0.28	2.72	0.22	0.29	0.76

Table 7-8 The calculated CF_{β} for the outer edge of the wheel paths in Section II

Depth	Transverse direction at Test Point 1			Transverse direction at Test Point 5			Longitudinal direction at Test Point 1			Longitudinal direction at Test Point 5		
	β_F	β_L	CF_{β}	β_F	β_L	CF_{β}	β_F	β_L	CF_{β}	β_F	β_L	CF_{β}
7.5 cm	0.40	0.10	3.86	0.25	0.10	2.55	0.23	0.17	1.33	0.20	0.14	1.40
8.5 cm	0.53	0.10	5.16	0.49	0.10	4.64	0.29	0.20	1.42	0.23	0.16	1.45
9.5 cm	0.70	0.11	6.54	0.61	0.11	5.75	0.55	0.28	1.98	0.30	0.19	1.57
10.5 cm	0.72	0.12	6.11	0.62	0.12	5.29	0.74	0.40	1.85	0.44	0.28	1.61
11.5 cm	0.70	0.13	5.24	0.67	0.13	5.13	0.78	0.53	1.47	0.58	0.42	1.36
12.5 cm	0.61	0.15	4.07	0.70	0.15	4.65	0.75	0.57	1.31	0.58	0.52	1.13
13.5 cm	0.54	0.17	3.15	0.67	0.18	3.62	0.68	0.58	1.17	0.56	0.55	1.02
14.5 cm	0.47	0.19	2.52	0.58	0.21	2.69	0.62	0.58	1.06	0.54	0.56	0.96
15.5 cm	0.42	0.20	2.13	0.50	0.22	2.24	0.57	0.58	0.99	0.51	0.56	0.92
16.5 cm	0.39	0.20	1.97	0.44	0.22	1.99	0.53	0.58	0.92	0.49	0.56	0.88
17.5 cm	0.37	0.18	1.98	0.41	0.22	1.91	0.48	0.57	0.84	0.44	0.55	0.80
18.5 cm	0.34	0.18	1.91	0.40	0.21	1.95	0.44	0.57	0.77	0.42	0.55	0.77
19.5 cm	0.34	0.18	1.88	0.42	0.19	2.21	0.42	0.56	0.75	0.42	0.54	0.77
20.5 cm	0.31	0.17	1.86	0.43	0.20	2.10	0.41	0.56	0.73	0.40	0.53	0.76
21.5 cm	0.31	0.16	1.93	0.45	0.23	1.96	0.40	0.54	0.73	0.39	0.51	0.77
22.5 cm	0.31	0.15	1.99	0.49	0.20	2.42	0.40	0.52	0.76	0.38	0.48	0.78
23.5 cm	0.30	0.15	1.99	0.51	0.20	2.59	0.39	0.48	0.82	0.37	0.43	0.84
24.5 cm	0.31	0.15	2.06	0.54	0.19	2.81	0.40	0.39	1.02	0.37	0.35	1.06
25.5 cm	0.31	0.15	2.01	0.55	0.19	2.91	0.40	0.29	1.37	0.37	0.27	1.37
26.5 cm	0.32	0.16	1.99	0.57	0.19	2.99	0.41	0.24	1.68	0.38	0.23	1.64
27.5 cm	0.32	0.17	1.94	0.58	0.19	3.03	0.41	0.23	1.75	0.38	0.22	1.71

Table 7-9 The calculated CF_{β} for the center of the wheel paths in Section II

Depth	Transverse direction at Test Point 2			Transverse direction at Test Point 4			Longitudinal direction at Test Point 2			Longitudinal direction at Test Point 4		
	β_F	β_L	CF_{β}	β_F	β_L	CF_{β}	β_F	β_L	CF_{β}	β_F	β_L	CF_{β}
7.5 cm	0.23	0.17	1.36	0.16	0.15	1.11	0.24	0.21	1.11	0.15	0.15	1.05
8.5 cm	0.30	0.20	1.48	0.17	0.18	0.95	0.37	0.26	1.46	0.23	0.17	1.31
9.5 cm	0.39	0.25	1.57	0.28	0.23	1.22	0.73	0.36	2.02	0.32	0.21	1.52
10.5 cm	0.52	0.31	1.67	0.57	0.30	1.90	0.80	0.47	1.68	0.54	0.25	2.12
11.5 cm	0.65	0.42	1.52	0.75	0.41	1.82	0.77	0.60	1.30	0.59	0.32	1.85
12.5 cm	0.65	0.54	1.19	0.75	0.56	1.34	0.63	0.63	0.99	0.68	0.48	1.41
13.5 cm	0.60	0.61	0.98	0.73	0.62	1.19	0.59	0.66	0.89	0.65	0.56	1.15
14.5 cm	0.55	0.62	0.89	0.68	0.62	1.10	0.54	0.66	0.81	0.60	0.58	1.05
15.5 cm	0.52	0.61	0.85	0.63	0.60	1.05	0.51	0.65	0.79	0.56	0.57	0.99
16.5 cm	0.50	0.60	0.84	0.59	0.54	1.10	0.48	0.63	0.76	0.50	0.56	0.89
17.5 cm	0.47	0.59	0.79	0.52	0.44	1.19	0.45	0.62	0.72	0.41	0.56	0.73
18.5 cm	0.44	0.58	0.77	0.31	0.52	0.60	0.41	0.61	0.67	0.37	0.56	0.66
19.5 cm	0.43	0.55	0.77	0.26	0.49	0.53	0.37	0.60	0.62	0.36	0.56	0.63
20.5 cm	0.40	0.54	0.73	0.25	0.43	0.58	0.32	0.60	0.53	0.34	0.57	0.60
21.5 cm	0.39	0.50	0.77	0.23	0.35	0.66	0.29	0.59	0.50	0.35	0.58	0.61
22.5 cm	0.39	0.38	1.03	0.23	0.24	0.97	0.28	0.57	0.48	0.36	0.58	0.62
23.5 cm	0.37	0.23	1.62	0.23	0.18	1.26	0.25	0.55	0.46	0.38	0.57	0.66
24.5 cm	0.39	0.20	1.94	0.24	0.19	1.27	0.26	0.40	0.66	0.40	0.46	0.88
25.5 cm	0.40	0.26	1.51	0.24	0.22	1.09	0.26	0.26	1.00	0.42	0.25	1.70
26.5 cm	0.40	0.34	1.17	0.25	0.27	0.91	0.27	0.26	1.01	0.43	0.23	1.84
27.5 cm	0.41	0.40	1.02	0.25	0.31	0.80	0.27	0.32	0.86	0.43	0.28	1.52

The analysis of data in the tables demonstrates that the conversion factor varies with the structure of the pavement and is influenced by the depth of the asphalt layer. Even within the same pavement structure, the values of CF_β differ at various depths. Further analysis reveals that, even at identical depths, the values of CF_β are not consistent across different test points and directions.

These observations highlight the complexity of the relationship between the shape factor β obtained from laboratory tests and those derived from F-sAPTs data. Since β is indicative of the patterns of fatigue damage, and these findings further elucidate the limitations of the laboratory fatigue tests in terms of their representativeness. It becomes evident that the damage progressions obtained from laboratory fatigue tests may not effectively or directly represent the fatigue damage progression in asphalt layers.

To facilitate practical application in engineering projects, the study has aggregated and averaged the conversion factors for different positions and directions within each section, as detailed in Table 7-10. This approach simplifies the application of these findings, making them more accessible and utilizable in real-world engineering contexts, while still acknowledging the nuanced complexities inherent in the data.

Table 7-10 The summarized CF_β for both sections

Section	Outer edge of the wheel paths		Center of the wheel paths		Average
	Transverse	Longitudinal	Transverse	Longitudinal	
Section I	6.33	2.05	1.91	1.48	2.94
Section II	3.04	1.15	1.12	1.03	1.58

The examination of the data indicates that the conversion factor CF_β attains its maximum value in the direction perpendicular to the loading at the outer edge of the wheel paths, and its minimum value in the direction parallel to the loading at the center of the wheel paths, with all values exceeding 1. This implies a greater disparity in the shape of the fatigue damage curves between the field asphalt layer and the laboratory asphalt mixture at the outer edge of the wheel paths, where the curves tend more towards an S-shape or convex configuration. Conversely, at the center of the wheel paths, parallel to the loading direction, the shape of the fatigue damage curves between the field asphalt layer and the laboratory asphalt mixture shows a smaller variance.

Further analysis of the two sections reveals that CF_β for Section I, characterized by a semi-rigid base, exceeds that of Section II, which has a flexible base. This pattern mirrors the findings

from the CF_α analysis and suggests that the existing laboratory fatigue testing and design methodologies are less applicable to semi-rigid pavements as compared to flexible ones. This observation underscores the need for enhancements and modifications in these methods to better cater to the specificities and demands of semi-rigid pavements.

7.3 Summary

This chapter establishes a definitive correlation between the evolution of fatigue damage in laboratory asphalt mixtures and asphalt layers in structural applications. It employs regression analysis from the SBF to conduct a comparative analysis that aligns the life factor α and the shape factor β across laboratory and real-world settings. The process begins by incorporating in-situ loading parameters into equations for interpreting laboratory-based α and β. Then, a conversion factor is introduced for each parameter, meticulously designed to bridge the gap between parameters derived from laboratory tests and those from the F-sAPTs. This approach is pivotal for translating laboratory fatigue test results into practical, applicable insights for pavement condition assessments and engineering applications.

The main findings of this chapter are as follows:

(1) A complex relationship exists between the fatigue damage progressions observed in laboratory settings and actual asphalt layers. The conversion factors for both α and β show variability depending on pavement structure and are notably influenced by the depth of the asphalt layer. Furthermore, at identical depths, the values of conversion factors exhibit differences across different test points and directions.

(2) The conversion factor for α reaches its lowest value perpendicular to the loading direction at the outer edge of wheel paths, while its highest value is noted parallel to the loading direction at the center of the wheel paths. This indicates that laboratory tests may overestimate the fatigue damage of asphalt layers at the outer edges of wheel paths, leading to potential underdesign in these areas and a higher risk of cracking. Conversely, the tests tend to conservatively estimate the fatigue damage at the center of wheel paths, possibly resulting in an overly cautious design approach in these locations.

(3) The conversion factor for β is also found to peak in the direction perpendicular to the loading

at the outer edge of the wheel paths and is at its lowest parallel to the loading at the center of the paths. This variation suggests a significant discrepancy in the fatigue damage curve shapes between field and laboratory conditions, particularly at the outer edge of the wheel paths, where the curves tend more toward an S-shape or convex form. In contrast, the variance in curve shape is less marked at the center of the paths.

(4) Both the conversion factors for α and β are higher for Section I with a semi-rigid base than for Section II with a flexible base. This suggests that current laboratory fatigue testing and design methods are less suitable for semi-rigid pavements compared to flexible ones, highlighting a need for methodological improvements to accommodate the unique requirements of semi-rigid pavement structures.

8 CONCLUSIONS AND CONTRIBUTIONS

8.1 Conclusions

The study synthesizes the insights into the fatigue damage evolution of asphalt mixtures and asphalt layers, bridging a significant gap in existing understanding. Initially, it explores the fatigue behavior assessments of asphalt mixtures through ITFT and 4PB tests under varied loading conditions, analyzing the impact of key factors on the initial stiffness and fatigue life. Then, it further compares various nonlinear models to accurately depict the laboratory-derived fatigue damage evolution, aiming to identify the most suitable model that accounts for the multifaceted influences of various factors and enhances the interpretability in response to different tensile fatigue loadings. Additionally, it employs F-sAPT and a damage variable of SSR, with refined temperature and frequency adjustments, to evaluate the fatigue damage progressions of asphalt layers. This leads to a comparative study of the Weibull survival function (WSF) and the structural behavior function (SBF), focusing on their applicability in real-world pavement conditions. Furthermore, this study delves into the mechanical mechanisms behind fatigue damage, identifying the critical damage locations in different pavement types and introducing the novel tensile-shear loading mode factor. Finally, it integrates in-situ loading parameters with laboratory-based models, introducing a conversion factor for a seamless correlation between laboratory and real-world environments, thereby translating theoretical insights into practical engineering solutions for pavement fatigue management. The key conclusions of this study include:

(1) Based on the laboratory ITFT and 4PB test results, the study underlines the criticality of considering the load's magnitude and duration, or the loading rate, when measuring mixture stiffness, necessitating corrections for a unified standard. Equally important is the fatigue life assessment, which must factor in the load's magnitude and the balance of rest time to loading time, regardless of the test method used. Notably, the fatigue loading mode also has a significant influence on fatigue life. Correspondingly, this study introduces a unified prediction approach for fatigue life, advancing beyond traditional conversion function methods. This novel approach accounts for the nonlinearity in the fatigue damage process of asphalt mixtures and the complex

relationship between the conversion function and the varying fatigue loading modes.

(2) Based on the F-sAPT results, it was found that the detected modules of asphalt layers can be effectively temperature-corrected by employing a semi-logarithmic relationship between the modulus and temperature and frequency-adjusted by utilizing a modulus master curve. Additionally, utilizing SSR as the damage variable, this study observes a significant increase in the damage of asphalt layers with increasing load repetitions, characterized by a non-uniform pattern, varying with depth and detection specifics, indicating the complex nature of asphalt layer fatigue under operational conditions.

(3) The structural behavior function (SBF) emerges as the most effective and rational model for depicting fatigue damage progressions of asphalt mixtures and asphalt layers. While all analyzed models, including the Weibull survival function (WSF), satisfy boundary conditions and demonstrate a consistent increase in the damage variable with load applications, the SBF stands out due to its clear and independent parameterization. In the SBF, the model parameters α and β distinctly represent the fatigue life and the shape of the fatigue damage evolution curve, respectively, showing definitive correlations with various loading factors. This correlation indicates that any complex damage progression can be effectively related to these parameters. Additionally, the SBF model offers clearer parameter interpretations and maintains stability against minor data variations, making it more suitable than the WSF, whose parameters exhibit less stability and clarity in physical significance. Consequently, the SBF is recommended for describing the fatigue damage progression, especially under the influence of multiple loading factors.

(4) The critical damage locations within the asphalt layers can be obtained by comparing the profile of α, tensile strain, and shear strain, along with the sum of these strains across depths. It concludes that these critical damage positions are determined by the interplay of tensile and shear forces. Notably, for asphalt pavements with semi-rigid bases, the critical damage location is identified within the middle of the asphalt layer. In contrast, asphalt pavements with flexible bases exhibit multiple critical damage locations – one in the middle and another at the bottom of the asphalt layer.

(5) The analysis of fatigue mode at various depths within the asphalt layer reveals a complex and varied fatigue evolution process. It is evident that for the same pavement structure, the fatigue

loading mode of asphalt layers differ not only at different depths but also at different test points and detection directions at the same depth. This complexity indicates that a single pavement structure cannot be linked with a specific fatigue loading mode, nor can the fatigue loading mode of the asphalt layer be simply correlated with its thickness. Additionally, the study concludes that using only the tensile fatigue mode factor is insufficient to accurately reflect the fatigue damage process within the asphalt layer. Instead, a tensile-shear fatigue mode factor is recommended for a more representative assessment of fatigue damage.

(6) A definitive correlation between the evolution of fatigue damage in laboratory asphalt mixtures and in structural asphalt layers can be established by a direct comparison between the model parameters of SBF derived in both laboratory and real-world environments. This study reveals the complexity of this relationship. Crucially, it identifies that the conversion factors for the SBF parameters α and β vary significantly depending on the pavement structure and are particularly influenced by the depth of the asphalt layer. This variability is further pronounced at identical depths across different test points and directions. This highlights that damage progressions derived from laboratory fatigue tests may not effectively or directly represent the real-world fatigue damage progression in asphalt layers. Additionally, it is noted that current laboratory fatigue testing and design methods are less suited for semi-rigid pavements compared to flexible pavements. This finding underscores the need for methodological advancements to better address the distinct characteristics of semi-rigid pavement structures.

8.2 Contributions

This research makes pivotal advancements encapsulated in four key areas:

(1) Development of damage evolution equations: This study identifies the efficacy of the SBF. The SBF model exhibits superior fitting capabilities for the fatigue damage evolution processes. Importantly, the parameters of this model are characterized by high interpretability, with a clear physical significance in their depth-wise distribution, laying a robust foundation for advanced fatigue damage research.

(2) Analysis of critical damage locations: This research provides a groundbreaking analysis of critical damage locations within the asphalt layers. Contrary to previous assumptions, it reveals

that these critical locations correlate not just with the distribution of tensile and shear strains along the depth of the asphalt layer, but also align with the maximum cumulative depth of these strains. The study further elucidates that in a single pavement structure, multiple critical damage locations can exist, challenging the traditional view of considering only the bottom of the asphalt layer as the primary site for fatigue analysis.

(3) Introduction of tensile-shear fatigue loading modes: The study introduces a novel concept in pavement engineering – the tensile-shear fatigue loading mode. Through detailed analysis, it establishes that fatigue loading modes differ across various depths of the same pavement structure and even vary at the same depth when considering different test points and orientations. This finding underscores the complexity of fatigue evolution in pavement structures, indicating that a single, standardized fatigue loading mode is not universally applicable. It also decouples the simplistic association of fatigue loading modes with asphalt layer thickness, highlighting a more nuanced understanding of pavement behavior.

(4) Correlation of fatigue damage evolution: A significant contribution of this research is establishing a correlation between the evolution of fatigue damage in laboratory asphalt mixtures and in structural asphalt layers, based on the SBF model. This innovative approach, recognizing the nonlinear nature of fatigue damage progression, deviates from the conventional methodology of translating laboratory-derived fatigue life into field applications. Instead, it proposes a unified framework for understanding and analyzing fatigue damage processes in both controlled laboratory environments and real-world field conditions.

8.3 Limitations and Future Study

While this research has achieved significant breakthroughs in understanding and managing fatigue damage in asphalt pavements, it is not without its limitations. Recognizing these constraints is essential for guiding future studies in this field. Accordingly, the scope for subsequent research is delineated below, meticulously addressing the identified limitations and proposing strategic pathways for further investigation.

(1) Diversification of pavement structures and asphalt mixtures: The current study's scope was confined to a limited range of pavement structures and asphalt mixture types, specifically

focusing on two types of asphalt pavements for full-scale accelerated loading tests and one asphalt mixture for laboratory fatigue tests. Future research should aim to encompass a wider variety of pavement structures and asphalt mixtures. This expansion is essential for a more comprehensive validation and refinement of the study's findings, ensuring the applicability of the results across diverse scenarios.

(2) Refinement of the established predictive models for asphalt mixtures: The study's proposed equations for estimating the fatigue life of asphalt mixtures and the interpretative equations for parameters of the SBF primarily account for initial strain levels, diverse loading factors, or the damage state. However, the internal factors influencing the asphalt mixture's stiffness may also play a crucial role in the progression of damage. Future studies should integrate these internal factors into the existing models to enhance their predictive accuracy and applicability, thereby advancing the methodology for fatigue damage estimation in asphalt mixtures.

(3) Holistic analysis of the environmental and material influencing factors for asphalt layers: The study acknowledges that factors such as the material characteristics of asphalt mixtures, their aging status, traffic lateral wandering, and environmental conditions (including temperature and humidity) can significantly influence the damage evolution in asphalt layers. Subsequent research should undertake a multifaceted analysis that also incorporates these crucial aspects. This comprehensive approach would facilitate a more nuanced and accurate refinement of the current study's outcomes, enhancing the understanding of fatigue damage in asphalt layers.

(4) Quantitative analysis of the variations of fatigue loading mode: While this research conducted a qualitative analysis of the variations of fatigue loading mode with the depth of asphalt layers, there is a clear need for a quantitative approach. Future studies could leverage big data analytics to establish a detailed quantitative relationship between the fatigue loading mode and their influencing factors.